Spatial Selectivity of Photodeposition Reactions on Centrosymmetric, Polycrystalline Oxide Photocatalysts

Submitted in partial fulfillment of the requirements for the

degree of

Doctor of Philosophy in

Department of Materials Science and Engineering

Ajay S. Pisat

B.Tech., Metallurgical and Materials Engineering, Indian Institute of Technology Madras
M.Tech., Metallurgical and Materials Engineering, Indian Institute of Technology Madras
M.S., Materials Science and Engineering, Carnegie Mellon University

Carnegie Mellon University
Pittsburgh, PA

December 2019

Acknowledgements

I would like to take this opportunity to express my gratitude and thank those who have made my doctoral journey a smooth and a stress-free one. Firstly, I want to say that I could not have asked for better advisors than Prof. Gregory Rohrer and Prof. Paul Salvador. They guided me superbly throughout my research and encouraged me in the times when I was stuck at a problem for weeks on end. If I want to summarize their role in this, it is that I cannot remember even one meeting where I left without being inspired to carry out the work for the week ahead.

Next, I want to thank my committee members - Prof. David Laughlin, Prof. Mohammad Islam and Prof. Kaushik Dayal. I received valuable feedback and insights into the gaps of my work as well as ways to fill them. Prof. Laughlin especially inspired me to read more about ferroelastic materials with a more fundamental approach.

I want to thank Mr. Tom Nuhfer, Dr. Adam Wise, and Dr. Elizabeth Clark for their guidance in my microscopy and diffraction experiments. I also want to thank Mr. Brett Riale, who has helped us fix our furnaces and other equipment a countless number of times. Also, I want to thank the administrative staff – Ms. Jeanna Pekarcik for helping me acquire all the materials I needed to carry out my experiments, Ms. Kelly Rockenstein and Ms. Suzanne Smith for arranging all meetings and making sure all the paperwork was in order. I would like to thank the NSF for funding my work.

My colleagues and friends at CMU supported me throughout my time here, and I would like to acknowledge them. My lab members – Dr. Madeleine Kelly and Dr. Yisi Zhu, who taught me how to use all the facilities at the beginning of my degree. My friends and colleagues - Dr. Aditya

Menon, Ms. Srujana Rao Yarasi, Dr. Arnab Debnath, Ms. Devdutta Mukherjee, Ms. Devika Khowala, Dr. James Glickstein, Dr. Tim Hsu, Mr. Rubayyat Mahbub, Mr. Siyuan Liu, Ms. Kayla Zitello, Ms. Wenjia Song, Ms. Catherine Zhou, Ms. Elizabeth Mao, Mr. Mingyi Zhang, Ms. Mingzhen Feng, Ms. Xiaoting Zhong. My batchmates – Rafael, Raveena, Ananya, Mohammad, Nigel, Saurabh, Alice, and Harsh, and anyone else I have missed out here. I would also like to acknowledge the music group of the Indian graduate student association at CMU, which I was lucky to be a part of since my first semester at CMU and provided me with friendships for life.

Finally, I'd like to thank my family for supporting and encouraging me throughout my time here at CMU.

Abstract

Spatial selectivity, that is the separation of reduction and oxidation reaction sites on the photocatalyst surface, is very important for efficient photocatalysis. It reduces charge recombination by driving photogenerated electrons and holes away from each other, reducing charge recombination, and thus loss of energy as heat. Additionally, it keeps the intermediates of reduction and oxidation reactions away from each other, reducing their reaction to form the original compound. Thus, studying spatial selectivity in photocatalysis is important to bring them a step closer to commercial and large-scale deployment. This is especially true for centrosymmetric photocatalysts, that cannot have built-in dipole moments to create spatial selectivity. However, there are other features like presence of different crystal facets and different surface chemistry that can create spatial selectivity. It has also been observed on centrosymmetric ferroelastic $BiVO_4$. Centrosymmetric materials and ferroelastics being a large part of the available materials space, the focus of this work is thus on studying the three features listed above and how they create spatial selectivity. The central idea is to use photodeposition marker reactions, that are reduction or oxidation reactions which leave an insoluble product on the surface. These products can be imaged with an SEM or AFM to comment on which areas are more reductive/oxidative.

The first two features listed above, crystalline facets and chemical terminations, were investigated in the context of spatial selectivity on bulk, polycrystalline $SrTiO_3$. Perovskites being highly tunable with respect to chemistry and band gap, showing spatial selectivity via these features on this crystal structure is important. It will enable charge separation on band gap tunable materials, which is a great combination for photocatalysis. Both of these features have

been studied separately, but this is the first study that takes both into account simultaneously. After synthesizing pellets and polishing them, the arbitrarily oriented surfaces were seen to break into facets on annealing at a high temperature of 1250 °C. The orientations of these surfaces were identified to be {100} and {110} by using a EBSD, AFM, and MATLAB. Photodeposition of Ag, MnO_x, and PbO_x was carried out to determine that {100} facets were reductive, and {110} facets were oxidative. Secondly, the {110} facets were changed to be partially reductive, when the samples were heated in a Sr-rich atmosphere. The charge separation from facets was obvious before effecting any thermochemical treatment, after which the chemical terminations dominated the charge separation on the {110} facets.

Next, to establish that ferroelastic materials can function as spatially selective photocatalysts, the polarization of ferroelastic domains and the reasons for this effect on centrosymmetric ferroelastics were studied . An effect similar to ferroelectrics was seen on $BiVO_4$, a non-polar ferroelastic, where the photodeposition was specific to alternating ferroelastic domains, as if they were polarized positive-negative in an alternating manner. To ensure that this is not specific to $BiVO_4$, another centrosymmetric ferroelastic with a different crystal structure – WO_3, was investigated. The same effect was seen on the ferroelastic domains of WO_3, with photodeposition being driven by alternating ferroelastic domains, along with a correlating Piezoforce response. This supports that the ferroelectric domain-like effect may be general to the entire class of ferroelastics.

Lastly, It is necessary to understand the origin of this effect to be able to tailor spatial selectivity on ferroelastic materials, similar to that shown on $SrTiO_3$ in the first part of this work. Flexoelectricity had been proposed as a possible reason. It means that the breaking of symmetry due to a strain gradient can create dipoles even in centrosymmetric materials. There were no experiments carried out in literature to test this hypothesis. So, in the final part of this work, systematic experiments were carried out to determine whether flexoelectricity could play a role. The stresses near the surface of a grain in a polycrystal were classified into two: Those arising due to the change in crystal system from the ferroelastic phase transition, and those due to the surrounding grains. The stresses from the surrounding grains were relaxed by milling out a trench around the region of interest. Further, these stresses were completely eliminated in the next set of experiments on hydrothermally-grown crystals. Finally, the bulk stresses from the lattice change were eliminated by heating the sample above the ferroelastic transition temperature. In all cases, spatial selectivity was observed. Most interestingly, it was present even in the absence of a ferroelastic domain structure, when photodeposition was carried out above the FTT. It implies that there is a factor that is not driven by stress/strain (and hence, flexoelectricity) which creates spatial selectivity in $BiVO_4$.

These results show that tailoring spatial selectivity using crystal facets and chemical terminations is possible in centrosymmetric Perovskite photocatalysts. However, more experiments are needed to pinpoint to origin of spatial selectivity on centrosymmetric ferroelastics.

List of Publications

1) "Spatial selectivity of photodeposition reactions on polar surfaces of centrosymmetric ferroelastic γ-WO_3" A. S. Pisat, G. S. Rohrer, P. A. Salvador, *J. Mater. Chem. A* **2017**, *5*, 8261.
2) "Spatially selective photochemical activity on surfaces of ferroelastics with local polarization" A. S. Pisat, G. S. Rohrer, P. A. Salvador, *Semicond. Sci. Technol.* **2017**, *32*, DOI 10.1088/1361-6641/aa84cf.
3) A. S. Pisat, P. A. Salvador, G. S. Rohrer, *Adv. Mater. Interfaces* **2019**. (In press) DOI: https://onlinelibrary.wiley.com/doi/full/10.1002/admi.201900731

Table of Contents

List of Figures

1 Introduction

With the ill-effects of climate change rapidly manifesting all around the world, it is of utmost importance to accelerate efforts to reverse it. Climate change is caused largely by non-condensable greenhouse gases (GHGs) such as CO_2 [1], that are a direct result of burning fossil fuels. Fossil fuels are a large part of our energy ecosystem, with 80 % of the energy being generated by them in the USA in 2017 [2]. All over the world, 81 % of energy is obtained using non-renewable sources of energy [3], contributing to GHG release into the atmosphere, and thus accelerating climate change.

Solar energy is a huge source of energy that is currently tapped far below its potential. 90 minutes of energy from the sun is enough to power the human race for an year [4]. However, only 1.3 % of electricity in the USA comes from solar cells [5]. Photocatalysis offers another way to tap into this vast source of energy. It is the acceleration of chemical reactions using light. The photocatalyst absorbs a photon, exciting an electron from its valence band to its conduction band, creating an electron hole pair, similar to solar cells. These electrons and holes carry out reduction and oxidation reactions in photocatalysis, and thus can be used to create useful products. Solar photocatalysis can split water [6] [7–9], creating hydrogen that can be used as a fuel. Solar photocatalysis can also be used to convert CO_2 into CH_4 [10], thus creating a carbon neutral cycle and creating a temporary solution to climate change [11]. It can also be used for air [12–14] and water [14,15] purification, using solar power instead of conventional sources and reducing the amount of GHGs released. Thus, solar photocatalysis has tremendous potential as a tool to reverse climate change.

With so much potential, why has photocatalysis not been adopted as a mainstream process? The reason is that there are multiple material requirements for efficient photocatalysis that need to be satisfied simultaneously – Charge separation, stability, efficient absorption of light, band alignment, overpotentials, and cost [16]. This limits the available materials space for photocatalysis.

The requirement of charge separation can be overcome by creating a spatially-selective photocatalytic system. Spatial selectivity of reactions in the context of photocatalysis, is defined as the occurrence of reduction and oxidation reactions on distinct regions of the photocatalyst. The separation of reaction sites can be achieved by two ways. Firstly, have spatially disjoint cathodes and anodes (as in the case of a photoelectrochemical cell [17]). Secondly, have a difference in electrochemical potential in a contiguous system, which will separate electrons and holes to different regions of the system [18]. This helps in reducing charge recombination and increasing the utilization of absorbed light, and hence, the external quantum efficiency of the process.

Spatial selectivity of photoreactions arises naturally in non-centrosymmetric, ferroelectric photocatalysts, where the photogenerated electron-hole pairs are separated due to polar ferroelectric domains. Ferroelectric materials like $BaTiO_3$, $BiFeO_3$, etc. have been well-studied [19–24] in this context. However, centrosymmetric materials make up a large part of the materials space, if not more than non-centrosymmetric materials [25]. Moreover, the mechanisms for charge separation on these materials are not so obvious as polar ferroelectric domains. Thus, it is important to study the material features that lead to spatial selectivity on centrosymmetric photocatalysts, and hence to increase the available materials space of spatially-selective photocatalysts. Investigating charge-separating features on polycrystalline, centrosymmetric oxide photocatalysts is the focus of this work.

The first part of this study investigates the simultaneous influence of crystal facets and chemical terminations in creating spatial selectivity of photoreactions on the surface of polycrystalline Perovskite $SrTiO_3$. This material is interesting because even though its band gap lies in the ultraviolet regime, Al-doped $SrTiO_3$, activated with a $Rh_{2-\gamma}Cr_{\gamma}O_3$ catalyst, has been shown to split water in sunlight [26]. Additionally, it is possible to apply the results from this study to other materials with the same structure. Bandgaps of inorganic organic hybrid Perovskites can be tuned by changing their chemistry. Thus, creating spatial selectivity in such materials has tremendous potential for photocatalysis as well as charge gathering in solar cells. Previously, the effect of crystal facets [27] and chemical terminations [28–30] in creating spatial selectivity has been individually studied. Considering crystalline facets, individual $SrTiO_3$ nanocrystals have been shown to have orientation dependent photochemical reactivity that depends on crystal shape. [31,32] When the crystals were terminated only by {100} planes, the {100} facets were both photocathodic and photoanodic. However, when the crystals were engineered to have {100} and {110} facets, the {100} surfaces were relatively photocathodic and the {110} surface were relatively photoanodic. [31,32] Considering chemical terminations, Giocondi et al. [28]

showed that single crystal $SrTiO_3$ (110) and (111) surfaces can simultaneously support relatively photoanodic and photocathodic terraces with different chemical terminations, and Zhu et al. [29,33] showed that it was possible to adjust the relative areas of these terraces. However, in a polycrystal with different facets and chemical terminations exposed simultaneously, the photochemical reactivity can vary from the results of the aforementioned studies. Different orientations will be exposed to the surface, that will break into multiple facets depending on the equilibrium shape at the annealing temperature. Each facet can have more than one stable chemical termination. Thus, the first question to be answered is whether the spatial selectivity from facets over-rides that from the terminations. Secondly, photocatalysis can involve complex multi-electron/hole reactions. For example, in the water-splitting reaction, four holes are required to generate O_2, whereas only two electrons are needed for H_2. Thus, to keep the oxidation and reduction rates equal, there needs to be more area promoting oxidation. Consequently, the next question is whether or not it is possible to tune reactivity by controlling the terminations using a process similar to the work of Zhu [29,30] et. al.

Our results show that both crystalline facets and chemical terminations are influential in determining the photochemical reactivity. {100} facets were found to be photocathodic, while {110} facets were photoanodic. When thermochemical treatments similar to those reported by Zhu et. al. [29] were carried out, the {110} facets went from being completely photoanodic to partially photocathodic. This work was published in Advanced Materials Interfaces recently.

To further expand the materials space of spatially-selective centrosymmetric photocatalysts, we decided to investigate the class of ferroelastic photocatalysts. Ferroelastic materials are abundant, making up about 30 % of the Earth's crust [34]. Ferroelastic domains were shown to be polar and spatially-selective, similar to ferroelectrics [35]. This was very surprising, given that there should be no dipoles in this centrosymmetric compound that can create internal fields to separate the photogenerated electron-hole pairs. Thus, we decided to pursue the very interesting and fundamental problem of why ferroelastics should possess polar domains. First, to ensure that this effect is not specific to $BiVO_4$, we investigated WO_3, another centrosymmetric ferroelastic, and a promising visible light-active photocatalyst [36–39]. Similar ferroelastic domain-specific photoreactivity was observed on the surface of polycrystalline WO_3 [40]. Thus, our results supported that this ferroelastic domain-driven spatial selectivity can be a feature of all semiconductor ferroelastics. The next natural question is why do centrosymmetric ferroelastics possess polar ferroelastic domains in the first place. If the origin of this effect is determined, it will enable the engineering of ferroelastic photocatalysts to adjust photocathodic-photoanodic areas and optimize the reaction rate. Munprom et. al. [35] had proposed the flexoelectric effect as a possible reason. Flexoelectric effect is the creation of a dipole moment due to a strain gradient, that breaks the centrosymmetry of the material [41]. There is a gap in the literature with respect to systematic experiments testing the possibility of the flexoelectric effect leading to polarization of ferroelastics domains in centrosymmetric ferroelastics. Thus, the final part of this work investigates the effect of different stress states that can drive flexoelectric polarization of ferroelastic domains in $BiVO_4$. This was done by carrying out photodeposition reactions and checking for the presence or absence of spatial selectivity under different stress conditions. These conditions are described in section 5 of this document. The effect of stresses from surrounding grains was investigated by isolating sections of the polycrystalline sample by milling trenches. The trenches prevented neighboring grains from interacting with the area under investigation, eliminating their contribution via tensile or compressive stresses to flexoelectric polarization. Spatial selectivity of photoreactions was observed on the milled pillars in this experiment. Here, there was still some possible contribution from the underlying grains. However, the hydrothermally-grown crystals in the subsequent experiment were completely free from any neighboring grain interaction. Multiple crystals were studied, some of which were supported only by a small area by other crystals. Spatial selectivity of photoreactions was observed in all crystals. Finally, photodeposition was carried out on a polycrystal sample above the FTT of $BiVO_4$, effectively in the absence of ferroelastic domains. Interestingly, spatial selectivity of photoreactions was observed even in this case. It implied that there is some factor other than the flexoelectric effect that is contributing to creating spatial selectivity on the ferroelastic domains. Because spatial selectivity was observed in all our experiments, we were not able to conclude anything about flexoelectricity being a possible reason for creating spatial selectivity on ferroelastic domains.

To summarize, the focus of this work is investigating charge separating features in polycrystalline, centrosymmetric oxide materials. Our results show that multiple features

Detailed descriptions of the experiments are in the following sections of this document. To help the reader gain a better understanding of the relevant terms and techniques, the fundamentals section discusses some background literature, along with details on the experimental techniques and setups used for all parts of this work. It is followed by the main body of the work, split into three chapters. Chapter 3 details the experiments on $SrTiO_3$, followed by Chapter 4 on WO_3 and Chapter 5 on $BiVO_4$. The conclusions and possible future experiments /follow-up studies that can be done are in chapter six. Finally, the appendix lists some supporting information that can aid in understanding of this work.

1.1 References

[1] Andrew A Lacis, Gavin A Schmidt, David Rind, and Reto A Ruedy: *Science*, 2010, vol. 330, pp. 356–59.

[2] U.S. Energy Information Administration: *Monthly Energy Review*, n.d.

[3] IEA: *World Energy Balances 2018*, 2018.

[4] Jeff Tsao, Nate Lewis, and George Crabtree: *US Dep. Energy*, 2006, pp. 1–24.

[5] University of Michigan Center for sustainable systems: *Photovoltaic Energy Factsheet*, 2018.

[6] A Fujishima and K Honda: *Nature*, 1972, vol. 238, pp. 37–38.

[7] Kazuhiko Maeda and Kazunari Domen: *J. Phys. Chem. Lett.*, 2010, vol. 1, pp. 2655–61.

[8] Tahereh Jafari, Ehsan Moharreri, Alireza Amin, Ran Miao, Wenqiao Song, and Steven Suib: *Molecules*, 2016, vol. 21, p. 900.

[9] Jawad Nisar, Luciana Almeida Silva, Cristiane Gomes Almeida, José Artur Santos Mascarenhas, Baochang Wang, Carlos Moysés Araújo, Rajeev Ahuja, Iuri Pepe, Jailton Souza de Almeida, and Antonio Ferreira da Silva: *Phys. Status Solidi Curr. Top. Solid State Phys.*, 2012, vol. 9, pp. 1593–96.

[10] TOORU INOUE, AKIRA FUJISHIMA, SATOSHI KONISHI, and KENICHI HONDA: *Nature*, 1979,

vol. 277, pp. 637–38.

[11] Wenguang Tu, Yong Zhou, and Zhigang Zou: *Adv. Mater.*, 2014, vol. 26, pp. 4607–26.

[12] Juan Zhao and Xudong Yang: *Build. Environ.*, 2003, vol. 38, pp. 645–54.

[13] Yash Boyjoo, Hongqi Sun, Jian Liu, Vishnu K. Pareek, and Shaobin Wang: *Chem. Eng. J.*, 2017, vol. 310, pp. 537–59.

[14] Agatino Di Paola, Elisa García-López, Giuseppe Marcì, and Leonardo Palmisano: *J. Hazard. Mater.*, 2011, vol. 211, pp. 3–29.

[15] Meng Nan Chong, Bo Jin, Christopher W.K. Chow, and Chris Saint: *Water Res.*, 2010, vol. 44, pp. 2997–3027.

[16] S.R. Morrison: *Electrochemistry at Semiconductor and Oxidized Metal Electrodes*, 1980.

[17] Sixto Giménez and Juan Bisquert: *Photoelectrochemical Solar Fuel Production: From Basic Principles to Advanced Devices*, 2016.

[18] Li Li, Paul a Salvador, and Gregory S Rohrer: *Nanoscale*, 2014, vol. 6, pp. 24–42.

[19] Jennifer L. Giocondi and Gregory S. Rohrer: *MRS Proc.*, 2000, vol. 654, pp. 1–10.

[20] Yongfei Cui, Joe Briscoe, and Steve Dunn: *Chem. Mater.*, 2013, vol. 25, pp. 4215–23.

[21] Weiguang Yang, Yanhao Yu, Matthew B. Starr, Xin Yin, Zhaodong Li, Alexander Kvit, Shifa Wang, Ping Zhao, and Xudong Wang: *Nano Lett.*, 2015, vol. 15, pp. 7574–80.

[22] Andrew M. Schultz, Yiling Zhang, Paul A. Salvador, and Gregory S. Rohrer: *ACS Appl. Mater. Interfaces*, 2011, vol. 3, pp. 1562–67.

[23] Chang Hengky, Xavier Moya, Neil D. Mathur, and Steve Dunn: *RSC Adv.*, 2012, pp. 11843–49.

[24] Yiling Zhang, Andrew M. Schultz, Paul a. Salvador, and Gregory S. Rohrer: *J. Mater. Chem.*, 2011, vol. 21, p. 4168.

[25] Alan Jircitano: 2013 - http://chemistry.bd.psu.edu/jircitano/6symmetry.pdf

[26] Yosuke Goto, Takashi Hisatomi, Qian Wang, Tomohiro Higashi, Kohki Ishikiriyama, Tatsuya Maeda, Yoshihisa Sakata, Sayuri Okunaka, Hiromasa Tokudome, Masao Katayama, Seiji Akiyama, Hiroshi Nishiyama, Yasunobu Inoue, Takahiko Takewaki, Tohru Setoyama, Tsutomu Minegishi, Tsuyoshi Takata, Taro Yamada, and Kazunari Domen: *Joule*, 2018, vol. 2, pp. 509–20.

[27] Linchao Mu, Yue Zhao, Ailong Li, Shengyang Wang, Zhiliang Wang, Jingxiu Yang, Yi Wang, Taifeng Liu, Ruotian Chen, Jian Zhu, Fengtao Fan, Rengui Li, and Can Li: *Energy Environ. Sci.*, 2016, vol. 9, pp. 2463–69.

[28] J L Giocondi and G S Rohrer: *J. Am. Ceram. Soc.*, 2003, vol. 86, pp. 1182–89.

[29] Yisi Zhu, Paul A. Salvador, and Gregory S. Rohrer: *Phys. Chem. Chem. Phys.*, 2017, vol. 19, pp. 7910–18.

[30] Yisi Zhu, Paul A Salvador, and Gregory S Rohrer: *Chem. Mater.*, 2016, vol. 28, pp. 5155–62.

[31] Jennifer L Giocondi, Paul A Salvador, and Gregory S Rohrer: *Top. Catal.*, 2007, vol. 44, pp. 529–33.

[32] Linchao Mu, Yue Zhao, Ailong Li, Shengyang Wang, Zhiliang Wang, Jingxiu Yang, Yi Wang,

Taifeng Liu, Ruotian Chen, Jian Zhu, Fengtao Fan, Rengui Li, and Can Li: *Energy Environ. Sci.*, 2016, vol. 9, pp. 2463–69.

[33] Yisi Zhu, Paul A. Salvador, and Gregory S. Rohrer: *Chem. Mater.*, 2016, vol. 28, pp. 5155–62.

[34] Z Zhao, X Ding, J Sun, and E K H Salje: *J. Phys. Condens. Matter*, 2014, vol. 26, p. 142201.

[35] Ratiporn Munprom, Paul A. Salvador, and Gregory S. Rohrer: *Chem. Mater.*, 2014, vol. 26, pp. 2774–76.

[36] Mahesh Datt Bhatt and Jae Sung Lee: *J. Mater. Chem. A*, 2015, vol. 3, pp. 10632–59.

[37] Rui Liu, Yongjing Lin, Lien Yang Chou, Stafford W. Sheehan, Wangshu He, Fan Zhang, Harvey J M Hou, and Dunwei Wang: *Angew. Chemie - Int. Ed.*, 2011, vol. 50, pp. 499–502.

[38] Yossy Wicaksana, Sanly Liu, Jason Scott, and Rose Amal: *Molecules*, 2014, vol. 19, pp. 17747–62.

[39] Gratian R Bamwenda and Hironori Arakawa: 2016.

[40] Ajay S Pisat, Gregory S Rohrer, and Paul A Salvador: *J. Mater. Chem. A*, 2017, vol. 5, pp. 8261–66.

[41] Alberto Biancoli, Chris M Fancher, Jacob L Jones, and Dragan Damjanovic: *Nat. Mater.*, 2014, vol. 14, pp. 224–29.

Chapter 1: Introduction

2 Fundamentals

This section has relevant background literature that may aid in understanding this work. It starts with a detailed description of the greenhouse effect, in order to better understand the motivation behind this work. It is followed by an explanation of photocatalysis, its applications, and material requirements. Next, the charge separating mechanisms studied in this work (Chemical terminations, facets, and ferroic domains) are discussed in detail. Finally, all experimental techniques used are elaborated upon.

2.1 Greenhouse effect

Solar radiation is continuously incident on the Earth. Hence, there is a constant influx of radiative energy from the sun. Some part of this energy gets reflected back into space due to gases in our atmosphere. The other part, that reaches the Earth's surface, is either absorbed by it or reflected towards space. The Earth itself sends out infrared radiation according to its temperature. This radiation is absorbed by gases like H_2O and CO_2, and is re-emitted in all directions, including back towards the earth. A schematic of the various reflections and paths of radiation is given in Figure 2-1 [1].

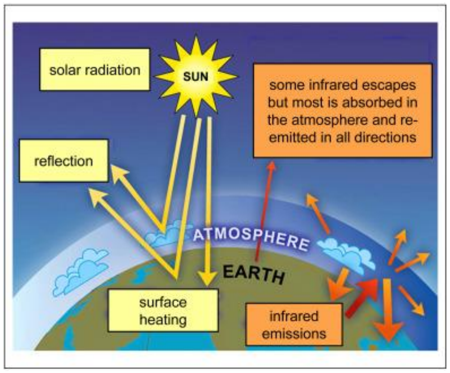

Figure 2-1: The absorption and emission of solar radiation by the Earth [1]

Thus, it is due to presence of these gases that the energy reflected by the Earth is, in part, sent back to the earth. This causes the temperature of the Earth to increase by much more than if these gases were not present. This increased effect of warming due to the gases is called the 'Greenhouse effect'. To put it into perspective, without the greenhouse effect, the average temperature of the Earth's surface would be -21 °C instead of 14 °C [2].

The greenhouse gases are divided into two categories, condensing (H_2O) and non-condensing (CO_2, Ozone, etc.). The condensing gases are variant in the atmosphere, due to cycles like evaporation-precipitation (rain, snowfall). The non-condensing gases, that account for 25% of the greenhouse effect, provide the stability in warming that supports the cycles involving condensable gases, that account for 75 % of the effect [2]. Thus, non-condensing gases like CO_2 are very impactful in driving the overall warming of the Earth, even if they directly contribute in a relatively smaller fraction.

CO_2 is very powerful in driving the overall warming of a planet due to this effect. Pioneering work by Arrhenius reported that halving (doubling) the atmospheric CO_2 would bring down (up) the temperature of the Earth by 5-6 °C [1,3]. Mars, which has very little CO_2 in its atmosphere, has a surface temperature of -60 °C, while Venus that has a lot of CO_2 in its atmosphere, has a surface temperature of 430 °C [4]. This does not imply that CO_2 alone drives the temperature, but is highly supportive of the fact that it plays a large role in doing so.

Contrasting reports showing inconsistencies in the climate change models and questioning the existence of the atmospheric greenhouse effect have been published [5] [6], and whether or not global warming is accelerated is also under debate. However, burning fossil fuels for energy and transport causes air pollution, that has adverse effects on human health that are well-documented [7] [8]. Fossil fuels are limited, which means that mankind cannot keep relying on them for its energy needs. Hence, in any case, cleaner sources of energy need to be used.

2.2 What is Photocatalysis?

Photocatalysis is the process where a certain material (catalyst), accelerates a reaction by using light but does not itself undergo any permanent change. Photocatalysis is of two kinds: homogeneous and heterogenous.

In homogeneous (heterogeneous) photocatalysis, both the reactant and the catalyst are in the same (different) phase. Photocatalysis has tremendous potential in green technology, i.e. to produce clean fuel, to synthesize compounds and to remove harmful organic pollutants from water and air [9], all whilst using solar energy.

2.2.1 Applications of photocatalysis

2.2.1.1 Water splitting

Ever since Fujishima and Honda discovered that TiO_2 could split water into hydrogen and oxygen by using UV light [10], photocatalytic water splitting has been a topic of tremendous study. It is not hard to think why this is so. Imagine using sunlight (an almost everlasting source of energy) to split water (that occupies 71 % of the Earth's surface) to generate hydrogen (that produces water on combustion) to provide us with energy!

The advantages of using water splitting to generate hydrogen are manifold. Firstly, hydrogen combustion creates water vapor only, which means that there is minimal air pollution. Some pollution can occur when air is used as an oxygen source, and a part of N_2 also combusts to give NO_x. Secondly, the energy content of hydrogen is quite high at 141.9 MJ/kg [11]. The energy content of gasoline is relatively much lower at 46.4 MJ/kg. Lastly, hydrogen can be stored in tanks like many other fuels. Storing solar energy generated using photovoltaics is much more difficult, requiring large batteries or a system to buy/sell from the power grid.

Water splitting is a heterogeneous photocatalytic process. The photocatalyst is immersed in water. The basic process is explained using Figure 2-2.

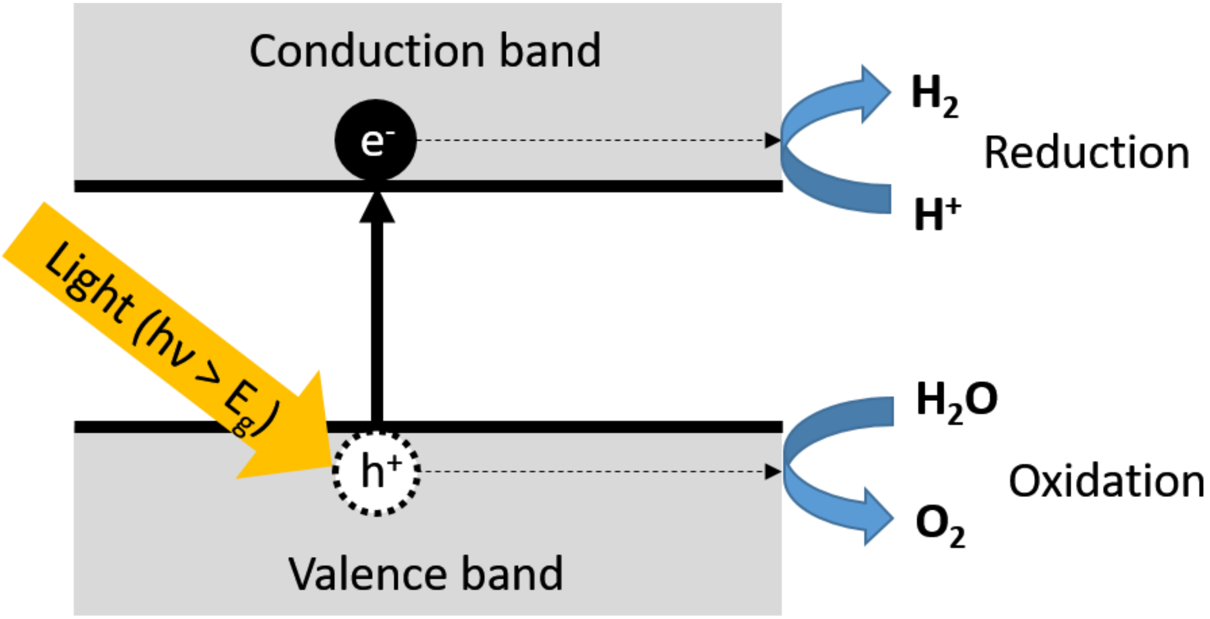

Figure 2-2: Photocatalytic water splitting

Once light with a higher energy than the band gap of the photocatalyst is absorbed by it, electrons are excited from the valence band to the conduction band. Both charge carriers are now free to carry out reactions at the photocatalyst-environment interface. We will discuss the charge carrier recombination later in this section. Thus, the electrons reduce hydrogen ions to liberate hydrogen gas, while the holes oxidize water to liberate oxygen gas. The overall reaction is given below.

$$\begin{array}{ll} \text{Photoexcitation} & : 4h\nu \rightarrow 4e^- + 4h^+ \\ \text{Reduction} & : 4H^+ + 4e^- \rightarrow 2H_2 \\ \text{Oxidation} & : 2H_2O + 4h^+ \rightarrow 4H^+ + O_2 \\ \hline \text{Overall} & : 2H_2O + 4h\nu \rightarrow 2H_2 + O_2 \end{array}$$

Photocatalytic water splitting is discussed in detail in the later parts of this chapter. Van De Krol and Graetzel have published an excellent book detailing the entire process of water splitting [12].

2.2.1.2 Photocatalytic water/air purification

Environmental remediation is possible via photocatalysis, by removing harmful organic compounds in air and water [9,13–16]. The basic principle of air/water purification via photocatalysis is the formation of highly reactive free radicals that break down complex and harmful organics into simpler compounds. Photocatalysts like TiO_2 have been researched for indoor air purification [15] [14,16]. A review on usage of Perovskite materials for remediation has also been published by Wang et. al. [17]

Hence, by using photocatalytic materials with sunlight, it is possible to produce directly usable clean fuel and also purify the environment we live in, paving the way for a healthier future.

2.3 Material requirements for photocatalysis

We have now looked at the basics of solar water splitting and its advantages. Let us now look at what stops us from deploying these technologies for widespread, everyday use.

a) Absorption of visible light
b) Energy of charge carriers
c) Over-potentials
d) Stability of the photocatalyst
e) Charge separation and Separation of reaction sites
f) Cost

2.3.1 Absorption of visible light

The solar to hydrogen efficiency is fundamentally limited by the band gap of the photocatalyst. Any light below the bandgap is not energetic enough to excite the charge carriers to higher energy states. Thus, such light is useless for the purpose of photocatalysis. Figure 2-3 shows the spectral intensity reaching the Earth's surface. From the Figure, we can say that visible light makes up most of the light from the sun. In fact, 50 % of solar light lies in the visible region [18].

The theoretical electrical potential, given by thermodynamics, required to split water is 1.23 V [12]. Hence, for charge carriers to have equivalent energy, a minimum band gap of 1.23 eV is needed. However, considering losses and overpotentials for sufficient reaction kinetics, the minimum band gap is 1.9 eV [12]. This gives a maximum wavelength of 650 nm ($E = hc/\lambda$). Murphy et. al. [19] calculated that a band gap of 2.03 eV would be optimal for the process, giving a solar to hydrogen efficiency of 16.8 % [12], that is well over the minimum 10 % accepted for commercialization [20].

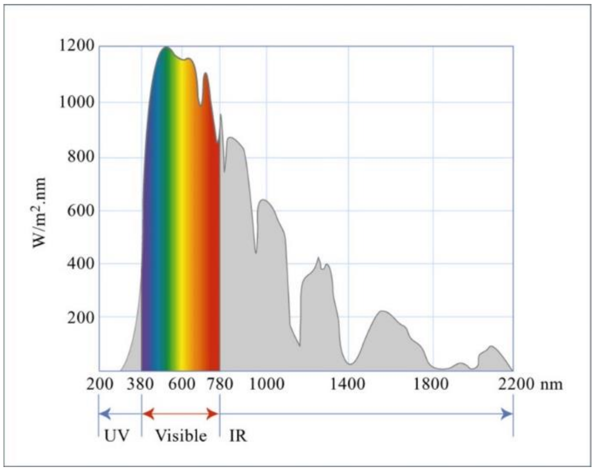

Figure 2-3: Spectral intensity vs wavelength of light energy reaching the Earth's surface. Figure taken from MIT opencourseware.

2.3.2 Energy of charge carriers

Just having an optimum band gap does not mean that the photocatalyst will be able to split water on its own. The theoretical potential for reduction of H^+ ions is 0 V (at pH = 0). For oxidation of water, the potential is (-ve) 1.23 V. Hence, the electrons need to be at a +ve potential to be able to liberate hydrogen. Similarly, the holes need to have an energy below -1.23 eV (at pH = 0) to evolve oxygen. Thus, only those photocatalysts that have their conduction band minimum above the hydrogen reduction potential and valence band maximum below the oxygen reduction potential, after considering band bending (discussed later), can split water on their own in a photocatalytic system. Figure 2-4 shows the band edges of different materials in relation to these two potential levels.

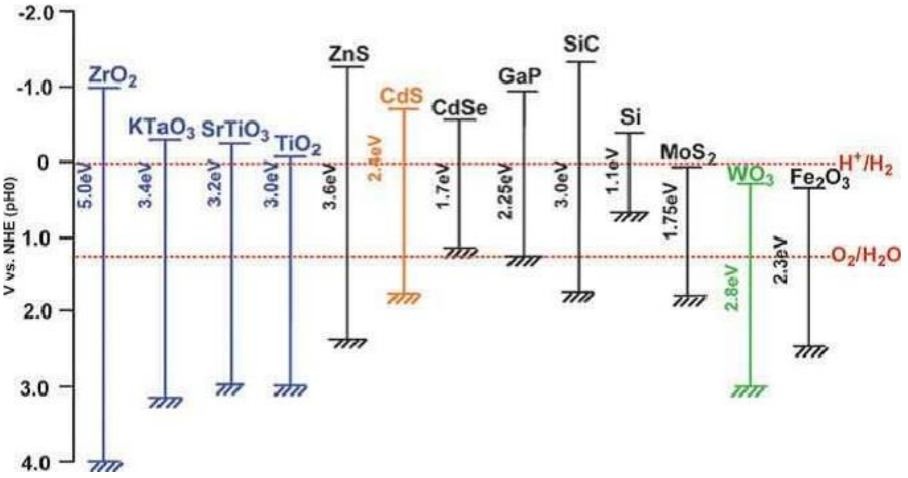

Figure 2-4: Comparison of band edges of various photocatalysts with the standard reduction potentials for hydrogen and oxygen (at 0 pH). Figure taken from [44]

Take WO_3 for example. Its band gap is 2.8 eV, which is much higher than a required minimum of 1.23 eV. However, the top of its conduction band is below the hydrogen reduction potential. Hence, it cannot reduce hydrogen ions into H_2 gas as is. On the other hand, CdSe cannot oxidize water on similar lines. Photocatalysts like TiO_2 and CdS can perform both parts (oxidation and reduction) of water splitting.

2.3.3 Overpotentials

In photoelectrochemistry, overpotential is defined as the difference between the applied potential and the open circuit potential under illumination [12]. Overpotentials, as the name suggests, are excess energies that the charge carriers need to possess over and above the theoretical values to carry out the photocatalytic process.

Figure 2-5 below explains overpotentials in relation to the band levels.

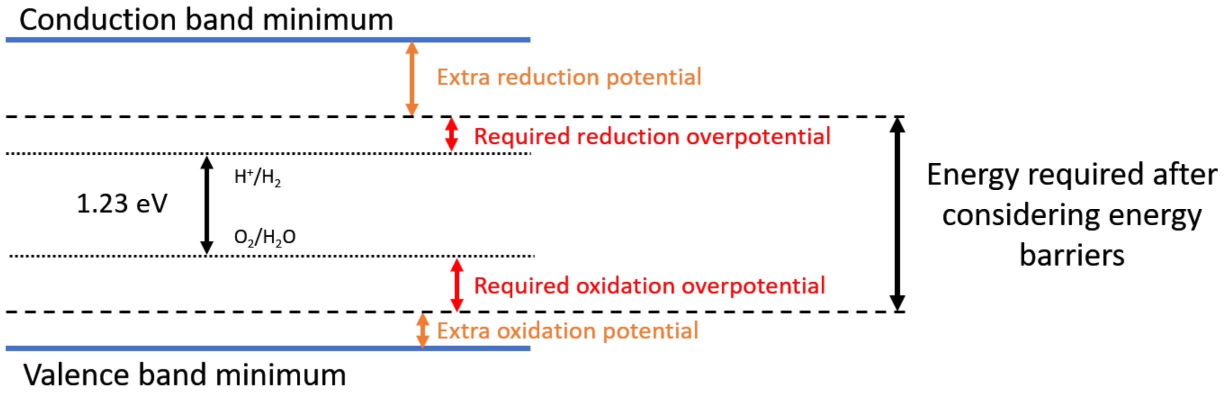

Figure 2-5: Schematic of different energy levels associated with overpotentials in a photocatalyst.

For example, the valence band edge of WO_3 (approximately -3 V) is considerably below the required value of -1.23 V. Thus, the holes have enough energy to overcome an overpotential of even 1.77 eV (if at all required), making it a very good material (energetically) for oxidation of water.

The extra supplied overpotential must be optimized. Too much extra potential (by having a large band gap) reduces the fundamental limit of efficiency that can be reached. On the other hand, having a band gap that just about misses the energetic requirements can mean that the reaction does not occur at all.

Co-catalysts are used to reduce the required overpotentials [21]. Noble metals are commonly used as reduction co-catalysts while RuO_2 can be used for reducing the oxidation overpotentials [21].

2.3.4 Stability of the photocatalyst

The photocatalyst is said to be unstable if it itself undergoes reduction/oxidation instead of hydrogen ions/water respectively. This is possible when the reduction (oxidation) potential of the photocatalyst is below (above) the conduction band minimum (valence band maximum) of the photocatalyst. The reduction potential (oxidation potential) of the photocatalyst itself is termed as $E_{n,d}$ ($E_{p,d}$). If the electrons (holes) have a lower (higher) energy state to occupy, it is possible that they will do so. Hence, corrosion is thermodynamically possible in these cases. If the electrons (holes) have to go to higher (lower) energy states to corrode the photocatalyst, it is unlikely it will happen. The possibilities when the photocatalyst may undergo photocorrosion are illustrated in Figure 2-6.

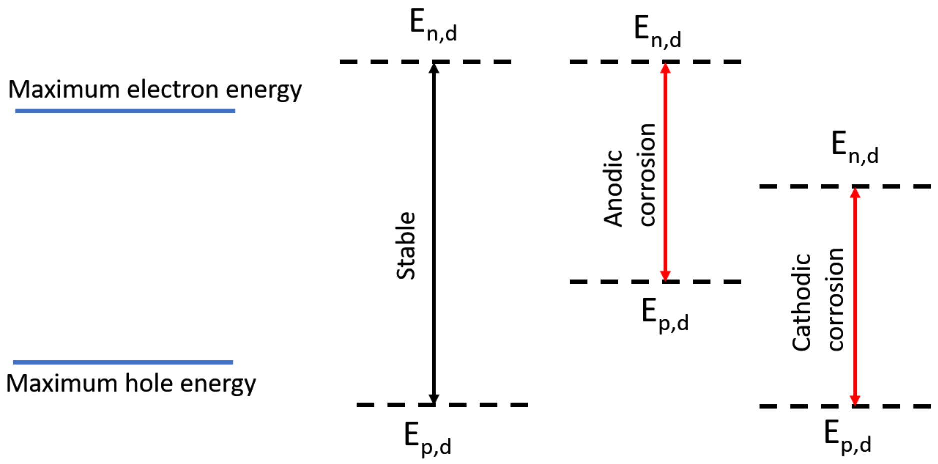

Figure 2-6: Different scenarios for photocorrosion of photocatalysts

If the excited electrons reduce the photocatalyst, it is termed as 'cathodic photocorrosion'. If the excited holes oxidize the photocatalyst, it is termed as 'anodic photocorrosion'. The corrosion equations are given below.

$M_xO_y + 2ye^- + 2yH^+_{(aq)} \leftrightarrow xM_{(s)} + yH_2O$ …Cathodic photocorrosion (acidic solution)

$M_xO_y + 2ye^- + yH_2O \leftrightarrow xM_{(s)} + 2yOH^-_{(aq)}$ …Cathodic photocorrosion (basic solution)

$M_xO_y + 2(y/x)h^+ \leftrightarrow xM_{(aq)}^{(2y/x)+} + (y/2)O_2$ …Anodic photocorrosion (acidic solution)

(The equations are adapted from [12])

From the reactions, it can be seen that cathodic corrosion causes deposition of metal while the anodic corrosion results in depletion of the photocatalyst as ions in the solution.

Figure 2-7 shows the band edges of various photocatalysts in comparison with their respective photocorrosion potentials.

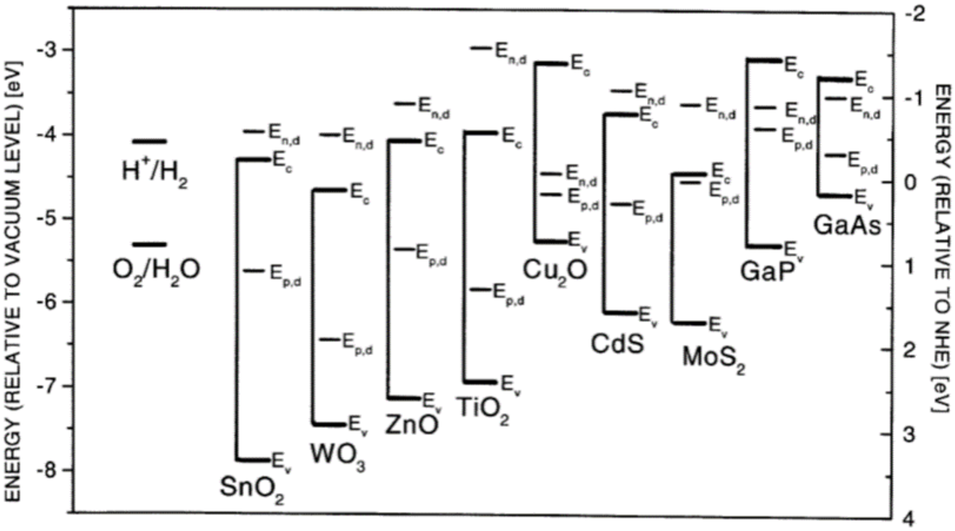

Figure 2-7: Comparison of corrosion potentials ($E_{n,d}$ and $E_{p,d}$) of photocatalysts with their band edges and reduction potentials for water splitting (at 0 pH)

Take WO_3 for example. Its conduction band minimum is lower than its $E_{n,d}$. It implies that WO_3 cannot undergo cathodic photocorrosion thermodynamically. However, its valence band maximum is lower than its $E_{p,d}$, which implies that anodic photocorrosion is possible. TiO_2 can also undergo photocorrosion, but the reaction kinetics in this case are very slow [12].

2.3.5 Charge separation and separation of reaction sites

As discussed before, the electrons and holes once excited tend to recombine. Recombined charge carriers give off their energy in the form of heat and are useless for photocatalysis. Hence, to get good yields, the charge carriers need to be separated by some mechanism. The various paths electrons and holes can take after excitation by photons are illustrated in Figure 2-8 below.

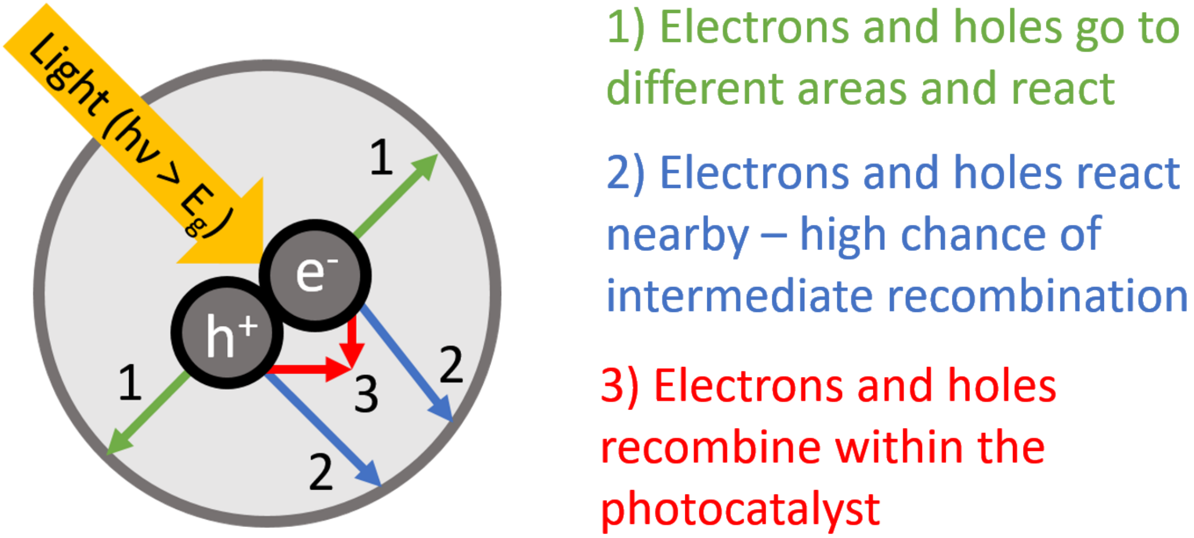

Figure 2-8: Possible paths for charge carriers after excitation by photons

Internal recombination is only one way where incident energy is not used for photocatalysis. Energy can still be wasted if the reduction and oxidation reactions take place in close proximity of each other, as there is a risk of recombination of intermediate products.

Thus, having distinct areas that only promote one reaction (either reduction or oxidation) tackles both problems simultaneously. The length scale over which charges are separated can be macroscopic or microscopic, depending on the kind of photocatalytic system in consideration. Photoelectrochemical cells have separate cathodes and anodes, both immersed in water. Hence, the areas for reduction and oxidation are separated by a distance of the order of centimeters. The second kind is where both reactions happen on a single surface. An example of this system can be a dispersion of photocatalyst powders in water. This can be viewed as a short-circuited PEC [22]. In this work, we are concerned with the second type.

Potential differences have to be introduced into the system so that oppositely-charged electrons and holes have opposite forces acting on them, resulting in separation. These potential differences change the electronic structure of the photocatalyst, and bend the bands so that some energy states are lower (higher) than others ad are preferred by electrons (holes). This is illustrated in the figure below.

The left part of Figure 2-9 shows that there is no preferred direction for the charge carriers to drift towards after photoexcitation. Hence, they may go to the surface and react or recombine in the bulk, as shown by the blue arrows in the image. In the right part of Figure 2-9, there are surface charges on two sides of the photocatalyst. The positive charges attract negatively charged electrons, and this is reflected in the lower energy states at that surface. The negative charges attract holes, because the charge creates higher energy states that holes prefer thermodynamically. This is the basis of charge separation. Moreover, reaction sites are automatically separated in this case.

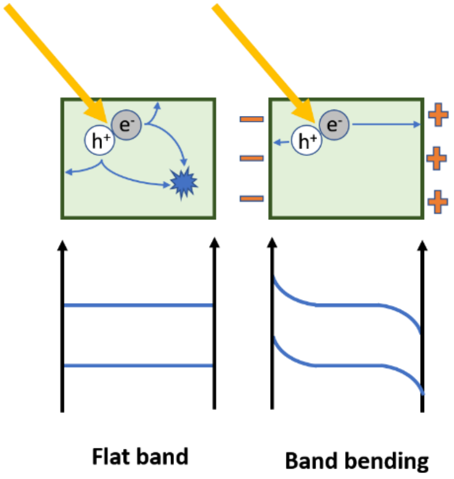

Figure 2-9: (left) Charge recombination in a photocatalyst with no band bending (right) charge separation in a photocatalyst with surface charges

Li et. al. have published a review on charge separation due to internal electric fields [22]. The charges can be separated by morphological and physical features of photocatalysts, that result in internal fields. Some of which are listed below.:

1) Phase boundaries
2) Chemical surface terminations
3) Crystallographic orientations
4) Ferroelectric/Ferroelastic domains

This work is focused on investigating charge separation from features 2, 3 and 4.

2.3.6 Cost

Certain systems have shown good solar-to-hydrogen efficiency, but are prohibitively expensive for industrial scale implementation [23]. Lot of systems use noble metals like Pt and Au as co-catalysts that are expensive and limited in quantity [24]. Earth-abundant materials and cheaper manufacturing processes are needed to be able to deploy this technology on a global scale.

Thus, effectively implementing photocatalytic solutions to improve quality of human life on Earth is not trivial. All of the above problems have to be tackled simultaneously.

2.4 Charge separating features

Charge separation in a photocatalyst occurs due to a gradient in the electrochemical potential in it. Electrons move down the gradient to lower energy levels, while holes move up the gradient to higher levels. Thus, the charge carriers are separated, reducing recombination and wastage of absorbed photons as heat. Such differences in electrochemical potential can occur due to p-junctions, presence of different chemical terminations [25–27], presence of different crystalline facets [28,29], and ferroic domains [30]. This work studies the latter three, and they are detailed below.

2.4.1 Chemical termination driven spatial selectivity

2.4.1.1 What are chemical terminations?

Chemical terminations are the topmost layer of a particular surface chemistry on a given orientation that are exposed to the environment. They can be visualized by cleaving the unit cell of the crystal on a particular plane and looking at the surface chemistry present. Thus, in a ABO_3 perovskite, if the crystal is cleaved along (100), then the exposed layer may be composed of AO or BO_2. A unit cell of ABO_3 is given below (Figure 2-10) with different layers along [100] being highlighted [34].

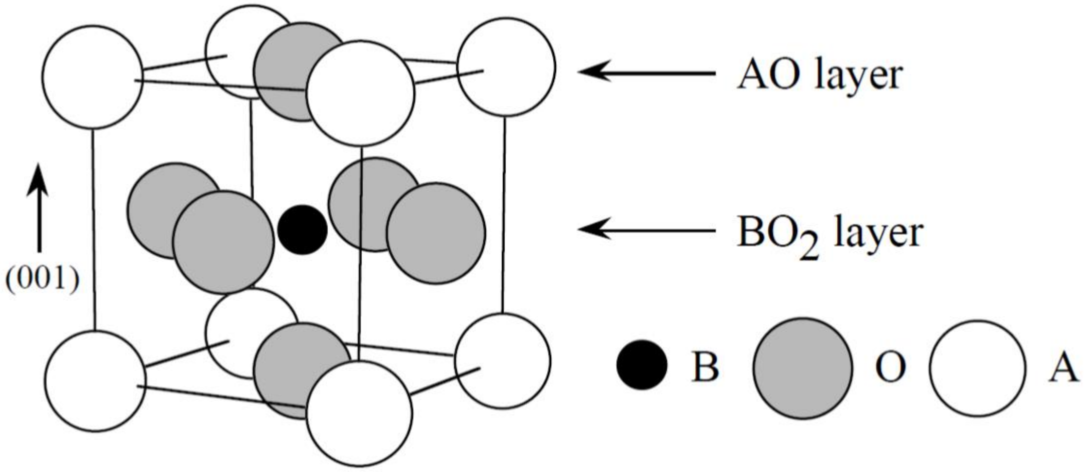

Figure 2-10: Schematic of a Perovskite unit cell showing different layers along [001] direction

These are ideal chemical terminations, as their structure and surface chemistry are that of the bulk crystal. Giocondi and Rohrer [35] have illustrated chemical terminations on (100), (110) and (111) surfaces of $SrTiO_3$.

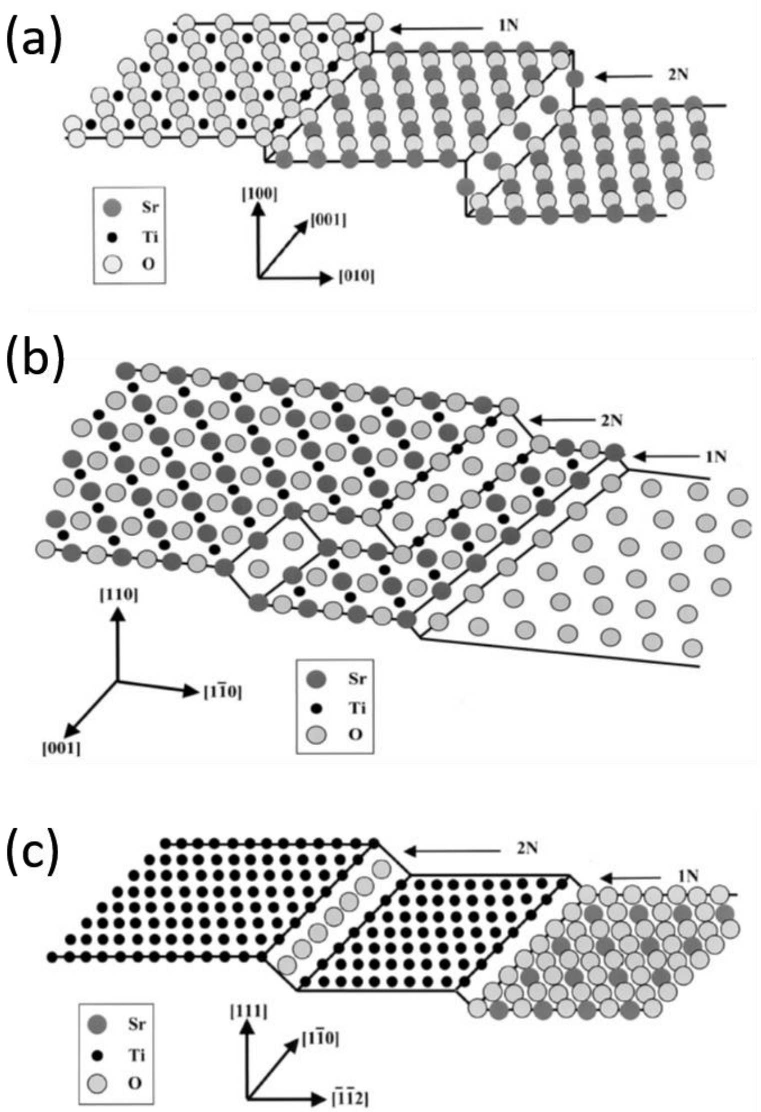

Figure 2-11: Schematic of chemical terminations on (a) {100} (b) {110} and (c) {111} planes of $SrTiO_3$

As seen in Figure 2-11(a), (100) can support two possible chemical terminations – SrO and TiO_2. Both are non-polar. The terminations on (110) – O_2^{4-} and $SrTiO^{4+}$ and (111) – SrO_3^{4-} and Ti^{4+} are polar as shown in Figure 2-11(b) and Figure 2-11(c). The ‘N’s in the figure signify half unit cell layers. So, a 2N difference implies that there is a complete unit cell layer between terminations.

These are the ideal terminations if the crystal is cleaved under vacuum. Usually however, the ideal surface structure has a lot of unsatisfied bonds when exposed to the surface. Hence, it undergoes reconstruction to reduce surface energy. Some surface reconstructions occur in the presence of air [36–40]. In this work, we have not determined the exact chemistry and structure of the terminations. Instead, we denote the two possibilities on any orientation as Sr-rich or Sr-deficient.

Chemical terminations can be controlled to tailor thin film growth [41]. A 2D electron gas has been reported at the $LaAlO_3/SrTiO_3$ interface after controlling the termination of the substrate [42]. This work investigates how chemical terminations can be controlled on polycrystals and how they affect photoreactivity.

2.4.1.2 How do chemical terminations affect photochemical activity?

Different chemical terminations have different chemistry, and as a result, have a different surface potential [26,43]. It has been reported on ferroelectrics [44–47] and Fe_2O_3 polycrystals [48] that a higher surface potential means less upward band bending (or a higher downward bending) at the surface.

Electrons want to reduce their energy and go towards a lower energy state. Downward band bending ensures that electrons are driven to the surface because the energy at the surface is lower than that in the bulk. Similarly, a reduced upward bending means a lower barrier to reach the surface. Hence, both scenarios help electrons reach the interface for reactions. For holes, increased upward band bending due to a lower surface potential terrace is advantageous.

Hence, it is to be expected that if two different chemical terminations are present, the termination with the higher surface potential will promote photoreduction, while the one with a lower surface potential will promote photo-oxidation. This is shown schematically in Figure 2-12 below.

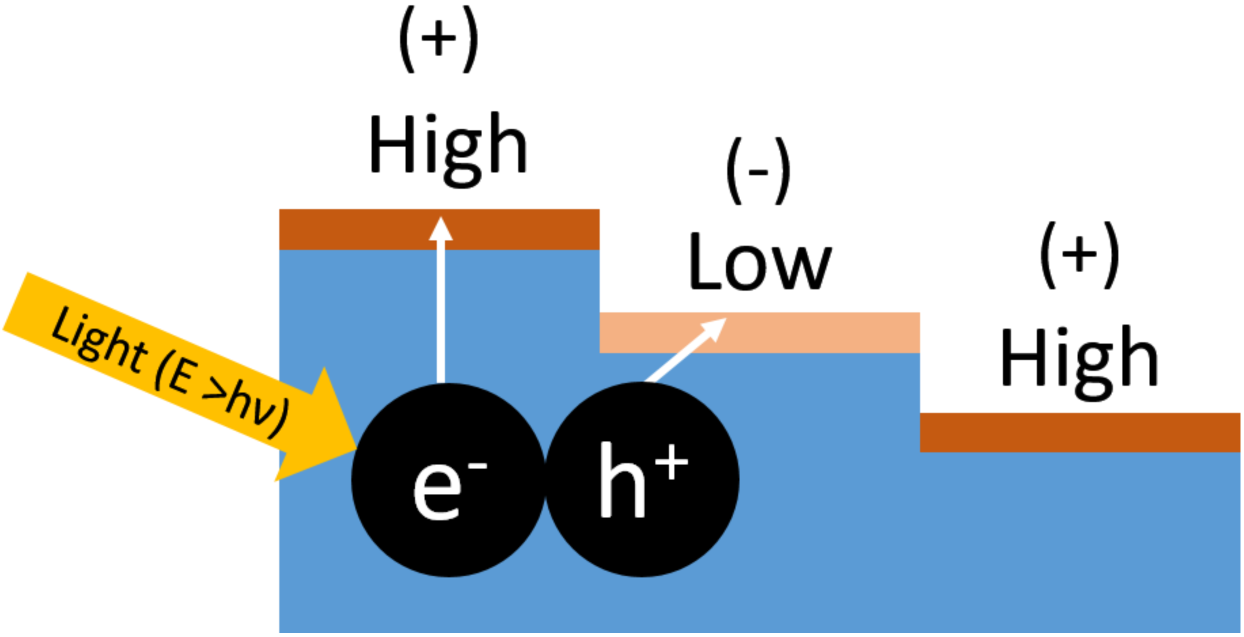

Figure 2-12: Charge separation due to different chemical terminations

2.4.2 Facet-driven spatial selectivity

2.4.2.1 What are facets and how are they formed?

Facets are planes of different orientations that form the outer surface of a crystal. Crystals, when grown in thermodynamic equilibrium, form specific shapes bound by flat planes. Facets can also arise as a result of differential growth rates of orientations. For example, NaCl crystals are bound by {100} facets at temperatures below 650 °C [49]. The SEM image below (Figure 2-13) from the characterization facility at University of Minnesota shows many inter-grown NaCl crystals with {100} facets.

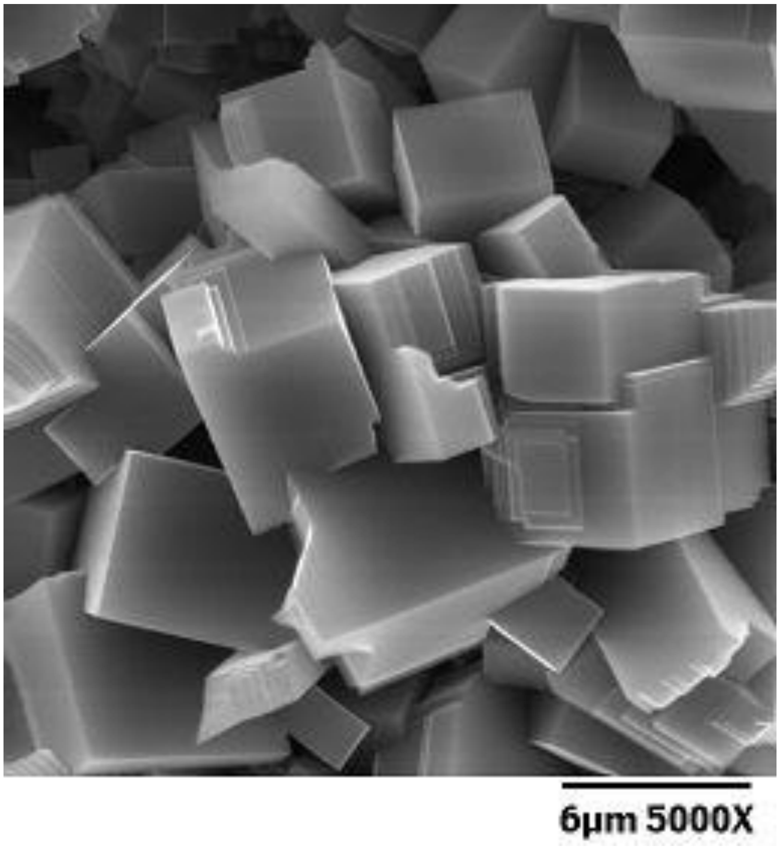

Figure 2-13: SE image of NaCl crystals bound by {100} facets. Taken from the webpage of the characterization facility at the University of Minnesota

2.4.2.2 Why do facets form?

When crystals grow, their atoms form an ordered structure. While growing, the crystal wants to minimize its total energy. There are two components to this (in addition to entropy terms). The first one is the bulk energy, and the other is the surface energy. For a given volume, the goal is to minimize both the total surface area as well as surface energy per unit area. Hence, the surface assumes a combination of planes that gives the minimum surface energy for that volume [50]. These bounding planes are facets. Facets are thus, planes that are thermodynamically favored at the growing conditions. Kinetics favored facets (that do not result in the lowest energy system) may also form under certain growth conditions.

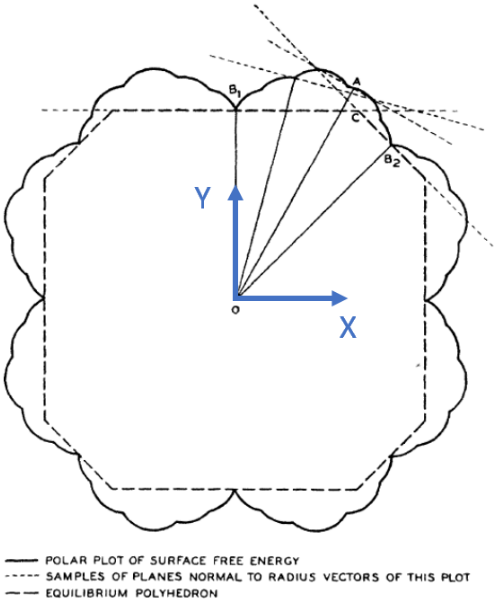

Figure 2-14: Projection along [001] of a polar plot of the surface energy function of a hypothetical material. The solid line gives the surface energy value at a particular theta. The dashed lines (bold) give the equilibrium shape of the crystal. The dashed line (thin) show some sample high energy planes that are not a part of the equilibrium shape (adapted from [32]).

The surface energy determines the equilibrium shape of the crystal, known as the Wulff shape. The Wulff shape is determined by the surface energy function. An example of a projection of the surface energy function is shown in Figure 2-14 (adapted from [32]).

Here, the solid black line is the polar plot of the surface energy function (projection on the plane of this paper). Consider any point on the polar plot. The distance from the origin is proportional to the magnitude of the surface energy of a plane which is perpendicular to the radial vector at that point. According to Wulff [51], the smallest volume that can be formed without crossing any plane gives the equilibrium shape of the crystal. For example, that shape in the figure is given by the dashed line. In this example, the bounding facets for the crystal are {100} and {110}.

2.4.2.3 Facets in single crystal substrates and polycrystals

Compared to random high energy planes that are exposed in polycrystals, polished single crystals are almost on axis. For example, MTI corporation sells $SrTiO_3$ single crystals that are within 0.5 ° of the advertised orientation (miscut angle). As a result, the proportion of facets that are formed on annealing is highly skewed towards the advertised orientation. The situation in polycrystals is interesting. In a polycrystalline substrate, it is highly unlikely that a grain is polished exactly parallel to one of its low energy facets. Usually, most of the grains get polished on a random, high-index plane, that is not a part of the Wulff shape of the material. The ratio of facets is then dependent on the polishing plane, and hence varies from grain to grain. Figure 2-15 below shows how the high energy planes break into facets.

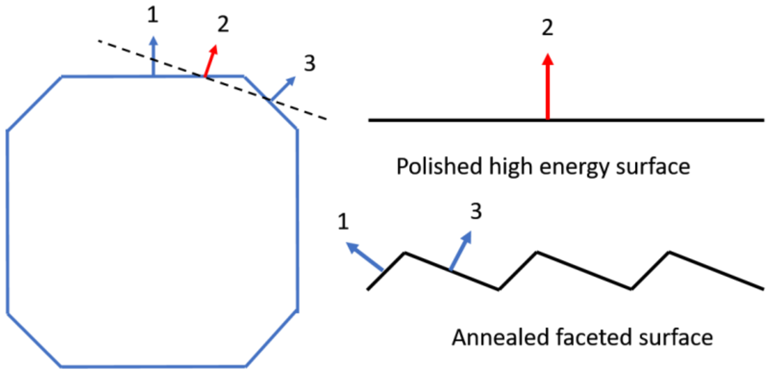

Figure 2-15: (left) The equilibrium shape of a hypothetical crystal. 1,3 - normals to the equilibrium facets. 2 - normal to the plane along which crystal is cleaved (right) The cleaved plane (top) before and (bottom) after annealing

The dotted line in the sample equilibrium crystal shape on the left is where the crystal has been hypothetically cleaved. The plane normal (2) is given in red. The two blue normals (1 and 3) are those for the stable planes. Any plane that has its normal between these two is going to be an unstable, high energy plane. On the right top is the magnified version of the polished plane before annealing. On annealing, the atoms gain thermal energy to diffuse and form facets as shown. These facets are the same orientations 1 and 3 from the equilibrium crystal shape. Even though the total surface area is increased, the surface energy function dictates that this configuration lowers the overall energy.

The image below (Figure 2-16) shows multiple grains broken into low energy facets on a $SrTiO_3$ polycrystal.

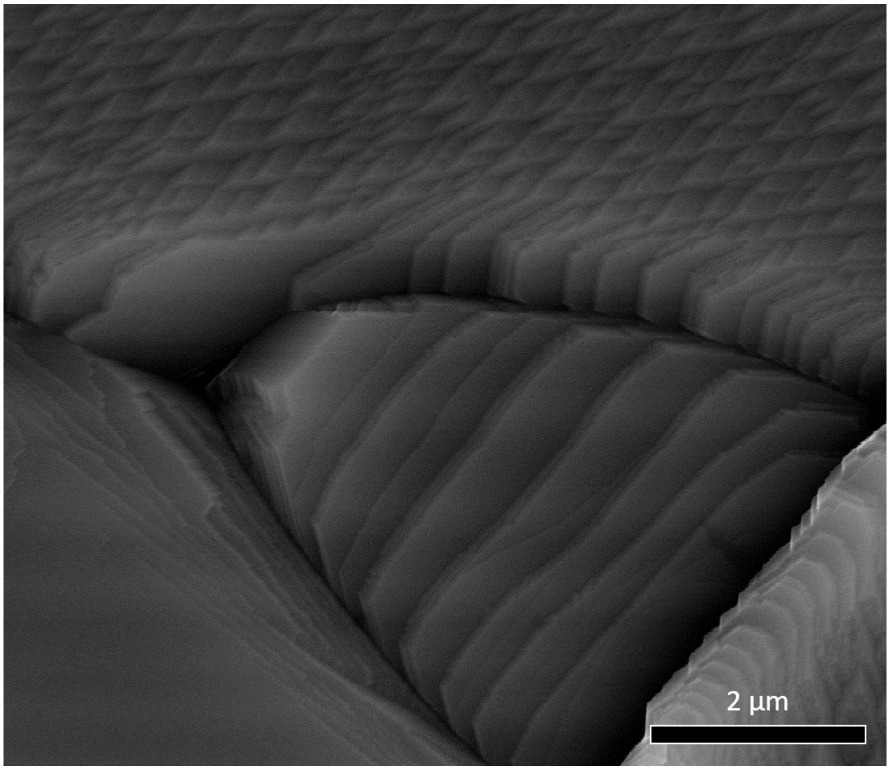

Figure 2-16: SE image of multiple, faceted grains on $SrTiO_3$

Thus, a reordering of atoms on the polished surface of a polycrystal results in development of facets on its grains. Not all compounds will facet. The degree of faceting is dependent on its Wulff shape. If there is a significant anisotropy in the surface energy function, one can expect the grains to facet. However, if the surface energy function is isotropic and the Wulff shape represents a sphere, there will be minimal faceting.

2.4.2.4 How do Facets separate excited charge carriers?

Different facets have different band edges, and hence can shuttle carriers between them as per the existing differences. Figure 2-17 below explains how a 'surface heterojunction' is formed, resulting in a driving force for charges to be shuttled to different facets.

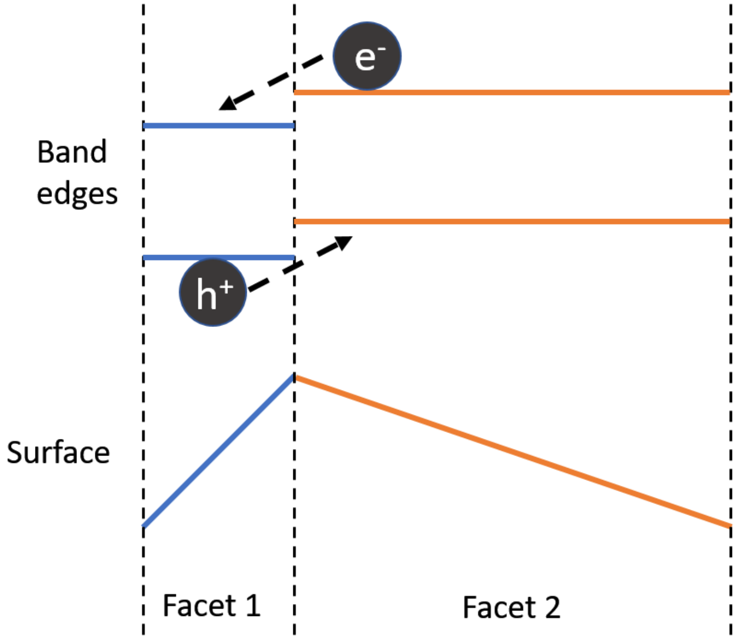

Figure 2-17: Schematic of a surface heterojunction formed due to band level differences between facets. The separation of excited electrons and holes is shown with the help of band edges. Figure not to scale.

The surface is made up of two facets here – blue and orange. The blue facets band edges are slightly shifted from those of the orange facet. In general, the band gaps may be different as well. The electrons can attain a lower energy level by moving from the orange facet to the blue. Similarly, the holes should move from the blue to the orange facet. This results in the formation of a surface heterojunction.

The presence of a surface heterojunction has been computationally shown by Wei et. al. [52]. Yu et. al. [53] showed that {101} and {001} facets of anatase TiO_2 have different band structures and band edges positions using DFT. They also found experimentally that a ratio of {101}:{001} :: 45:55 is optimal for reduction of CO_2. A deviation from this resulted in lowering of the reduction rate, which supports that one set of facets promoted one particular reaction.

Li et. al. [29] investigated charge separation on $BiVO_4$ crystals using photodeposition. The {110} were active for oxidation while the {010} facets were active for reduction. The inter-facet charge transfer was attributed to difference in band levels of both facets. The band bending due to different surface structures may also affect the charge separation.

2.4.3 Ferroelastic domain-driven spatial selectivity

Ferroic materials, such as ferromagnets, ferroelastics, and ferroelectrics, share some common features. They all involve the long-range parallel order of a local tensor quantity, namely magnetic moment, strain, and polarization respectively, below a critical temperature referred to as the Curie Temperature (T_C). This leads to a net local magnetization, strain, or polarization.

Importantly, the ordered tensor quantity can be switched between a small number of energetically degenerate directions.

Ferroelastic domains are analogous to ferroelectric domains, and it is easier to understand them once there is an understanding of ferroelectrics. Hence, the next sections compare the formation of ferroelectric and ferroelastic domains. Following these, the mechanisms of how ferroelectric and ferroelastic domains affect photodeposition are discussed.

2.4.3.1 What are ferroelectric domains and how are they formed?

Ferroelectric domains are regions of the crystal that form below the Curie temperature, whose comprising unit cells all contribute a dipole of the same magnitude in the same direction. In short, the polarization within a ferroelectric domain is the same everywhere. The ferroelectric domains form to reduce the overall energy of the crystal. On cooling below the Curie temperature, the polar displacements of ions in the crystal lead to formation of dipoles. This results in the formation of an internal electric field, which is compensated by surface charges. These surface charges store energy in the crystal like a capacitor. This is illustrated in the schematic below (Figure 2-18). To reduce the effective surface charge, domain walls form across which the polarization changes direction. The more the number of domain walls, the more evenly the positive and negative charges will be distributed. However, we cannot have an infinite number of domain walls. The domain walls themselves require energy to form. Hence, a balance has to be struck between the two.

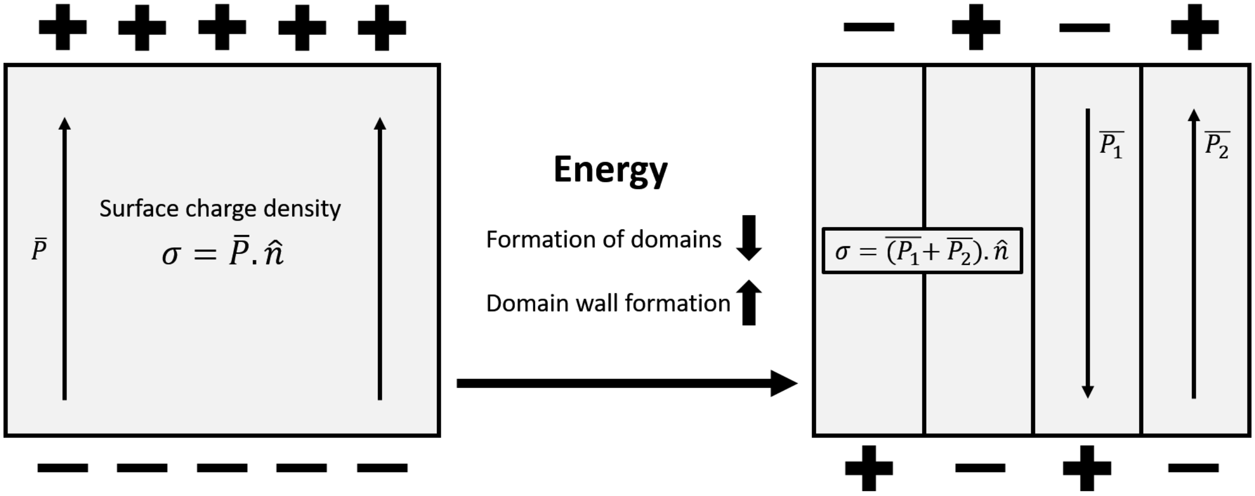

Figure 2-18: Energy balance during ferroelectric domain formation

2.4.3.2 What are ferroelastic domains and how they formed?

Similar to ferroelectric domains where the polarization is constant over the entire domain, the strain state in a ferroelastic domain is the same. The strain state alternates across ferroelastic domains, analogous to polarization in ferroelectric domains. Ferroelastic domains also form to reduce the strain energy arising from a phase change.

A schematic of the transformation is given in Figure 2-19, where an orthorhombic high-temperature structure (all angles are 90°) transforms into a monoclinic low-temperature structure (β is not 90° in this plane). States 1 and 2 are energetically degenerate states, each having the same structure but state 2 is a mirror image of state 1. Generally, the ferroelastic transformation is driven by atomic displacements within the unit cell that lower the overall energy and create a local strain relative to the parent structure.

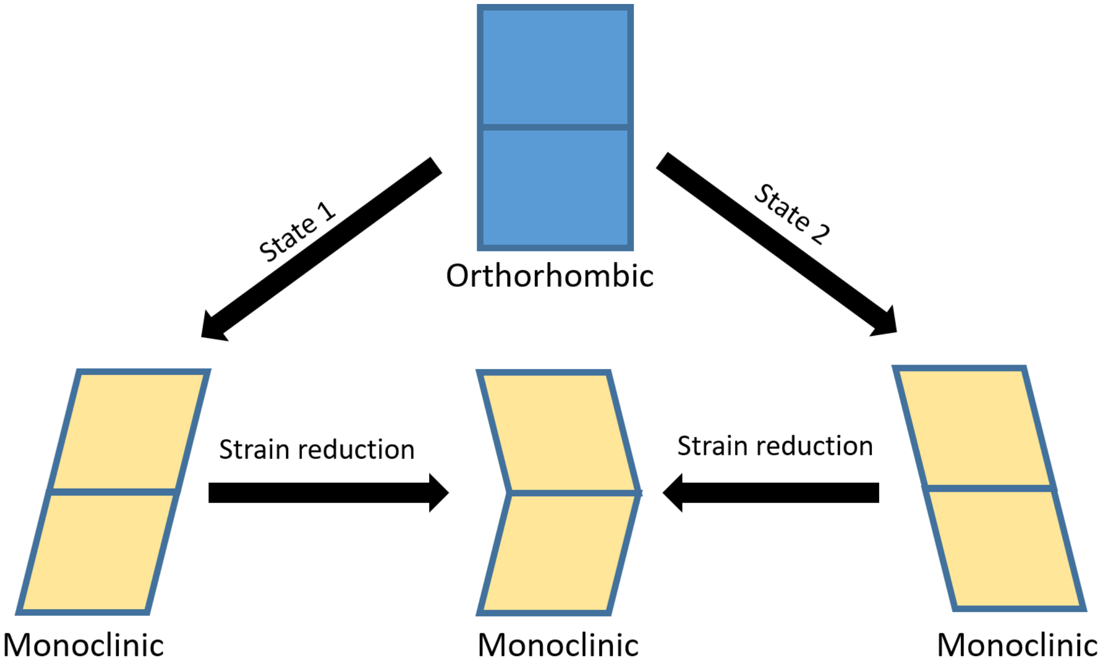

Figure 2-19: Morphological transformation from orthorhombic to monoclinic on ferroelastic phase transformation

To minimize the overall energy below T_C, ferroelastic materials (ferroic materials in general) organize into volumetric regions that have the same strain state within a ferroelastic domain, but different strain states across ferroelastic domain boundaries. A schematic is given in the lower central portion of Figure 2-19 for two unit cells of adjacent ferroelastic domains stacked vertically (state 2 on state 1). Comparing the three lower panels to the parent structure, the central one with two ferroelastic domains is closest to the shape of the parent (and thus has the lowest overall strain energy). In ferroelastics, the crystallographic orientation of the unit cells in each ferroelastic domain is the same, but changes across domain boundaries.

2.4.3.3 Symmetry requirements for ferroelectric and ferroelastic materials

Ferroelectrics

For a material to be ferroelectric, its ferroic phases must belong to one of the 10 polar/pyroelectric point groups [54]. Firstly, there can be no centrosymmetry in the point group to allow for a polar vector to develop, and hence, only those point groups without an inversion operator (1-bar) are allowed. Out of 32 point groups, only 21 of these are non-centrosymmetric. Out of these, only 10 are pyroelectric and polar. These polar groups allow for a dipole moment within the unit cell, as is required by definition of ferroelectrics

Ferroelastics

As per Aizu [55], the point groups of prototypic phases need to be time symmetric. This is the only point group symmetry requirement for ferroelastic materials, unlike ferroelectrics, where non-centrosymmetry or an absence of the inversion operator is necessary. Note that the ferroic phases (after symmetry breaking phase transition) can be time-asymmetric. In this case, the ferroics are not full ferroelastics or ferroelectrics. This is because the strain tensor and polarization vector are time invariant [55]. Hence, a time inversion operation performed on an orientation state would not change them, leading to two orientation states having the same orientation/polarization in case of ferroelastics/ferroelectrics respectively. These are then called 'partial' ferroelastics, where there is at least a pair of orientation states that are identical. The entire list of possible ferroic transitions (ferroelastic, ferroelectric, and ferromagnetic) is deduced by Aizu [55].

For ferroelastic materials, the requirements are listed below:

1) The prototypic point group should be a subgroup of the time-symmetric point groups [55]
2) Breaking of symmetry during phase transition – at least one symmetry operator is removed from the point group of the prototypic phase
3) Point group of the ferroelastic phase should be a proper subgroup of the point group of prototypic phase – no new symmetry operators should arise as a result of the phase transition
4) There should be spontaneous strain on phase transition – non-zero strain at zero stress. Strain is compared to prototypic unit cell
5) There should be at least two switchable domain states. Domain switching is a necessary condition of ferroelastics. In case the domain switching is allowed by symmetry but not observed experimentally, there are two types of ferroelastics. If the attempt to switch domains leads to destruction of the sample, it is termed as a 'hard ferroelastic'. If no hysteresis measurements have been performed, it is termed as a 'potential ferroelastic'. [56]

2.4.3.4 Domain boundaries in ferroelastics

Domain boundaries in ferroelastics are named with respect to the angular rotation about a low index axis that brings the unit cells in the two adjacent ferroelastic domains into coincidence. The domain boundary (horizontal boundary between the two monoclinic cells constituting the lower central figure) in the schematic of Figure 2-19 is a 90° domain boundary: a 90° rotation about the horizontal axis brings the cells into coincidence. Because the domain boundaries separate regions of distinct crystallographic orientations, the boundary plane is usually subject to significant crystallographic restrictions [47].

2.4.3.5 Poling in ferroic compounds

By the application of an external field (electric potential/stress for ferroelectrics/elastics respectively), the relative volumes of different domains can be modified, ideally allowing an entire crystal to adopt a single domain. This is called poling. For example, domain switching between energetically degenerate configurations (state 1 and 2 in Figure 2-19) can be carried out by the application of a shear stress. Poling occurs when one degenerate state becomes lower in energy that the other, due to application of a field. Thus, the states are no longer degenerate, and the crystal tends to go the lower energy state.

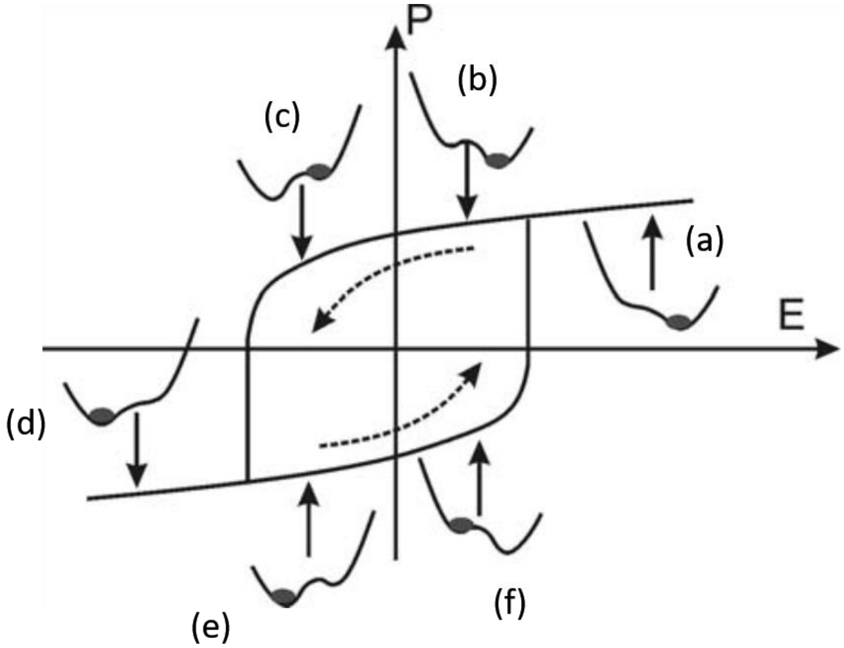

Figure 2-20: Change in energy of degenerate states of a ferroelectric with applied electric field. The black dot shows the current state of the material for a particular E.

Consider Figure 2-20 [57]. There are two possible energy states at all values of E. They are degenerate only at E = 0 (not shown in the figure). Let us term them as the right side state and left side state, according to the side of the middle hump in the energy curve they are present. In the region where E > 0, the right side state is more preferred and is lower in energy, due to application of the field (E). In the region where E < 0, the left side state is more preferred. At position (a), the system is at the lowest energy and most stable, and increasing the field after that will only increase the difference between the higher energy state and the current stable state. Going towards (b), as the field is lowered, the two states come closer in energy, but the system is still in the right side state. At (c), once the field crosses into the negative region, the left side state becomes more stable. However, at this point, the system has not yet made the switch to the more stable state. Just before (d), the system makes the switch to the more stable left side state and the polarization (P) switches sign instantly. This is signified by the almost vertical line. It means that the polarization went from a positive to a negative value with no change of field. This was possible because of a lower energy state alternative being present. At (d), the system is in its stable state. From (e), the cycle then repeats. As we increase the field, the two states start getting closer in energy. Just before (f), the field crosses into the positive regime and the right side state becomes the stable state again. A similar scenario can be drawn for ferroelastics using a strain vs. stress curve. In photocatalysis, poling [58–60] or local domain writing [61] has been used to correlate the direction of the local polarization to the type of chemical reactivity.

2.4.3.6 How do domains affect photocatalysis?

Now that we have discussed what domains are, how are they formed in ferroelectrics and ferroelastics and how they can be manipulated, let us look at how they can affect photocatalytic activity. The process of photocatalysis is the same in ferroic materials as any other systems. It is the mechanism of charge separation that differs.

The first part of this section describes the photocatalytic process in a ferroelectric crystal and gives possible explanations as to why the reactivity is as seen. The second part gives the same information for a ferroelastic system.

Ferroelectrics

As seen in the previous section, the surface of the ferroelectric domains exposed to the environment is charged. As photocatalysis is an electrochemical process, we naturally expect is to be affected by the presence of these charges. In Figure 2-21, an electron hole pair is generated when light of energy higher than the band gap of the material is absorbed by it (shown by the yellow arrow).

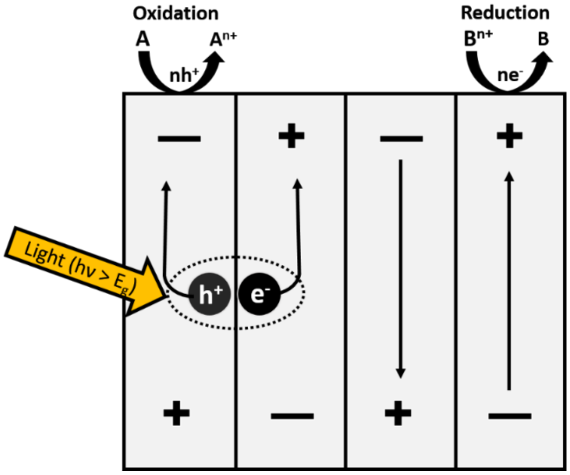

Figure 2-21: Charge separation due to ferroelectric domains

The electrons, being negatively charged, are attracted towards positive charges, and hence go towards the ferroelectric domains with a positively charged surface. The holes similarly go towards the negatively charged ferroelectric domains.

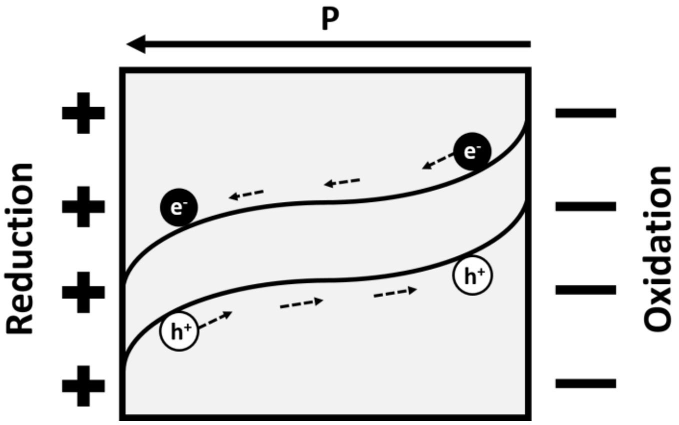

Figure 2-22: Charge separation due to polarization-induced band bending in a ferroelectric single crystal

Thus, the charges are separated, reducing the possibility of recombination. The holes carry out oxidation of species on negative ferroelectric domains, as shown on the first domain from the left. Similarly, the electrons carry out reduction on positive ferroelectric domains (shown on the right-most domain).

The next figure (Figure 2-22) shows how the surface charges change the electronic structure of the crystal. It schematizes the energy bands in a single crystal, with the polarization direction (P) being right to left. The valence and conduction bands are bent near the surface. In this particular case, the ferroelectric domain is just thick enough to have no region in the bulk where the bands are not bent. If there are free electrons (holes) in the conduction (valence) band, they prefer to go to a lower (higher) energy state. There is a continuous gradation of energy states in this hypothetical crystal extending from one side to the other. Hence, all the charge carriers formed in this crystal have a driving force to be swept away to one side, depending on their polarity. Had there been a region in the bulk where the bands were flat, the charge carriers formed in that region would have no driving force to go either way. The probability of those reaching the surface depended on which side they would randomly diffuse to.

Here, the hole in the valence band can continuously increase its energy till it reaches the negatively charged side. Similarly, the electron can keep reducing its energy if it goes from right to left in the crystal. This is how surface charges change the electronic structure, and enable charge separation in ferroelectric compounds.

Ferroelastics

Ferroelastics do not have surface charges unlike ferroelectrics. Yet, $BiVO_4$ has shown ferroelastic domain specific reactivity on its surface [62]. Hence, there is some driving force imparted by the ferroelastic domains which cause the charges to separate. One possible theory put forth by the authors is polarization by flexoelectricity. Flexoelectricity is polarization caused by a strain gradient in the material [63]. There are no crystallographic requirements for a material to display this phenomenon. The figure below (Figure 2-23) is a schematic of how ferroelastic domains in a ferroelastic compound with a centrosymmetric crystal structure can develop dipoles when subjected to a strain gradient.

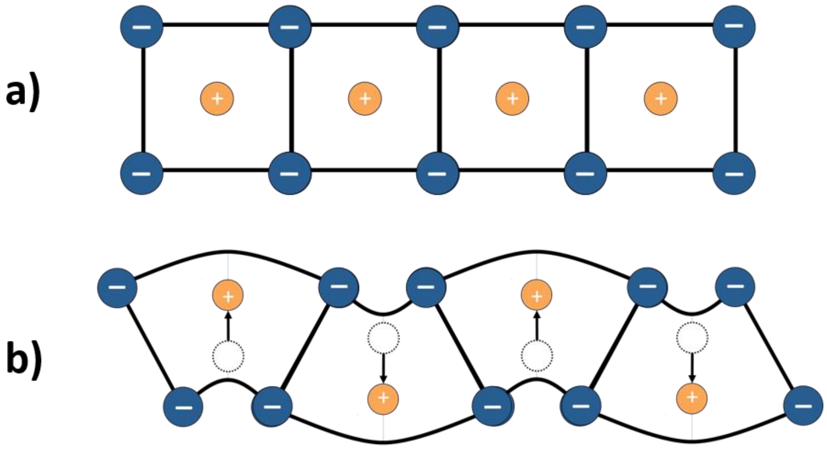

Figure 2-23: (a) Unstrained, non-polar structure (b) Dipole formation due to alternating strain gradients

The blue circles represent singly-charged anions in a hypothetical cubic structure. The yellow circles represent singly-charged cations. In (a), before ferroelastic domain formation, there are no strain gradients and hence, no polarization. The center of the negative charge coincides with that of the positive charge. In (b), there are alternating strain gradients on every unit cell. The cells which are curved upward have tensile forces on their top surface and compressive forces on the bottom. Hence, there is a strain gradient from bottom to top in these cells. The cations are driven off-center due to the differential strain. Hence, there is a difference in positions of the effective negative and positive charges. This is how a dipole is formed, which leads to polarization. Please note that the undulation is exaggerated in the schematic to alternate across every unit cell, to describe the atomic displacements.

Once the alternating dipoles are formed, the mechanism of charge separation is similar to that in ferroelectric compounds.

2.4.3.7 What are Anti-ferroic materials?

Anti-ferroic materials, such as anti-ferromagnets, anti-ferroelastics, and anti-ferroelectrics, have anti-parallel ordering of their local order vectors below a critical temperature referred to as the Neél temperature (T_N). The anti-parallel alignment results in no net magnetization, strain, or polarization, because the local vector moments cancel out over relatively small length scales. A schematic of atomic displacements in a ferroelectric and an anti-ferroelectric are shown in Figure 2-24(a) and Figure 2-24(b) respectively. Although there still are local polar units, the net polarization is zero in the case of an anti-ferroelectric. Interestingly, application of an external field can drive some anti-ferroics into a ferroic state. This is a common expectation for anti-ferroelectrics, whose parallel alignment is only stable under the applied field. One could envision converting the atomic distribution in Figure 2-24(b) to that in Figure 2-24(a), under the correct field. In such cases, the energy difference between the anti-ferroic and ferroic states must be small, as is the case for nearby metastable states. Anti-ferroelectrics do not require non-centrosymmetry, but usually have nearby non-centrosymmetric structures (energetically) into which they transform under the appropriate field.

Figure 2-25 shows the AFE-FE transition in a lead zirconate thin film (from [64]). The ferroelectric behavior manifests itself after applying an electric field.

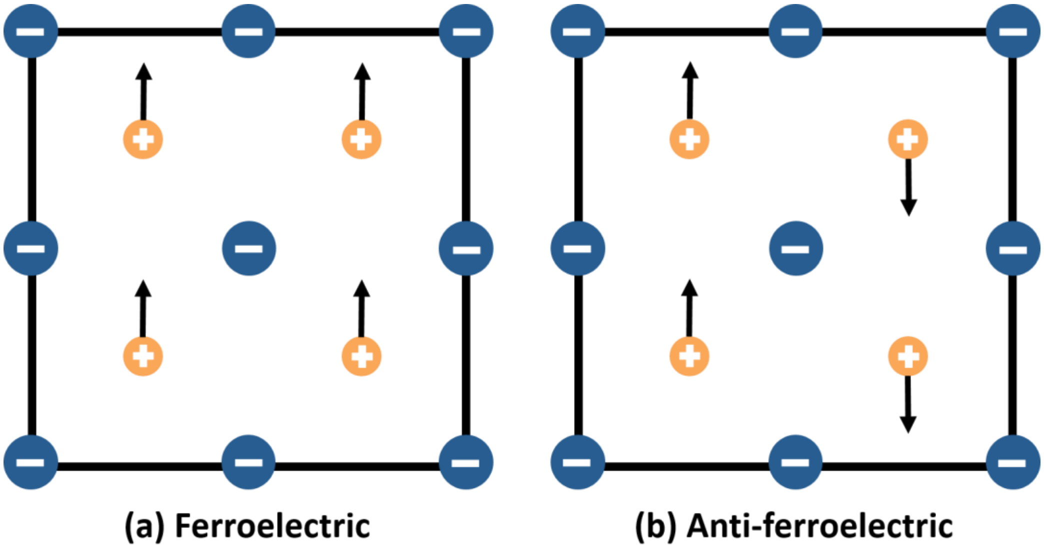

Figure 2-24: Example of (a) Ferroelectric unit cell with all dipoles aligned (b) Anti-ferroelectric unit cell with dipole moments being cancelled out

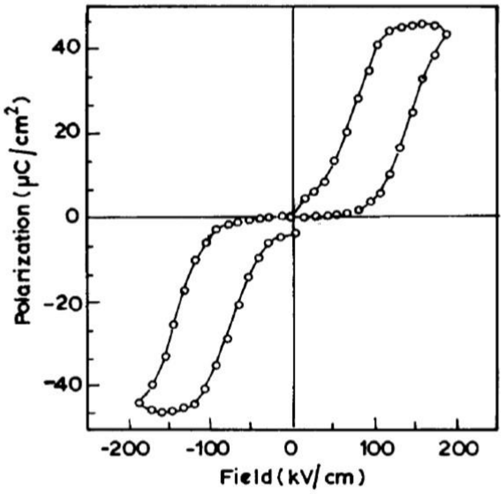

Figure 2-25: Double hysteresis loop (polarization vs field) of a lead zirconate thin film [64].

2.5 Experimental methods

2.5.1 Photodeposition and marker reactions

Photodeposition is the method employed to study spatial selectivity of photoreactions throughout this work. A detailed description of the method and apparatus has been given in the previous section.

Photodeposition is a process of depositing insoluble particles using light on a photoactive substrate. Photodeposition has other uses like selective deposition of co-catalysts on photocatalytic materials for purification of air [14,15] and water [13]. The co-catalyst + photocatalyst systems have also been studied for solar fuel production [65,66]. Wenderich and Mul [67] have written a comprehensive review about photodeposition in photocatalysis.

2.5.1.1 Marker reactions

Marker reactions are used to ‘mark’ the areas that promote one of the reduction or oxidation photoreactions over the other. These are a subset of photodeposition reactions, which are primarily used to deposit catalytic nanoparticles on surfaces to enhance surface functionalization. The intention here is not of functionalization, but to determine the specific reaction promoting areas on photocatalyst surfaces. Wenderich and Mul [67] have published an excellent review of photodeposition methods and mechanisms.

A schematic of the room temperature system using UV light is shown in Figure 2-26. The general workflow is as follows:

Firstly, submerge the photocatalyst in a solution containing metal ions. Then, shine light on the photocatalyst with a higher energy than the bandgap of the photocatalyst to excite electrons and holes. This is done using a UV lamp (with a visible light filter if necessary). The electrons (holes) go to the surface and reduce (oxidize) the metal ions in solution to deposit insoluble products on the surface. The deposits are then imaged to determine the reduction or oxidation promoting areas

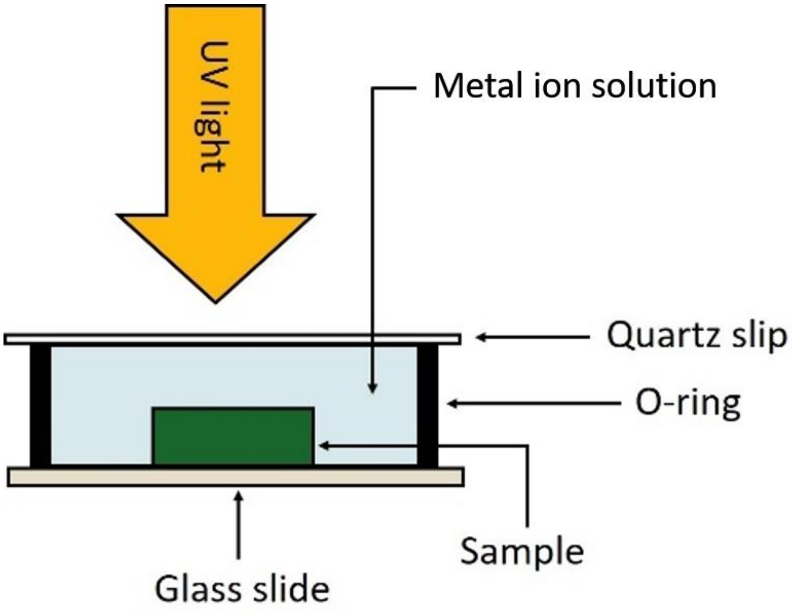

Figure 2-26: Schematic of experimental setup for carrying out photodeposition

In our room temperature setup, we fix the sample on a glass slide using double-sided tape. A Viton O-ring is then placed around it to create a space for the solution. A quartz slip is used to cover and close off the entire setup. A fused quartz slip is used instead of plain glass because of its high transmissivity (>90 %) from around 250 nm to 1500 nm). (https://www.tedpella.com/histo_html/GE124-Quartz.html)

We have used water as our solvent in the experiments concerning $SrTiO_3$, WO_3 and $BiVO_4$ because of the easy availability of soluble metal salts and the stability of the substrate in it. Silver nitrate ($AgNO_3$) is used as the metal ion source for reduction marker reactions. Lead acetate ($Pb(CH_3COO)_2$) and Manganese sulphate ($MnSO_4.4H_2O$) are used as the metal salts for oxidation marker reactions. EDTA (ethylenediaminetetraacetic acid) and its disodium salt have been used as hole scavengers.

The photoreactions concerning different metal ions are given below:

1) **Ag^+ (in solution) + e^- → Ag (insoluble)**

   Counter reaction - Oxygen evolution: $2H_2O + 4h^+ \rightarrow 4H^+ + O_2$

   Overall – $4Ag^+ + 2H_2O \rightarrow 4Ag + 4H^+ + O_2$

2) **Pb^{2+} (in solution) + $2h^+ + 2H_2O$ → PbO_2 (insoluble) + $4H^+$**

   Counter reaction – Hydrogen evolution: $2H^+ + 2e^- \rightarrow H_2$

   Overall – $Pb^{2+} + 2H_2O \rightarrow PbO_2 + H_2 + 2H^+$

3) **Mn^{2+} (in solution) + $2h^+ + 2H_2O$ → MnO_2 (insoluble) + $4H^+$**

   Counter reaction – Hydrogen evolution: $2H^+ + 2e^- \rightarrow H_2$

   Overall – $Mn^{2+} + 2H_2O \rightarrow MnO_2 + H_2 + 2H^+$

The counter reactions have not been studied and the listed ones are assumed. There may be other products.

The insoluble deposits of Ag, PbO_2 and MnO_2 are then imaged using SEM/AFM to determine regions promoting either reduction or oxidation.

2.5.2 Scanning Electron Microscopy

Scanning Electron Microscopy (SEM) is an imaging technique that uses focused electron beams to image as opposed to visible light in optical microscopes. The magnification obtainable by optical microscopes is limited to 1000x because of the wavelength of visible light (~400-700 nm). For larger magnifications, lower wavelengths are needed. Such short wavelengths are obtained when electrons are accelerated by a potential difference of 2 kV onwards. This gives the electron microscope magnification limits around 100000x. An excellent article on SEM basics is given by Vernon-Parry [70]. On the other hand, Goldstein et al. [71] have published a book detailing all the intricacies of the technique.

In the SEM, the electron beam is rastered or 'scanned' over the area of interest, giving rise to various signals. For our experiments, we have used three modes and resultant signals detailed below:

2.5.2.1 Secondary electron imaging (SE)

Secondary electrons are those which are knocked off the electron shells of the atoms of the material being imaged. They are termed 'secondary' because they are generated by the primary electron beam from the electron gun. These electrons are captured by the detector to generate the signal. An Everhart-Thornley detector is used to capture these electrons under high vacuum. The energy of the secondary electrons is such that only those emitted from the top 5 - 50 nm can reach the detector [71]. Hence, this gives a very good topographic contrast. We have used this mode as a primary imaging technique at the nanoscale. The surface topography before and after the marker reactions and the facet morphology in $SrTiO_3$ was imaged in the SE mode. All SE images have been recorded on FEI Quanta 200 FEG (field emission gun) or FEI Quanta 600 FEG scanning electron microscope. The accelerating voltage ranges from 10 kV to 20 kV with a spot size of 3-5. The resolution of the images has largely been kept to 2048x1768. The recording time is between 1-3 minutes per image. In case of $SrTiO_3$, the images were recorded in low vacuum mode at 0.83 Torr to avoid charging of the sample.

2.5.2.2 Backscatter electron imaging (BSE) – Electron Channeling contrast

Backscatter electrons are those whose trajectory takes them close to the nucleus of the atom, and are then elastically scattered through a large angle, re-emerging through the surface [70]. As a result, they have a higher energy than the secondary electrons and can be captured from greater depths of the sample (up to 5 µm) [72]. The BSE signal gives compositional contrast as the signal increases with the atomic number of the element [72]. The signal is also dependent on the orientation of the crystal lattice, that affects the number of the elastic scattering events. This is known as the electron channeling effect. A small review on this has been published by Kamaladasa and Picard [73]. We have used this effect in BSE mode to determine the ferroelastic domain structure of WO_3 and $BiVO_4$. Adjacent ferroelastic domains in a tier have alternating orientations, that gives rise to alternating contrast due to the channeling effect. In rare cases, both ferroelastic domains are orientated in a manner such that the signal from both of them is equal, resulting in no contrast. Largely however, the ferroelastic domains can be imaged easily in this mode.

2.5.2.3 Electron Backscatter Diffraction (EBSD)

The diffraction of electrons from lattice planes of a sample tilted at a high angle (70° for our experiments) results in formation of band-like patterns, which give information regarding the orientation of the crystal lattice for every point in the raster. A book detailing aspects of EBSD has been published by Schwartz et al. [74] The orientation information was used to ascertain the presence of ferroelastic domains in WO_3, as well as to get the Euler angles of grains in $SrTiO_3$ polycrystals. The Euler angles were used to determine the facet planes present on the grains to comment on the nature of reactivity as a function of their orientation.

EBSD was carried out using an FEI Quanta 600 FEG SEM equipped with an Oxford HKL EBSD system and an HKL NordlysNano camera. The accelerating voltage was 20 kV. The sample was mounted on a pre-tilted sample holder (70°).

2.5.3 Atomic Force Microscopy

Atomic force Microscopy (AFM) is a form of Scanning probe microscopy, wherein a probe is rastered across the surface of the material to give different kinds of information depending on the mode used. The technique gets its name from the parameter it measures – forces between the probe and the material surface at atomic length scales. They are indirectly measured by measuring the bending of the probe. The interaction between the tip and the surface is governed by Van der Waal’s interactions, Nuclei – Nuclei repulsions and electrostatic forces. An excellent book written by Voigtländer [75] gives information on the everything ranging from the history of the technique to the usage of scanning probe microscopy.

We will look at how the AFM works on the basis of a schematic given below in Figure 2-27 [75]. A laser beam (in red) is focused on the back of a cantilever with a tip (shown in gray). The tip diameter is one of the factors that determines the spatial resolution of the output signal. For atomic resolution, super sharp tips with a high aspect ratio and tip diameter of 1-2 nm are available. General purpose tips for topographic measurements are usually 10 nm in diameter. Conductive tips have a larger diameter (~30 nm) due to the presence of a conductive coating.

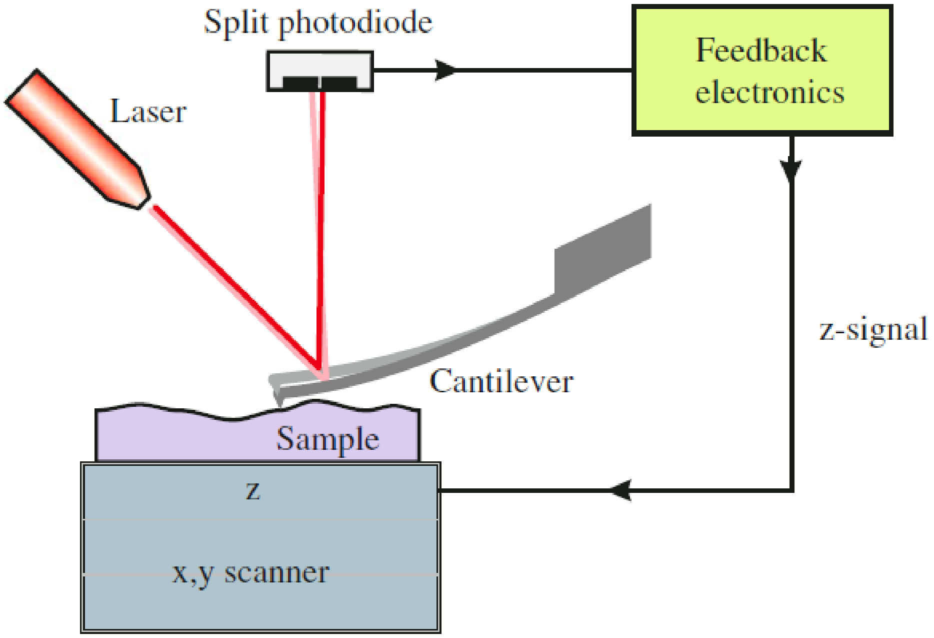

Figure 2-27: Basic working principle of an Atomic Force Microscope (AFM)

The laser bounces off the cantilever into a 4-section photodiode, by which it measures the vertical and lateral deflections of the tip. The vertical deflections of the tip vary the position of the laser spot on the photodiode between the top and bottom halves, and similarly between the left and right halves for lateral deflections. The signal from the photodiode is sent to a feedback controller, which sends out a command (z-signal) to the piezostage to restore the setpoint. This completes the feedback loop and the tip advances to the next point in the raster. The setpoint of the process is the parameter set by the user, against which the change in the parameter is measured to give the feedback signal, which brings the change to zero. The feedback signal is then noted as the actual signal output given to the user. The setpoint may be the amplitude/frequency of the oscillation of the cantilever or the force experienced by the cantilever, depending on the mode used.

Similar to the SEM, we have used three modes of AFM for our experiments. All of these have been detailed below.

2.5.3.1 Topography by Tapping mode AFM

Compared to Contact AFM, the tip wear is reduced in tapping mode. Also, the high frequency of the oscillations enables scanning at higher speeds.

In $SrTiO_3$, the topography information was used along with Euler angles from EBSD to determine the orientation of the facet planes. On WO_3 and $BiVO_4$, the topography scans are used to image the deposits of the marker reactions. AFM imaging of the deposits is more reliable as compared to the SEM because quantitative height information is available. There is no depth information from the SE mode in the SEM. Some contrast from channeling is also overlaid on top of topographical contrast in the SE mode, which can add ambiguity to the interpretation of SEM images of marker reactions on ferroelastic domains.

2.5.3.2 Piezoforce microscopy (PFM)

Piezoforce microscopy gives the magnitude and direction of the polarization of the material being imaged [76]. PFM is a contact mode AFM technique. As before, we will look at the mechanism of PFM using the schematic in Figure 2-28. In PFM, an alternating voltage is applied to the tip. Here, the voltage signal has been shown in blue in Figure 2-28(b) and Figure 2-28(d). Now, consider Figure 2-28(a). The tip has been biased positively. Also, the polarization of the ferroelectric domain is downwards. Hence, the sample expands, as shown by the dotted lines. However, if the polarization of the ferroelectric domain is upwards (positive charge at the surface), then as the applied field becomes more and more positive, the sample is compressed. The phase difference is however, not 180° for most cases due to a background signal [77].

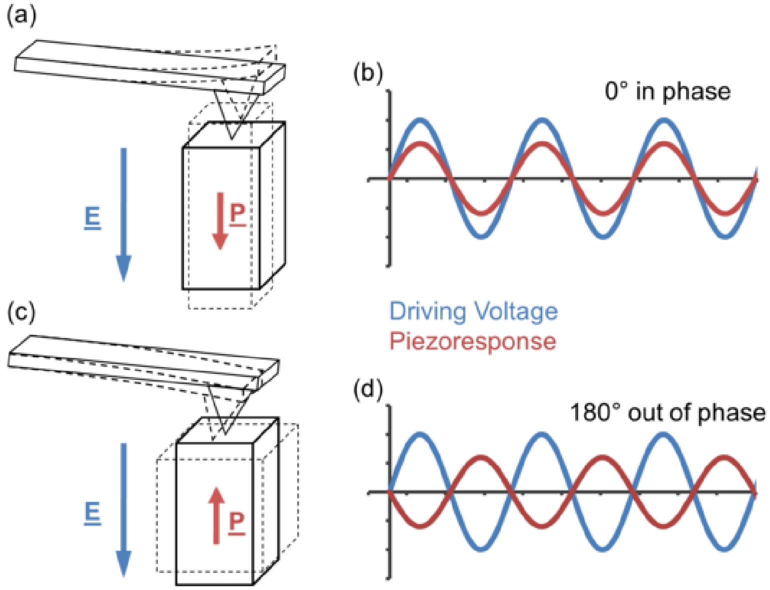

Figure 2-28: Piezoresponse when polarization points (a), (b) - downwards and (c), (d) – upwards in a ferroelectric domain.

2.5.3.3 Kelvin Probe Surface Microscopy

Kalinin et al. [78] used surface potential microscopy (also known as kelvin probe force microscopy or KPFM) to image the polarity of ferroelectric domains on BaTiO3. Bhardwaj et al. [79] followed up by using KPFM to correlate reactivity to ferroelectric domain polarization on BaTiO3. A KPFM image of the surface of a BaTiO3 ceramic is shown in Figure 2-29(a), with a grain boundary running slightly off vertical in the center. In this image, contrast arises from regions having different work functions.

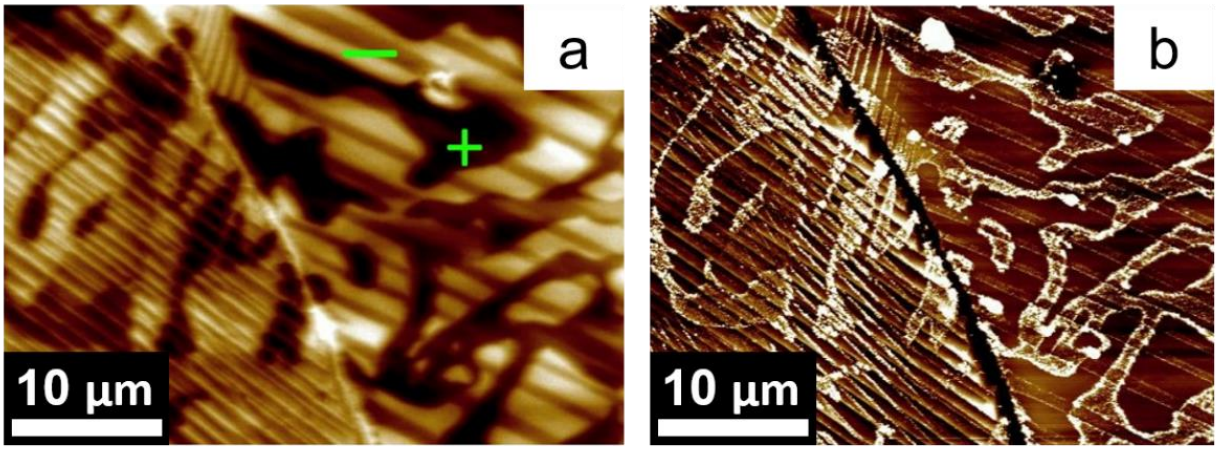

Figure 2-29: (a) KFM potential map and (b) AFM topography after photoreduction of Ag^+ of a $BaTiO_3$ substrate

Different work functions arise from different near-surface band bending owing to the local dipole moments or charges [80], which in this case correspond to different ferroelectric domain polarizations. The KPFM image maps the ferroelectric domains clearly. An AFM image of the surface after Ag photoreduction is shown in Figure 2-29(b). The photochemical reactivity is clearly correlated with the ferroelectric domains mapped by KPFM. The dark regions in KPFM, which were identified as the positive polarized ferroelectric domains, are photocathodic (reactive for Ag photoreduction), while the light (negative polarized ferroelectric domains) regions are not. It has been widely reported that ferroelectrics have improved photochemical reactivity in comparison to similar non-ferroelectric materials.

2.5.4 X-ray diffraction

X-ray Diffraction is a widely used technique in Materials science to determine physical properties like structure, texture, strain etc. of crystalline materials. X-rays are produced when accelerated electrons hit a target (usually Cu or Mo). They are then filtered to produce intensity of a narrow width in the energy spectrum. These x-rays are incident on the sample at an angle that is varied. At certain angles depending on the crystal structure of the material, the diffraction of the incident x-rays from the lattice planes of the material is constructive. This constructive interference leads to high magnitudes of diffraction intensities at certain angles governed by the Bragg's law. The diffraction peak positions can be obtained from Bragg's law: $n\lambda=2d*\sin\Theta$

Where,

n is the order of diffraction

λ is the wavelength of X-rays used (Cu K_α – 0.154 nm for our experiments)

d is the interplanar lattice spacing

Θ is the angle between the surface normal and the incident direction of X-rays

The plot of intensity vs. $2*\Theta$ is commonly known as the X-ray diffraction pattern. However, the structure factor is very important when it comes to the intensity of the peaks. Some peaks can vanish even if they satisfy the Bragg's law. There are other factors like multiplicity factor that determine the overall intensity of the peak [63]. Comparing the observed pattern with the standard patterns provided by the ICDD (International Centre for Diffraction Data) yields information regarding the structure of the sample.

2.5.5 Thermochemical treatments for $SrTiO_3$

As shown by Zhu et al. [25–27], $SrTiO_3$ samples heated in the presence of excess Sr showed a higher proportion of areas promoting reduction on (110) and (111) single crystals. The surface concentration of Sr varied as per the exposure time and temperature. For our experiments, we have heated the sample in a crucible with 0.1 g of $Sr_3Ti_2O_7$ next to it. A schematic is shown in Figure 2-30.

To provide a Sr-rich atmosphere, we heated the samples in presence of $Sr_3Ti_2O_7$ to create a concentration gradient from it towards the sample to enable transport. It was found that heating in the presence of $SrCO_3$ or SrO oversaturated the surface with Sr leading to secondary phase formation.

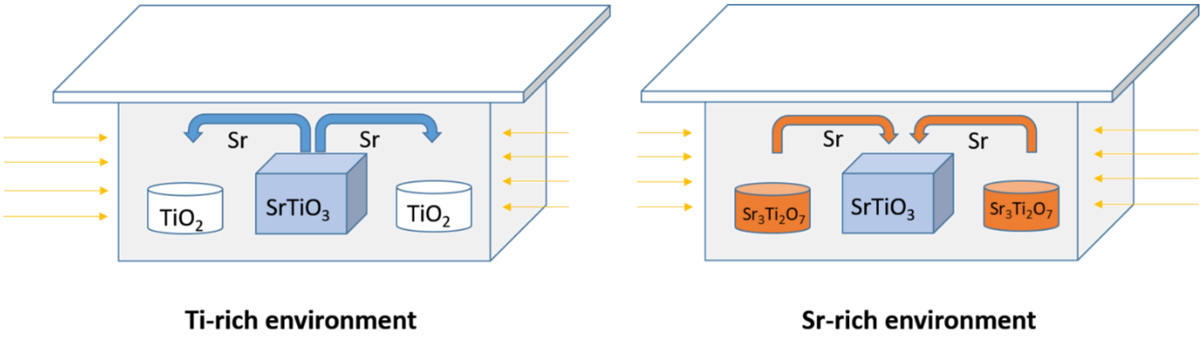

Figure 2-30: Thermochemical treatment in (left) Sr-deficient and (right) Sr-rich environment

It was easier to control the saturation of Sr by using $Sr_3Ti_2O_7$. To make the surface Sr-deficient, the samples were heated in presence of TiO_2. This created a concentration gradient to enable Sr transport from the sample surface to titania. However, the kinetics could not be controlled easily. The morphological changes are discussed in the later sections.

2.6 References

Chapter 2: Fundamentals

[1] Thomas R. Anderson, Ed Hawkins, and Philip D. Jones: *Endeavour*, 2016, vol. 40, pp. 178–87.

[2] Andrew A Lacis, Gavin A Schmidt, David Rind, and Reto A Ruedy: *Science*, 2010, vol. 330, pp. 356–59.

[3] Svante Arrhenius: *Philos. Mag. J. Sci. Ser.*, 1896, vol. 5, pp. 237–76.

[4] Dagobert G Kessel: *J. Pet. Sci. Eng.*, 2000, vol. 26, pp. 157–68.

[5] GERHARD GERLICH and RALF D. TSCHEUSCHNER: *Int. J. Mod. Phys. B*, 2009, vol. 23, pp. 275–364.

[6] Gerhard Kramm and Ralph Dlugi: *Nat. Sci.*, 2011, vol. 03, pp. 971–98.

[7] Marilena Kampa and Elias Castanas: n.d.

[8] C Arden and Pope Ill: *-Environ Heal. Perspect*, 2000, vol. 1, pp. 8713–23.

[9] Davide Ravelli, Daniele Dondi, Maurizio Fagnoni, and Angelo Albini: *Chem. Soc. Rev.*, 2009, vol. 38, p. 1999.

[10] A Fujishima and K Honda: *Nature*, 1972, vol. 238, pp. 37–38.

[11] National Research Council and National Academy of Engineering: *The Hydrogen Economy: Opportunities, Costs, Barriers, and R&D Needs*, National Academies Press, Washington, D.C., 2004.

[12] Roel Van De Krol and Michael Grätzel: *Photoelectro-Chemical Hydrogen Production*, 2012.

[13] Meng Nan Chong, Bo Jin, Christopher W.K. Chow, and Chris Saint: *Water Res.*, 2010,

vol. 44, pp. 2997–3027.

[14] Agatino Di Paola, Elisa García-López, Giuseppe Marcì, and Leonardo Palmisano: *J. Hazard. Mater.*, 2011, vol. 211, pp. 3–29.

[15] Juan Zhao and Xudong Yang: *Build. Environ.*, 2003, vol. 38, pp. 645–54.

[16] Yash Boyjoo, Hongqi Sun, Jian Liu, Vishnu K. Pareek, and Shaobin Wang: *Chem. Eng. J.*, 2017, vol. 310, pp. 537–59.

[17] Wei Wang, Moses O Tade, and Zongping Shao: *Chem. Soc. Rev.*, 2015, vol. 44, pp. 5371–5408.

[18] Johan Moan: n.d.

[19] A.B. Murphy, P.R.F. Barnes, L.K. Randeniya, I.C. Plumb, I.E. Grey, M.D. Horne, and J.A. Glasscock: *Int. J. Hydrogen Energy*, 2006, vol. 31, pp. 1999–2017.

[20] Allen J. Bard and Marye Anne Fox: *Acc. Chem. Res.*, 1995, vol. 28, pp. 141–45.

[21] Jinhui Yang, Hongjian Yan, Xu Zong, Fuyu Wen, Meiying Liu, and Can Li: *Philos. Trans. R. Soc. London A Math. Phys. Eng. Sci.*, 2013, vol. 371, p. 20110430.

[22] Li Li, Paul a Salvador, and Gregory S Rohrer: *Nanoscale*, 2014, vol. 6, pp. 24–42.

[23] Jieyang Jia, Linsey C. Seitz, Jesse D. Benck, Yijie Huo, Yusi Chen, Jia Wei Desmond Ng, Taner Bilir, James S. Harris, and Thomas F. Jaramillo: *Nat. Commun.*, 2016, vol. 7, p. 13237.

[24] Pingwu Du and Richard Eisenberg: *Energy Environ. Sci.*, 2012, vol. 5, p. 6012.

[25] Yisi Zhu, Paul A Salvador, and Gregory S Rohrer: *Chem. Mater.*, 2016, vol. 28, pp. 5155–62.

[26] Yisi Zhu, Paul A. Salvador, and Gregory S. Rohrer: *Phys. Chem. Chem. Phys.*, 2017, vol. 19, pp. 7910–18.

[27] Yisi Zhu, Paul A. Salvador, and Gregory S. Rohrer: *ACS Appl. Mater. Interfaces*, 2017, vol. 3, pp. 7843–51.

[28] Linchao Mu, Yue Zhao, Ailong Li, Shengyang Wang, Zhiliang Wang, Jingxiu Yang, Yi Wang, Taifeng Liu, Ruotian Chen, Jian Zhu, Fengtao Fan, Rengui Li, and Can Li: *Energy Environ. Sci.*, 2016, vol. 9, pp. 2463–69.

[29] Rengui Li, Fuxiang Zhang, Donge Wang, Jingxiu Yang, Mingrun Li, Jian Zhu, Xin Zhou, Hongxian Han, and Can Li: *Nat. Commun.*, 2013, vol. 4, pp. 1432–37.

[30] Ajay S. Pisat, Gregory S. Rohrer, and Paul A. Salvador: *J. Mater. Chem. A*, 2017, vol. 5, pp. 8261–66.

[31] Cheng-En Cheng, Heng-Jui Liu, Franco Dinelli, Yi-Chun Chen, Chen-Shiung Chang, Forest Shih-Sen Chien, and Ying-Hao Chu: *Sci. Rep.*, 2015, vol. 5, p. 8091.

[32] Ratiporn Munprom, Paul A. Salvador, and Gregory S. Rohrer: *Chem. Mater.*, 2014, vol. 26, pp. 2774–76.

[33] Ajay S. Pisat, Gregory S. Rohrer, and Paul A. Salvador: *Semicond. Sci. Technol.*, 2017, vol. 32.

[34] G S Rohrer: *Oxide Interfaces*, 2001, pp. 485–513.

[35] J L Giocondi and G S Rohrer: *J. Am. Ceram. Soc.*, 2003, vol. 86, pp. 1182–89.

[36] D S Deak: 2013.

[37] Matthew S J Marshall, Andres E Becerra-Toledo, Laurence D Marks, and Martin R Castell: in *Defects at Oxide Surfaces*, Jacques Jupille and Geoff Thornton, eds., Springer International Publishing, Cham, 2015, pp. 327–49.

[38] Laurence D Marks, Ann N Chiaramonti, Fabien Tran, and Peter Blaha: 2009, vol. 603, pp. 2179–87.

[39] † Natasha Erdman, ‡ Oliver Warschkow, § Mark Asta, ‖ Kenneth R. Poeppelmeier, ‡ and Donald E. Ellis, and † Laurence D. Marks*: *J. Am. Ceram. Soc.*, 2003, vol. 125, pp. 10050–56.

[40] R Herger, P R Willmott, O Bunk, C M Schlepütz, B D Patterson, and B Delley: 2014.

[41] Florencio Sánchez, Carmen Ocal, and Josep Fontcuberta: *Chem. Soc. Rev.*, 2014, vol. 43, pp. 2272–85.

[42] a. Ohtomo and H. Y. Hwang: *Nature*, 2004, vol. 427, pp. 423–26.

[43] Yisi Zhu, Paul A Salvador, and Gregory S Rohrer: *Chem. Mater.*, 2016, vol. 28, pp. 5155–62.

[44] Nina V. Burbure, Paul A. Salvador, and Gregory S. Rohrer: *Chem. Mater.*, 2010, vol. 22, pp. 5831–37.

[45] Nina V. Burbure, Paul A. Salvador, and Gregory S. Rohrer: *Chem. Mater.*, 2010, vol. 22, pp. 5823–30.

[46] Yiling Zhang, Andrew M. Schultz, Paul a. Salvador, and Gregory S. Rohrer: *J. Mater. Chem.*,

2011, vol. 21, p. 4168.

[47] Andrew M. Schultz, Yiling Zhang, Paul A. Salvador, and Gregory S. Rohrer: *ACS Appl. Mater. Interfaces*, 2011, vol. 3, pp. 1562–67.

[48] Yisi Zhu, Paul A Salvador, and P Chris Pistorius: n.d.

[49] P A Mulheran: *Model. Siul. Mater. Sci. Eng*, 1994, vol. 2, pp. 1123–29.

[50] Conyers Herring: *Phys. Rev.*, 1951, vol. 82, pp. 87–93.

[51] G. Wulff: *Zeitschrift Für Krist. - Cryst. Mater.*, 1901, vol. 34, pp. 449–530.

[52] Zhengde Wei, Yi Zhao, Fengtao Fan, and Can Li: *Comput. Mater. Sci.*, 2018, vol. 153, pp. 28–35.

[53] Jiaguo Yu, Jingxiang Low, Wei Xiao, Peng Zhou, and Mietek Jaroniec: *J. Am. Chem. Soc.*, 2014, vol. 136, pp. 8839–42.

[54] Vinod K. Wadhawan: *Introduction to Ferroic Materials*, Gordon and Breach Science Publishers, 2000.

[55] Kêitsiro Aizu: *Phys. Rev. B*, 1970, vol. 2, pp. 754–72.

[56] E Salje: *Ferroelectrics*, 1990, vol. 104, pp. 111–20.

[57] K. M Rabe, Ch. H. Ahn, J. M -M. Triscone, M Dawber, and C Lichtensteiger: *Physics of Ferroelectrics*, 2007.

[58] Yasunobu Inoue, Kazunori Sato, and Shinichi Suzuki: *J. Phys. Chem.*, 1985, vol. 03, pp. 2827–31.

[59] Yasunobu Inoue, Masayoshi Okamura, and Kazunori Sato: *J. Phys. Chem.*, 1985, vol. 89, pp. 5184–87.

[60] Yasunobu Inoue, K Sato, and H Miyama: *J. Phys.*, 1986, vol. 90, pp. 2809–10.

[61] S. V. Kalinin, D. A. Bonnell, T. Alvarez, X. Lei, Z. Hu, J. H. Ferris, Qi Zhang, and S. Dunn: *Nano Lett.*, 2002, vol. 2, pp. 589–93.

[62] Ratiporn Munprom, Paul A. Salvador, and Gregory S. Rohrer: *J. Mater. Chem. A*, 2016, vol. 4, pp. 2951–59.

[63] Pavlo Zubko, Gustau Catalan, and Alexander K. Tagantsev: *Annu. Rev. Mater. Res.*, 2013, vol. 43, pp. 387–421.

[64] S S. N. Bharadwaja and Saluru Krupanidhi: *J. Appl. Phys.*, 2000, vol. 88, pp. 2072–80.

[65] Akihiko Kudo and Yugo Miseki: *Chem. Soc. Rev.*, 2009, vol. 38, pp. 253–78.

[66] Kazuhiko Maeda and Kazunari Domen: *J. Phys. Chem. Lett.*, 2010, vol. 1, pp. 2655–61.

[67] Kasper Wenderich and Guido Mul: *Chem. Rev.*, 2016, vol. 116, pp. 14587–619.

[68] Hsien Yi Hsu, Li Ji, Hyun S. Ahn, Ji Zhao, Edward T. Yu, and Allen J. Bard: *J. Am. Chem. Soc.*, 2015, vol. 137, pp. 14758–64.

[69] Gordana Dukovic, Maxwell G. Merkle, James H. Nelson, Steven M. Hughes, and A. Paul Alivisatos: *Adv. Mater.*, 2008, vol. 20, pp. 4306–11.

[70] K.D. Vernon-Parry: *III-Vs Rev.*, 2000, vol. 13, pp. 40–44.

[71] J.R. Goldstein, J., Newbury, D.E., Joy, D.C., Lyman, C.E., Echlin, P., Lifshin, E., Sawyer, L.,

Michael: *Scanning Electron Microscopy and X-Ray Microanalysis*, Third, 2013.

[72] Bob Hafner: n.d.

[73] R J Kamaladasa and Y N Picard: *Microsc. Scince, Technol. Apl. Educ.*, 2010, pp. 1583–90.

[74] D.P. (Eds.) Schwartz, A.J., Kumar, M., Adams, B.L., Field: *Electron Backscatter Diffraction in Materials Science*, 2nd ed., Springer US, 2009.

[75] Bert Voigtlander: *Scanning Probe Microscopy*, Springer US, 2015.

[76] D a Bonnell, S V Kalinin, a L Kholkin, and a Gruverman: *MRS Bull.*, 2009, vol. 34, pp. 648–57.

[77] Elisabeth Soergel: *J. Phys. D. Appl. Phys.*, 2011, vol. 44.

[78] Sergei V. Kalinin, C. Y. Johnson, and Dawn A. Bonnell: *J. Appl. Phys.*, 2002, vol. 91, pp. 3816–23.

[79] Abhilasha Bhardwaj, Nina V. Burbure, Andrew Gamalski, and Gregory S. Rohrer: *Chem. Mater.*, 2010, vol. 22, pp. 3527–34.

[80] Abhilasha Bhardwaj, Nina V. Burbure, and Gregory S. Rohrer: *J. Am. Ceram. Soc.*, 2010, vol. 93, pp. 4129–34.

[63] B.D. Cullity: Elements of X-ray Diffraction, 1956

3 Influence of Terminations and Facets on Photodeposition in Polycrystalline $SrTiO_3$

3.1 Introduction

The kinetics of oxidation-reduction reactions are of paramount importance to the efficiency of the photocatalytic process [1]. If the reduction reaction is faster than oxidation, the photo-excited electrons are utilized faster than holes. Hence, a surplus of holes is generated in the photocatalyst. This leads to increased recombination of the photo-excited charge carriers, and a reduction in the efficiency. The reason being that the carriers react with themselves and not with the species at the photocatalyst-environment interface. Hence, it is important to equalize the number of charge carriers required for both reactions. As an example where balancing charge availability is necessary, evolution of one mole of hydrogen from water splitting requires two electrons while a mole of oxygen takes four holes [2,3]. This implies that a larger area of the photocatalyst surface should promote oxidation as compared to reduction for water-splitting, assuming same transport properties for both.

Spatial selectivity can help in achieving balanced kinetics. In addition to promoting a single reaction and opening up the possibility to engineer the surface to a particular ratio of oxidation to reduction, the resultant spatial separation of reaction sites helps to reduce back reactions of any intermediates formed during the electrochemical reactions [3], [4]. Hence, A kinetically optimized photocatalytic system with spatial separation of reaction sites is highly desirable for efficient photocatalysis.

One such way of controlling spatial selectivity has been demonstrated by Zhu et. al. on $SrTiO_3$ single crystals, by controlling surface terminations [5,6]. By heating in Sr-rich/deficient conditions, the samples were made more photocathodic/photoanodic respectively. However, for large-scale implementation of any photocatalytic process, using single crystals is economically infeasible. Dispersions of photocatalytic powders in water for purification or coatings for surface sanitization are cheaper and easier to implement. Hence, it is important to be able to tune the reactivity of such systems, keeping in mind the requirements for upscaling and commercialization.

Polycrystals however, bring an added layer of complexity with them when considering spatial selectivity. The presence of different grains engages orientation dependent reactivity, which has been studied before on Fe_2O_3 [7], TiO_2 [8], $BaTi_4O_9$ [9] and $BiVO_4$ [10], amongst others. Even within a grain, polycrystals might facet depending on their surface energy function, creating a charge separation mechanism on an even smaller length scale than the grain size. The chemical terminations themselves will create an electrochemical potential difference on every facet, should both be present simultaneously. Thus, a length scale-based hierarchy of charge separation mechanism exists in polycrystals.

Hence, to deploy polycrystalline photocatalysts on an industrial scale, it is first necessary to check whether controlling terminations to tune reactivity is possible in the first place, and to study the impact of multiple charge separation mechanisms on photoreactivity. Polycrystalline $SrTiO_3$ (used in this work) is a good model for a primary study in this area. $SrTiO_3$ is an archetypical perovskite compound [11]. It is not ferroelectric or ferroelastic in nature (at room temperature-pressure). There are two mechanisms that can create charged regions on $SrTiO_3$. The first is that differently oriented surfaces are relatively more photocathodic or photoanodic. [12,13]. At 1250 °C (baseline annealing temperature for this work), $SrTiO_3$ surfaces are mostly made up of {100} and {110} facets and, at higher temperatures, {111} facets also appear on the equilibrium crystal shape, [14,15] and each of these surfaces has a different photochemical reactivity.[17] Hence, only two facet orientations are expected. The second mechanism that can create charged region is that $SrTiO_3$ surfaces can have different chemical terminations, with different charges, that promote the photocathodic and photoanodic half reactions differently. [16] For example, the two possible chemical terminations of the $SrTiO_3$ (100) surface are SrO or TiO_2, and the two possible chemical terminations of the $SrTiO_3$ (110) are O_2^{4-} and $SrTiO^{4+}$. It should be emphasized that here we refer to the ideal terminations when the crystal is cleaved, and the atomic positions do not significantly change. In reality, the surface is likely to reconstruct and this will depend on the external environment, [17,18] but such changes do not completely eliminate the surface charge. Thus, there are 4 possible facet-termination combinations on polycrystals of $SrTiO_3$ annealed at 1250 °C - (100) + SrO, (100) + TiO_2, (110) + O_2^{4-}, and (110) + $SrTiO^{4+}$.

This material is interesting because Al-doped $SrTiO_3$, activated with a $Rh_{2-y}Cr_yO_3$ catalyst, has been shown to split water in sunlight. [19] The studies can also be extended to other perovskites with more favorable attributes for visible light photocatalysis.

Small, polygonal $SrTiO_3$ crystals have been shown to have orientation dependent photochemical reactivity that depends on crystal shape. [12,13] When the crystals were terminated only by {100} planes, the {100} facets were both photocathodic and photoanodic. However, when the crystals were engineered to have {100} and {110} facets, the {100} surfaces were relatively photocathodic and the {110} surface were relatively photoanodic. [12,13] This work has been described in detail in the next section – 3.2.2.1. Giocondi et al. [16] showed that single crystal $SrTiO_3$(110) and (111) surfaces can simultaneously support relatively photoanodic and photocathodic terraces with different chemical terminations, and Zhu et al. [5,6] showed that it was possible to adjust the relative areas of these terraces. By exposing $SrTiO_3$ single crystals to Sr-rich and Sr-deficient atmospheres at high temperatures, the surfaces were made Sr-rich or deficient respectively (likely by vapor transport of $Sr(OH)_2$). This work has been described in detail in the next section – 3.2.1.3. These results indicate that, by controlling the particle shape and chemical termination, it is possible to control the relative areas of photocathodic and photoanodic areas on the $SrTiO_3$ surface.

In this chapter, we qualitatively demonstrate that the reactivity on polycrystalline $SrTiO_3$ pellets can be explained by considering spatial selectivity arising from both, facets and chemical terminations. Also, it can be tuned in a manner similar to single crystal $SrTiO_3$, by controlling the chemical terminations via thermochemical treatments. What is new about the current experiments is that samples are used that simultaneously have different relative areas of different surface orientations and different charged regions with different chemical terminations. This situation makes is possible to explore the simultaneous influence of multiple surface orientations and different chemical terminations on the spatial selectivity of photodeposition reactions. We found that heating the substrate in a Sr-rich atmosphere activated the facets that were previously unreactive for reduction. The results show that both surface orientation and surface chemistry are influential in determining the photochemical reactivity.

3.2 Background

3.2.1 Chemical terminations

3.2.1.1 Chemical termination change in single crystals by HF etching

This is the most common method used to obtain an atomically flat surface. Kawasaki et. al. [20] first used a buffered HF solution on (001) $SrTiO_3$ to obtain a Ti-terminated atomically flat sample. Biswas et. al. [21] have demonstrated that 100 % Ti-terminated surfaces can be obtained on (110) and (111) in addition to (001) single crystals of $SrTiO_3$ by using a similar buffered etching plus annealing treatment. Similar methods for different oxide materials are covered in review papers by Biswas et. al. [22] and Sanchez et. al. [23]

3.2.1.2 Chemical termination change in single crystals by purely thermal treatment

Bachelet et. al. [24] have demonstrated tunability of (001) terminations on $SrTiO_3$ by annealing in air. The authors report that the annealing conditions used allow Sr exdiffusion from the bulk to the surface, resulting in Sr-enrichment leading to a progressive increase in SrO terminations. Figure 3-1 below shows their results.

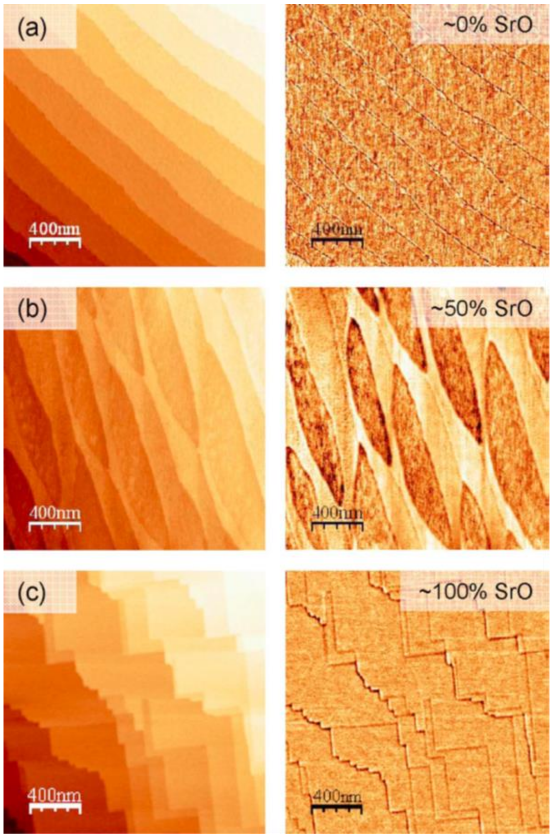

Figure 3-1: Topography (left column) and Phase signal (right column) from AFM showing different coverages of SrO terminations on a (100) single crystal substrate of $SrTiO_3$ [24]

The left column shows the AFM topography images while the right column shows the phase lag images of the same area. The sample surface is initially completely terminated by TiO_2. The phase lag differentiates between the two different terminations.

The authors distinguished between SrO and TiO_2 terminations by two methods.

Firstly, they imaged the topography after dipping the sample in water. The water adsorbs preferentially on SrO terminations, which then show a rough morphology. Second, a sub-monolayer of SrRuO3 was grown on the annealed substrates. This is known to nucleate preferentially on the TiO2 terminations of (001) $SrTiO_3$. This is shown in Figure 3-2 below.

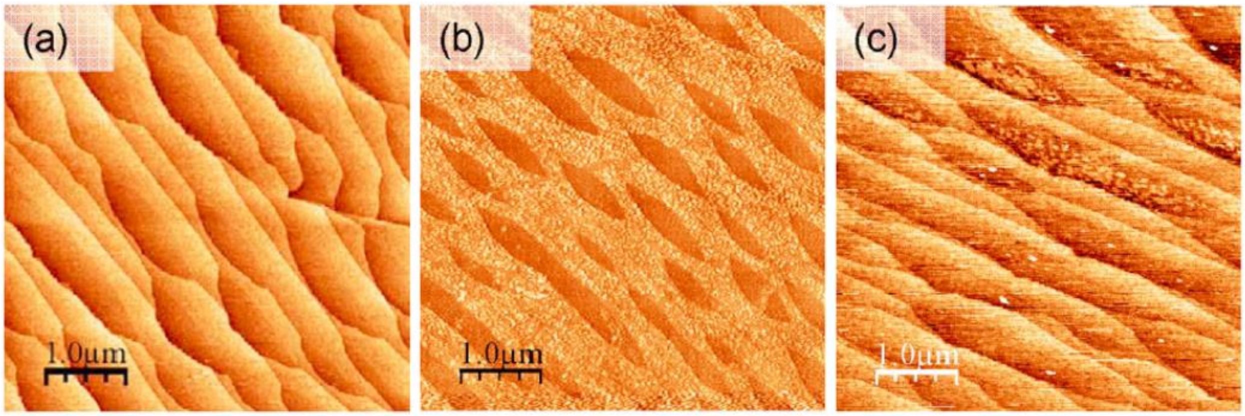

Figure 3-2:(a) AFM topography of (a) Annealed (001) $SrTiO_3$ single crystal substrate (b) same substrate after dipping in water (c) After nucleating $SrRuO_3$ [24]

Figure 3-2(a) shows the AFM topography of the substrate before dipping it in water. Figure 3-2(b) shows that the topography profile is split into two categories – smooth + darker, and rough + brighter. The smooth + darker terminations are expected to be TiO2, while the ones where water molecules have contributed to an increase in height as well as roughage. Figure 3-2(c) shows small white dots on the darker terminations, supporting that these are indeed TiO2.

Hence, annealing in air can be a possible method to tune other orientations of $SrTiO_3$.

3.2.1.3 Chemical termination control on single crystal {110} and {111} $SrTiO_3$

Zhu et al. showed that by changing the chemical termination ratio on (111) [5] and (110) [6] oriented single crystals of $SrTiO_3$ is possible.

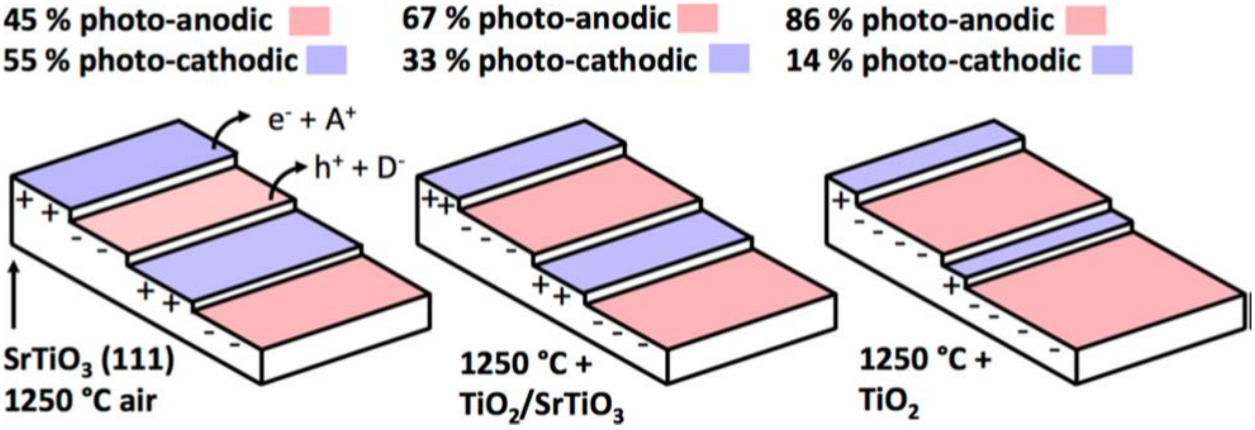

Figure 3-3: Schematic showing change in terminations on (111) $SrTiO_3$ after different thermochemical treatments [5]

By exposing the single crystals to Sr-rich and Sr-deficient atmospheres at high temperatures, the surfaces were made Sr-rich or deficient respectively via vapor transport of $Sr(OH)_2$. The terminations were tuned by controlling the time and temperature of annealing. Figure 3-3 illustrates the change in the ratio of different terminations on heating in the given environment at the given temperature. From left to right, the photo-anodic terminations increased when heated in a progressively increasing Ti-atmosphere.

The ratios of Sr-rich to Ti-rich terminations was studied indirectly by comparing the photodeposition on the substrates. Figure 4 shows the photodeposition on (111) $SrTiO_3$. Figure 3-4(a) shows that Ag is reduced preferentially on particular terminations. The white dots are silver particles in the AFM topography image. In Figure 3-4(b), the terminations that were highly reactive for silver do not oxidize lead as much as the other terminations. The highly oxidative terminations are shaded in yellow while the ones that show a lower capacity to oxidize are shaded in brown. Thus, the percentage of termination area that promotes reduction/oxidation can be determined.

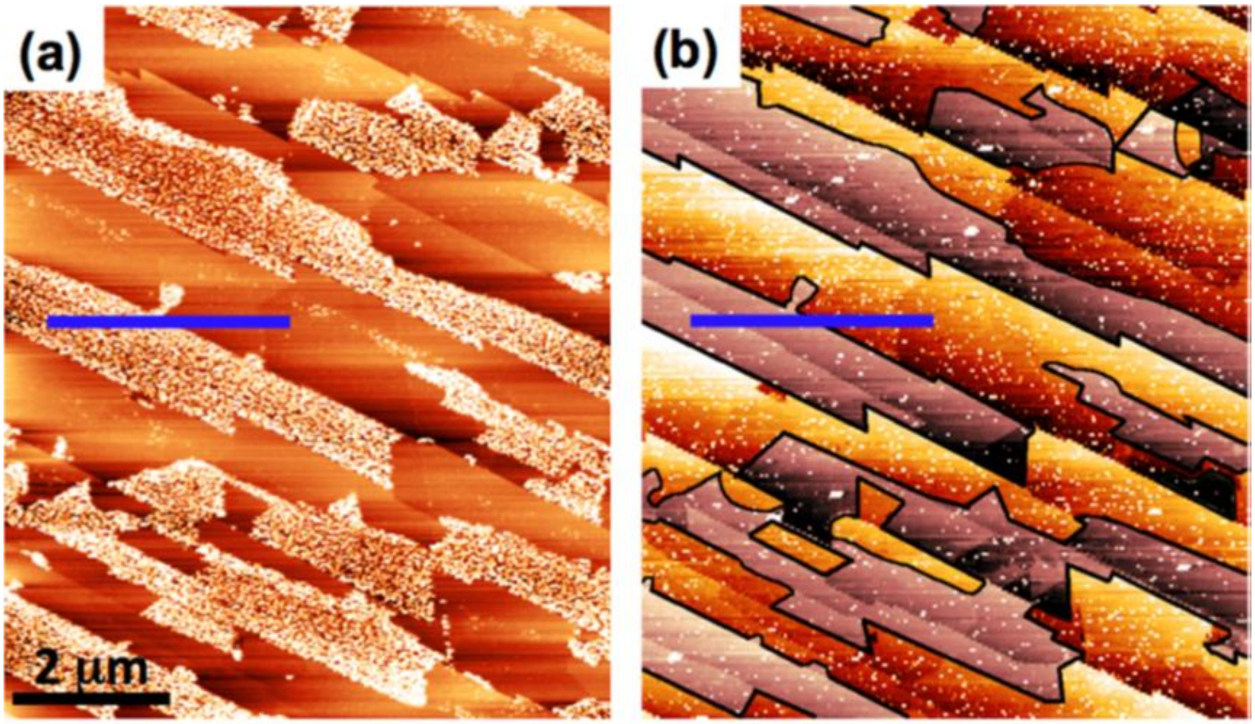

Figure 3-4: Preferential deposition of (a) Ag and (b) PbO_2 on (111) $SrTiO_3$ single crystal substrate [5].

This technique has been used to quantify the effect of thermochemical treatments on the change in chemical terminations, and hence, on photoreactivity.

Similar measurements were made after the samples were subjected to thermochemical treatments. Figure 3-5 shows the effect of heating with progressively Ti-rich powder mixtures of $TiO_2/SrTiO_3$. From (a) to (d), the fraction of photocathodic terminations reduces from 55% to 14 % as the samples are heated with (a) no powder (b) 31.4 % weight of Ti (c) 36.4 % weight of Ti and (d) 60 % weight of Ti. Thus, the Ti-rich terminations are photoanodic and Sr-rich terminations are photocathodic. This was confirmed by using XPS [5].

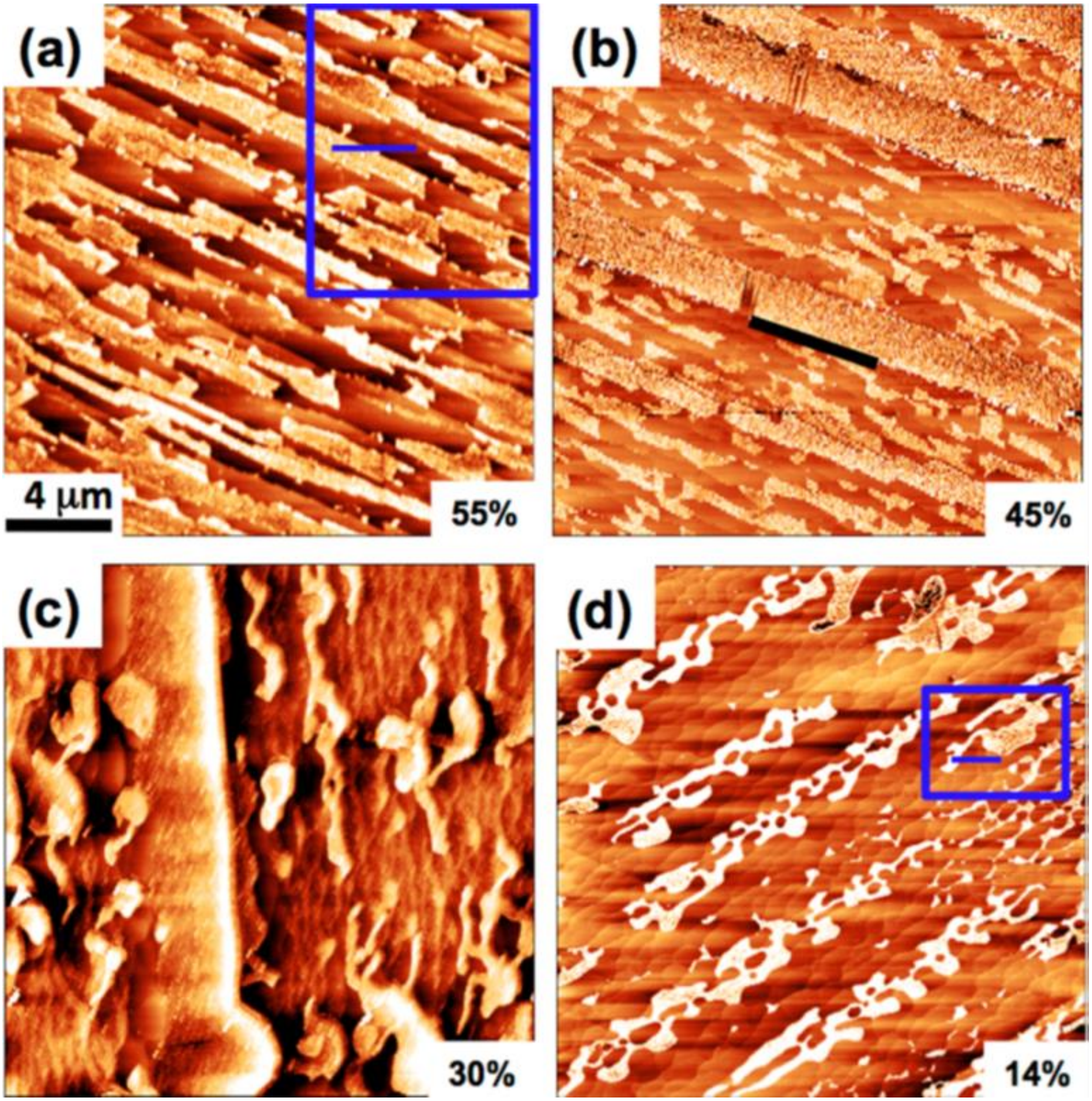

Figure 3-5:Progressive decrease in reductive terminations on effecting increasing Ti-rich thermochemical treatments on (111) single crystal substrate of $SrTiO_3$ (from (a) to (d)) [5].

The authors correlated the reactivity with KFM signal from the terminations for (110) single crystal $SrTiO_3$. They found that the signal was almost bi-modal, with terminations having a higher surface potential being photocathodic and the ones with a lower surface potential being photoanodic [6]. Figure 3-6 below shows the correlation on a (110) substrate of $SrTiO_3$ [6].

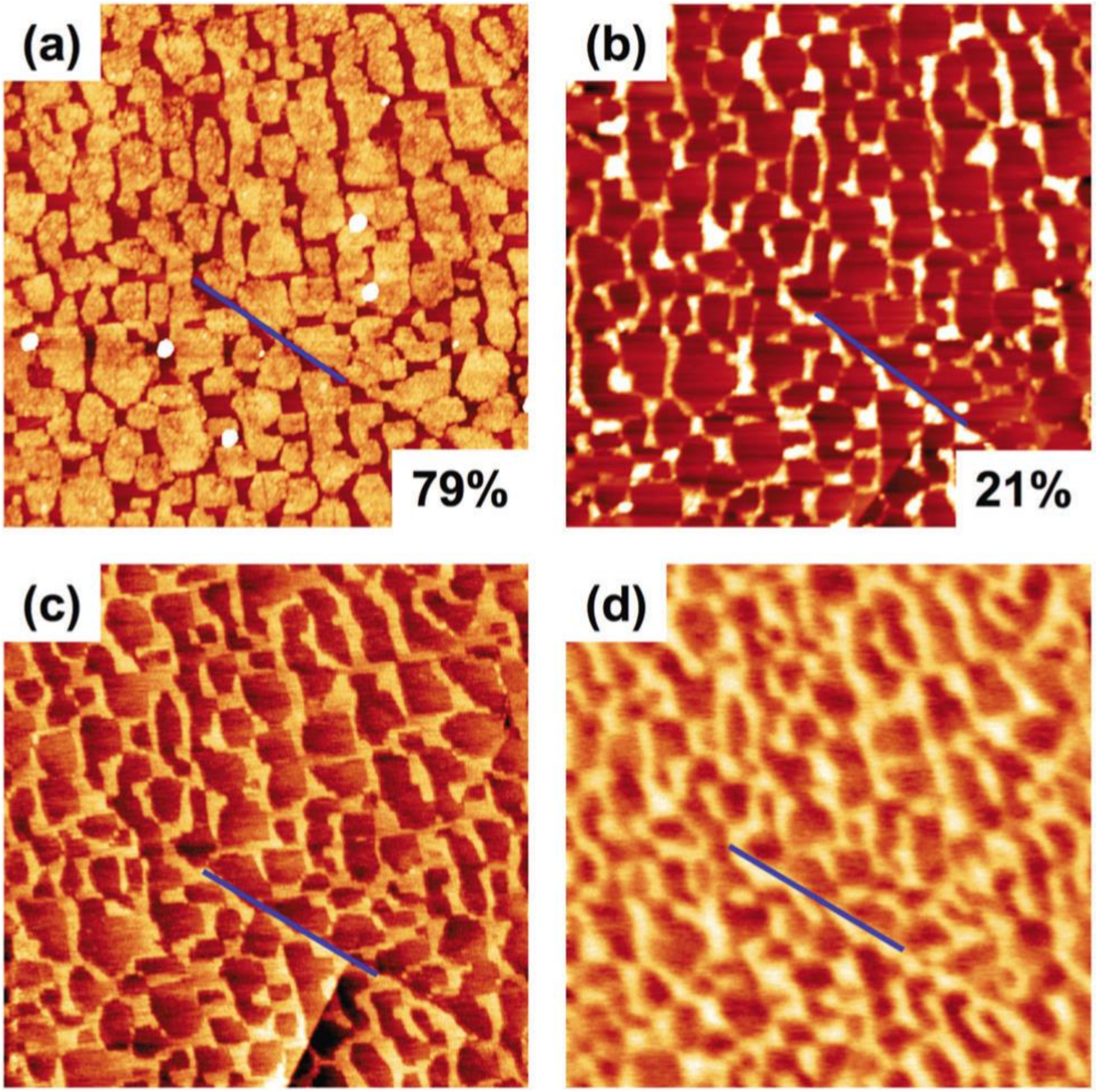

Figure 3-6: AFM topography image of Photodeposition of (a) PbO_2, (b) Ag and (c) (110) single crystal $SrTiO_3$ substrate before reaction. (d) shows a KFM surface potential map of the same area.

Figure 3-6(a), (b) and (c) are AFM topography images of photodeposited lead oxide, silver and the sample before reaction respectively. Fig (d) is the KFM surface potential map of the same area. The blue line in all four images marks the same area and is given as a guidance to the reader for easy comparison. From the figure, the areas with the higher surface potential (brighter in (d)) are those that reduce silver. The darker regions in (d) oxidize lead.

The (111) surface was tunable from 14% to 55% reductive [5] while the (110) surface was tunable from 0% to 98% reductive [6]. This is an example of tuning the spatial selectivity through engineering surface chemical terminations.

3.2.2 Crystalline facets

3.2.2.1 Tailoring facets on $SrTiO_3$

Facet tailoring is usually done using 1) Taking advantage of thermodynamic anisotropies (Wulff shape) 2) Using capping agents that adsorb and retard growth of specific facets. Facet design specially for photocatalytic materials has been covered by Bai et. al. [25] In this sub-section, the background literature on facet control for $SrTiO_3$ has been discussed.

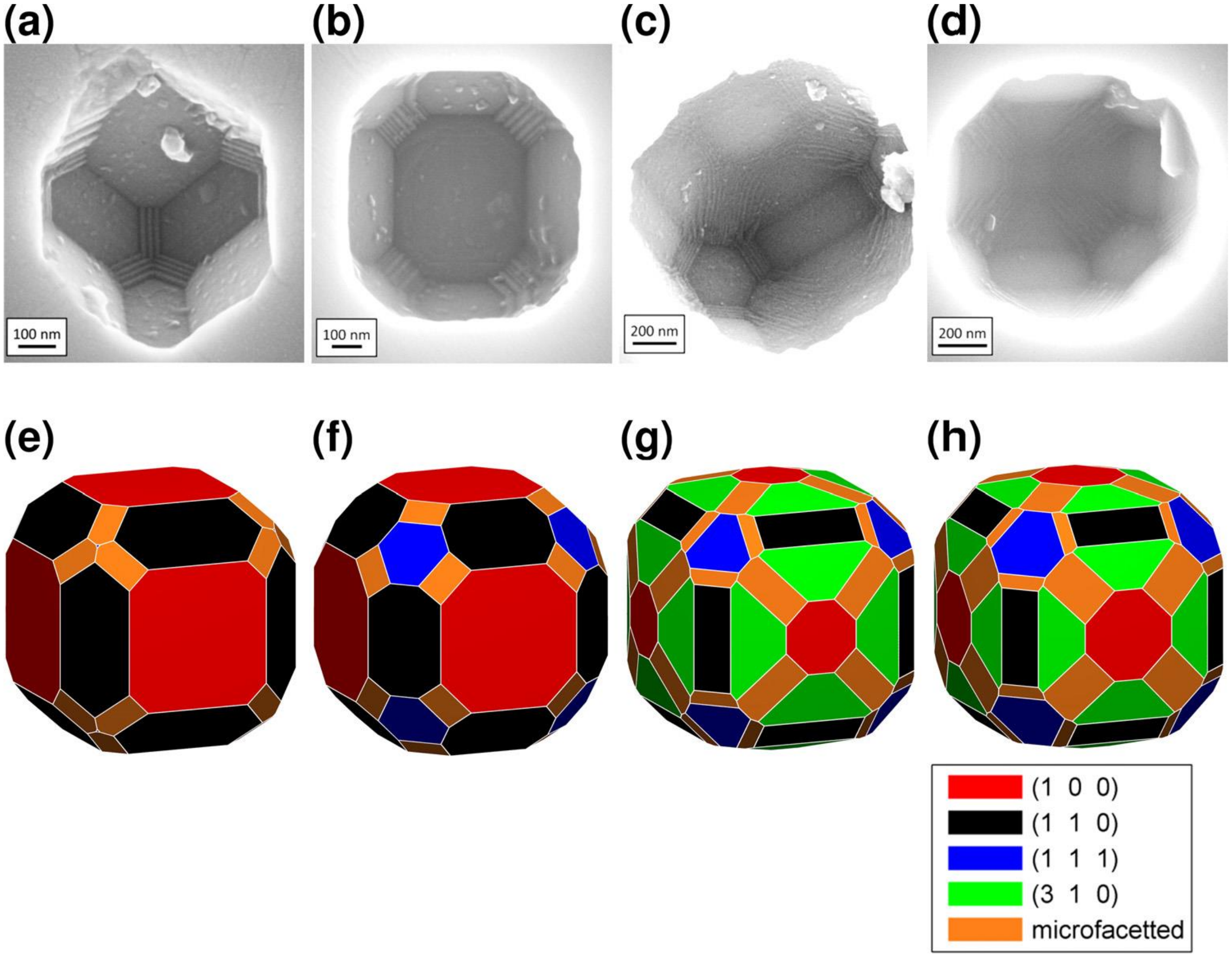

Figure 3-7: SEM images of pores annealed in oxygen at (a) 1250 °C, (b) 1380 °C, (c) 1460 °C and (d) 1600 °C. (e–h) Reconstructed pore shapes corresponding to (a)-(d) respectively

The orientations of facets present after annealing are dependent on the Wulff shape of the material, as described in section 2.4.2. For some compounds, there is a strong temperature dependence for these energies, and hence, the Wulff shape changes drastically with the annealing temperature. In case of $SrTiO_3$, Rheinheimer et. al. [14] annealed samples at different temperatures and studied the pores. The pore shape reflects the equilibrium Wulff shape when sufficient time has been allowed for diffusion. They found that after annealing at 1250 °C, the stable facets were {110} and {100} in $SrTiO_3$, which is consistent with our results. As the annealing temperature was increased, different families of facets were stabilized. Figure 3-7 (above) from their work shows the equilibrium shapes at different annealing temperatures. Hence, it is possible to obtain different facets simply by annealing at different temperatures, provided there is sufficient surface energy anisotropy in the material.

In the hydrothermal growth of $SrTiO_3$ crystals using alcohols [26], it was found that addition of alcohols results in a Lewis acid-base interaction of the -OH group with surfaces of $SrTiO_3$. The alcohols acted as capping agents on {110} and reduced their surface energy (thermodynamic anisotropy) as well as retarding their growth, enabling {100} facets to grow out (kinetic anisotropy). This enabled control of the ratio of {110} to {100} facets in the grown crystals.

In case of controlling the relative ratios of facets on a polycrystal surface after synthesis, there are two options. Firstly, annealing out till equilibrium at different temperatures will result in different ratios of facets as well as different families of facets, as discussed above. This control arises from thermodynamic anisotropy (difference in surface energies at different temperatures). The second possible way is to use the polycrystal as a seed in the hydrothermal procedure carried out by Dong et. al. [26] discussed above. Although not demonstrated, it should be possible to control relative ratios of facets in the same way after the baseline ratio of facets has been established due to annealing conditions.

3.2.2.2 Charge separation on nanocrystals of $SrTiO_3$

$SrTiO_3$ nanocrystals were reported to show spatial selectivity depending on their facet morphology [27]. Figure 3-8 below shows the photodeposition on (010) and (110) facets of nanocrystals of $SrTiO_3$.

When the crystals were terminated with only {100} planes, there was no preference for either reaction to occur on any particular facet. However, when the crystals were engineered to have other facets in addition to {100}, the anisotropy in reactivity was evident. The photoreduction reactions showed a preference for the {100} facets while photooxidation reactions showed a preference for the {110} facets. In Figure 3-8 (remade from [28]), the Au deposits can be seen on the (001) facets while CoO_x deposits can be seen on (110) facets. Figure 3-8(c) shows that if the crystals are bounded by {100}, then there is no selectivity seen with respect to reduction/oxidation.

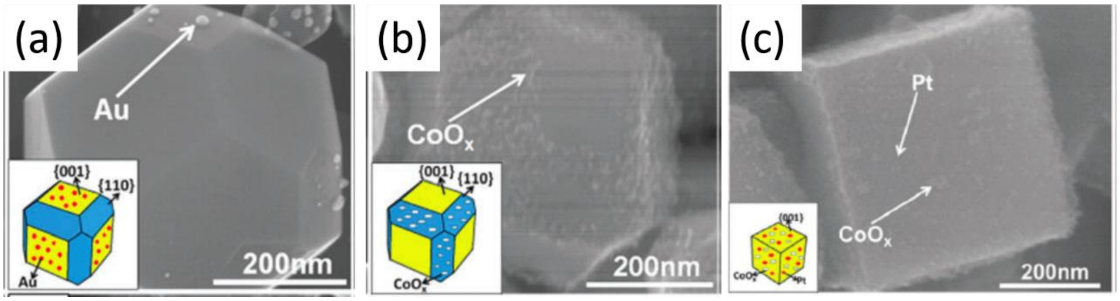

Figure 3-8: Photodeposition of (a) Au, (b) CoO_x and c) Pt + CoO_x on nanocrystals of $SrTiO_3$ [27]

It implies that the presence of different facets separates charges. This is an example of facet-driven spatial selectivity in $SrTiO_3$.

In another study that gave contrasting results, Giocondi et. al. showed that in microcrystals of $SrTiO_3$, (100) facets were reactive for both oxidation and reduction. The Figure 3-9(a) shows that silver is preferentially reduced on {100} facets while Lead is oxidized to give PbO_2 deposits also on the {100} facets (Figure 3-9(b)). The reason for the discrepancy is unknown.

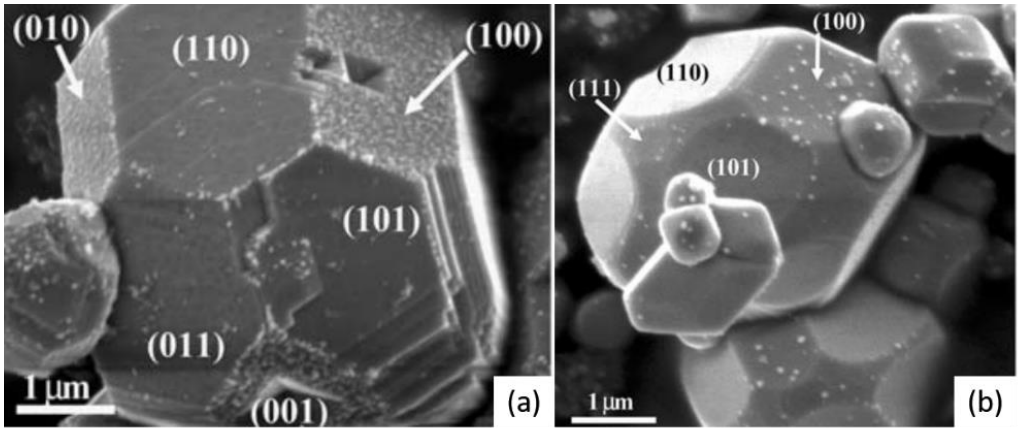

Figure 3-9: Photodeposition of (a) Ag and (b) PbO_2 on faceted microcrystals of $SrTiO_3$ [12]

3.2.2.3 Charge separation on $BiVO_4$ crystals

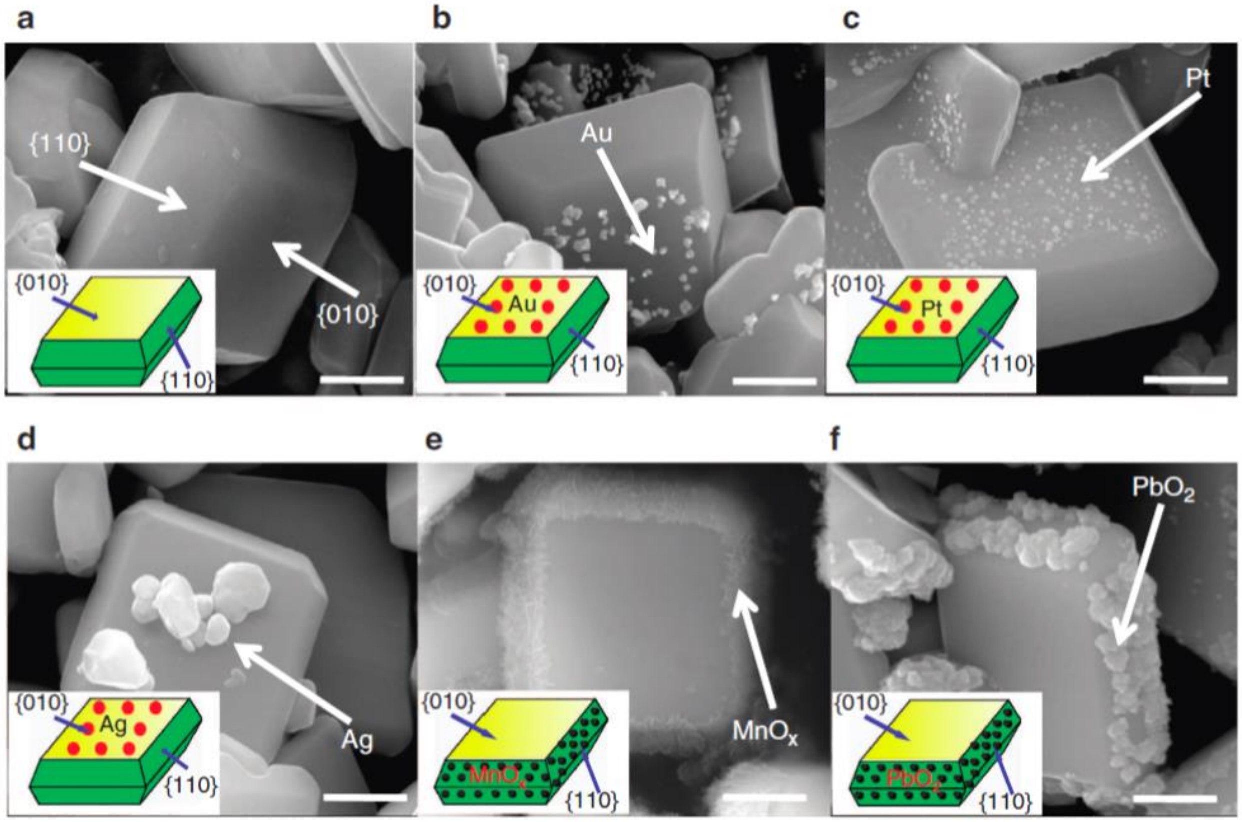

Figure 3-10: Photodeposition of various materials on hydrothermally grown faceted crystals of $BiVO_4$. The reduction deposits (b,c,d) are seen on {010} facets while the oxidation deposits (e,f) are on {110} facets [28]

Li et. al. [28] showed that (110) facets of $BiVO_4$ crystals were highly reactive for photo-oxidation, while the (010) facets were active for photoreduction. Figure 3-10(a) shows the crystal morphology before photodeposition. Figure 3-10(b), (c) and (d) show that photoreduction reactions (Au, Pt and Ag) take place on the (010) facet while the oxidation reactions (MnO_x and PbO_2) take place on the (110) facets.

3.3 Aim and Motivation

3.3.1 Aim

The purpose of this work is to show that the photochemical reactivity of arbitrarily oriented $SrTiO_3$ surfaces can be tuned in a manner similar to the low index orientations of single crystal $SrTiO_3$. While one might expect a low index facet on an arbitrarily oriented surface to behave in the same way as a single crystal with that low index orientation, there is an important difference. For the case of a single crystal with a near atomically flat surface, both the reduction and oxidation half reactions have to occur on the same surface. For the case of an arbitrarily oriented crystal whose equilibrium crystal shape is made up of a limited number of facets, surfaces exposed to high temperature annealing will be constructed of facets with multiple orientations, and the reduction reaction can occur on the more photocathodic orientation and the oxidation reaction on the more photoanodic orientation. The role of different chemical terminations in this case is not clear. Therefore, thermochemical treatments inspired by reference [6] were used to alter the relative areas of photocathodic and photoanodic terraces on thermally induced low index facets on $SrTiO_3$ and the influence of this on the photochemical reactions was determined.

3.3.2 Motivation

The motivation for controlling terminations and studying spatial selectivity on $SrTiO_3$ polycrystals is two-fold. Firstly, all the charge separation mechanisms listed earlier have been investigated separately. The surface heterojunctions formed by different facets in the same crystal have the potential to separate charges and cause spatial selectivity of reactions. It remains to be seen how different facets affect reactivity in a polycrystals with faceted grains. However, most polycrystalline photocatalysts, owing to presence of multiple crystallographic orientations on the surface, simultaneously engage more than one of the listed mechanisms in the process. Hence, it is important to study the relative influence of these effects when present together.

Secondly, there are a host of scientific benefits in the demonstration of an ability to change surface termination chemistry in polycrystals. Firstly, it will enable systematic studies on the effect of varying the ratio of oxidation promoting terminations to reduction promoting terminations on overall photocatalytic efficiency, for which there is no literature available currently. There are many reports studying the effects of the presence of spatial selectivity on photocatalytic efficiency, but very few on the control of spatial selectivity. Specifically, there are no systematic studies on the impact on efficiency of controlling chemical terminations on polycrystals. Additionally, future photochemical studies for which single crystal substrates are not readily available will be made possible. Finally, controlling surface terminations will enable to iron out any imbalance in charge availability already present due to uneven facet morphology or intrinsic properties like different carrier velocities.

3.4 Hypotheses

Hypothesis 1

The area occupied by Sr-rich, photocathodic terminations will increase when the sample is heated with a Sr-source, because of vapor transport of Sr to the sample. This is the same method used to control terminations on single crystal $SrTiO_3$ [5,6].

Hypothesis 2

The presence of another charge separation feature (surface heterojunctions due to facets) in addition to surface terminations will result in both driving the overall spatially selective reactivity.

Alternate hypothesis 2.1

The facet-driven spatial selectivity overpowers chemical termination driven spatial selectivity because of a higher electrochemical potential difference, or vice versa

3.5 Experimental section

3.5.1 Sample Synthesis

Polycrystalline $SrTiO_3$ pellets were prepared from $SrTiO_3$ powder (99.9%, Sigma Aldrich) that was ground for 10 minutes using a mortar and pestle. Two drops of 5% w/v (5 g of PVA in 100 ml of water) polyvinyl alcohol (PVA) solution were added to 0.7 – 1 g of powder for every pellet. The mixture was pressed using a table top hydraulic press (Carver) using a half-inch diameter punch and die. The pressed pellets were then sintered using the heat treatment procedure given in Table 1.

Table 1. Annealing parameters for pellet synthesis

Ramp rate (°C/min)	Temperature (°C)	Dwell time (hrs)
5	600	1
5	1000	8
10	1425	6

Sintered pellets were polished with an automated polisher (Buehler AutoMet 250). First, SiC grit papers with grit size 320, 400 and 600 (Buehler) were used, followed by diamond suspensions (9 µm, 3 µm, 1 µm and 0.05 µm). The polishing procedure has been given in detail in table 2:

Table 2. Polishing procedure

Serial number	Base speed (RPM)	Polishing paper/cloth + suspension	Time (min)
1	120	320 grit Carbimet	0.5
2	120	600 grit Carbimet	1
3	120	800 grit Carbimet	1.5
4	150	1200 grit Carbimet	2
5	180	Satyn MB + 9 µm diamond suspension	3
6	180	Satyn MB + 3 µm diamond suspension	4
7	180	Satyn MB + 1 µm diamond suspension	5
8	200	Micro MB + 0.05 µm diamond suspension	8

3.5.2 Baseline thermal treatment

Polished samples were annealed for 8 hours at 1250 °C in the absence of any additional powder, which established the initial faceted surface and chemical surface terminations. This heat treatment is termed baseline herein, and is sufficiently long to avoid further facet formation during subsequent thermochemical treatments. Baseline pellets were then made into 4 mm x 4 mm square areas (thickness ≈ 1 mm) using a diamond wire cutter.

3.5.3 Thermochemical treatments (Sr-rich atmosphere)

Samples were subjected to thermochemical treatments at 1100 °C, with the sample placed in an alumina crucible adjacent to 0.1 g of either $Sr_3Ti_2O_7$ or $SrCO_3$ powder, for times varying from an hour to 5 hours. We found that carrying out the treatment for over 6 hours with 0.1 g of $Sr_3Ti_2O_7$ resulted in formation of second phases on the surfaces of some grains (Images are given in the SI). Similarly, using Ti as an Sr-sink resulted in second phases and degradation of areas near grain boundaries. Thus, the window of thermochemical parameters (amount of Sr source/sink, temperature and time) appears to be relatively narrower, although systematic studies were not carried out. The setup for carrying out these treatments is elaborated in Section 2.5.5

3.5.4 Photodeposition

Photoreactions were carried (as described in chapter 2) out using parameters described in Table 3.

Table 3. Experimental parameters for marker reactions

Number	Solute	Reaction	Product	Concentration[Molar]	Power [Watts]	Time [Seconds]
1	$AgNO_3$	Reduction	Ag	0.115 M	75 W	6 s
2	$Mn(NO_3)_2.4H_2O$	Oxidation	MnO_x	0.038 M	100 W	60 s
3	$Pb(CH_3COO)_2.3H_2O$	Oxidation	PbO_x	0.115 M	150 W	75 s

3.5.5 Imaging of deposits

The silver deposits after photoreaction were imaged using a Quanta 200 scanning electron microscope in the secondary electron (SE) mode. The images were recorded at 20 kV beam in low vacuum mode (to prevent charging of the sample) with a spot size number of 5. The scan time ranged from 20 s to 2 minutes. The resolution of the images was 2048 x 1768 pixels.

3.5.6 Facet orientation determination

After the baseline heat treatment, the high-index surfaces of the exposed grains broke up into sets of lower energy facets. To determine the orientations of these facets, the following procedure was adopted, as illustrated in Figure 11.

3.5.6.1 Procedure

Grains with large facets were first identified by imaging the sample using Scanning Electron Microscopy (SEM) (Figure 3-11a). After obtaining Euler angles for those grains (Figure 3-11b) from Electron Backscatter Diffraction (EBSD), the central regions of these grains were scanned by contact Atomic Force Microscopy (AFM) - Fig 11c. The large size of the facets is important to avoid topography crosstalk from the adjacent facet while imaging the other. A second order correction was applied to the image. The regions close to grain boundaries or pores were avoided as the AFM tip cannot record the topographic information accurately due to tip - side wall interactions. The AFM scan was exported as a `*.XYZ’ file using Gwyddion software. This file gives the Z coordinate for a set of (X,Y) coordinates, for all points in the image. This file was inputted into Microsoft Excel to convert the ‘*.XYZ’ file to a `*.xlsx’ file that can be easily read by MATLAB. Code C1 (available for download) takes this (scan area x 3) sized matrix and splits it into separate X, Y and Z vectors. For example, a 100x100 scan gives a 10000 x 3 matrix that will be split into 3 different 10000 x 1 matrices. Then, the ‘surf’ function from MATLAB is called to integrate these three matrices to give a reconstructed version of the AFM image (Figure 3-11d). The ‘surfnorm’ function is then called to give the surface normal components for every point of this reconstruction. These components are in the frame of reference of the microscope.

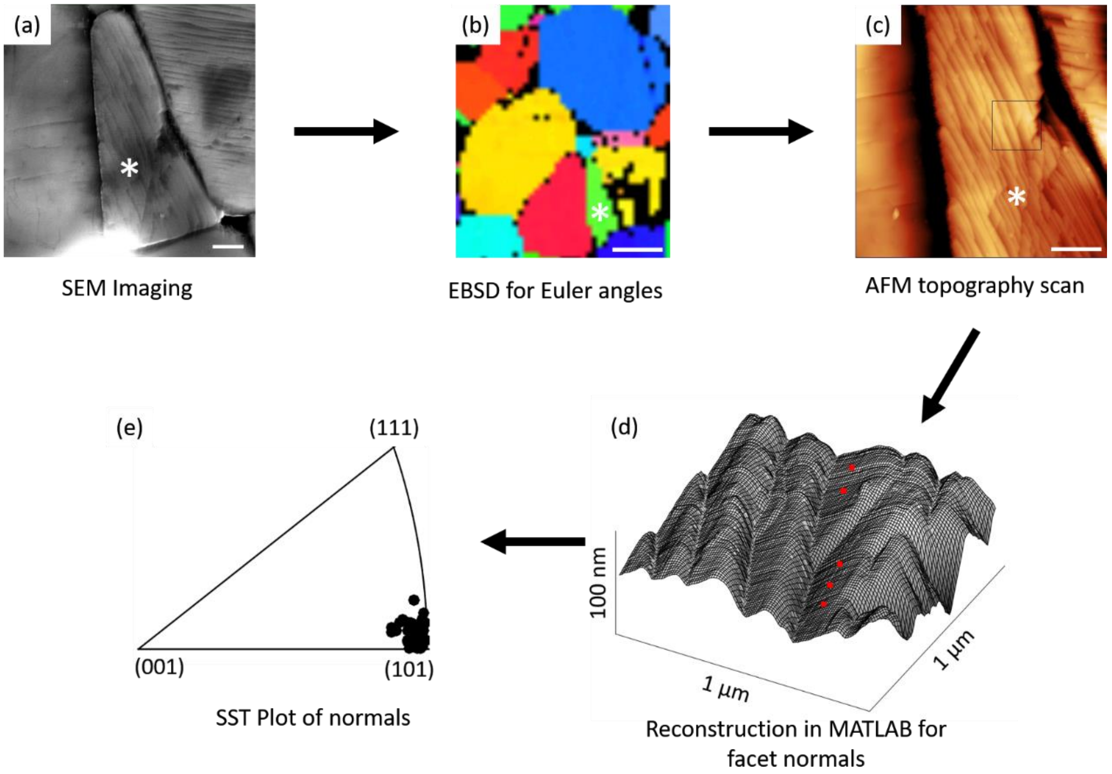

SEM Imaging

EBSD for Euler angles

AFM topography scan

Reconstruction in MATLAB for facet normals

SST Plot of normals

Figure 3-11: Process to obtain orientations of surface facet normals – (a) Imaging of grains using SEM to identify grains with facets optimal for AFM scanning (b) EBSD scan to obtain Euler angles (c) Topographic scan using AFM to obtain components of surface facet normals in the frame of reference of the microscope. (d) 3D reconstruction using MATLAB for the user to choose 50 points from which to obtain the components. The small red squares are examples of points on two facets on the reconstruction (e) Plot of stereographic projections of those 50 surface normals in a SST. A white asterisk marks the same grain in (a),(b), and (c). Scale bars: (a) 1 µm (b) 5 µm (c) 1 µm

The code then asks the user to choose 50 points from the reconstruction and gives the components of normals from those points in a separate matrix ‘interactivenormals_surfnorm’. These are illustrated in Figure 3-11d. It is advisable to choose points from parts of the facets without perturbations (on a single grain). Code C2 (available for download) is then used on the ‘interactivenormals_surfnorm’ matrix to transform the components into the frame of reference of the particular grain from which the normals were extracted.

Code C3 (available for download) then plots these transformed normals onto a Standard Stereographic Triangle (SST) – Figure 3-11e. Please note that the file paths in the codes have to be changed in accordance with the user’s files. We recommend placing all the codes in a single folder and giving the file paths for all xlswrite commands as the same folder to avoid issues when running. In the example of Figure 3-11a, the central grain in the SEM image has large facets that can be imaged easily and with minimal side wall interactions. An EBSD scan gave the Euler angles of the grain with respect to the frame of reference of the microscope. It is important to note here that the Euler angles will change from system to system because of different microscope frames of reference. Our code has been written for the default settings on the OXFORD system. If the user wishes to use angles obtained from a different EBSD system, they would have to amend the codes accordingly. Then, the AFM topographic image gives the XYZ data of the grain, which is then inputted into MATLAB. A reconstruction is obtained using the codes. The user would select 50 points from the reconstruction whose normal they think would give an accurate orientation. Here, we have chosen three and two points (shown in red) from two different facets for illustration purposes. After obtaining the normals, they are plotted on a SST. Here, after choosing

50 points from the same facets for which the illustrative points have been chosen, the SST shows that these facets are close to {100}.

3.5.6.2 Example of determining facet-orientation in grain frame of reference

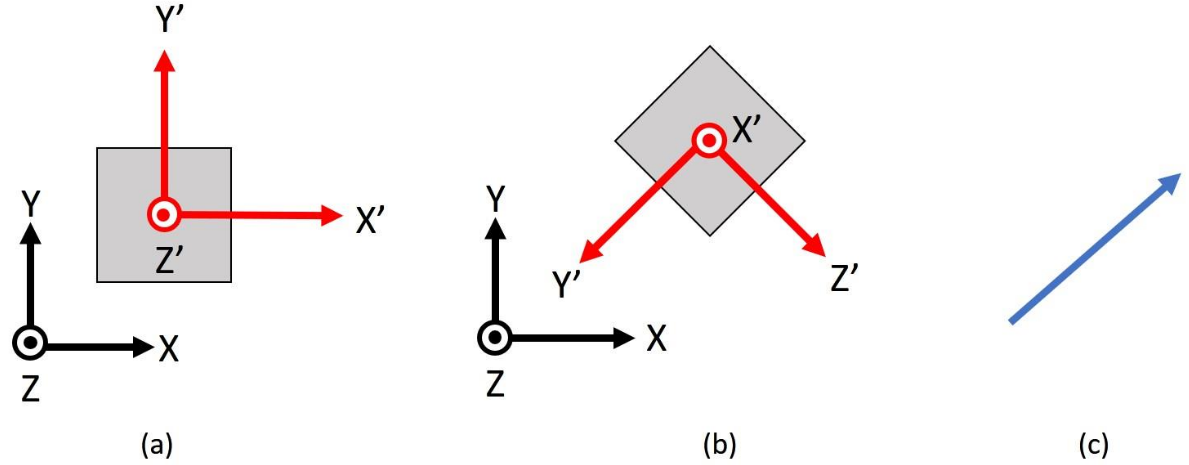

Figure 3-12: Frames of reference of the microscope (black) and crystal (red) (a) before and (b) after rotation of crystal by (45,90,90). (c) Vector for comparison in both frames of reference

A schematic cubic crystal is shown in the form of a square on the X-Y projection in Figure 3-12. The frame of reference (FOR) in black is that of the microscope. The FOR in red is that attached to the crystal. Both FORs before rotation are shown in Figure 3-12(a). Let us assume that the crystal now undergoes a rotation by (45°,90°,90°) – a set of three Euler angles. This means that the crystal is rotated by 45° about the original Z-axis, followed by 90° degrees about the new X-axis (The X-axis after previous rotation about the Z-axis), and finally by 90° about the new Z-axis (the Z-axis after the previous two rotations). These rotations are successive in the sense that a rotation is applied to the frame of reference that arises from the previous rotation. The rotated version of the crystal along with its FOR is shown in Figure 3-12(b). Now, consider a vector (Figure 3-12(c)) in both FORs. In the FOR of the microscope, the vector is [110]. We want the components of the surface normals in the crystal FOR to determine the facet orientations. For this purpose, as seen above, we need to do two things. a) Use EBSD to determine a set of Euler angles that gives the rotation from the microscope FOR to the crystal FOR. In the example, this is (45°,90°,90°). b) Use an AFM topography image to determine components of surface facet normals in the FOR of the microscope. In the example, this is [110]. The rotation matrix for converting the microscope FOR into the crystal FOR is determined by a matrix product of three individual rotations about Z, X, and Z axes as mentioned above. The final matrix is given by G.

$$G = A1 * A2 * A3$$

$$A1 = \begin{bmatrix} \cos\theta & -\sin\theta & 0 \\ \sin\theta & \cos\theta & 0 \\ 0 & 0 & 1 \end{bmatrix} \text{...Rotation about Z-axis}$$

$$A2 = \begin{bmatrix} 1 & 0 & 0 \\ \cos\theta & -\sin\theta & 0 \\ \sin\theta & \cos\theta & 0 \end{bmatrix} \text{...Rotation about X-axis}$$

$$A3 = \begin{bmatrix} \cos\theta & -\sin\theta & 0 \\ \sin\theta & \cos\theta & 0 \\ 0 & 0 & 1 \end{bmatrix} \text{...Rotation about Z-axis}$$

So, for example, consider a triplet of Euler angles - (45,90,90),

$$G = \begin{bmatrix} \cos 45 & -\sin 45 & 0 \\ \sin 45 & \cos 45 & 0 \\ 0 & 0 & 1 \end{bmatrix} \times \begin{bmatrix} 1 & 0 & 0 \\ \cos 90 & -\sin 90 & 0 \\ \sin 90 & \cos 90 & 0 \end{bmatrix} \times \begin{bmatrix} \cos 90 & -\sin 90 & 0 \\ \sin 90 & \cos 90 & 0 \\ 0 & 0 & 1 \end{bmatrix}$$

$$G = \begin{bmatrix} 0.707 & -0.707 & 0 \\ 0.707 & 0.707 & 0 \\ 0 & 0 & 1 \end{bmatrix} \times \begin{bmatrix} 1 & 0 & 0 \\ 0 & -1 & 0 \\ 1 & 0 & 0 \end{bmatrix} \times \begin{bmatrix} 0 & -1 & 0 \\ 1 & 0 & 0 \\ 0 & 0 & 1 \end{bmatrix}$$

$$G = \begin{bmatrix} 0.707 & 0.707 & 0 \\ 0.707 & -0.707 & 0 \\ 1 & 0 & 0 \end{bmatrix} \times \begin{bmatrix} 0 & -1 & 0 \\ 1 & 0 & 0 \\ 0 & 0 & 1 \end{bmatrix}$$

$$G = \begin{bmatrix} 0.707 & -0.707 & 0 \\ -0.707 & -0.707 & 0 \\ 0 & -1 & 0 \end{bmatrix}$$

$$Input\ vector = [1\ 1\ 0]$$

$$Rotated\ vector = [1\ 1\ 0] * G' = [1\ 1\ 0] * \begin{bmatrix} 0.707 & -0.707 & 0 \\ -0.707 & -0.707 & -1 \\ 0 & 0 & 0 \end{bmatrix} * (\frac{1}{mag[110]})$$

$$= [0\ -1\ 0]$$

To get the vector in the crystal FOR, it has to be multiplied by G. Depending on whether the surface normal components are inputted as row or column vector, we have to transpose G. In our code, the input is a row vector and premultiplies G’ (Transpose of G). Thus, we now have the surface normal components in the rotated form. The result is normalized by multiplying it with (1/magnitude[110]). In this simple case, it is easy to verify the solution given by the code. The orientation of the vector from Figure 3-12(c) in the FOR of the crystal (after rotation) is [0 -1 0].

3.5.6.3 Projection of facet normals onto Standard stereographic triangle (SST)

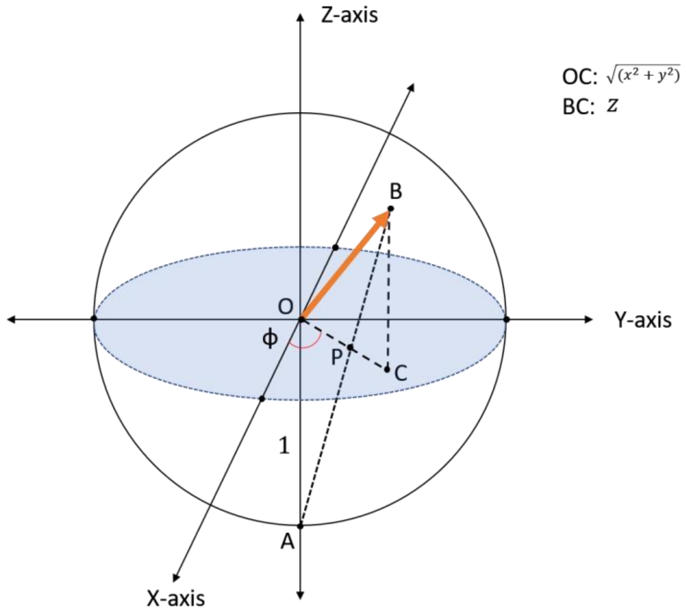

Figure 3-13: Stereographic projection of a vector

After we obtain the rotated vectors, we need to plot them on a SST for analysis. Figure 3-13 illustrates a unit sphere. O is the origin. OB is a normal with a magnitude equal to one. The tip of the normal (point B) lies on the unit sphere. The stereographic projection of the normal is obtained by connecting the south pole (A) of the unit sphere to the tip (B) as B lies in the northern hemisphere. P is the stereographic projection on the X-Y plane. Using simple geometry, the coordinates of P can be found out.

$$\varphi = \tan^{-1}\frac{y}{x}$$

$$\frac{OA}{OP} = \frac{CB}{CP} \ldots As\ \Delta AOP \sim \Delta BCP$$

$$\frac{1}{OP} = z/(OC - OP)$$

$$OC = OP(1 + z)$$

$$OP = \frac{\sqrt{(x^2 + y^2)}}{(1 + z)}$$

Hence, the projections can be plotted using (Φ,OP) for all normals. The SST is constructed separately by plotting x=y, y=0, and the projection of the great circle of [-1 0 1] pole in MATLAB or any other software of choice. The coordinates of the great circle can be given by two conditions: a) [x y z].[-1 0 1] = 0 and b) x^2+y^2+z^2 = 1. The stereographic projections of the surface facet normals are then plotted as a scatter plot in the fundamental zone of orientation space.

3.5.6.4 Example of plotting directions on SST

Consider a normal [1 1 2]. Normalizing the coordinates, we get [$\frac{1}{\sqrt{6}}\ \frac{1}{\sqrt{6}}\ \frac{2}{\sqrt{6}}$]. Thus, $\phi = \tan^{-1}(y/x) = \tan^{-1}(1) = 45°$. Also, $OP = \frac{\sqrt{2}}{2+\sqrt{6}} = 0.3146$. This point has been shown as a black dot in Figure 3-14.

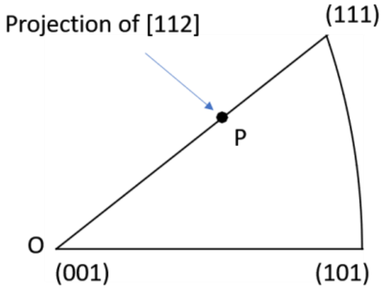

Figure 3-14: Projection of [112] on a Standard Stereographic Triangle

3.6 Results

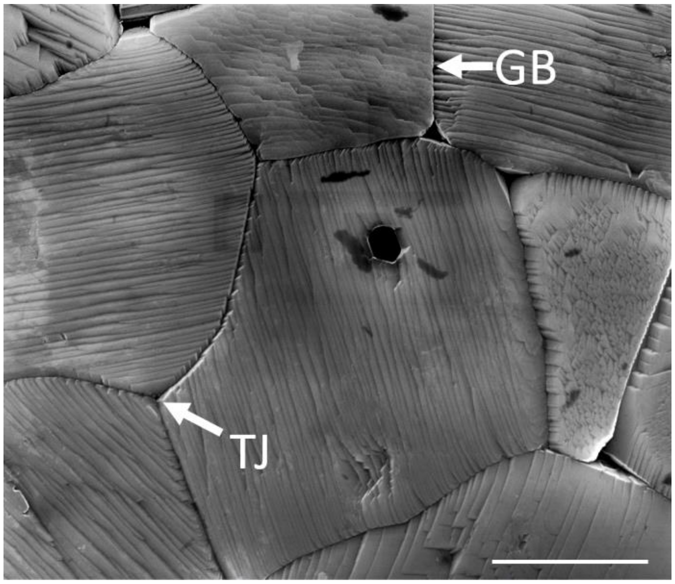

Figure 3-15: Secondary electron image of the $SrTiO_3$ sample surface after the baseline thermal treatment. The scale bar is 3 µm.

The surface of the $SrTiO_3$ crystal after the baseline thermal treatment is shown in Figure 3-15. A grain boundary and a triple junction are labeled GB and TJ, respectively. The contrast within the grains results from sets of facets that replaced the original, flat, polished surface. While the facets increase the surface area, they lower the total surface energy by replacing the original surface with lower energy surfaces. [29] The surface orientations of the facets on seven grains were determined using topographic AFM data, EBSD crystal orientation data, and the procedure described in the experimental section. An example of a three-dimensional (3D) representation of the topographic AFM data from a faceted surface is shown in Figure 3-16a. Two directions normal to the surface are illustrated by the white arrows. For seven different grains, 750 surface normals were extracted and they are shown in the crystal reference frame in Figure 3-16b.

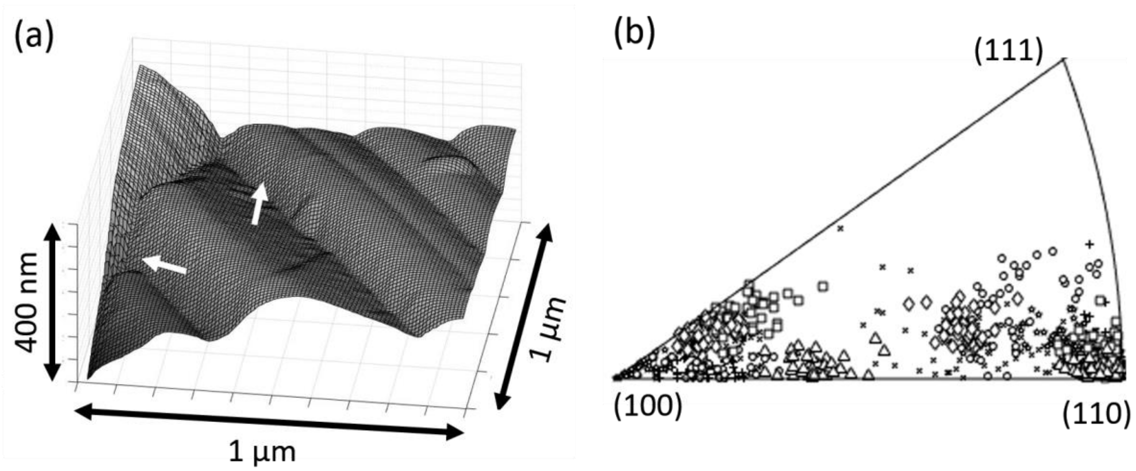

Figure 3-16: (a) A 3D representation of the topographic AFM data; two surface normals are indicated by the white arrows. The vertical height is 140 nm. (b) The orientations of 750 surface normals from seven grains projected onto the standard stereographic triangle

The orientations are plotted in the standard stereographic triangle, which represents all distinguishable surface orientations in the cubic system. The surface normals are strongly clustered about the (001) and (101) orientations. Deviations from the ideal (001) and (101) orientations are most likely the result of uncertainties in the surface normal measurement; because of the finite curvature of the AFM tip, the sharp facet intersections are rounded so that locally, there is a more continuous range of orientations. It is also possible that a finite and continuous range of vicinal orientations are permitted near the ideal low index orientations, as reported for samples annealed at higher temperature. [15] In either case, we interpret the result to mean that the faceted $SrTiO_3$ surfaces that result from annealing at 1250 °C are constructed of {100} and {110} surfaces, and possibly some orientations vicinal to these surfaces. We note that this interpretation is consistent with the data reported by Rheinheimer et al. [14], who concluded that the equilibrium crystal shape at this temperature consists of {100} and {110} facets.

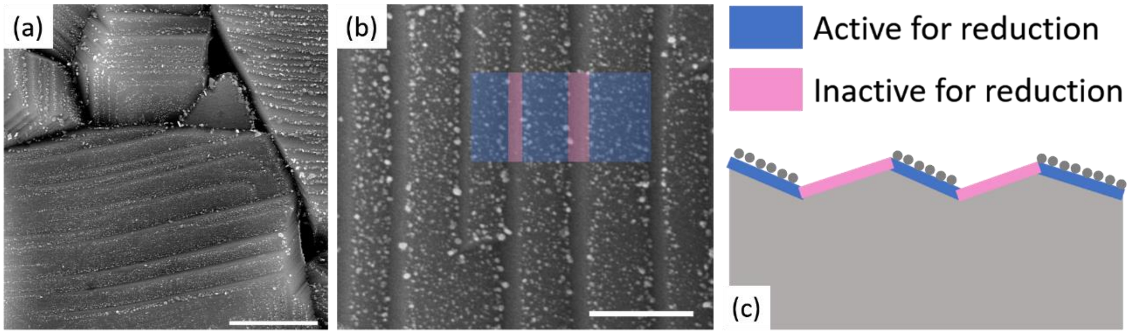

Figure 3-17: (a) SEM image of a surface after the photoreduction of Ag^+. The scale bar is 2 µm. (b) Zoomed-in image of a single grain surface made up of two facets, where one is active for photoreduction and the other is not. The scale bar is 1 µm. (c) Schematic of the hill-and-valley topography of the facets. The blue-colored facets are photocathodic and correspond to the area in (b) marked with the same color, and the grey circles represent photoreduced silver.

The photochemical reactivity of the faceted surfaces suggests that the two different facets have distinctly different reactivities. For example, the secondary electron (SE) images in Figure 3-17 show the surface after the photochemical reduction of Ag^+; this is a surface that was subjected to the baseline treatment. The silver appears as small particles with white contrast in Figure 3-17a and Figure 3-17b. In Figure 3-17a, at least one set of facets in all grains is decorated with reaction product (white contrast). Conversely, at least one set of facets on each grain has almost no observable reduced silver. The selectivity of the silver reduction shows that one of the two orientations is strongly photocathodic while the other is not. The same phenomenon was observed for all grains. A higher magnification image of the surface of a single grain is shown in Figure 3-17b. False color has been added in a region of Figure 3-17b to demarcate photocathodic (blue) and non-photocathodic (pink) sets of facets. For added clarity, this is represented schematically in Figure 3-17c. The schematic illustrates the hill-and-valley structure formed by the facets, with only the blue-colored facets active for silver reduction.

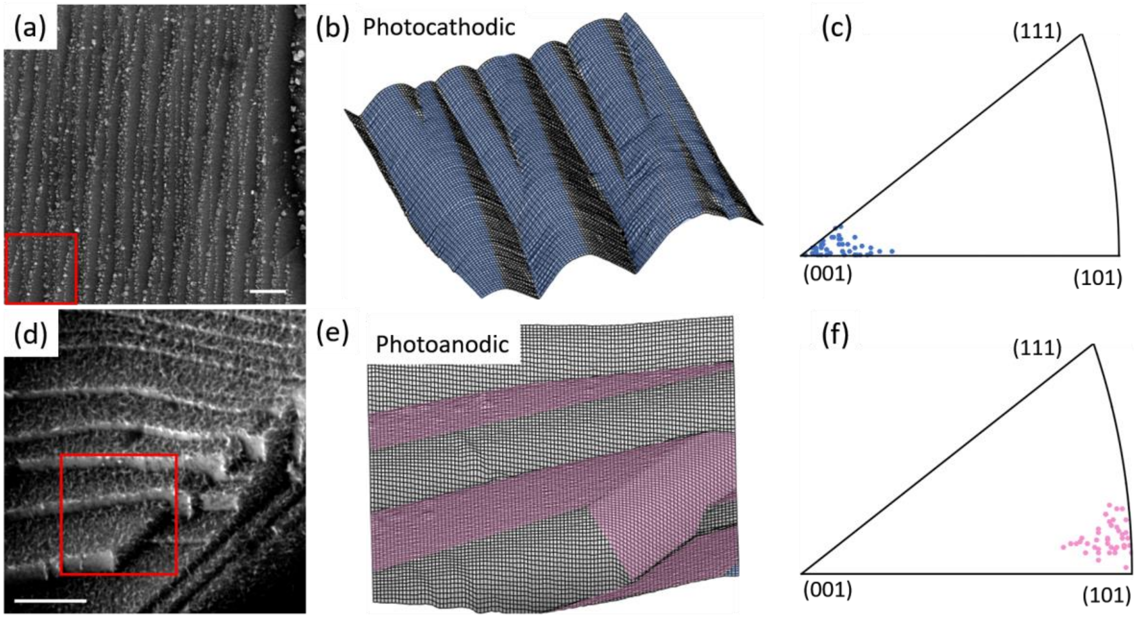

Figure 3-18: (a) SE image of a grain after photoreduction. (b) 3D representation of an AFM image from the area in (a) denoted by the red square. (c) Standard stereographic projection showing the orientations of 50 surface normals in the crystal reference frame from (b). (d) SE image of a grain after photooxidation. In (a) and (d), the scale bar is 500 nm. (e) 3D representation of an AFM image from the area in (d) denoted by the red square. (f) Standard stereographic projection showing the orientations of 50 surface normals in the crystal reference frame from (e). Vertical scales: (b) 330 nm (e) 55 nm

To determine the orientations of photocathodic (photoanodic) facets, the surfaces were used to photoreduce (photooxidize) Ag^+ (Mn^{2+}). The SE images in Figure 3-18a and Figure 3-18d show grains after a 6 s photoreduction reaction and a 1 min photooxidation reaction, respectively. The particles with white contrast in Figure 3-18a are photodeposited silver. The filamentary, web-like deposit in Figure 3-18d is MnO_x. 3D representations of the areas enclosed in red squares in Figure 3-18a and Figure 3-18d are illustrated in Figure 3-18b and Figure 3-18e, respectively. The reactive facets in both instances have been labeled and colored (blue/pink) to make it easy to identify the facet reactivity (cathodic/anodic). As mentioned before, it is assumed that the facets meet at a sharp edge, but the intersection appears rounded because of the finite curvature of the AFM tip. The surface normal vectors, obtained from the AFM data and transformed into the crystal reference frame using the grain orientation data, are plotted on a standard stereographic triangle in Figure 3-18c and Figure 3-18f for the photocathodic and photoanodic reaction, respectively. Each orientation distribution contains 50 randomly selected points from the photocathodic and photoanodic facet surfaces shown in Figure 3-18b and Figure 3-18e respectively. The results in Figure 3-18c and Figure 3-18f clearly show that the photocathodic facets have near {100} orientations and the photoanodic facets have near {110} orientations. This conclusion was reached from all areas examined. In cases where three facets were observed, two of the three promoted either reduction or oxidation and were found to be in the {100} or the {110} family, respectively. Again, the scatter in the measured orientations is attributed to the curvature introduced by the shape of the AFM tip.

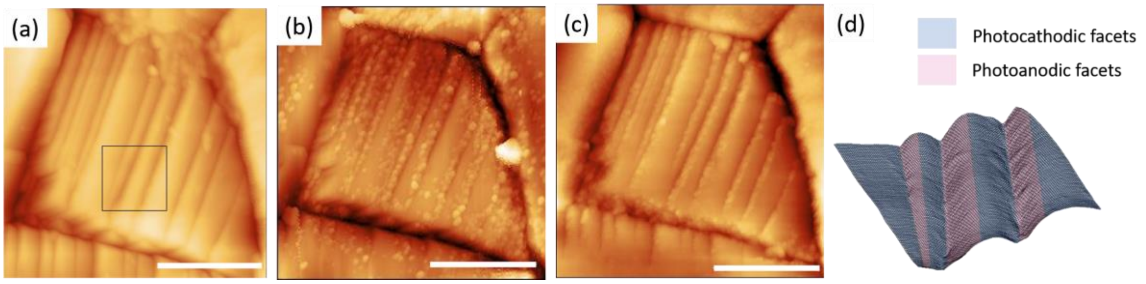

Figure 3-19: AFM topography of a grain (a) before reaction, (b) after photoreduction and (c) after photooxidation. (d) 3D representation of area inside black box in (a) colored by reactivity. The scale bar is 1 µm. Vertical scales (dark to bright): (a) 210 nm (b) 162 nm (c) 187 nm.

To confirm that different sets of facets carry out different reactions on a single grain, we examined by the photoreduction of silver and the photooxidation of manganese on the same grain. The AFM images in Figure 3-19a through Figure 3-19c show the topography of the same area of one $SrTiO_3$ grain before any reaction, after photoreduction, and after photooxidation, respectively. There are two sets of facets on this grain. Comparing Figure 3-19a (before reaction) with Figure 3-19b (after photoreduction), one of these sets of facets is covered with higher (white contrast) features that result from the photoreduction of Ag^+. Therefore, these are the photocathodic facets. When one compares Figure 3-19a (before reaction) with Figure 3-19c (after photooxidation), the other set of facets is covered with higher (white contrast) features that result from the photooxidation of Mn^{2+}. Therefore, these are the photoanodic facets. To illustrate the distinct characteristics of these facets, Figure 3-19d shows a 3D representation of the area in the black outline from Figure 3-19a, where the photocathodic (photoanodic) facets have been colored blue (pink). The finding from these observations is that reduction and oxidation take place on complementary sets of facets on the same grain in the baseline samples. This is observed consistently for all grains.

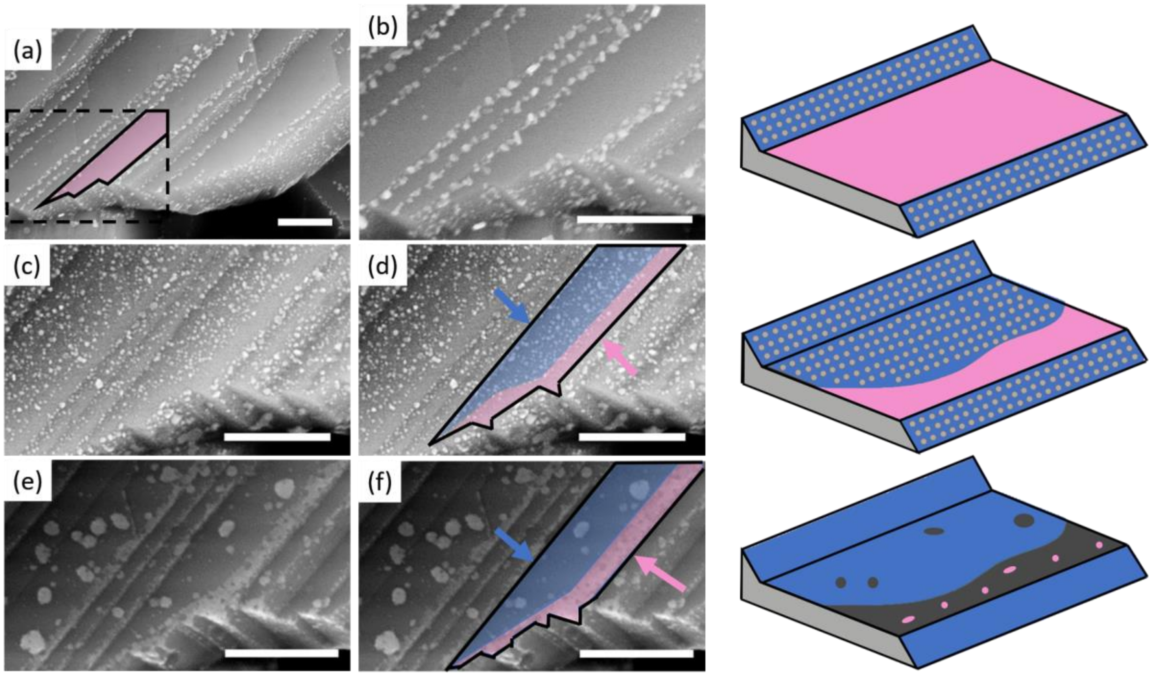

Figure 3-20: SEM images of the same area of $SrTiO_3$ grain after different treatments. (a) large field of view image showing large (110) terraces after the reduction of silver. (b) View of the area of interest. (c) After a thermal treatment (5 h/1100 °C/0.1 g $Sr_3Ti_2O_7$) to make the surface Sr-rich, silver is reduced on more of the surface, including area with the (110) orientation. (d) False color has been added to (c) to highlight areas with silver (blue) and areas without silver (pink). (e) The same surface after the oxidation of lead. (f) False color has been added to (e) to highlight areas covered by oxidized lead (pink) and those with less lead (blue). In the schematics, photocathodic areas are blue, photoanodic areas are pink, silver particles are light grey, and lead deposits are dark grey. In all images, the scale bar is 500 nm.

Finally, the photochemical reactivity of a surface was studied before and after a thermochemical treatment in an environment with a Sr-excess to determine if the surface reactivity could be changed. The SEM images in Figure 3-20 show a grain whose large, flat terraces have the {110} orientation. Figure 3-20a shows the surface after photoreduction of silver. There is almost no reduced silver on the {110} facets. Instead, silver particles with white contrast decorate only the {100}-oriented ledges. For the images in Figure 3-20b through Figure 3-20f, we focus only on the area within the black, dashed, rectangle and the photocathodically inert terrace that is colored pink. This region is shown, with no markings, in Figure 3-20b, and the terrace is illustrated schematically to the right.

After being used to reduce silver, the surface was cleaned and heated for 5 h at 1100 °C with 0.1 g of $Sr_3Ti_2O_7$. Following Zhu et al. [5,6], this thermal treatment makes the surfaces relatively Sr-rich. When silver is photochemically reduced on the thermally treated surface (15 s exposure), in addition to {100} ledges, reduced silver is found on a greater fraction of the {110} flat terraces (see Figure 20c) than after the baseline treatment (see Figure 20b). Some areas appear to be free of silver particles and for clarity, one of them is marked by pink in Figure 3-20d. The sample was then cleaned and subjected to photooxidation of lead (16 s exposure). As shown in Figure 20e, the areas that reduced the most silver now have a few larger lead deposits, while the areas that did not reduce silver are coated with oxidized lead. The areas coated with oxidized lead are highlighted in pink in Figure 3-20f, and the oxidized lead is shown as dark gray in the schematic, with the pink photoanodic surface visible between breaks in the oxidized lead coating. Because the thermal treatment increased the relative area of the surface that reduces silver, it is more photocathodic. Note that while the {110} surface was originally photoanodic after the baseline treatment, it becomes bi-functional after the treatment in excess Sr, with part of the surface being photocathodic. This change is illustrated by the schematics on the right side of Figure 3-20 (and is consistent with observations made for single crystals [6]).

3.7 Discussion

The photochemical reactivity of arbitrarily oriented crystals at the surface of a $SrTiO_3$ polycrystal can be interpreted in a surprisingly simple way. Because a general crystal orientation {hkl} of

$SrTiO_3$ always breaks up into a combination of {100} and {110} facets under the annealing conditions used, the reactivity of the surface is simply a combination of the reactivity of the {100} and {110} orientations. The relative areas of the {100} and {110} facets vary with the macroscopic crystal orientation, {hkl} [30]. The results show that the {110} oriented facets are more photoanodic and the {100} facets are more photocathodic. This suggests that it is possible to transfer photogenerated electrons to the more photocathodic orientation and photogenerated holes to the more photoanodic orientation. The result is that when a high index surface orientation breaks up into {100} and {110} facets, these two orientations provide an abundance of photocathodic and photoanodic sites to promote the overall reaction.

For an ideally orientated single crystal surface (nearly atomically flat), the situation is different. In this case, if there are no steps, the oxidation and reduction reactions must occur on the same surface. For $SrTiO_3$, the photocathodic and photoanodic reactions can be supported by different chemical terminations that arise from differences in the surface chemistry. [16] However, the results presented here suggest that different chemical terminations are not apparent, nor are they necessary, when {100} and {110} facets are simultaneously present on surfaces annealed in standard conditions (1250 °C, 8 h, in air). This is consistent with the findings of Mu et al., [13] who studied the photochemical reactivity of sub-micron, polygonal $SrTiO_3$ crystals. They found that cube-shaped crystals terminated by only {100} surfaces supported both photocathodic and photoanodic reactions. However, when crystals had both {100} and {110} facets, the photocathodic reaction occurred exclusively on {100} and the photoanodic reaction occurred exclusively on {110}. From this, one can conclude that the photoanodic sites on the {110} surface are more favorable than any such sites on the {100} surface.

Chapter 3: Influence of Terminations and Facets on photodeposition in polycrystalline $SrTiO_3$

One of the questions motivating this study was to understand the relative importance of surface termination (the chemical composition of the surface) versus the surface orientation. Information from the earlier single crystal studies can be used to identify the most likely terminations after the baseline thermal treatment (1250 °C, 8 h, in air). Zhu et al. [6] reported that after heating a (110) orientated $SrTiO_3$ single crystal at 1200 °C for 12 h, 90 % of the surface area is photoanodic and after 24 h it was 100 % photoanodic. Although our baseline treatment was for only 8 h, is was at a higher temperature, so it is safe to assume that the surface is also mostly, if not entirely, photoanodic. In fact, the results show that {110} surfaces are almost completely photoanodic, with only negligible amounts of silver reduced on these surfaces. The other principal facet is {100}. Although the chemical properties of this surface have not been reported, details of the surface structure after similar thermal treatments have been reported. Bachelet et al. [24] reported that after heating a (100) orientated $SrTiO_3$ single crystal at 1300 °C for 8 h, the surface had a roughly equal mix of SrO and TiO_2 terminated surfaces. Considering the similarity of our annealing conditions, it is reasonable to assume that the surfaces in the present study had a similar composition. Ocal et al. [31] reported that the measured surface potential difference between the SrO and TiO_2 terminations on a (100) oriented single crystal is approximately 45 mV. On the $SrTiO_3$ (110) surface, potential differences as small at 10 mV [6] led to the spatial separation of reaction products, so it seems likely that the same thing should occur {100} surfaces, but this was not observed. This is probably because of the simultaneous presence of {110} facets. As noted above, the {110} surface appears to be more anodic than any sites on the {100} surface, so that the photocathodic reaction occurs exclusively on the {100} surface and the photoanodic reaction occurs exclusively on the {110} surface.

If one considered only the experiments after the baseline thermal treatment, where there is no evidence that termination differences influence the reactivity, it would be concluded that the surface orientation is more important than the chemical termination. However, the observations after the thermal treatment with $Sr_3Ti_2O_7$ shows that this does not have to be the case. According to Zhu et al. [6], annealing in the presence of $Sr_3Ti_2O_7$ should increase the relative area of photocathodic region on the {110} surface. This is confirmed in Figure 3-20, which shows that parts of the {110} terraces become photocathodic (and less photoanodic) after the heat treatment. In previous work [5], photocathodic behavior was associated with a surface composition that had a greater Sr/Ti ratio, and this is consistent with the expected result of heating the surface in the presence of $Sr_3Ti_2O_7$. It is currently not known what effect the heat treatment might have on the surface terminations of the {100} surface. However, the treatment promotes photocathodic reactivity and it is therefore not surprising that the originally photocathodic {100} surface remains photocathodic after the thermal treatment.

The relative areas of photocathodic and photoanodic surfaces on a catalyst particle are important for the overall reactivity. The schematic crystal shown in Figure 3-21a can simultaneously promote oxidation and reduction, which is necessary for the photochemical reaction to proceed. In this case, the six {100} surfaces promote the photocathodic reaction and the twelve {110} surfaces promote the photoanodic reaction. It is assumed that electrons and holes generated in the bulk can migrate to the appropriate surface. This is supported by simulations that showed that small differences in surface potential cause electrons and holes to migrate to oppositely charged surfaces with little recombination. [32,33] However, for the reaction to proceed at the maximum rate, the oxidation and reduction must proceed at their maximum equal rates. One way to manipulate the relative reaction rates it to control the photocathodic to photoanodic surface area ratio. This could be accomplished by changing the shape of the crystal (the relative areas of {100} and {110} surface). Another possibility is to use thermochemical treatments, as demonstrated here, that create photocathodic regions on the {110} surfaces. For example, Figure 3-21b schematically illustrates how photocathodic-to-photoanodic surface area ratio of the particle in Figure 3-21a could be increased by annealing in a Sr-rich environment.

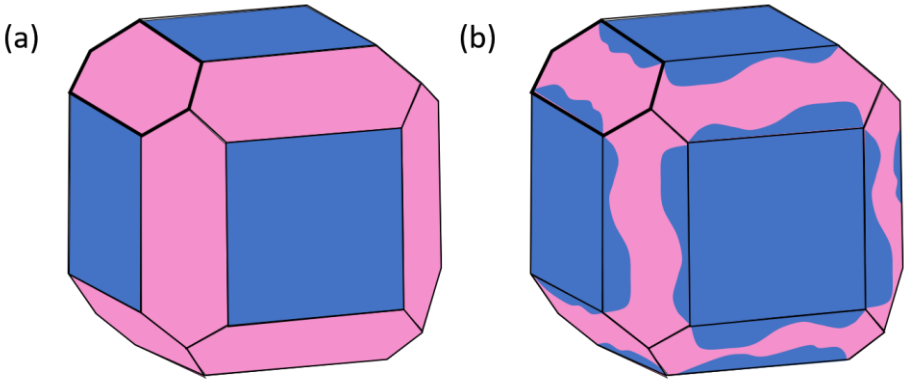

Figure 3-21: Schematic illustrations of $SrTiO_3$ crystals terminated by {100} and {110} surfaces. (a) After the baseline treatment, the {100} surfaces are photocathodic (blue) and the {110} surfaces are photoanodic (pink). (b) After annealing at 1100 °C in a Sr-rich environment, portions of the {110} surfaces become photocathodic.

3.8 Conclusions

The surfaces of $SrTiO_3$ crystals with arbitrary orientations, after heating in air at 1250 °C for 8 h, are terminated by a combination of {110} and {100} facets and the relative areas of the two facets depends on the orientation, {hkl}. The {100} facets appear to be uniformly photocathodic and serve as reduction sites. The {110} facets appear to be uniformly photoanodic and serve as oxidation sites. This is consistent with previous results on nanocrystalline $SrTiO_3$ [13]. After heating in an Sr-rich atmosphere, regions of {110} facets (on a {110} grain) became active for photoreduction of Ag^+, similar to previous results on single crystal {110} $SrTiO_3$ [34]. Hence, chemical terminations on {110} grains can be controlled via thermochemical treatments on polycrystals, analogous to single crystals. The regions on {110} which were unreactive towards photoreduction after thermochemical treatment, were active for photo-oxidation of Pb^{2+}, confirming complementarity even after thermochemical treatment.

Considering hypothesis 1, Sr transport was seen to increase the photocathodic (reductive) areas on {110} facets. Considering hypothesis 2 and 2.1, chemical terminations were seen to create photocathodic areas on previously photoanodic facets. Hence, it can be said that the influence of the terminations was higher at least on {110} facets. The interplay between these two features in determining the reactivity could not be ascertained on {100} as they were completely photocathodic before and after the Sr-rich treatment.

3.9 References

[1] Song Bai, Jun Jiang, Qun Zhang, and Yujie Xiong: *Chem. Soc. Rev.*, 2015, vol. 44, pp. 2893–2939.

[2] Akihiko Kudo and Yugo Miseki: *Chem. Soc. Rev.*, 2009, vol. 38, pp. 253–78.

[3] Roel Van De Krol and Michael Grätzel: *Photoelectro-Chemical Hydrogen Production*, 2012.

[4] S.R. Morrison: *Electrochemistry at Semiconductor and Oxidized Metal Electrodes*, 1980.

[5] Yisi Zhu, Paul A. Salvador, and Gregory S. Rohrer: *Chem. Mater.*, 2016, vol. 28, pp. 5155–62.

[6] Yisi Zhu, Paul A. Salvador, and Gregory S. Rohrer: *Phys. Chem. Chem. Phys.*, 2017, vol. 19, pp. 7910–18.

[7] Yisi Zhu, Andrew M Schultz, Gregory S Rohrer, and Paul A Salvador: n.d.

[8] P. a. Morris Hotsenpiller, J. D. Bolt, W. E. Farneth, J. B. Lowekamp, and G. S. Rohrer: *J. Phys. Chem. B*, 1998, vol. 102, pp. 3216–26.

[9] Jennifer L Giocondi, Shahrzad Samadzadeh, and Gregory S Rohrer: *MRS Proc.*, 2002, vol. 755.

[10] Ratiporn Munprom, Paul A. Salvador, and Gregory S. Rohrer: *J. Mater. Chem. A*, 2015, vol. 3, pp. 2370–77.

[11] Matthew S J Marshall, Andres E Becerra-Toledo, Laurence D Marks, and Martin R Castell: in *Defects at Oxide Surfaces*, Jacques Jupille and Geoff Thornton, eds., Springer International Publishing, Cham, 2015, pp. 327–49.

[12] Jennifer L Giocondi, Paul A Salvador, and Gregory S Rohrer: *Top. Catal.*, 2007, vol. 44, pp. 529–33.

[13] Linchao Mu, Yue Zhao, Ailong Li, Shengyang Wang, Zhiliang Wang, Jingxiu Yang, Yi Wang, Taifeng Liu, Ruotian Chen, Jian Zhu, Fengtao Fan, Rengui Li, and Can Li: *Energy Environ. Sci.*, 2016, vol. 9, pp. 2463–69.

[14] Wolfgang Rheinheimer, Michael Bäurer, Harry Chien, Gregory S. Rohrer, Carol A. Handwerker, John E. Blendell, and Michael J. Hoffmann: *Acta Mater.*, 2015, vol. 82, pp. 32–40.

[15] Tomoko Sano, David M. Saylor, and Gregory S. Rohrer: *J. Am. Ceram. Soc.*, 2003, vol. 86, pp. 1933–39.

[16] J L Giocondi and G S Rohrer: *J. Am. Ceram. Soc.*, 2003, vol. 86, pp. 1182–89.

[17] N. Erdman and L.D. Marks: *Surf. Sci.*, 2003, vol. 526, pp. 107–14.

[18] † Natasha Erdman, ‡ Oliver Warschkow, § Mark Asta, ‖ Kenneth R. Poeppelmeier, ‡ and Donald E. Ellis, and † Laurence D. Marks*: *J. Am. Ceram. Soc.*, 2003, vol. 125, pp. 10050–56.

[19] Yosuke Goto, Takashi Hisatomi, Qian Wang, Tomohiro Higashi, Kohki Ishikiriyama, Tatsuya Maeda, Yoshihisa Sakata, Sayuri Okunaka, Hiromasa Tokudome, Masao Katayama, Seiji

Akiyama, Hiroshi Nishiyama, Yasunobu Inoue, Takahiko Takewaki, Tohru Setoyama, Tsutomu Minegishi, Tsuyoshi Takata, Taro Yamada, and Kazunari Domen: *Joule*, 2018, vol. 2, pp. 509–20.

[20] M Kawasaki, K Takahashi, T Maeda, R Tsuchiya, M Shinohara, O Ishiyama, T Yonezawa, M Yoshimoto, and H Koinuma: *Science*, 1994, vol. 266, pp. 1540–42.

[21] A. Biswas, P. B. Rossen, C. H. Yang, W. Siemons, M. H. Jung, I. K. Yang, R. Ramesh, and Y. H. Jeong: *Appl. Phys. Lett.*, 2011, vol. 98.

[22] Abhijit Biswas, Chan Ho Yang, Ramamoorthy Ramesh, and Yoon H. Jeong: *Prog. Surf. Sci.*, 2017, vol. 92, pp. 117–41.

[23] Florencio Sánchez, Carmen Ocal, and Josep Fontcuberta: *Chem. Soc. Rev.*, 2014, vol. 43, pp. 2272–85.

[24] R. Bachelet, F. Sánchez, F. J. Palomares, C. Ocal, and J. Fontcuberta: *Appl. Phys. Lett.*, 2009, vol. 95, p. 141915.

[25] Song Bai, Lili Wang, Zhengquan Li, and Yujie Xiong: *Adv. Sci.*, 2017, vol. 4, p. 1600216.

[26] Lingqing Dong, Hui Shi, Kui Cheng, Qi Wang, Wenjian Weng, Weiqiang Han, and Springer-Verlag Berlin: n.d.

[27] Linchao Mu, Yue Zhao, Ailong Li, Shengyang Wang, Zhiliang Wang, Jingxiu Yang, Yi Wang, Taifeng Liu, Ruotian Chen, Jian Zhu, Fengtao Fan, Rengui Li, and Can Li: *Energy Environ. Sci.*, 2016, vol. 9, pp. 2463–69.

[28] Rengui Li, Fuxiang Zhang, Donge Wang, Jingxiu Yang, Mingrun Li, Jian Zhu, Xin Zhou,

Hongxian Han, and Can Li: *Nat. Commun.*, 2013, vol. 4, pp. 1432–37.

[29] Conyers Herring: *Phys. Rev.*, 1951, vol. 82, pp. 87–93.

[30] John W Cahn and Carol A Handwerker: *Equilibrium Geometries of Anisotropic Surfaces and Interfaces*, 1993.

[31] Carmen Ocal, Romain Bachelet, Luis Garzo, Massimiliano Stengel, and Florencio Sa: *Chem. Mater.*, 2012, vol. 24, pp. 4177–84.

[32] James J. Glickstein, Paul A. Salvador, and Gregory S. Rohrer: *J. Phys. Chem. C*, 2016, vol. 120, pp. 12673–84.

[33] James J. Glickstein, Paul A. Salvador, and Gregory S. Rohrer: *J. Mater. Chem. A*, 2016, vol. 4, pp. 16085–93.

[34] Yisi Zhu, Paul A Salvador, and Gregory S Rohrer: *Chem. Mater.*, 2016, vol. 28, pp. 5155–62.

4 Spatial Selectivity of Photodeposition Reactions on Polar Surfaces of γ-WO_3

4.1 Introduction

As listed in chapter 2, there are multiple features that can lead to spatial selectivity of photoreactions on photocatalyst surfaces. In chapter 3, spatial selectivity arising from facets of different orientations and different chemical terminations was discussed. In this chapter, we will be focusing on ferroelastic domain driven spatial selectivity. Ferroelastic domain-based spatial selectivity, in general, has tremendous potential in increasing the internal quantum efficiency (IQE) of the process of photocatalysis. Glickstein et. al. [1,2] have computed that the IQE can be increased from below 1 % to around 90 % for ferroelectric photocatalysts, by optimizing the ferroelectric domain polarizations and widths within reasonable values. They have explained that in other charge separating systems such as a Z-scheme, the carriers pushed towards the bulk recombine and the maximum possible IQE here is 50 % (one pair is recombined for every two pairs formed). 90 % of the theoretical maximum is made possible by the fact that charge carriers pushed away from the surface of one ferroelectric domain react on its alternately polarized adjacent ferroelectric domains. This kind of lateral distribution of charge carriers is the major advantage of ferroelectric/ferroelastic domain-based selectivity. Having regions of different polarization within the diffusion lengths of charge carriers is what can potentially deliver such high values of IQE. The ferroelectric domain widths between 100-400 nm have been computed to be optimal for high IQE by Glickstein [1,2] et. al. Hence, materials which possess ferroelastic/ferroelectric domains and have EDLs in this range can potentially have 90 % efficiency.

Dunn [3] advocated the use of ferroelectric materials for water splitting, and Tiwari and Dunn [4] reviewed photochemistry on ferroelectric surfaces. For ferroelectrics, individual materials that spatially separate reactions, the overlap with the solar spectrum is generally low. The few known solar active ferroelectrics have deficiencies with respect to the other materials criteria. Thus, their utility in solar photocatalysis is low. Clearly, a wider range of solar absorbing spatially selective materials is needed. Recently, we found that some centrosymmetric ferroelastics, which are not polar, surprisingly exhibit spatially selective reactivity and absorb visible light. This spatial selectivity was similar to that observed on ferroelectrics (that are polar in nature).

This chapter is organized as follows. The background section compares the similarities and differences between ferroelectrics and ferroelastics. It also discusses the methods previous studies have employed to correlate ferroelectric/ferroelastic domains to photoreactivity. The motivation section gives the reader an insight into the material properties and the reasons to study this material in the context of ferroelastic domain based water splitting. It is followed by a brief description of the experimental workflow, methods and equipment used for the work. The results of our experiments come next, followed by an overarching discussion and conclusions.

4.2 Background

4.2.1 Single-crystal poled ferroelectric LiNbO3

Before getting into the multiple-ferroelectric domain, multiple-polarization based polycrystalline systems, let us look previous results from a simpler case involving only one orientation and domain. Inoue et al. [5–7] first studied the effects of ferroelectric polarization on surface properties using coated poled ferroelectric crystals. They showed that O_2 adsorption (surface conductivity) was much higher for NiO films supported on negatively-poled (positively-poled) $LiNbO_3$ crystals than for similar films on oppositely poled LiNbO3 [6]. Additionally, the photocatalytic activity of TiO_2 films supported on poled-$LiNbO_3$ [7] was enhanced compared to standard titania. Later, they also showed that the photocatalytic hydrogen evolution from uncoated lead zirconate titanate (PZT) crystals was 10-40 times higher on positively-poled PZT than on negatively-poled PZT [5]. All of these observations could be explained by the effects that the ferroelectric polarization had on band bending in the substrate or film, where negative (positive) polarizations lead to upward (downward) band bending in the adjacent substrate or film. Electronic carriers were influenced by these fields, with holes (electrons) attracted to the negative (positive) polarization.

4.2.2 Unpoled, polycrystalline ferroelectrics

Our group has previously studied photodeposition of Ag and PbO_2 on $BaTiO_3$ [8–10], TiO_2-coated $BaTiO_3$ [11] [12], TiO_2-coated $PbTiO_3$ [13], $BiFeO_3$ [14] and TiO_2-coated $BiFeO_3$ [15,16] [17].

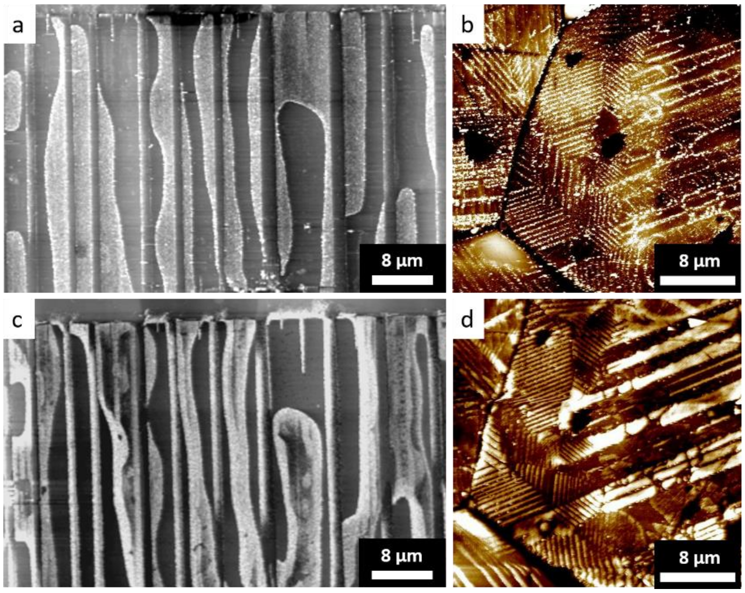

Figure 4-1: Topography of (a), (c) ferroelectric $BaTiO_3$ and (b), (d) coated ferroelectric $TiO_2/BaTiO_3$ substrates after photodeposition of (a), (b) Ag and (c), (d) PbO_2. Vertical scales: a) 100 nm b) 55 nm c) 110 nm d) 80 nm. Figures (a),(c) and (b),(d) are reproduced from [18] *and* [11].

Figures 1(a) and 1(c) are AFM topography images after Ag photoreduction and Pb photo-oxidation on the same surface of $BaTiO_3$. The bright regions in each image are photodeposited solid products. It is immediately clear that the reactivity of the surface is spatially heterogeneous. The reactivity patterns are exactly correlated with the ferroelectric domain patterns of the underlying substrate. Importantly, the regions of the surface that are reactive (unreactive) for reduction in figure 1(a) are unreactive (reactive) for oxidation in figure 1(c). This is an example of complementary reactivity: some ferroelectric domains are cathodic and some are anodic. One can describe such a surface as a series of short-circuited photoelectrochemical cells dictated by the ferroelectric domain structure on the surface. Using the polycrystalline nature of the samples, it was shown that similar complementary and spatially selective, spatially selective reactivity was observed across all of orientation space, implying the ferroelectric effects were more important than orientation effects (which are known for other photocatalysts like $BiVO_4$ [19], $SrTiO_3$ [20,21] and $NaNbO_3$ [22], amongst others).

Figures 1(b) and 1(d) are AFM topography scans after Ag photoreduction and Pb photo-oxidation respectively on the same surface of TiO_2-coated $BaTiO_3$. Similar to the bare substrate, the coated ferroelectric exhibits complementary reactivity, with some ferroelectric domains promoting Ag photoreduction and others promoting PbO_2 photo-oxidation [11]. Importantly, for these 15 nm films, the photocathodic (photoanodic) regions of the bare substrate are also photocathodic (photoanodic) regions for the supported film. This is consistent with the mechanism that carriers photogenerated in the ferroelectric substrate are responsible for the reactivity on the non-ferroelectric film surface. The substrate dominated photocatalytic activity of the film was supported by the observations that spatially selective reactivity was independent of the phase of the titania in the film or the orientation of the substrate or film. Of course, the ferroelectric domain influence disappears when the film is too thick [7,11] and the interfacial charge of the polar ferroelectric domains is screened by the film or the film's absorption is greater than that of the substrate. For example, 100 nm thick films did not exhibit spatially selective patterns of reduced silver [23]. Schultz et al. [14] carried out photodeposition experiments on ferroelectric BiFeO3 and correlated reactivity with polarization using PFM. The PFM out-of-plane phase difference is shown in figure 2(a), which shows clear polygonal piezoresponsive ferroelectric domains. The topography of the same area after Ag photoreduction with blue light is shown in figure 2(c). The bright regions in figure (c) are coated with Ag, and these correspond to the dark ferroelectric domains in the PFM image of figure 2(a).

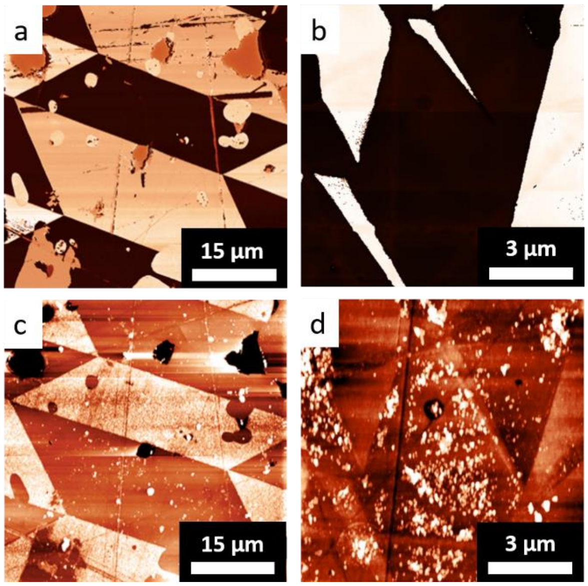

Figure 4-2: (a) and (b) are PFM images (out-of-plane phase difference) of (a) ferroelectric $BiFeO_3$ and (b) TiO_2 coated ferroelectric BiFeO3. (c) and (d) AFM topographic images after Ag photoreduction. Dark to bright vertical scales are: (a) 180° to 0°, (b) 180° to -180 °

Even for the solar absorbing $BiFeO_3$, it was shown that reactivity on certain ferroelectric domains was greater than others and that the influence of ferroelectric domain polarization overwhelmed effects of crystallographic orientation. Zhang et al. [16] carried out similar photodeposition investigations on TiO_2-coated $BiFeO_3$. As was the case for other coated ferroelectrics, when the film was thin (10 nm), spatially selective reactivity was observed. The PFM out-of-plane phase difference of the coated $BiFeO_3$ system is shown in figure 6(b). The topography of the same area after Ag photoreduction with blue light is shown in figure 6(d). The bright regions in figure (d) are coated with Ag, and these correspond to the dark ferroelectric domains in the PFM image figure 6(b). Because TiO_2 does not absorb visible light, the primary photo-generation of charge carriers takes place in the ferroelectric substrate. The ferroelectric domain polarization from the substrate then influences the drift of photogenerated carriers to the film/substrate interface. The carriers then traverse the coating and react at the TiO_2 surface in patterns identical to those of the substrate. Notably, a small polarization of 6.1 μC/cm^2 exists along the <111> direction of $BiFeO_3$ [14]. Hence, for any other orientation, the out-of-plane component is expected to be even smaller. This smaller component was seen to be enough to influence reactivity through a 10 nm film of TiO_2 [16]. Hence, it suggests that smaller polarizations below 10 μC/cm^2 are enough to drive spatially selective reactivity on photocatalysts coated with thin films.

4.2.3 Polycrystalline ferroelastics

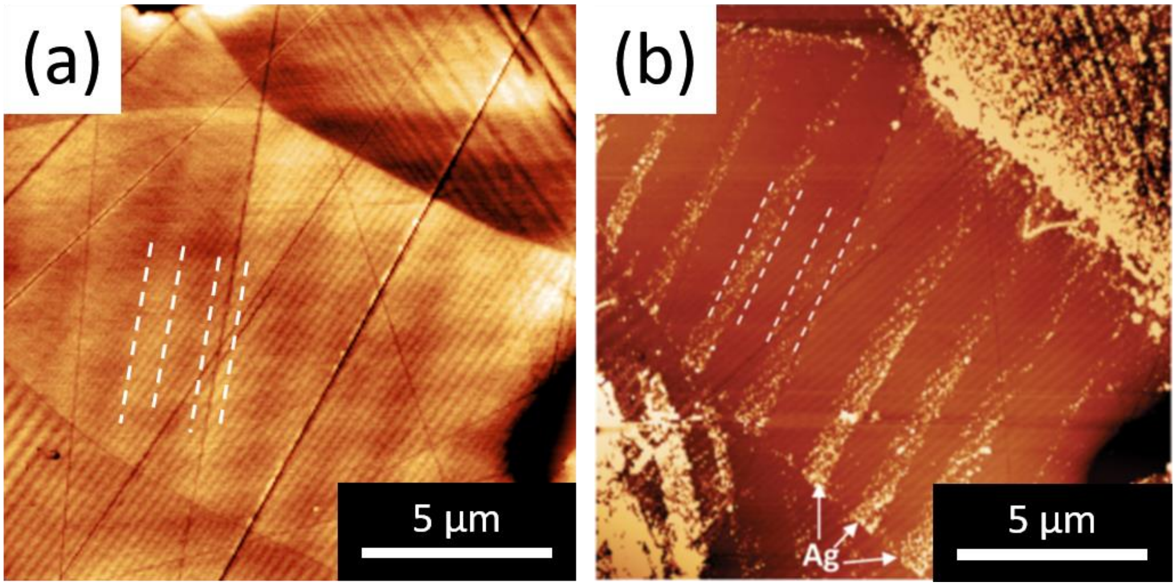

Figure 4-3: (a) AFM topography image (a) before and (b) after photodeposition of Ag^+

Recently, it was shown that some non-polar solar absorbing ferroelastics also exhibit spatially selective photochemical activity that is analogous to ferroelectric photochemical surface reactivity. Munprom et al. [24] were the first to report spatially selective reactivity on $BiVO_4$, a centrosymmetric ferroelastic. $BiVO_4$ exhibits ferroelasticity on cooling through a phase transformation from the tetragonal scheelite to the monoclinic fergusonite structure at 255 °C [25]. Ferroelastic $BiVO_4$ is centrosymmetric and potentially anti-ferroelectric [26]. The ferroelastic domains are clearly observable by AFM, as shown in figure 3(a). When Ag photoreduction was carried out using UV light or blue LEDs, the surface reactivity was observed to be correlated to the ferroelastic domain structure, as shown in figure 3(b) [24]. The ferroelastic domain structure of $BiVO_4$ is complex, and only some of the ferroelastic domains promote Ag photoreduction, which is apparent in the central grain of figure 3(a) and (b). The set of ferroelastic domains highlighted with white lines are photo-active. Within those photo-active domains, the other set of ferroelastic domains modulates the reactivity, reinforcing the importance of the ferroelastic domains on surface reactivity.

4.3 Motivation

Ferroelectrics show domain specific selectivity (as seen in the earlier section), but are unstable, few in number and mostly absorb light in the UV regime. Ferroelastics are abundant in the earth's crust, making up more than 30% of it [27]. Hence, having ferroelastics, as a class of materials, display polar behavior (like $BiVO_4$) is an attractive proposition. Because the report on $BiVO_4$ was the first of its kind to report polar ferroelastic domains on centrosymmetric materials [24], there was a need to reinforce those results by studying another similar material. We would then have a stronger case to extend these observations to the class of ferroelastics, and specifically, to anti-ferroelectric ferroelastics.

Chapter 4: Spatial selectivity of photodeposition reaction on polar surfaces of γ-WO_3

There are four reasons why we chose to study the ferroelastic domain structure – reactivity correlation on polycrystalline WO_3.

a) Visible light absorber

WO_3 is a visible light absorber with a band gap of 2.6 eV [28,29]. This means that it can be readily used as a photocatalyst activated by sunlight. This is especially important in the context of renewable energy, because the "free" energy of sunlight can be harnessed directly.

b) Hierarchical ferroelastic domain structure

WO_3 adopts different crystal structures as a function of temperature, all related to displacive distortions of the pseudo-perovskite ReO_3 structure (for which the *A*-site of the cubic perovskite ABO_3 structure is unoccupied). The sequence of phase transitions has been a matter of debate. [30–33] The ones of relevance herein are the ferroelastic transformations above room temperature: tetragonal (α) WO_3 transforms to orthorhombic (β) at around 740 °C, and β-WO_3 transforms to monoclinic (γ) at around 310 °C (Other transformations occur below room temperature [29] [34] [31–33]). The α-β and β-γ transformations (which happen on cooling during synthesis) are ferroelastic [35–39]. The ferroelastic domain structures in γ-WO_3 are known to be complex and hierarchical, and can evolve with time or stress [40–42]. Interestingly, Kim et al. [43] demonstrated that the surface layer in heavily reduced single crystals of WO_3 is piezoresponsive. More recently, hierarchical ferroelastic domain structures were found in epitaxial γ-WO_3 thin films, and one level of ferroelastic domains was shown to be piezoresponsive (polar) [40].

In short, there are multiple ferroelastic transitions in the material when cooling from sintering temperature to room temperature. Also, some piezoresponse has been measured on one tier of ferroelastic domains in thin films.

c) Photocatalyst used for water-splitting

WO_3 has been researched as a photoanode for water splitting [44–48]. The valence band potential (flat-band) is below that required for oxidation of water. However, the conduction band level (flat-band) is also below the reduction potential for hydrogen. Hence, it cannot do both simultaneously. Nevertheless, being a visible light absorbing photoanode, spatial selectivity on WO_3 will increase the efficiency of the system.

d) Anti-ferroelectric

$BiVO_4$ is usually not categorized as an anti-ferroelectric compound. However, it has the crystallographic requirements [26]. Hence, to study a compound similar to $BiVO_4$, WO_3 is a good candidate because it is an anti-ferroelectric [30,49], with an anti-polar dipole arrangement [50] and ferroelectric phases stable below room temperature [33].

Additionally, we chose to focus on polycrystalline samples of WO_3, that offer two advantages. Firstly, many orientations can be studied at a single time. If ferroelastic domain polarization/selectivity depended on crystallographic orientation, studying polycrystals would be a high-throughput way to arrive at the relation. Yun et. al. have seen piezoresponsive ferroelastic domains on {100} orientations of WO_3 in a thin film form [40]. We can determine whether the piezoresponse is limited to only {100} orientations. Secondly, showing spatial selectivity on polycrystalline ferroelastics would offer a way to integrate efficiency increasing spatial selectivity in inexpensive polycrystalline photocatalytic systems.

Considering all of this, the questions which we sought to answer were:

a) Does the surface of polycrystalline WO_3 show ferroelastic domain-driven spatial selectivity of photoreactions?
b) Are the ferroelastic domains of WO_3 polar on bulk, polycrystalline WO_3? How many levels are polar?
c) Does the reactivity correlate to the photochemical deposits on the surface?

4.4 Hypotheses

Hypothesis 1

Similar to $BiVO_4$, photoreactivity will be driven by ferroelastic domains on centrosymmetric, ferroelastic γ-WO_3 due to polarization (most likely due to either flexoelectricity or an AFE-FE surface phase transformation).

Alternate hypothesis 1.1

The spatial selectivity arises out of purely orientational differences between ferroelastic domains (leading to formation of surface heterojunctions), in which case the ferroelastic domains are non-polar but photoreactivity still reflects the ferroelastic domain structure.

Hypothesis 2

Because the ferroelastic domains are expected to attract/repel charge carriers depending on the polarization, the reactivity will be complementary reflecting the alternating strain state of ferroelastic domains in a single tier. Also, because the structure is multi-tiered, the smallest tier of ferroelastic domains is expected to drive the reactivity because of two reasons: 1) A single ferroelastic domain of a single polarization direction, has another tier within it. Hence, the single polarization will be perturbed by the alternating polarization from the smaller tier, which will be reflected in the photodeposition. 2) The flexoelectric effect being dependent on strain gradients, the smaller ferroelastic domains may be more polarized than the larger ones due to shorter widths.

Alternate hypothesis 2.1

The effect of the secondary ferroelastic domains is not strong enough to perturb primary ferroelastic domain reactivity, and the reactivity follows only the primary ferroelastic domain structure. This is possible as it has been calculated that the influence of ferroelectric domains starts decreasing below 100 nm in $BaTiO_3$ [2]

Hypothesis 3

The ferroelastic domains will give an alternating PFM signal that reflects the ferroelastic domain structure due to alternating polarization.

Alternative hypothesis 3.1

The secondary and tertiary ferroelastic domain PFM contrast is too weak to perturb the primary ferroelastic domain contrast.

<u>Alternative hypothesis 3.2</u>

The ferroelastic domains may not be polarized at all, in which case there will be no PFM contrast.

4.5 Experimental methods

The experimental workflow was as follows. The prepared samples were examined for the presence of different phases of WO_3. Once the phases were ascertained, the ferroelastic domain structure was imaged using BSE. EBSD was carried out to determine the orientations of grains to comment on the domain wall plane orientation. PFM was carried out to check for polar ferroelastic domains. Finally, photodeposition marker reactions were carried out and the products were analyzed using SE imaging and AFM topographic imaging. The processes are given in detail below.

4.5.1 Sample preparation

WO_3 powder (99.9% purity) was purchased from Sigma Aldrich for use in all experiments involved in this work. The powder was wet ground in acetone using a mortar and pestle for 5 minutes. 2 grams of powder was then mixed with a drop of polyvinyl alcohol as a binder and cold-pressed into a pellet using a tabletop hydraulic press (Carver). The pressed pellets were then sintered in an alumina crucible. The pellets were laid on a bed of WO_3 powder to prevent any reaction with the alumina during sintering. The pellets were fired at 1100 °C for four hours using a ramp rate of 10 °C/minute during heating and cooling cycles. One of the sides was then polished to a mirror finish using the following recipe:

Serial number	Base speed (RPM)	Polishing paper/cloth + suspension	Time (min)
1	120	320 grit Carbimet	0.5
2	120	600 grit Carbimet	1
3	120	800 grit Carbimet	1.5
4	150	1200 grit Carbimet	2
5	180	Satyn MB + 9 μm diamond suspension	3
6	180	Satyn MB + 3 μm diamond suspension	4
7	180	Satyn MB + 1 μm diamond suspension	5
8	200	Micro MB + 0.05 μm diamond suspension	8

The cadence of the head was 60 RPM for all polishing steps. The force used was 1 lb. for all polishing steps. The polishing was carried out on a Buehler Automet 250 machine. After polishing, to repair the surface damage as well as create ferroelastic domains, the pellets were then subjected to another annealing step. The pellets were annealed at 600 C for 1 hour using a ramp-up rate of 5 °C/min and a ramp down rate of 10 °C/min. After the annealing was complete, the pellets were sonicated successively in acetone, ethanol and DI water for 3 minutes each before further analysis.

4.5.2 X-ray Diffraction

One polished pellet was ground using a mortar and pestle for x-ray diffraction (XRD) analysis. The powder was spread on a glass slide and mounted in an X’Pert Pro MPD x-ray diffractometer. XRD was carried out using 45 kV and 40 mA with a Cu target (radiation wavelength 1.54 Å). ϴ-2ϴ patterns were collected, registering XRD intensity every 0.026 ° from 20 – 65 ° at a speed of 0.067 °/s. An x-ray diffractogram for γ-WO_3 was simulated using CrystalDiffract [51] software for comparison with the acquired patterns. The structural parameters for γ-WO_3 were taken from Loopstra and Rietveld [52].

4.5.3 Back-scatter electron imaging

BSE imaging was carried out using an FEI Quanta 200 FEG (field emission gun) and an FEI Quanta 600 FEG scanning electron microscope. Accelerating voltages ranged from 5 to 15 kV. The spot size was typically 4 or 5, but 3.5 was used for improved imaging of tertiary ferroelastic domains. The contrast was set to 80-90 % of the maximum possible value while the brightness was set to 0-15 % of the maximum possible value. The image acquisition times ranged from 3-6 minutes per image to achieve the desirable quality (i.e., signal-to-noise ratio). Contrast between ferroelastic domains arises from differences between electron counts from differences in electron channeling in different ferroelastic domains.

4.5.4 EBSD

EBSD was carried out using an FEI Quanta 600 FEG SEM equipped with an Oxford HKL EBSD system and an HKL NordlysNano camera. The accelerating voltage was 20 kV. The sample was mounted on a pre-tilted sample holder (70°). Patterns were collected using a dwell time between 140 and 200 ms per frame and averaging two frames together for the final pattern.

The patterns were then indexed using two variations of the space group No. 14: $P2_1/c$ and $P2_1/n$. In the $P2_1/c$ system, the cell parameters used were a = 7.69 Å, b = 7.54 Å, c= 10.525 Å and β = 136.05° (calculated from the $P2_1/n$ values given below). This setting was used to resolve crystallographic orientation differences for the secondary ferroelastic domains. In the $P2_1/n$ system, the cell parameters were a = 7.36 Å, b = 7.54 Å, c = 7.69 Å and β = 90.9° [52]. This setting corresponds well to the (doubled) pseudo-perovskite unit cell, and we used it to simplify the categorization of the primary and secondary domain wall crystallography.

4.5.5 PFM

Piezoforce Microscopy (PFM) was carried out using an NT-MDT Solver NEXT tabletop AFM. The samples were cleaned in acetone, ethyl alcohol, and distilled water, and then wiped with a methanol soaked Kimwipe (KimTech) before being imaged in the AFM. Conductive probes by Nanoworld (ARROW-EFM: cantilever frequency = 75 kHz, spring constant = 2.8 N/m, cantilever length = 240 µm) were used. A scanning speed of 3 µm/s was used, with an AC bias of 4 V. The AC frequency used was approximately 320 kHz, where the first contact resonance was observed.

4.5.6 Marker reactions

For Ag^+ reduction, a 0.115 M solution of $AgNO_3$ was used, prepared by dissolving 0.097 g of $AgNO_3$ in 5 ml of distilled water. For Pb^{+2} (Mn^{2+}) photo-oxidation, a 0.345 M solution of $Pb(CH_3COO)_2$ (0.345 M solution of $MnSO_4.4H_2O$) was used, prepared by dissolving 0.561 g of $Pb(CH_3COO)_2$

(0.384 g of $MnSO_4$-$4H_2O$) in 5 ml of distilled water. The Ag^+ photoreduction (Pb^{2+}/Mn^{2+} photo-oxidation) reactions were carried out by exposing the above setup to UV light with a power of 75 W for 6 s (150 W for 180 s).

4.5.7 AFM (topography mode)

Topography profiling of the WO_3 surface before and after photodeposition reactions was carried out on NT-MDT Solver NEXT tabletop AFM. Tapping mode tips from Budget Sensors (Tap 300-G) were used for generating the topography maps. The maximum scan speed used was 20 µm/s (for scans exceeding 20 µm x 20 µm). Smaller images were recorded at 0.5 Hz (2 seconds per line).

4.6 Results

4.6.1 X-ray Diffraction of WO_3 polycrystals

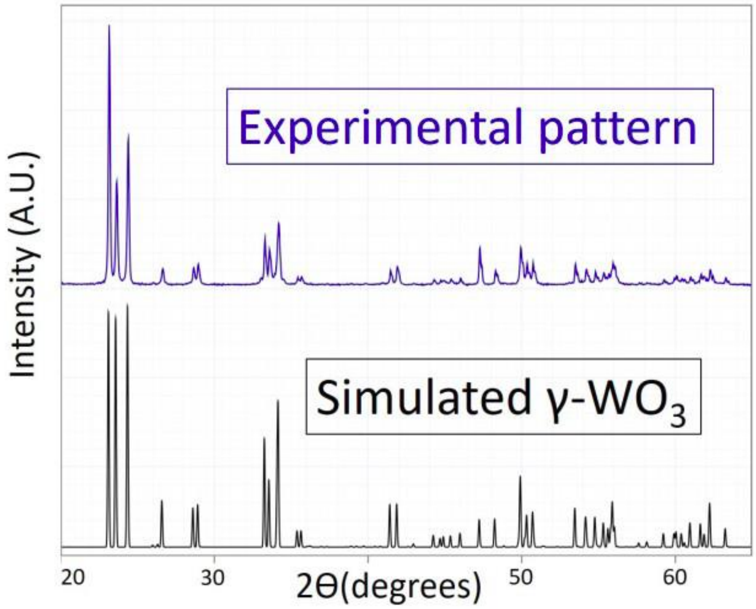

Figure 4-4: (top) XRD diffractogram of synthesized sample and (bottom) simulated from CrystalDiffract [51]

Figure 4 shows a comparison between the experimental and simulated X-ray diffraction spectra of γ-WO_3. All the peaks of the simulated pattern exist in the experimental pattern. Peaks at higher angles show some shoulder peaks, which are reminiscent of $K_{\alpha 2}$ peaks. $K_{\alpha 2}$ peaks are evident at higher angles as the splitting is higher at greater values of theta [53]. Also, the intensity of the $K_{\alpha 2}$ peaks are usually half of the $K_{\alpha 1}$ peaks, and the convolution of the two can represent the peaks seen here at higher theta values. Hence, the XRD pattern supports that the samples were entirely composed of γ-WO_3.

4.6.2 Three – Tiered Ferroelastic domain structure of WO_3

A comparison of an SE and a BSE image of a 64x64 µm area is shown in Fig. 5(a) and Fig. 5(b) respectively. From the BSE image, ferroelastic domains can be seen in just about every grain, with varying degrees of contrast. Such ferroelastic domain structures arise from ferroelastic transformations, and are expected in the case of γ-WO_3 [35–40]. From Figure 5, it is difficult to decipher multiple tiers of ferroelastic domains. Figure 6 shows a close up of a single grain, where two tiers are seen easily.

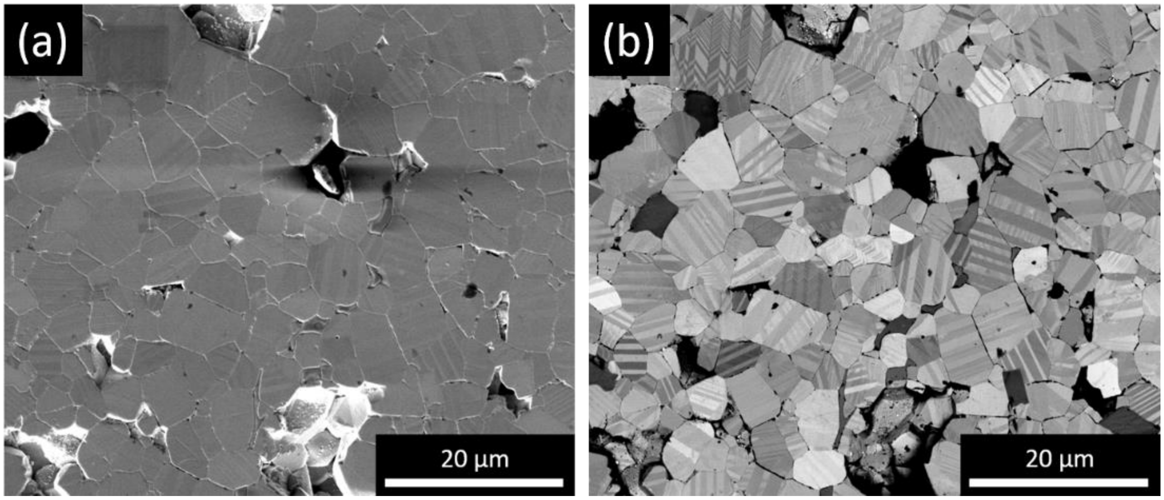

Figure 4-5: (a) Secondary electron and (b) Backscatter electron images of the γ-WO_3 polycrystalline surface after polishing and annealing

In Fig. 6(a), the large central grain shows two distinct tiers of ferroelastic domains. The first tier is comprised of ferroelastic domains running from bottom left to top right. One set of ferroelastic domains in this tier is solid grey while the alternating set is striped. The second tier of ferroelastic domains is seen in this striped set of primary ferroelastic domains. The alternating light and dark grey stripes are the secondary ferroelastic domains, which run from top left to bottom right.

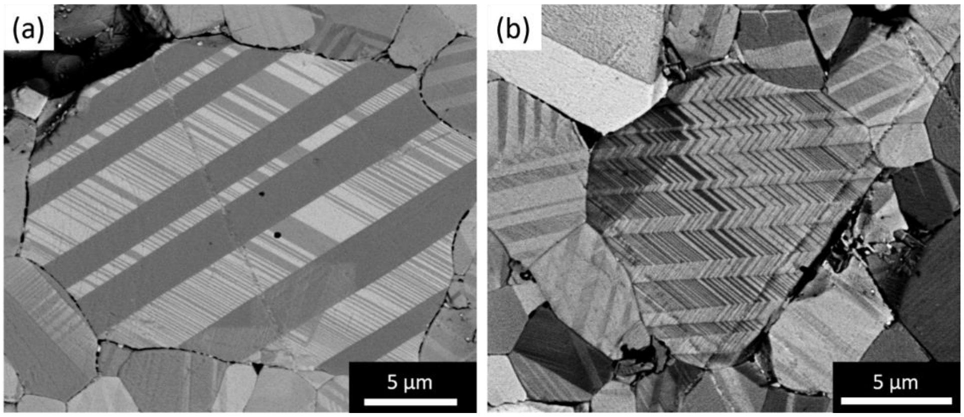

Figure 4-6: BSE images of grains showing two levels of ferroelastic domains. Secondary ferroelastic domains are seen only in the bright primary ferroelastic domains in (a) while they are seen in both sets in (b)

In this grain, the solid grey set of primary ferroelastic domains does not show any secondary ferroelastic domains, presumably due to the channeling conditions being similar for both sets of secondary ferroelastic domains comprising it.

The central grain in Fig. 6(b) clearly shows secondary ferroelastic domains in both sets of primary ferroelastic domains. The primary ferroelastic domains run horizontal. The secondary ferroelastic domains zig-zag through the primary ferroelastic domains, with alternating bright and dark contrast. On closer investigation of certain grains, we found that a third tier of ferroelastic domains exist with secondary ferroelastic domains. A BSE image of such a grain is shown in Figure 7(a). A schematic of the three-tiered structure is given in Figure 7(b) for ease in interpretation. The widest ferroelastic domains run from the bottom left to the top right of Fig. 7(a).

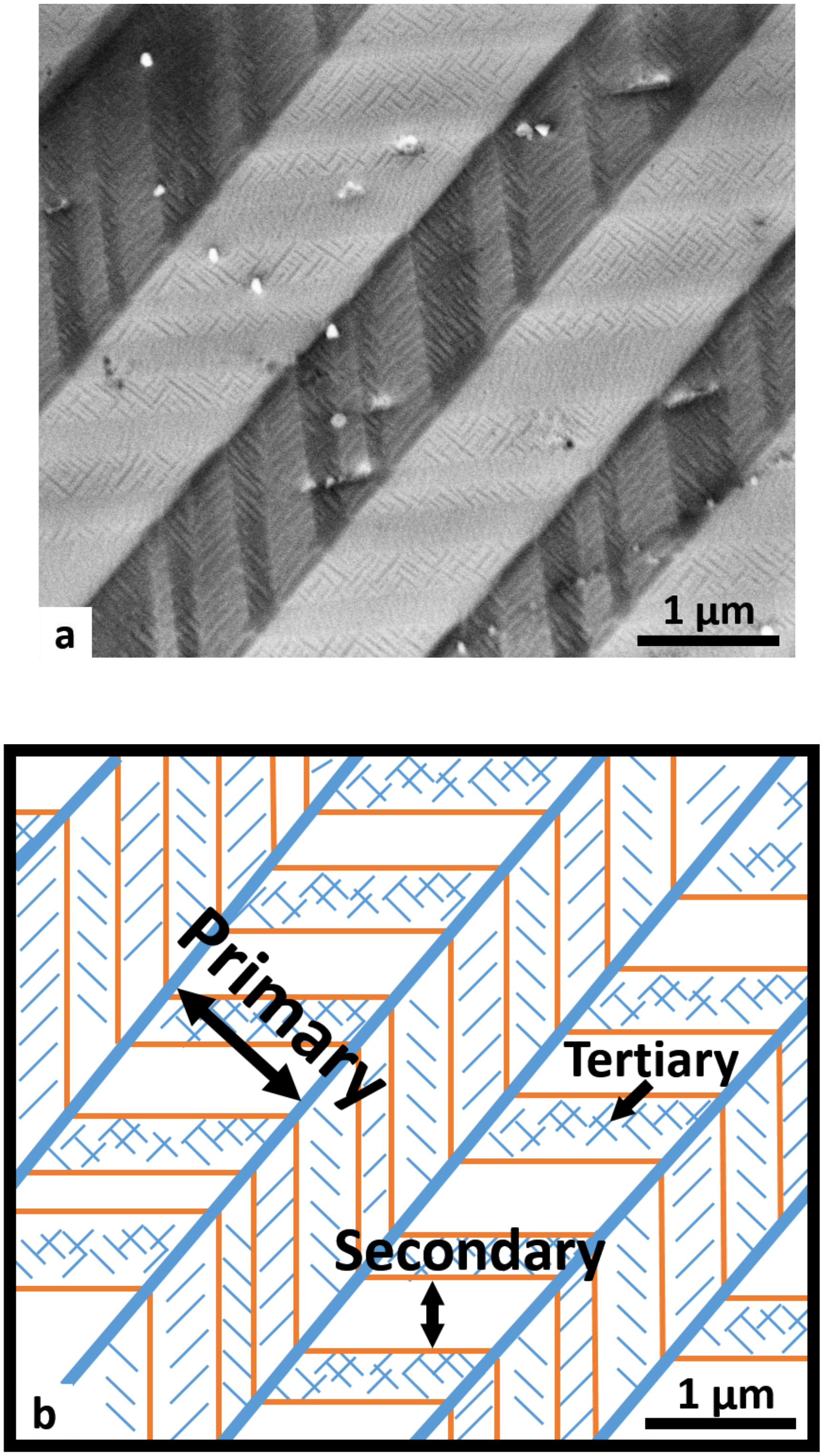

Figure 4-7: (a) BSE image of a grain magnified to 24000x, showing three levels of ferroelastic domains. (b) Schematic of the ferroelastic domain structure seen in (a).

They alternate between dark and bright contrast, and span the entire length of the image; we call these primary ferroelastic domains. Within any primary ferroelastic domain, another level of bright / dark contrast alternation is observed that spans the entire primary ferroelastic domain; we call these secondary ferroelastic domains. In this image, the secondary ferroelastic domain boundaries are oriented vertically (horizontally) in the darker (brighter) primary ferroelastic domains. They form a characteristic chevron pattern at the boundary of the primary ferroelastic domains. The third tier of contrast is associated with cross-hatched tweed and acicular patterns within the secondary ferroelastic domains; we call these tertiary ferroelastic domains. Within the brighter primary ferroelastic domains, a clear tweed (acicular) pattern is observed within the brighter (darker) secondary ferroelastic domains (the acicular ferroelastic domains are not shown in the schematic in Fig. 7(b)). Within the darker primary ferroelastic domains, the tertiary ferroelastic domains are acicular in each secondary ferroelastic domain, with the directions of the tertiary ferroelastic domains being rotated by ≈ 90° between the two secondary ferroelastic domains.

4.6.3 EBSD Analysis

EBSD was done in two systems of space group 14: $P2_1/n$ and $P2_1/c$. Both systems are monoclinic but the unit cell in $P2_1/n$ is pseudo-cubic, with dimensions as a = 7.36 Å, b = 7.54 Å, c = 7.69 Å and β = 90.9°. The lattice parameters are very close to a cubic system. The $P2_1/n$ monoclinic γ-WO_3 structure can be most easily understood as a distorted doubled perovskite with the A-sites completely empty [32]. The unit cell dimensions in $P2_1/c$ are a = 7.69 Å, b = 7.54 Å, c= 10.525 Å and β = 136.05°, and thus, is truly monoclinic. These two systems have been used for different purposes in the analysis of the WO$_3$ microstructure.

The pseudo-cubic nature also makes it easier to calculate the miller indices of the ferroelastic domain boundary planes, as compared to the monoclinic system where the sides are not orthogonal to each other. The monoclinic system, being the standard, was used to determine the ferroelastic domain orientation.

4.6.3.1 Determination of ferroelastic domain boundary plane orientations

To identify the crystallography associated to primary and secondary ferroelastic domain boundaries, we studied grains that had the a, b, or c axes oriented within 10° of the surface normal, based on the $P2_1/n$ EBSD data. Fig. 8 shows a BSE image of a grain whose primary ferroelastic domains have the [100] or [010] axes normal to the surface plane. Below the image, the crystal axes are shown for two ferroelastic domains (indicated by arrows).

Using the Euler angles of the primary ferroelastic domains, we determined the angles that the traces of planes in the {110} and {100} families would make with the surface plane. The calculated traces were then matched with the observed traces using ImageJ [54]. The traces of the (-101) and (011) planes (according to the two different coordinate systems of the two different primary ferroelastic domains), are depicted in blue in Fig. 8 (marked as {110}). These align well with the primary ferroelastic domain boundaries. The traces of the (100) and (001) planes (according to the two different coordinate systems of the two different primary ferroelastic domains), are depicted in orange in Fig. 8 (marked as {100}). These align well with the secondary ferroelastic domain boundaries. The measured angle between the traces of the secondary ferroelastic domain boundaries is 90 ± 1°, consistent with the expected angle between the traces of the (100) and (001) planes.

Similar analyses were carried out for several grains. In the cases investigated, the primary ferroelastic domain boundaries were consistent with $\{110\}_p$ planes and the secondary boundaries with $\{100\}_p$ planes, where the subscript p denotes these are given using the cubic pseudo-perovskite indexes. Further, the rotation across the primary ferroelastic domains was usually 90° about the $<100>_p$ and the rotation about the secondary ferroelastic domains were 180° about another $<100>_p$ direction. These types of planes are commonly observed as ferroelastic domain boundaries in WO_3 [31,35–38,41,42,55].

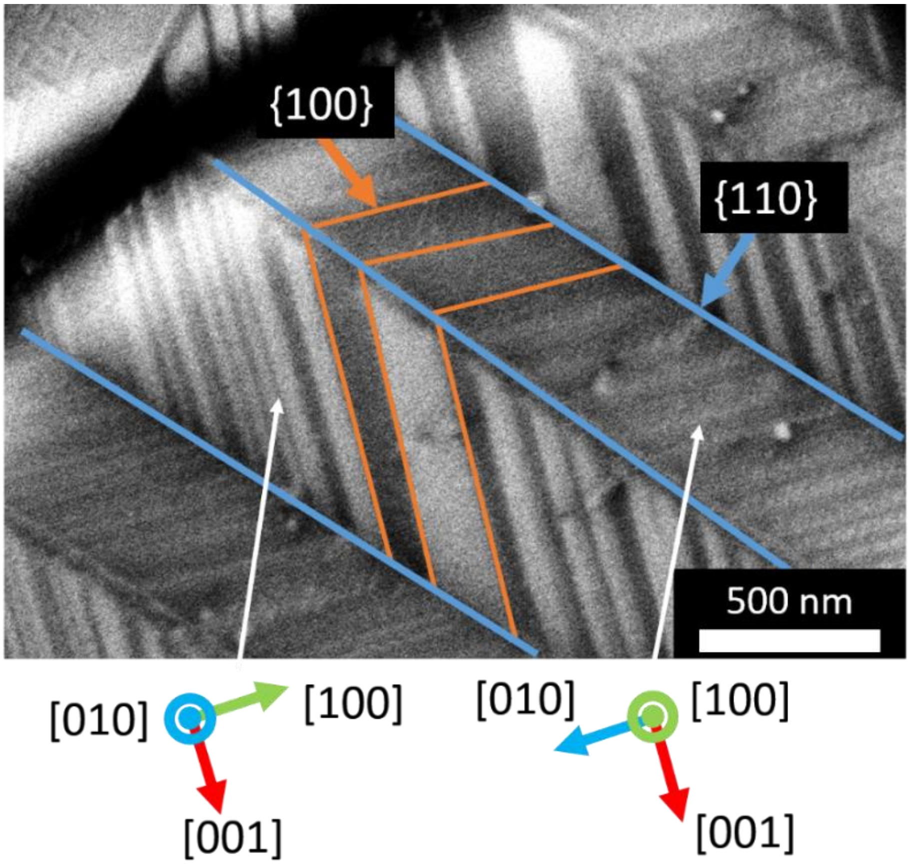

Figure 4-8: BSE image of a grain showing two levels of ferroelastic domains. The Blue lines indicate the primary ferroelastic domain boundaries. The orange lines indicate the secondary ferroelastic domain boundaries. The orientations of the primary ferroelastic domains as indexed in the $P2_1/n$ (pseudo-perovskite) system

Following Sapriel's [55] analysis suggests that ferroelastic domains formed as a result of the tetragonal to orthorhombic ferroelastic transition should have domain walls along x = y or x = -y. In γ-WO_3 terms, this means the ferroelastic domains associated with the α to β (tetragonal to orthorhombic) transformation could lie along the $\{110\}_p$ planes, which is consistent with the primary ferroelastic domain boundaries. Sapriel's [55] analysis also suggests that ferroelastic domains formed as a result of the orthorhombic to monoclinic ferroelastic transition should have domain boundaries along x=0 and z=0, which implies walls along (001) or (100), which are consistent with the secondary ferroelastic domains.

Thus, the primary ferroelastic domains, which span entire grains, are consistent with expectations from the α to β (tetragonal to orthorhombic) transition (at 740 °C) [31,35–38,40,55]. The secondary and tertiary ferroelastic domains are consistent with the β to γ (orthorhombic to monoclinic) transition (at 310 °C) [31,35–38,40–42,55]. These observations are also consistent with the ferroelastic domain boundary planes reported by Tanisaki [36] on single crystals of WO_3.

4.6.3.2 Orientation mapping of ferroelastic domains

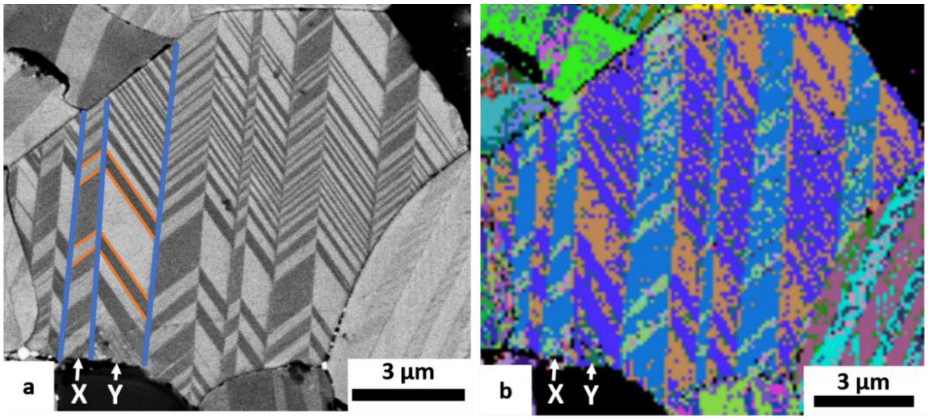

Figure 4-9: a) A BSE image and (b) a map of local Euler angles of a region of the γ-WO_3 surface. In (a), blue and orange lines mark some primary and secondary ferroelastic domain boundaries, respectively. In (b), different colors indicate different Euler angle values (crystallographic orientations). In both, X and Y mark the same primary ferroelastic domains.

A BSE image from another region of the γ-WO_3 surface is shown in Fig. 9(a). Primary ferroelastic domains are visible in all grains, terminating at grain boundaries. Secondary ferroelastic domains are visible in most primary ferroelastic domains. A map of local orientations is given in Fig. 9(b) (for the same region in Fig. 9(a)), collected using electron backscatter diffraction (EBSD). Different colors represent different values of the Euler angles in the $P2_1/c$ structure of γ-WO_3 (black pixels were unindexed). The colors alternate between related primary ferroelastic domains in Fig. 9(b), changing at the primary ferroelastic domain boundaries observed in Fig. 9(a). The changes in the crystallography across primary ferroelastic domains correspond to a rotation of ≈ 90° about the $\langle 100\rangle_p$ and the ferroelastic domain boundary planes were consistent with $\{110\}_p$, where p indicates the use of pseudo-perovskite indices. The calculation of these orientations was carried using methods similar to those described in reference to Fig. 8. These ferroelastic domains are consistent with expectations from the α—β (tetragonal to orthorhombic) transition [31,35–38,55].

The points within individual primary ferroelastic domains belong to one of two different colors, roughly correlating to the secondary ferroelastic domains observed in Fig. 9(a). In the central grain, the primary ferroelastic domains are purple/brown or blue/green. The secondary ferroelastic domains with dark contrast in Fig. 9(a) are approximately blue or purple in Fig. 9(b), and those with light contrast in Fig. 9(a) are generally green or brown in Fig. 9(b). That the secondary ferroelastic domains are not well resolved using automated EBSD is not surprising. First, the ferroelastic domains are all related by 90° rotations about $\langle 100\rangle_p$, and thus, the EBSD patterns are similar in these ferroelastic domains; accurately differentiating the monoclinic distortion using standard indexing procedures employed here is challenging. Second, the existence of a tertiary ferroelastic domain structure (see Fig. 7(a)) would lead to multiple tertiary ferroelastic domains contributing to individual EBSD patterns, further complicating indexing. Nevertheless, pairs of secondary ferroelastic domains were found to be related through a rotation of ≈ 180 ° about the a- or b-axes, and the ferroelastic domain boundary directions (seen best in Fig. 8(a)) to be consistent with $\{100\}_p$ planes. Thus, the secondary ferroelastic domains are consistent with expectation from the β—γ (orthorhombic to monoclinic) transition [31,35–38,40–42,55]. (The tertiary ferroelastic domain structure has also been related to this transition.) [31,35–38,40–42,55]

4.6.4 PFM contrast – Ferroelastic domain correlation

4.6.4.1 VPFM-Ferroelastic domain correlation

A BSE image from an area on the surface that includes multiple grains is given in Fig. 10(a) and an out-of-plane piezoforce microscopy (PFM) phase image of the same region is given in Fig. 10(b). PFM contrast is observed in almost all grains, having a strong spatial correlation to the primary ferroelastic domains (Fig. 10(a)), though the contrast variation between primary ferroelastic domains varies greatly from grain to grain. Even when the primary ferroelastic domains yield negligible contrast in the BSE image (see grain G'), they can yield good contrast in the PFM image. The grains shown are representative of the entire population; PFM contrast is detectable for grains of all orientations (characterized using EBSD) and is strongly correlated with the primary ferroelastic domains observed in a BSE image. Yun et al. [40] reported $\{100\}_p$ surfaces of epitaxial γ-WO_3 films were polar, with the PFM contrast correlating with their macro-ferroelastic domains (which had structure (sizes) similar to our primary (secondary) ferroelastic domains). Our observations support the existence of polar surfaces on γ-WO_3 and show they are not confined to specific orientations, epitaxial states [40] or heavily reduced states of WO_3 [43].

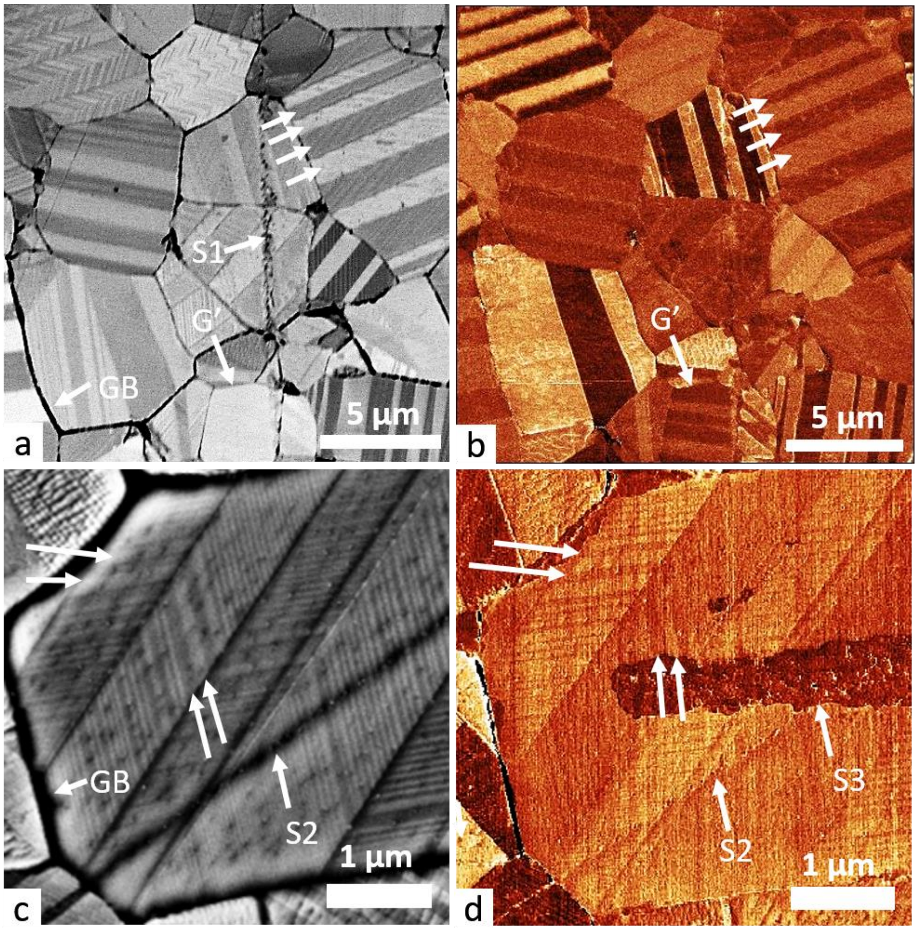

Figure 4-10: (a) A BSE image showing ferroelastic domain structures in multiple grains. S1 (GB) indicates a scratch (grain boundary). (b) A PFM phase signal of the same area (vertical scale 20 °). Arrows mark the same primary ferroelastic domains in (a) and (b). (c) A BSE image of a grain with primary and secondary ferroelastic domains. S2 (GB) indicates a scratch (grain boundary). (d) A PFM phase signal (vertical scale 23 °) from the same grain, with S3 indicating a new scratch. Arrows mark the same secondary ferroelastic domains in (c) and (d).

BSE and out-of-plane PFM images of an individual grain with clear primary and secondary ferroelastic domains are given in Fig. 10 (c) and (d), respectively. The secondary ferroelastic domains are rather fine, with widths between 50 and 150 nm. In the PFM images, these secondary ferroelastic domains also yield contrast, as indicated by several arrows (note the surface was scratched, marked as S3, during handling between BSE and PFM imaging). Thus, both primary and secondary ferroelastic domains have polar surfaces, and can be resolved to a similar spatial extent as that observed in films.

4.6.4.2 Lateral – Vertical PFM contrast variation

Lateral (In-plane) PFM was carried out on some areas along with vertical (Out-of-plane) PFM to establish that the polarization direction was not out-of-plane for all grains. A combination of the lateral and vertical data can give the polarization direction in 3-D [56] [5] [57–59]. Figure 11(a) and 11(b) show a comparison of the phase signals for the VPFM and the LPFM images respectively. The area is the same as that seen in Fig. 10 (a)/(b). Both signals are acquired during the same scan, and hence, all settings and the tip condition is same for both. This makes them easier to compare. The scale bar is 5 microns.

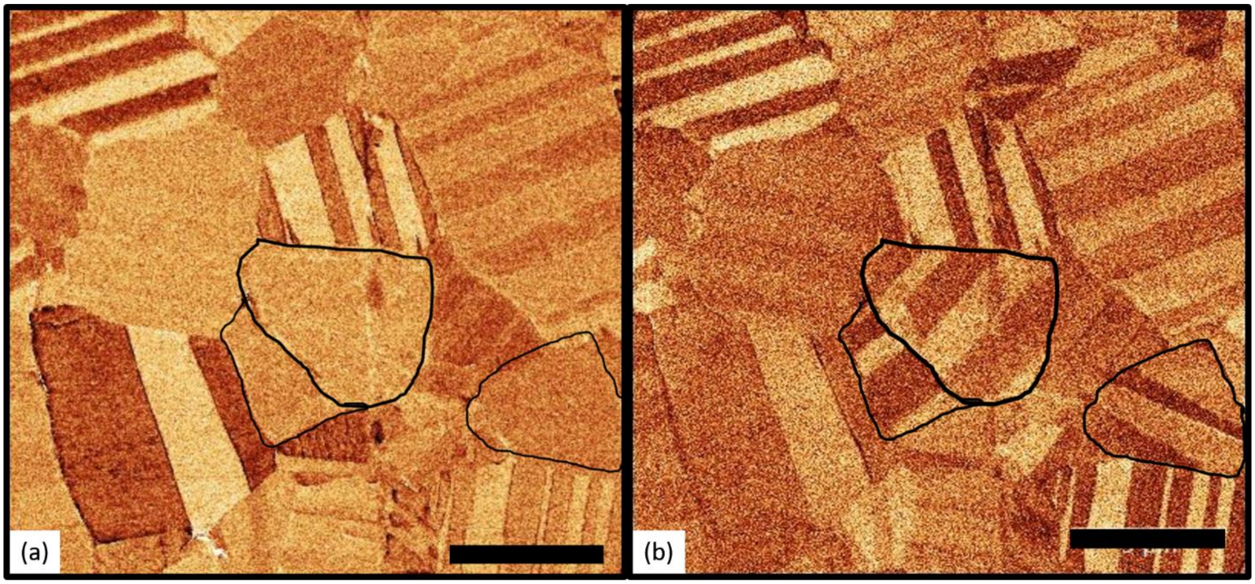

Figure 4-11: (a) Out-of-plane and (b) In-plane PFM phase signals from multiple grains of the γ-WO_3. The scale bar is 5 microns. The vertical scale is

The grains outlined with a black border show clear differences. Contrast is almost non-existent in the vertical signal while it is strong in the lateral signal. Some other grains show the same contrast in both, but differ in the magnitude. Some grains like the one in the top-left corner show similar pattern and magnitude of the contrast.

The slow scan direction (top-bottom or left-right) is not expected to change the signal. This is because any in-plane component of the polarization along the length of the tip results in buckling of the tip. Hence, when scanned in the top-bottom direction, the buckling leads to vertical variations in the laser diode detector, and are not measured in the LPFM signal. The LPFM mode records the deflection perpendicular to the tip length, where the deflections cause the laser spot to move laterally along the diodes. Figure 12(a) and 12(b) show the phase signals when the slow scan direction was from bottom to top and left to right respectively.

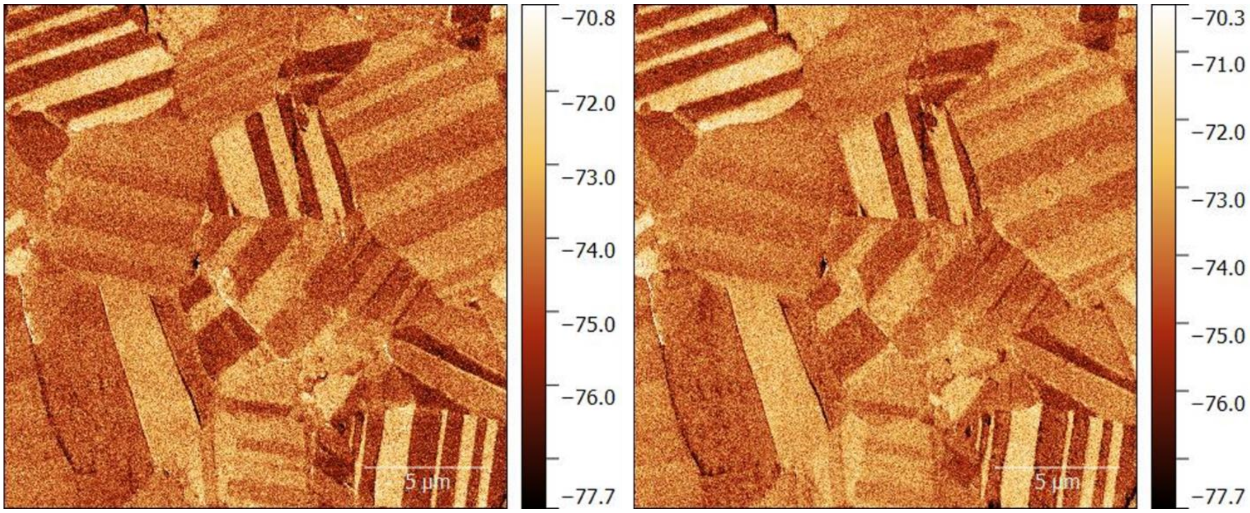

Figure 4-12: Out-of-plane PFM phase signals when the slow scan direction is (a) bottom to top and (b) left to right

Hence, to get the component of the polarization parallel to the length of the tip, the sample must be rotated. The two LPFM signals (before and after rotation by 90°) along with the VPFM signal can give the complete 3-D orientation of the polarization vector. One such set has been shown in Fig. 13 and described below.

Fig. 13(a) is a vertical PFM magnitude signal. Fig 13(b) and 13(c) are the LPFM magnitude signals acquired before and after a 90° rotation of the sample. The direction of scanning is left to right in all three (slow scan direction is bottom to top). Let us consider the largest grain (starting from the top left and extending to the middle) as an example.

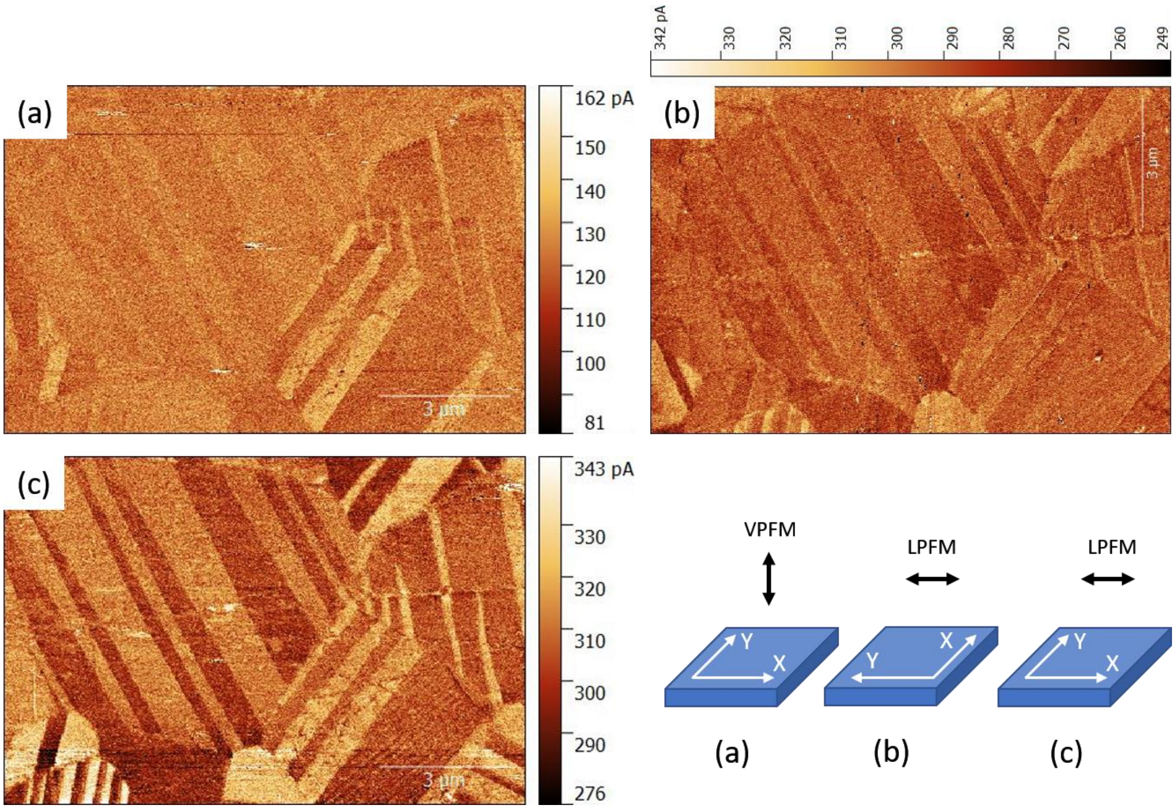

Figure 4-13: (a) Out-of-plane and (b),(c) In-plane Magnitude signals from PFM (after sample rotation by 90°).

The contrast is minimal in the VPFM signal and the absolute magnitude is comparable to the LPFM signals, which implies that most of the polarization is in-plane. The complexity in the interpretation of results arises from multiple factors. Firstly, the signals are acquired in two different runs. One set is comprised of the VPFM and one LPFM signal. The second set is the second LPFM signal. Tip degradation may occur between the two runs. Secondly, because the material is a non-ferroelectric (in the bulk), the phase differences of the signals do not differ in multiples of 90°. Even after optimization of parameters to maximize contrast, the vertical scale did not vary with a range of 180°, as is the case with ferroelectrics [14]. This makes it harder to comment on the direction of polarization. Lastly, the origin of the contrast is unknown. A few datasets were obtained (similar to Fig. 13) but further analysis was not carried out.

4.6.5 Marker reactions on the surface of γ-WO_3

4.6.5.1 Ferroelastic domain specific photoreactivity

The surface of WO_3 was used to photoreduce Ag^+ and photo-oxidize Pb^{2+} and Mn^{2+} ions in separate experiments. Photoreduction of Ag^+ on multiple grains is shown in Figure 14, while that on a single grain is shown in Figures 15 and 16. The reactivity in the images is representative of the overall reactivity on the surface. The topographic contrast from deposited silver particles shows up as bright contrast in both figures. The contrast from Ag particles is overlaid on the weaker crystallographic contrast.

In figure 11, Alternating primary ferroelastic domains in the large central grain are highly reactive. The remaining primary ferroelastic domains in the grain are still somewhat reactive, as can be seen by sparsely spread out white dots within them. Within the highly reactive primary ferroelastic domains, the particles are arranged in streaks running from top left to bottom right. These streaks of silver are representative of photodeposition on secondary ferroelastic domain patterns in grains all throughout the microstructure. Some grains, like the one in the top left, in the microstructure do not show ferroelastic domain selective reactivity.

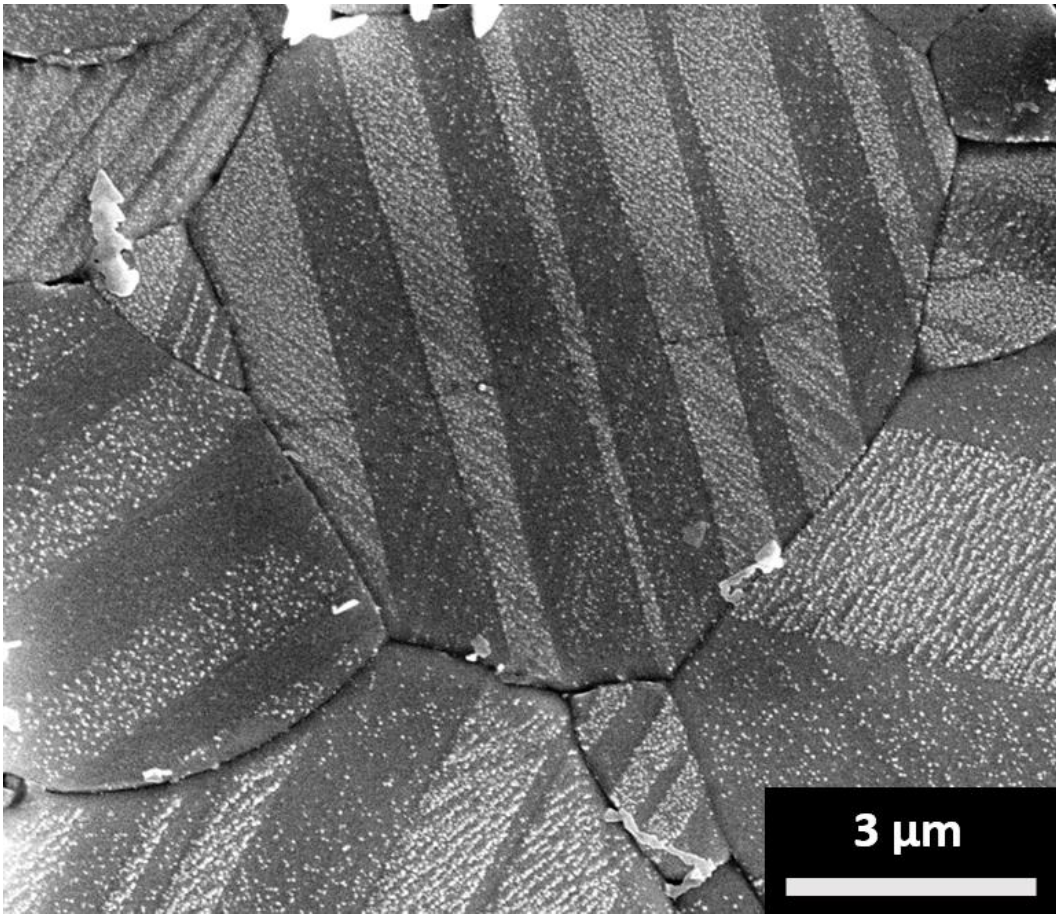

Figure 4-14: Ferroelastic domain specific photoreduction of Ag^+ in multiple grains

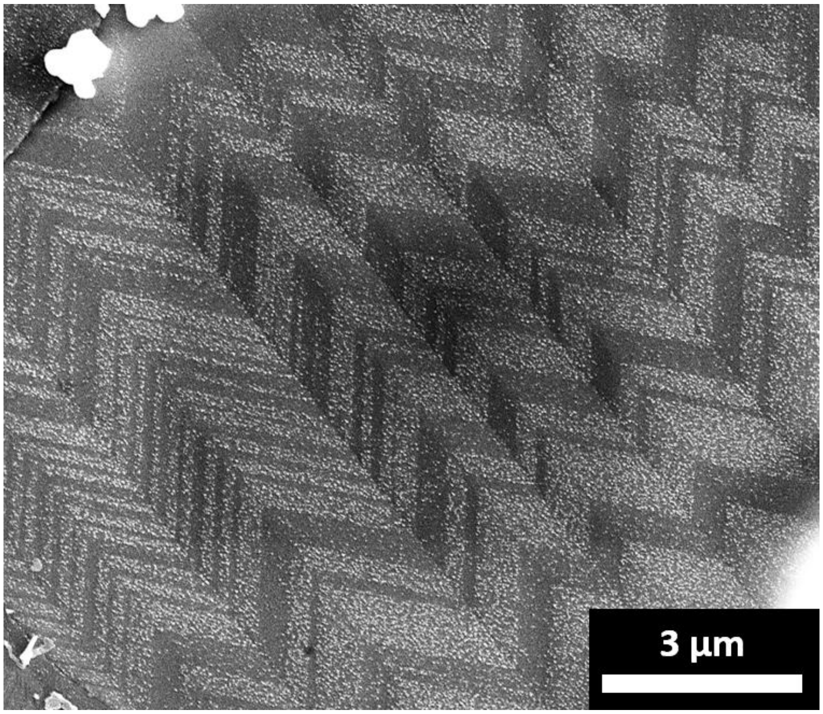

Figure 4-15: Ferroelastic domain specific photoreactivity seen on both sets of primary and secondary ferroelastic domains

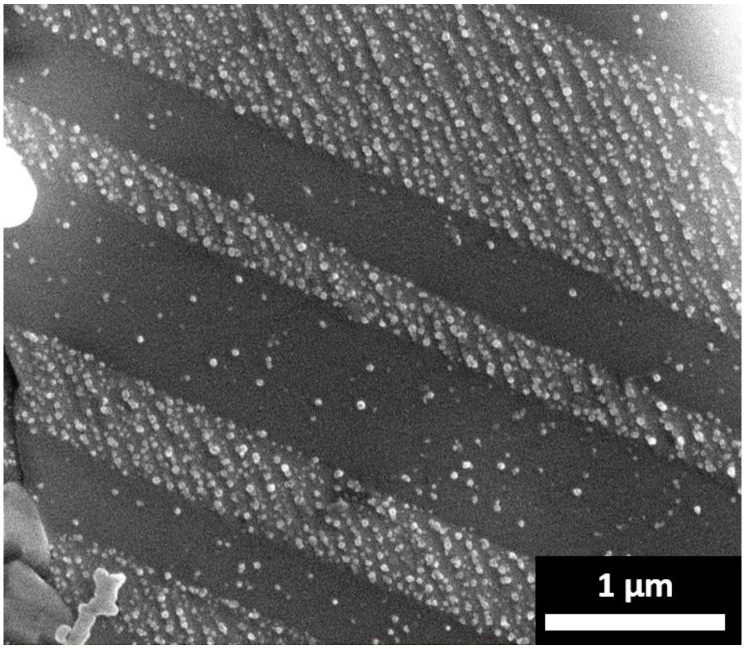

Figure 4-16: Ferroelastic domain specific reactivity on only one set of primary ferroelastic domains

In Fig. 15, clear chevron patterns are observed, with some secondary ferroelastic domains covered densely with Ag particles and others covered sparsely. Such chevron patterns are seen on many grains. Figure 16 shows a close up view of the secondary ferroelastic domain reactivity. Four bright primary ferroelastic domains (that run up and to the left at a shallow angle) are more reactive than the four dark ferroelastic domains. Within the reactive primary ferroelastic domain, the silver particles seem to be ordered into lines (that run up and to the left at a steep angle). These lines traverse the primary ferroelastic domains in a pattern that is similar to the expectation of secondary ferroelastic domains.

Photo-oxidation of Pb^{2+} and Mn^{2+} to insoluble PbO_2 and MnO_2 were also carried out on the WO_3 surfaces. SE images after Mn^{2+} and Pb^{2+} oxidation are shown in Fig. 17 (a) and 17 (b), respectively. The patterns of photodeposited products in Fig. 17 again correlate with the secondary ferroelastic domain patterns as observed in BSE, EBSD, and PFM images. Figure 17 is a representative image of the photo-oxidation over the WO_3 surface. Oxidation reactions are also correlated with the ferroelastic domain structure of WO_3, especially the primary and secondary ferroelastic domains.

4.6.5.2 PFM-reactivity correlation

An out-of-plane PFM phase image is shown in Fig. 18(a) and a secondary electron (SE) image from the same region after photochemical reaction is shown in Fig. 18(b). As described before, strong (weak) PFM contrast is associated with primary (secondary) ferroelastic domains. Both crystallographic and topographic contrast are present in the SE image. The crystallographic contrast between secondary ferroelastic domains is relatively weak, but observable. Grey levels are relatively uniform within secondary ferroelastic domains. The topographic contrast from deposited Ag particles is strong and bright, and is overlaid on the weaker crystallographic contrast. Interestingly, the patterns of deposited Ag correlate with the patterns of PFM contrast. In the central grain, the two bright primary ferroelastic domains (that run up and to the left) are more reactive than the three dark ferroelastic domains. The reactivity within the primary ferroelastic domains also varies spatially and correlates with secondary ferroelastic domains observed clearly in the crystallographic contrast in Fig. 18(b) and faintly in the PFM images in the darker ferroelastic domains in Fig. 18(a) (shown by the white arrows).

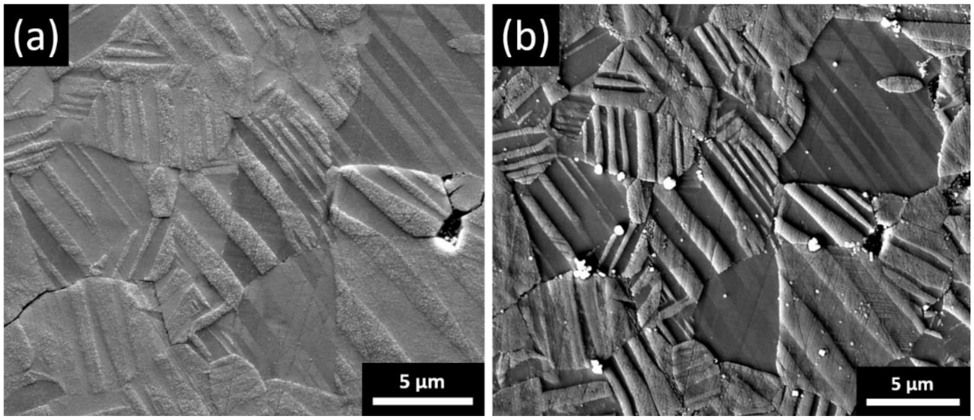

Figure 4-17: SE image of the substrate after photo-oxidation of (a) Mn^{2+} and (b) Pb^{2+}

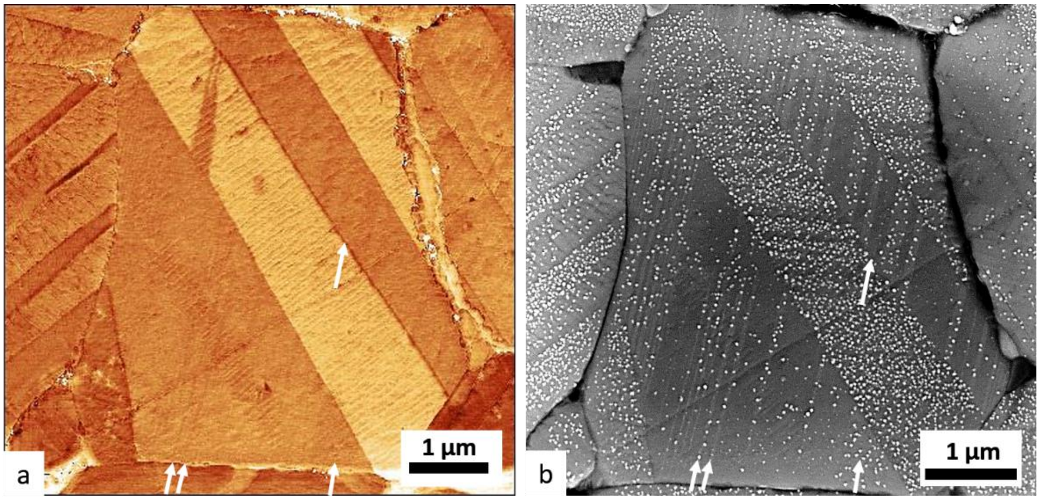

Figure 4-18: (a) PFM phase signal showing primary and secondary ferroelastic domain contrast. The vertical scale is 37°.(b) An SE image of photodeposited Ag. The white arrows point out the same secondary ferroelastic domains in both images.

4.6.5.3 Complementary reactivity

Complementary reactivity was seen on the surface of the polycrystalline WO_3 pellets. Complementarity is a subset of spatial selectivity. It means that amongst the areas which promote a certain kind of reaction (oxidation/reduction), there exist two sets of mutually exclusive areas. One of them promotes only reduction while the other promotes only oxidation. This complementary reactivity is also seen to follow the PFM signal.

An AFM topographic image and an out-of-plane PFM phase image are shown in Figures 19(a) and (b) respectively, with two primary ferroelastic domains running nearly vertical in the image and secondary ferroelastic domains generating chevron patterns around the primary ferroelastic domain boundary. In this region, which has relatively wide secondary ferroelastic domains (likely related to the grain's abnormal growth), the secondary ferroelastic domains exhibit strong contrast in the PFM image. AFM topographic images from the same location after photochemical

Ag^+ reduction and Pb^{2+} oxidation are shown in Figures 19(c) and (d), respectively. The topographic contrast from deposited Ag particles is strong and bright, with ferroelastic domains that have dark (bright) PFM contrast having dense and uniform (no or lower density) coverage of Ag particles.

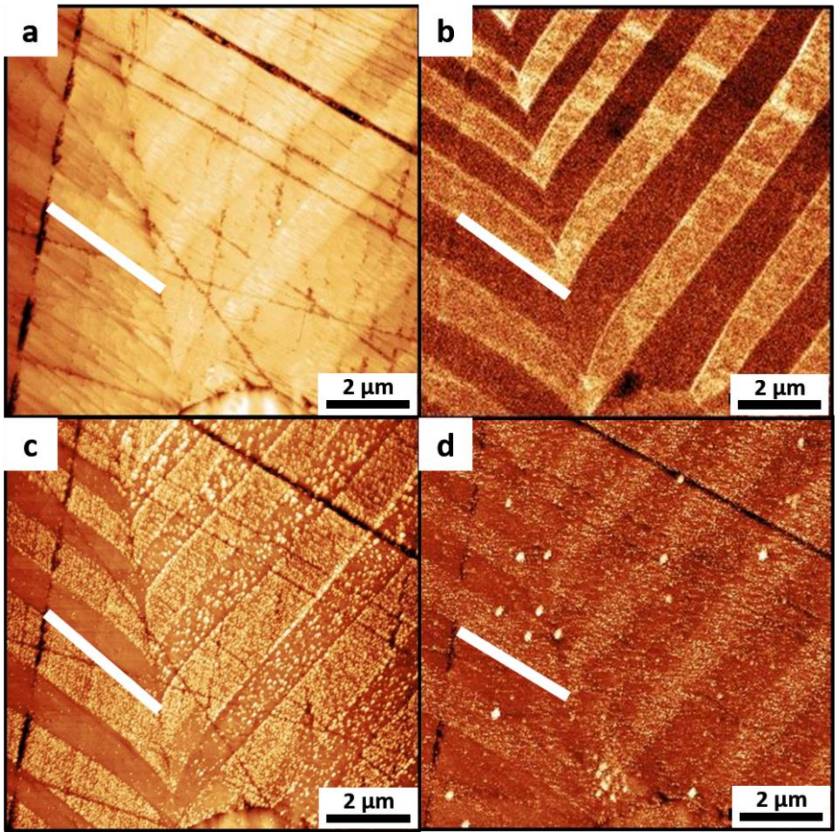

Figure 4-19: a) Topography b) PFM phase response c) Silver photodeposition d) Lead oxide photodeposition. The white lines are meant as a guide to the eye for comparing the images with respect to ferroelastic domains. Lead oxide is seen to deposit more on those ferroelastic domains where silver has deposited on a smaller scale

The topographic contrast from deposited PbO_2 particles is weaker than for the Ag particles, but spatially selective reactivity is clearly observed. Moreover, the reactions are complementary: ferroelastic domains that are more (less) reactive for Ag^+ reduction are less (more) reactive for Pb^{2+} oxidation. This indicates that the surface polarization between these ferroelastic domains is significant enough to influence the near surface band bending to render the surface spatially bifunctional: some ferroelastic domains favor oxidation while others favor reduction. This type of complementary bifunctionality has been shown to be extremely beneficial for increasing the IQE of ferroelectrics, even for modest surface polarization values. [1,2]

4.7 Discussion

The ferroelastic domain selective reactivity of γ-WO_3 is analogous to that of m-$BiVO_4$ [24,60]. For both materials, the orientation, ferroelastic domain structures, PFM response, and overall reactivity vary from grain to grain. Nevertheless, the patterns of photochemical reactivity, surface polarity, and ferroelastic domains are highly correlated. The reactivity of γ-WO_3 is correlated with both primary and secondary ferroelastic domain structures. Some primary ferroelastic domains are uniformly reactive (even when they have secondary ferroelastic domains) and some have reactivity correlated to the local secondary ferroelastic domain patterns. We were unable to resolve reactivity patterns dependent on tertiary ferroelastic domain structures, and the possibility that tertiary ferroelastic domains influence reactivity cannot be ruled out. Compared to m-$BiVO_4$, the complicated hierarchical ferroelastic domain structure of γ-WO_3 adds a significant level of complexity to interpreting the observations.

Because both γ-WO_3 and m-$BiVO_4$ are centrosymmetric and non-polar, the origins of their polar surfaces and their coupling to the ferroelastic domain structure is unclear. In the absence of a structural model, it is impossible to fully interpret the detailed patterns of polarity and surface reactivity observed. Flexoelectric effects were proposed as explanations of surface polarity in m-$BiVO_4$ [24] and γ-WO_3. [40] For γ-WO_3, however, stable polar phases have been reported to exist below room temperature [33] [61], and their stabilization at the surface owing to strain (or strain gradients) cannot be ruled out. These phases are energetically close to the ground state at room temperature, and hence, are within range of a strain-driven phase transformation at the surface. The existence of a ferroelectric phase at the surface would support all the conclusions from this article. Strain and strain gradients exist at surfaces naturally, and vary for a given grain as a function of its orientation and its neighborhood (i.e., the surrounding grains to which it is connected) owing to thermal stresses on cooling and, in ferroelastics, to transformation stresses. That both m-$BiVO_4$ and γ-WO_3 exhibit ferroelastic domain specific surface polarity and spatially selective photochemical reactivity indicate that these effects may be general to oxide ferroelastics.

While the surface polarization magnitude is unknown, it clearly impacts the reactivity of some surfaces. The Ag^+ photoreduction occurs at locations having significant photogenerated electron populations. The counter-reaction (oxidation of water) occurs at locations having significant populations of photogenerated holes. Positive polar ferroelastic domains (i.e., more positive surfaces) attract electrons and repel holes, while negative polar ferroelastic domains (i.e., more negative surfaces) repel electrons and attract holes more than the non-polar baseline surfaces. The baseline reactivity is known to be orientation dependent for non-ferroelectric oxides [62] [63], including m-$BiVO_4$ [19]. Differences in the relative magnitude of photochemical reactivity across grains likely arise from both orientation dependent reactivity and polarization driven modifications in the local reactivity, similar to m-$BiVO_4$. [19] For ferroelectrics, which have strong polar fields at the surface, the orientation dependence (polar dependence) is less (more) pronounced [1,2] [18,64] Importantly, it was shown that the polar ferroelastic surfaces of doped m-$BiVO_4$ were more photochemically active than the non-polar non-ferroelastic surfaces of similarly doped tetragonal $BiVO_4$. [60] Similar experiments are needed to demonstrate whether polar surfaces are more reactive than non-polar ones for γ -WO_3.

4.8 Conclusions

Coming back to the listed hypotheses, some of them have been disproved and some are supported by our results. Hypothesis 1 is supported by our results, although the reason for polarization is unknown. Hypothesis 1.1 is disproved as frequency-dependent PFM response was observed for the ferroelastic domains. Hypothesis 2 is supported, and the polarization from the second tier is enough to perturb photoreactivity on the primary ferroelastic domains. However, the PFM response from the secondary ferroelastic domains is milder than that from the primary ferroelastic domains. It indicates that even small polarizations are enough to cause spatially selective reactivity. Hypothesis 3.1 and 3.2 were disproved and Hypothesis 3 was supported, with both primary and secondary ferroelastic domains giving alternating responses. The tertiary ferroelastic domains were too fine to be resolved for both, reactivity and PFM response.

To summarize, the ferroelastic domain structure at the surface of polished γ-WO_3 ceramics is hierarchical, having three levels of ferroelastic domains. For all orientations, the coarser two levels of ferroelastic domains (primary and secondary) are piezo-responsive (i.e., polar). The amount of silver photochemically reduced by visible-light is correlated to the same two levels of ferroelastic domains that are piezoresponsive in PFM. These observations are similar to those reported for *m*-$BiVO_4$, and indicate that ferroelastics may be a general class of photocatalysts for which polar surfaces improve efficiencies.

4.9 References

[1] James J. Glickstein, Paul A. Salvador, and Gregory S. Rohrer: *J. Phys. Chem. C*, 2016, vol. 120, pp. 12673–84.

[2] James J. Glickstein, Paul A. Salvador, and Gregory S. Rohrer: *J. Mater. Chem. A*, 2016, vol. 4, pp. 16085–93.

[3] Steve Dunn: *Mater. Today*, 2011, vol. 14, p. 302.

[4] Divya Tiwari and Steve Dunn: *J. Mater. Sci.*, 2009, vol. 44, pp. 5063–79.

[5] Yasunobu Inoue, K Sato, and H Miyama: *J. Phys.*, 1986, vol. 90, pp. 2809–10.

[6] Yasunobu Inoue, Kazunori Sato, and Shinichi Suzuki: *J. Phys. Chem.*, 1985, vol. 03, pp. 2827–31.

[7] Yasunobu Inoue, Masayoshi Okamura, and Kazunori Sato: *J. Phys. Chem.*, 1985, vol. 89, pp. 5184–87.

[8] Jennifer L Giocondi, Shahrzad Samadzadeh, and Gregory S Rohrer: *MRS Proc.*, 2002, vol. 755.

[9] Jennifer L. Giocondi and Gregory S. Rohrer: *MRS Proc.*, 2000, vol. 654, pp. 1–10.

[10] Jennifer L Giocondi and Gregory S Rohrer: *Mat. Res. Soc. Symp. Proc.*, 2003, vol. 751, pp. 2–7.

[11] Nina V. Burbure, Paul A. Salvador, and Gregory S. Rohrer: *Chem. Mater.*, 2010, vol. 22, pp. 5823–30.

[12] Li Li, Xuan Liu, Yiling Zhang, Noel T. Nuhfer, Katayun Barmak, Paul A. Salvador, and Gregory S. Rohrer: *ACS Appl. Mater. Interfaces*, 2013, vol. 5, pp. 5064–71.

[13] Li Li, Yiling Zhang, Andrew M. Schultz, Xuan Liu, Paul a. Salvador, and Gregory S. Rohrer: *Catal. Sci. Technol.*, 2012, vol. 2, p. 1945.

[14] Andrew M. Schultz, Yiling Zhang, Paul A. Salvador, and Gregory S. Rohrer: *ACS Appl. Mater. Interfaces*, 2011, vol. 3, pp. 1562–67.

[15] Li Li, Xuan Liu, Yiling Zhang, Paul A. Salvador, and Gregory S. Rohrer: *Int. J. Hydrogen Energy*, 2013, vol. 38, pp. 6948–59.

[16] Yiling Zhang, Andrew M. Schultz, Paul a. Salvador, and Gregory S. Rohrer: *J. Mater. Chem.*, 2011, vol. 21, p. 4168.

[17] Yiling Zhang, Andrew M. Schultz, Li Li, Harry Chien, Paul A. Salvador, and Gregory S. Rohrer: *Acta Mater.*, 2012, vol. 60, pp. 6486–93.

[18] Jennifer L Giocondi and Gregory S Rohrer: *J. Phys. Chem. B*, 2001, vol. 105, pp. 8275–77.

[19] Ratiporn Munprom, Paul A. Salvador, and Gregory S. Rohrer: *J. Mater. Chem. A*, 2015,

vol. 3, pp. 2370–77.

[20] Jennifer L. Giocondi, Paul A. Salvador, and Gregory S. Rohrer: *Top. Catal.*, 2007, vol. 44, pp. 529–33.

[21] Linchao Mu, Yue Zhao, Ailong Li, Shengyang Wang, Zhiliang Wang, Jingxiu Yang, Yi Wang, Taifeng Liu, Ruotian Chen, Jian Zhu, Fengtao Fan, Rengui Li, and Can Li: *Energy Environ. Sci.*, 2016, vol. 9, pp. 2463–69.

[22] Guoqiang Li, Zhiguo Yi, Ying Bai, Weifeng Zhang, and Haitao Zhang: *Dalt. Trans.*, 2012, vol. 41, pp. 10194–98.

[23] Nina V. Burbure, Paul A. Salvador, and Gregory S. Rohrer: *J. Am. Ceram. Soc.*, 2006, vol. 89, pp. 2943–45.

[24] Ratiporn Munprom, Paul A. Salvador, and Gregory S. Rohrer: *Chem. Mater.*, 2014, vol. 26, pp. 2774–76.

[25] J.D. Bierlein and A.W. Sleight: *Solid State Commun.*, 1975, vol. 16, pp. 69–70.

[26] Pierre Toledano and Mael Guennou: *Phys. Rev. B - Condens. Matter Mater. Phys.*, 2016, vol. 94, pp. 1–7.

[27] Z Zhao, X Ding, J Sun, and E K H Salje: *J. Phys. Condens. Matter*, 2014, vol. 26, p. 142201.

[28] Ra Dixon, Jj Williams, D Morris, J Rebane, Fh Jones, Rg Egdell, and Sw Downes: *Surf. Sci.*, 1998, vol. 399, pp. 199–211.

[29] E Salje and K Viswanathan: *Acta Crystallogr. Sect. A*, 1975, vol. 31, pp. 356–59.

[30] Hanen Hamdi, Philippe Ghosez, and Eric Bousquet: 2016, vol. 34, p. 4000.

[31] J. A. Perri, E. Banks, and B. Post: *J. Appl. Phys.*, 1957, vol. 28, pp. 1272–75.

[32] Tom Vogt, Patrick M Woodward, and Brett A Hunter: *J. Solid State Chem.*, 1999, vol. 144, pp. 209–15.

[33] P M Woodward, A W Sleight, and T Vogt: *J. Solid State Chem.*, 1997, vol. 131, pp. 9–17.

[34] Aird, A. and Salje, E. K.H.: *Eur. Phys. J. B*, 2000, vol. 15, pp. 205–10.

[35] R Ueda and T Ichinokawa: *Phys. Rev.*, 1950, vol. 80, p. 1106.

[36] Sigetosi Tanisaki: *J. Phys. Soc. Japan*, 1958, vol. 13, pp. 363–66.

[37] S Sawada and G C Danielson: *Phys. Rev.* , 1959, vol. 113, pp. 1005–8.

[38] R.G. Rhodes: 1952, p. 369.

[39] Fumio Uchikoba and Kentaro Sawamura: *J. Am. Ceram. Soc.*, 1994, vol. 77, pp. 1345–51.

[40] Shinhee Yun, Chang-su Woo, Gi-yeop Kim, Pankaj Sharma, Jin Hong Lee, Kanghyun Chu, Jong Hyun Song, Sung-yoon Chung, Jan Seidel, Si-young Choi, and Chan-ho Yang: 2015, vol. 252904, pp. 1–6.

[41] SinIchi Hamazaki, Naoko Tashiro, Fuminao Shimizu, and Masaaki Takashige: *J. Phys. Soc. Japan*, 1998, vol. 67, pp. 2144–45.

[42] Sin-Ichi Hamazaki, Naoko Tashiro, Fuminao Shimizu, Shozo Sawada, and Masaaki Takashige: *Ferroelectrics*, 1999, vol. 231, pp. 43–47.

[43] Yunseok Kim, Marin Alexe, and Ekhard K H Salje: *Appl. Phys. Lett.*, 2010, vol. 96, pp. 1–4.

[44] Gratian R Bamwenda and Hironori Arakawa: *Appl. Catal. A Gen.*, 2001, vol. 210, pp. 181–91.

[45] Rui Liu, Yongjing Lin, Lien Yang Chou, Stafford W. Sheehan, Wangshu He, Fan Zhang, Harvey J M Hou, and Dunwei Wang: *Angew. Chemie - Int. Ed.*, 2011, vol. 50, pp. 499–502.

[46] Imre M. Szilágyi, Balázs Fórizs, Olivier Rosseler, Ágnes Szegedi, Péter Németh, Péter Király, Gábor Tárkányi, Balázs Vajna, Katalin Varga-Josepovits, Krisztina László, Attila L. Tóth, Péter Baranyai, and Markku Leskelä: *J. Catal.*, 2012, vol. 294, pp. 119–27.

[47] Wilson Erbs, Jean Desilvestro, Enrico Borgarello, and Michael Graetzel: *J. Phys. Chem.*, 1984, vol. 88, pp. 4001–6.

[48] Kazuhiko Maeda and Kazunari Domen: *J. Phys. Chem. Lett.*, 2010, vol. 1, pp. 2655–61.

[49] K. M Rabe, Ch. H. Ahn, J. M -M. Triscone, M Dawber, and C Lichtensteiger: *Physics of Ferroelectrics*, 2007.

[50] Ryuzo Ueda and Jinzo Kobayashi: *Phys. Rev.*, 1953, vol. 91, p. 1565.

[51] Crystalmaker Software limited: n.d.

[52] B O Loopstra and H M Rietveld: *Acta Cryst. B*, 1969, vol. 25, pp. 1420–21.

[53] Scott A Speakman: n.d.

[54] Caroline A Schneider, Wayne S Rasband, and Kevin W Eliceiri: *Nat. Methods*, 2012, vol. 9, pp. 671–75.

[55] J Sapriel: *Phys. Rev. B*, 1975, vol. 12, pp. 5128–40.

[56] Yuanyuan Jing, John E. Blendell, and Keith J. Bowman: *J. Appl. Phys.*, 2011, vol. 109.

[57] Sergei V. Kalinin, Brian J. Rodriguez, Stephen Jesse, Junsoo Shin, Arthur P. Baddorf, Pradyumna Gupta, Himanshu Jain, David B. Williams, and Alexei Gruverman: *Microsc. Microanal.*, 2006, vol. 12, pp. 206–20.

[58] A. Roelofs, U. Böttger, R. Waser, F. Schlaphof, S. Trogisch, and L. M. Eng: *Appl. Phys. Lett.*, 2000, vol. 77, pp. 3444–46.

[59] L. M. Eng, H.-J. Güntherodt, G. A. Schneider, U. Köpke, and J. Muñoz Saldaña: *Appl. Phys. Lett.*, 1999, vol. 74, p. 233.

[60] Ratiporn Munprom, Paul A. Salvador, and Gregory S. Rohrer: *J. Mater. Chem. A*, 2016, vol. 4, pp. 2951–59.

[61] Ekhard K H Salje, Stephan Rehmann, Frank Pobell, Darryl Morris, Kevin S Knight, Thomas Herrmannsd, and Martin T Dove: *J. Phys. Condens. Matter*, 1997, vol. 9, pp. 6563–77.

[62] Yisi Zhu, Paul A Salvador, and P Chris Pistorius: n.d.

[63] J L Giocondi and G S Rohrer: *J. Am. Ceram. Soc.*, 2003, vol. 86, pp. 1182–89.

[64] J. L. Giocondi and G. S. Rohrer: *Chem. Mater.*, 2001, vol. 13, pp. 241–42.

5 Experimental insights on the origin of spatial selectivity of photodeposition in $BiVO_4$

5.1 Introduction

Photocatalysis is the process of increasing the reaction rate by using light. Photocatalysts can be used in air [1,2] [3] and water purification [3] as well as to produce energy in the form of hydrogen by water-splitting [4]. In particular, solar photocatalysis has tremendous potential because the amount of sunlight incident on the Earth's surface in around 90 minutes is more than we as a human race used in the entire year of 2016 [5] [6]. In this context, $BiVO_4$ has emerged as an excellent candidate material for hydrogen production by photoelectrochemical water splitting. It is made of inexpensive elements [7], is visible light active (with a bandgap of around 2.4 eV) [8], has low charge carrier masses as compared to commonly used photocatalysts like TiO_2 [7], has an optimal valence band position for water splitting [7], and can be synthesized using various low-cost techniques [8] [9]. The disadvantage of $BiVO_4$ is that it suffers from bulk [10] and surface recombination [11] of photogenerated charge carriers, leading to an overall low photocatalytic efficiency. However, it may be possible to engineer $BiVO_4$ to reduce such recombination as spatial selectivity of photoreactions has been demonstrated on it [12,13]. Spatial selectivity means that oxidation and reduction reactions take place on different regions of the surface. This happens when electrons and holes are driven to different regions on the surface due to differences in electrochemical potential, reducing recombination probability. Such differences arise due to crystal orientation [14] [15] [16], surface chemical terminations [17–19], and ferroelectric domains [20–22]. Spatial selectivity has also been demonstrated on another ferroelastic - WO_3. [23] However, the origin of differences in electrochemical potential in centrosymmetric and non-polar ferroelastic materials such as $BiVO_4$ and WO_3 leading to spatial selectivity is unknown. Hence, it is necessary to understand the origin of spatial selectivity in these compounds to enable their engineering, and increase their efficiency in photocatalytic processes.

In $BiVO_4$, the ferroelastic domains were found to be piezoresponsive, and photodeposition resulted in products following the ferroelastic domain patterns [12,13]. In the three-tiered ferroelastic domain structure of WO_3, two tiers of ferroelastic domains were found to be piezoresponsive and reactivity followed these same two tiers. [23] Thus, the spatial selectivity closely associated with the presence of ferroelastic domains in these two materials. There have been some theories proposed to explain the polarization of ferroelastic domains in these compounds in literature. Munprom et. al. [12] reported two possible mechanisms coupled to the ferroelastic domain structure in $BiVO_4$. They hypothesized that strain gradients coupled to the ferroelastic domain structure are possible due to (a) differential relaxation of surface cations (depending on their proximity to the free surface), with the direction of relaxation alternating between ferroelastic domains and (b) inhomogeneous relaxation of residual strain (after an initial reduction by ferroelastic domain formation) on the free surface. These strain gradients can then lead to alternating positive and negative polarization at the surface due to flexoelectricity. This is consistent with reduction and oxidation reactions occurring on alternate ferroelastic domains as shown by them in a subsequent report. [13] Another possible explanation for polar ferroelastic domains in centrosymmetric ferroelastics is the presence of a ferroelectric surface phase. This was proposed by us in the case of WO_3 [23], where a ferroelectric phase exists below room temperature. It is possible that the ferroelectric phase was stabilized at room temperature due to surface stresses. The presence of such a phase is consistent with the piezoresponsive ferroelastic domain structures promoting oxidation and reduction reactions on alternate ferroelastic domains over two tiers, as was observed. [23] All three theories for presence of polar ferroelastic domains in non-polar materials stem from stress/strain coupled to the ferroelastic domain structure, and have been elaborated on in a short review published previously. [24] However, more experiments are needed to ascertain which of such stress-strain-domain couplings is causes spatial selectivity, or if any other factor also contributes to it. This chapter aims to fill this gap partially by investigating spatial selectivity on $BiVO_4$ samples under different states of stress/strain. The background gives the previous work and hypotheses put forth to explain this phenomenon in $BiVO_4$. It also sets a base of assumptions made for the experimental work. This is followed by the Aim and motivation, a hypothesis section, Experimental details, results, discussion, and a conclusion.

5.2 Background

5.2.1 Previous work

Munprom et. al. [13] showed that the presence of ferroelastic domains increases the photochemical reactivity of $BiVO_4$. Hence, it would be worthwhile to determine the mechanism behind polar ferroelastic domains in this material, to enable its engineering. They also mentioned two possibilities about how flexoelectricity can lead to polar ferroelastic domains, causing differential reactivity [12]. Figure 5-1 shows the proposed strain gradient driven polarizations at the surface. Figure 5-1(a) and (b) show the downward and upward relaxations of cations in the $BiVO_4$ unit cell. The cations closest to the surface relax more as compared to the bulk, which leads

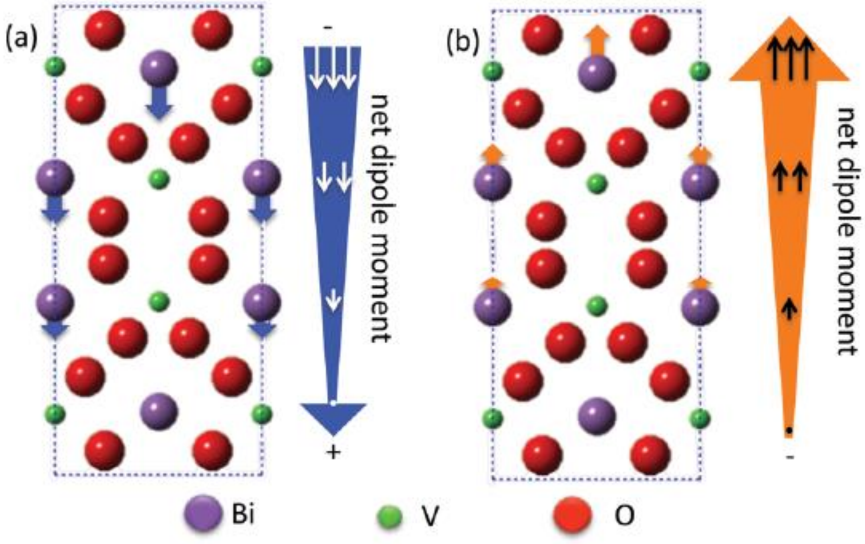

Figure 5-1: Schematic of surface relaxations of Bi cations in a $BiVO_4$ unit cell creating (a) downward and (b) upward dipole moments. The cations closer to the surface relax more, leading to the center of positive charge moving away from the center of the cell. Figure taken from Munprom et. al.[12]

to a net shift of negative charge from the center of the cell. This creates a dipole moment, as shown by the blue and yellow arrows adjacent to the unit cell. Munprom et. al. [12] proposed that such strain gradients are possible due to two reasons: a) The broken bonds at the surface lead to a different surface structure from the bulk, and ions closest to the surface relax more. This differential relaxation leads to a breakage in symmetry as shown in Figure 5-1. b) The cell dimensions change on phase transformation, and because they are constrained, any remnant stress after a partial relaxation by ferroelastic domain formation is relaxed at the free surface. These relaxations give rise to strain gradients, that can lead to polarization. These two possibilities are elaborated upon in the next section of the background. They also proposed a possible reason being accumulation of point defects [12]. However, there were no systematic experiments done to support/eliminate any of these hypotheses. In this chapter, we have based our experiments to draw conclusions regarding these hypotheses as well as another that was previously not discussed.

5.2.2 Ferroelastic domain structure in $BiVO_4$

To understand how stresses can lead to strain gradients and flexoelectric polarization, let us first look at how the ferroelastic domain structure and unit cells after undergoing a ferroelastic transition.

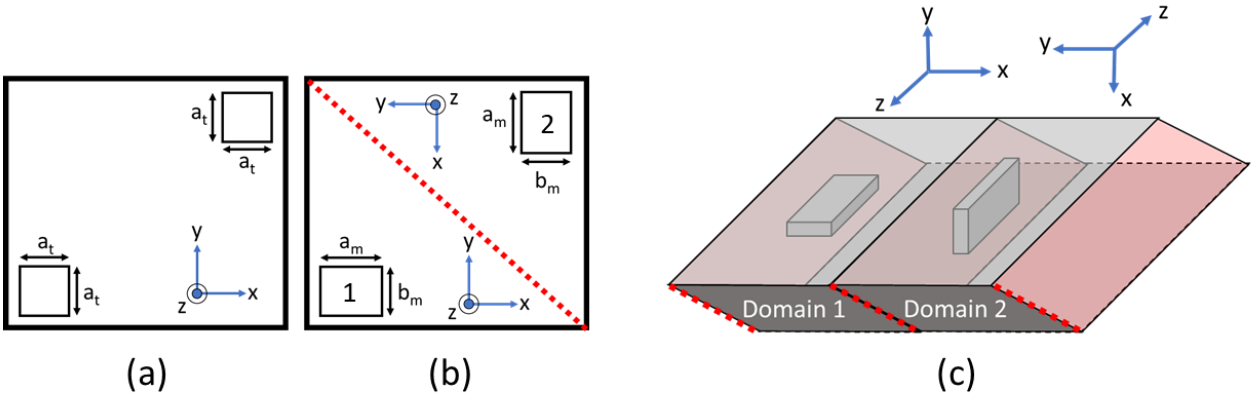

Figure 5-2: Lattice parameters of $BiVO_4$ (a) before and (b) after undergoing ferroelastic phase transition. Dotted red line - domain wall. (c) A pair of ferroelastic domains shown in 3D along with their corresponding unit cells (grey parallelepipeds).

Error! Reference source not found.(a) shows the front view of a tetragonal region of $BiVO_4$ before transition. Looking down the c-axis, we see that the lattice parameters are $a=b=a_t$ and c. After transition, the same view is shown in Figure 5-2(b). Due to the transition, a goes from a_t to a_m ($a_t<a_m$) and b goes from a_t to b_m ($a_t>b_m$) [25]. The subscript 't' denotes the parent tetragonal phase and the subscript 'm' denotes the ferroelastic monoclinic phase. The c-parameter decreases from c_t = 11.730 to c_m = 11.704 Angstroms. The small angular deviation (γ goes from 90° to 89.62°) [25] has been ignored in the figure. The dotted red line denotes the ferroelastic domain boundary. The two ferroelastic domain states are rotated by 90 degrees across the ferroelastic domain boundary, and are denoted by '1' and '2'. For ease of explanation, a W-wall (where the miller indices are determined only by symmetry) [26] is chosen. In $BiVO_4$, it runs at an angle of 44° to the [100] axis [27]. Thus, the two W-walls are the (110) and (1 -1 0) planes. A 3D view of two ferroelastic domains has been shown in Figure 5-2(c). The coordinate systems of the ferroelastic domains are shown adjacent to them in blue. Unit cells in the ferroelastic domains are shown as grey parallelepipeds. The ferroelastic domain boundary planes are shown in red.

5.2.3 Classification of stress/strain that can lead to polarization via flexoelectricity

To study the effect of stress/strain on spatial selectivity in a systematic manner, we have divided the overall stress acting on a surface grain in the polycrystal into two parts: (a) Stress from neighboring surface grains (abbreviated as S) (b) Internal stress after ferroelastic transition due to change in the crystal system (abbreviated as B).

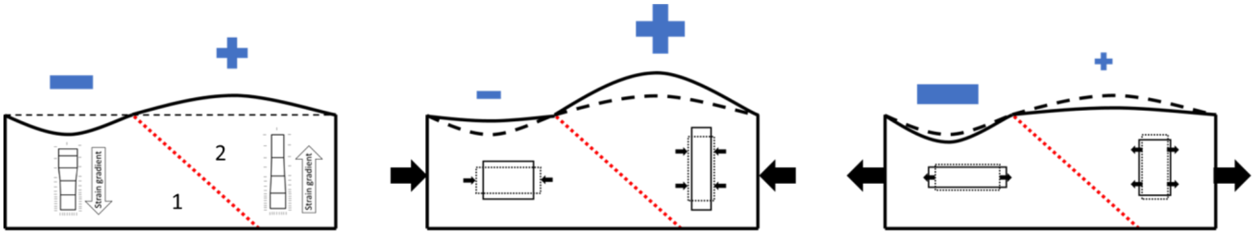

(a) Bulk stress (b) Stress from surrounding - Compressive (c) Stress from surrounding - Tensile

Figure 5-3: (a) Evolution of polar ferroelastic domains due to strain gradients from bulk stresses. Modification of the ferroelastic domain polarizations due to (b) compressive and (c) tensile stresses from neighboring grains

The first potential mechanism by which flexoelectric polarization can be induced is via strain gradients arising from bulk stresses. This is depicted in Figure 5-3(a). The types are ferroelastic domains are marked by ‘1’ and ‘2’, having the same unit cells as Figure 5-2. The unit cell of ferroelastic domain one (two) stretches along the horizontal (vertical) direction and shrinks in the vertical (horizontal) direction. In both ferroelastic domains, the cells towards the bulk are highly constrained and cannot stretch and shrink to come to their equilibrium shape. This is shown by the highly concentrated dashes surrounding these cells in both ferroelastic domains. As we approach the free boundary at the surface, the cells are not as constrained, and can attain their equilibrium shapes. This can lead to strain gradients as shown in Figure 5-3, giving rise to flexoelectric polarization.

The second potential mechanism is due to the polycrystalline nature of the sample, wherein the neighboring grains can create stresses. As shown in Figure 5-3(b) and (c), the added stress from the surrounding grains can lead to changes in the strain in the ferroelastic domains. For example, in Figure 5-3 (b), due to the added compressive stress, the unit cell in ferroelastic domain 1 is not able to stretch as much as it would under normal circumstances. This would lead to a smaller strain, and in turn, a smaller strain gradient from the bulk to the surface. Hence, the polarization would diminish in magnitude, as symbolized by the smaller '-' sign above ferroelastic domain 1 as compared to that in Figure 5-3(a). On the contrary, the added compression enhances the vertical stretching of the cells in ferroelastic domain 2, increasing the strain gradient and polarization. This is shown by the larger '+' sign above ferroelastic domain 2 in Figure 5-3(b) as compared to Figure 5-3(a). Figure 5-3(c) can be explained similarly, with the added tensile stress increasing (decreasing) the polarization in ferroelastic domain 1 (2). The added stresses are in the in-plane horizontal directions in Figure 5-3(b) and (c). A similar explanation can be given for added stresses in the out-of-plane direction. There cannot be any added stresses from the free surface in the in-plane, vertical direction. Clamping due to the neighboring grains can also play a role. Such stresses will similarly prevent the unit cell from expansion near the interface, possibly creating strain gradients identical to the ones described in Figure 5-3(a). The exact role of clamping and shear stresses is not known, but the central idea here is that surrounding grains create added stresses that can create strain gradients and polarization. We carry out three experiments that test these by successively relaxing the conditions.

5.3 Aim and Motivation

Aim: To experimentally determine which possible strain states can lead to ferroelastic domain polarization and whether flexoelectricity is a cause for it in the first place.

5.3.1 Why is it necessary to pinpoint the phenomenon that creates polar ferroelastic domains in $BiVO_4$?

Without knowing the exact mechanism that drives these centrosymmetric compounds to show polar ferroelastic domains, it is not possible to engineer them and get the best possible charge-separating benefits. Because polar ferroelastic domains are known to shuttle charge carriers laterally due to alternating fields [28], they are important not only in photocatalysts but also in other light-activated technologies such as solar cells. Thus, by knowing the mechanism that causes the ferroelastic domains to turn polar, materials engineers would be able to choose from not just ferroelectrics, but also a much larger pool of ferroelastics to increase efficiency via charge separation.

5.4 Hypotheses

A short overview of the experiments is given here to help correlate the background with the hypothesis and implications.

5.4.1 Overview of experiments

The first set of experiments partially relaxes the stresses from surrounding grains (S), by isolating the region of interest. Two regions, one consisting of a single grain and the other made of several grains, were chosen on a pellet synthesized by solid-state sintering. The multi-grain region was chosen to check for any orientational effects. These were isolated from its neighboring grains by laser-milling a trench around them. Hence, the central region does not interact with its surface neighbors. However, the pillars are still supported by the underlying grain(s). Thus, there is still some possibility of clamping stresses affecting ferroelastic domain polarization. Also, the depth of the trench needs to be larger than the grain size to be able to remove all but underlying grain interaction. Thus, trenching only partially relaxes the stresses from surrounding grains. The second experiment eliminates the stresses from surrounding grains completely. This is done by investigating spatial selectivity on hydrothermally grown crystals, that are almost free from any external stress. Thus, the only possible strains that can couple to the ferroelastic domain structure in this case are the bulk stresses (B). The third experiment eliminates the ferroelastic domain structure. This ensures that there are no bulk stresses and no possible coupling from added surrounding stresses. The ferroelastic domains are 'dissolved' during photodeposition by carrying out the reaction above the FTT. A Na, Mo co-doped sample of $BiVO_4$ was prepared by solid state sintering. The co-doping concentration in $(Bi_{1-0.5x}Na_{0.5x}V_{1-x}Mo_x)O_4$ was approximated using the work of Zhou et. al. [29] to bring down the FTT to below 100 °C from 255 °C. This enabled the photodeposition above the transition whilst ensuring the water-based solutions of ions do not boil.

5.4.2 Hypothesis

The general hypothesis is as follows:

Hypothesis 1

Constraints on the crystal lattice (bulk stress) and added stresses from surrounding grains in the ferroelastic phase can lead to creation of strain gradients, resulting in polar ferroelastic domains due to the flexoelectric effect.

5.5 Experimental Setup

5.5.1 Trenching around an area to eliminate interaction from neighboring grains

Samples were synthesized using Bi_2O_3 (99.999% pure – Strem Chemicals) and V_2O_5 (99.2 % pure – Johnson Matthey). The powders were mixed in a stoichiometric ratio of 1:1 and wet-ground (in ethanol) using a mortar and pestle for 10 minutes. After the ethanol evaporated, the mixture was heated in an alumina crucible at 600 °C for 3 hours. This cycle of grinding and heat treatment was repeated two more times to obtain the final powder. Pellets were then formed by adding 2-3 drops of PVA solution (made by dissolving 5 g PVA in 100 ml water) to every 2 grams of $BiVO_4$. They were pressed using a ½ inch die with a tabletop hydraulic press (Carver). They were then sintered in alumina crucibles at 600 °C for 2 hours followed by 800 °C for 20 hours. The ramp up rate (till 800 °C) was 10 °C/min while the ramp down rate (to room temperature) was 5 °C/min. The samples were then hand polished with minimal downward pressure using 1200 grit size SiC, 3 µm diamond, 1 µm, 0.05 µm diamond and 0.02 µm colloidal silica in succession. The samples were sonicated between each successive step. MD/DP-Mol cloths (Struers) were used for the 3 µm and 1 µm diamond while MD/DP-Nap cloths (Struers) for 0.05 µm diamond and 0.02 µm colloidal silica. The samples were later annealed at 400 °C for 3 hours to heal polishing damage before carrying out pre-trenching photodeposition reactions.

Two areas were selected for this study. The first region consisted of a single grain, so that a single crystal pillar would remain after milling. The second region consisted of multiple grains. To dig the trenches around selected areas, laser-milling was carried out using (QuikLaze 50ST2, ESI, Portland). The milling was done using the following parameters: 2 µm/s at 15 % power on a low setting (20 passes) - multigrain area and 5 µm/s at 30 % power on low setting (15 passes). The samples were polished again using 0.05 µm diamond afterwards to remove the milled material accumulated around the trench, and the sample was heated again for 3 hours at 400 °C in an alumina crucible. For photodeposition, the sample was fixed on a glass slide using double-sided tape. An O-ring was placed around it. Then, $AgNO_3$ solution (0.0115M) was filled in the cavity using a dropper. A quartz slip was used to cover the system. The setup was then exposed to visible light for 8.5-9.5 minutes at 150 W power. After reaction, the sample was dunked into deionized water for 5-6 times before being dried using compressed air.

5.5.2 Hydrothermally-grown crystals

Crystals of $BiVO_4$ were synthesized by the hydrothermal process by using parameters similar to those used by Li et. al. [14] 36 mmol of both NH_4VO_3 and $Bi(NO_3)_3.5H_2O$ were mixed in 300 ml of 2 M nitric acid solution. The pH was adjusted to 2 under stirring by adding ammonia solution slowly. The solution was aged for two hours. The precipitate was transferred to a 100 ml Teflon lined autoclave. The filling ratio was 1:1 (50% filled autoclave). The autoclave was then heated in a furnace to 200 °C (ramp up rate: 3 °C/min), held for 20 hours, and cooled at rate of 5 °C/min. The autoclave finally came to room temperature only once it was taken out of the furnace and kept for an hour. The powder was filtered using Whatman paper and deionized water. For photodeposition, sample preparation was done as follows: carbon tape was fixed on an AFM stub. A very small quantity of crystals was placed near the bottom of the tape and compressed air was lightly used to blow the powder on to the upper region of the tape. On spread, stronger blasts of compressed air were used to completely affix the crystals. An O-ring with a diameter smaller than the AFM stub was then placed onto it, encompassing the powder particles in the center. The cavity was filled with 0.015M $AgNO_3$ solution and was closed by using a quartz slip. The setup was then irradiated with visible light (150 W) for 10 minutes from a Newport Oriel research arc lamp. After reaction, the sample was dunked into deionized water for 5-6 times before being dried using compressed air.

5.5.3 Photodeposition above ferroelastic transition temperature

Na,Mo co-doped samples were synthesized using Bi_2O_3 (99.999% pure – Strem Chemicals), V_2O_5 (99.2 % pure – Johnson Matthey), Na_2CO_3 (99.95 % pure – Alfa Aesar), and MoO_6 (99.95 % pure – Alfa Aesar) purchased from Sigma Aldrich in the same way as undoped samples from experiment 1. The polishing and post-polish annealing treatments were also the same. The photodeposition process was altered to accommodate the photodeposition at high temperature. 5 ml water was measured in a small bottle. The O-ring to be used to surround the sample along with the quartz slip (that would be used to cover the setup) were also placed in the same bottle. The bottle was then sealed with a rubber stopper with a tube. This tube was connected to a vacuum pump and the water along with the O-ring and quartz slip were de-gassed. After this, the sample was quickly dried and placed on a glass slide (without any double-sided tape). The O-ring was dried and placed around the sample. The quartz slip was dried and kept ready to cover the setup. 0.14 g of $Mn(NO_3)_2.4H_2O$ was then dissolved in the degassed water. The cavity above the sample was filled with this solution using a dropper and then covered with the quartz slip. This setup was placed on a hot plate, and it was then turned on and set at 100 °C. The hot plate setting at 100 °C resulted in an actual water temperature of ~ 85 °C due to dynamic equilibrium due to cooling from surrounding air. This measurement was carried out using a Cole-Palmer Digi-sense flip stick thermometer by dipping into the solution after 4 mins. The lights were turned off in the room to prevent any photodeposition occurring as the temperature of the solution reached its equilibrium. After 4 minutes (enough time to achieve equilibrium), the lamp was switched on. The samples were exposed to UV light for 1 min to 75 seconds at a power of 300W. After reaction, the sample was placed in about 10 ml of de-ionized water at room temperature and the ambient lights were switched on. The sample was then dunked in the same water 4-5 times before being dried by compressed air. Control experiments were carried out to ensure that no substantial photodeposition occurred due to the minimal light in the lab that enabled transport of samples and general procedure of the experiment. We also ensured that there is no spontaneous deposition from the solution as a result of heating the setup to ~85 °C.

5.5.4 Imaging

Topography imaging of photodeposits was done by Scanning electron microscopy (SEM) using a Quanta 200 and a Quanta 600 as well as by Atomic force microscopy (AFM) using NT-MDT SOLVER NEXT and NTEGRA. The AFM images were analyzed using Gwyddion [30]. In experiment 2, only SEM was used as the crystals would move during AFM imaging, leading to loss of tip contact. Diamond-coated tips from Budget sensors (Tap300DLC) were used. Hot-stage SEM was done in the Quanta 600. A hook detector was used to record images at higher temperatures. Images were recorded at intervals of 10 °C from 40 °C to 80 °C. The sample was allowed to equilibrate for 5 minutes at each temperature before recording the images.

5.5.5 High-temperature XRD

A modified X-ray Diffraction setup was used to carry out the diffraction at elevated temperatures. A commercial hotplate (Thermo Scientific HP88857100 Cimarec+ Digital Hotplate) was aligned vertically and laterally. The hot plate was propped up on books and a jack to adjust the height of the sample to align it with the configured plane of the diffractometer. The sample had to be kept on the edge of the hot plate to accommodate the dimensions. The hot plate was set at a temperature of 100 °C to ensure the area where the powder was located was at around 85 °C. Please note that due to the nature of the setup, the sample does not sit exactly at the calibrated diffraction plane, and hence introduces a uniform shift in the patterns. The diffraction was carried out 40 kV with a 30 mA current and a step sizes of 0.006565 degrees (range = 33 – 34.45°) for peak-splitting high temperature studies and a larger one of 0.026248 degrees for larger 2-Theta scans (range = 25 – 80°). The setup is shown in Figure 5-4.

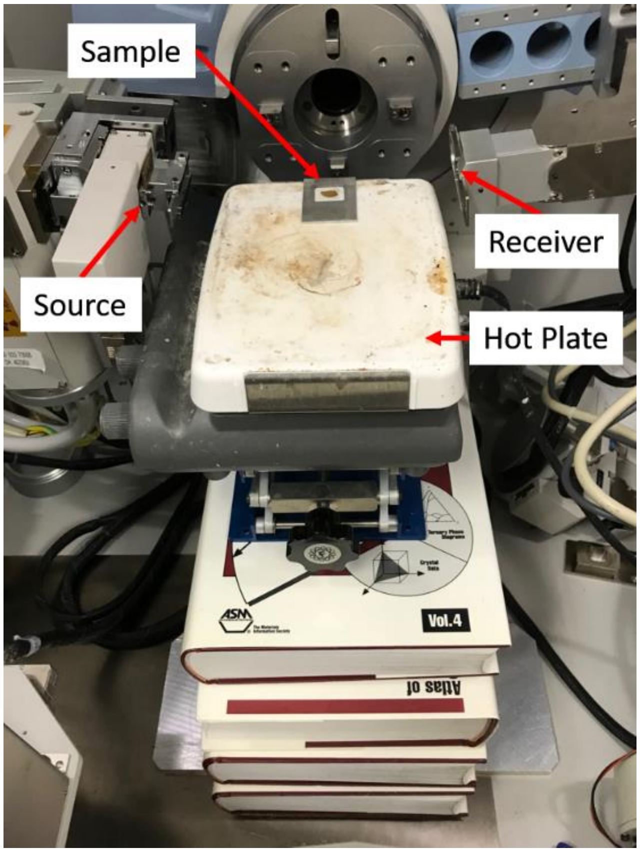

Figure 5-4: XRD setup for carrying out diffraction experiments above room temperature. The sample is placed on a hot plate, that is raised above the chamber floor using a jack and multiple books. The sample was carefully matched to the diffracting plane of the system with the jack.

5.5.6 High temperature photodeposition

The setup for carrying out photochemical reactions at elevated temperatures is a bit different from the usual room temperature setup. A schematic is given in Figure 5-5. A hot plate heats the entire system to above the required phase transformation temperature (described earlier). The high temperature photodeposition was carried out at a solution temperature of 85 °C (Temperature was measured after 4 minutes). This temperature ensured that the reaction was carried out after the phase transformation.

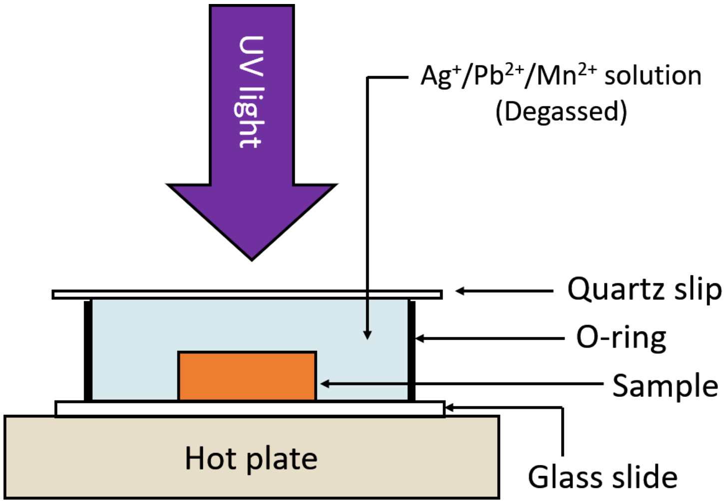

Figure 5-5: Schematic of setup used to carry out photodeposition above the ferroelastic transition temperature.

The solution was degassed before heating to ensure that the possibility of bubble formation was minimized during reaction. The photodeposition would be inconclusive if bubbles formed on the sample as it means that the solution-sample contact is lost.

5.6 Results

5.6.1 Trenched-$BiVO_4$

5.6.1.1 photodeposition before milling out trenches

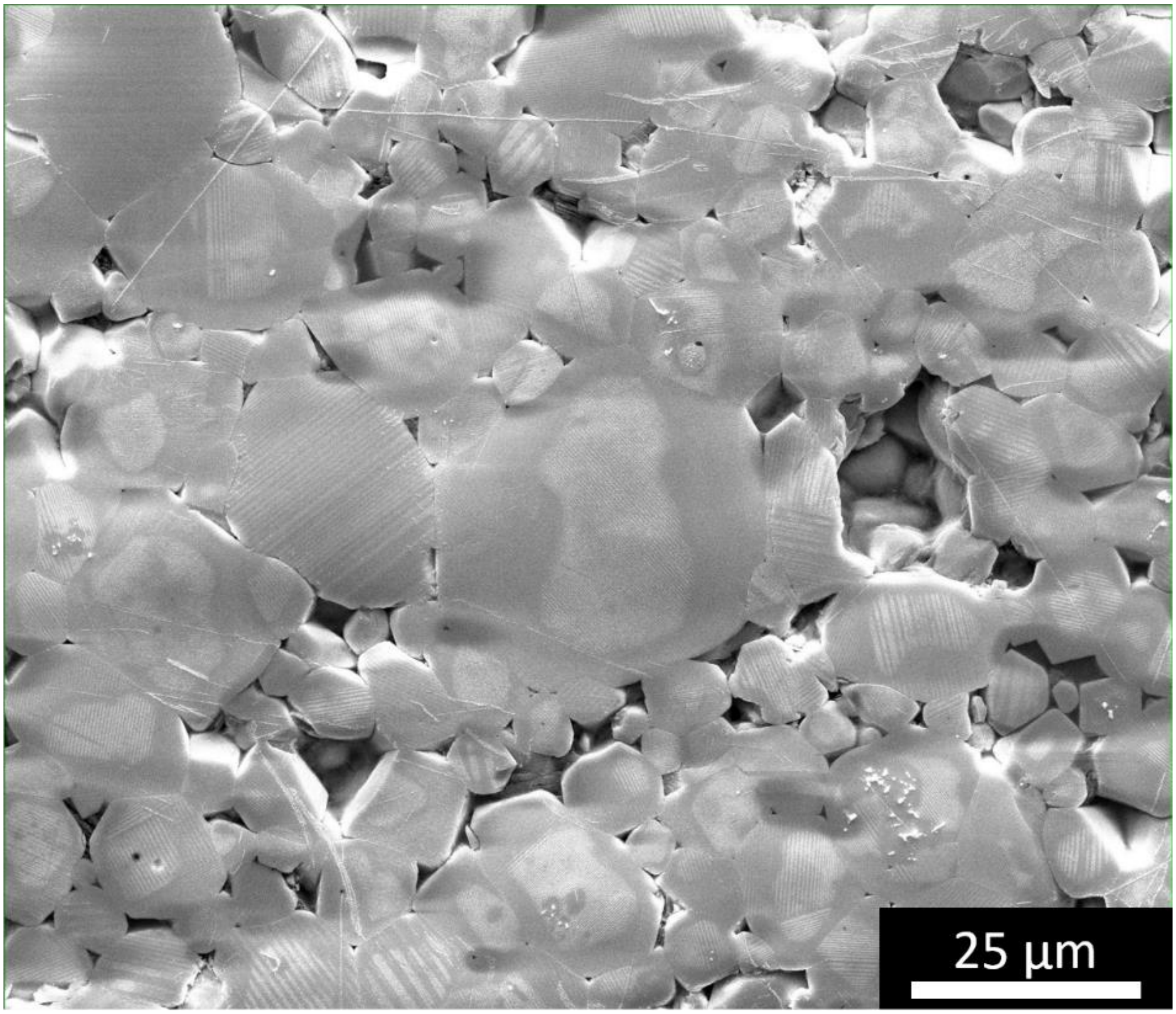

Figure 5-6: SE image at 1000x from an undoped $BiVO_4$ *sample after photoreduction of* Ag^+.

Figure 5-6 is an SE image of the substrate after photoreduction of Ag^+ (8.5 min exposure at 150 W) before the trenches were made. Dark and bright stripes can be seen in patches on most of the grains. The brighter and darker stripes are formed due to higher and lower photodeposition of silver respectively. Many grains have these patches in the center, where the reactivity is anomalously higher than the rest of the grain. Also, the spatially-selective reactivity is not just limited to the highly reactive patches. Almost all grains show ferroelastic domain specific photoreduction of Ag^+.

5.6.1.2 SEM Characterization of the pillars

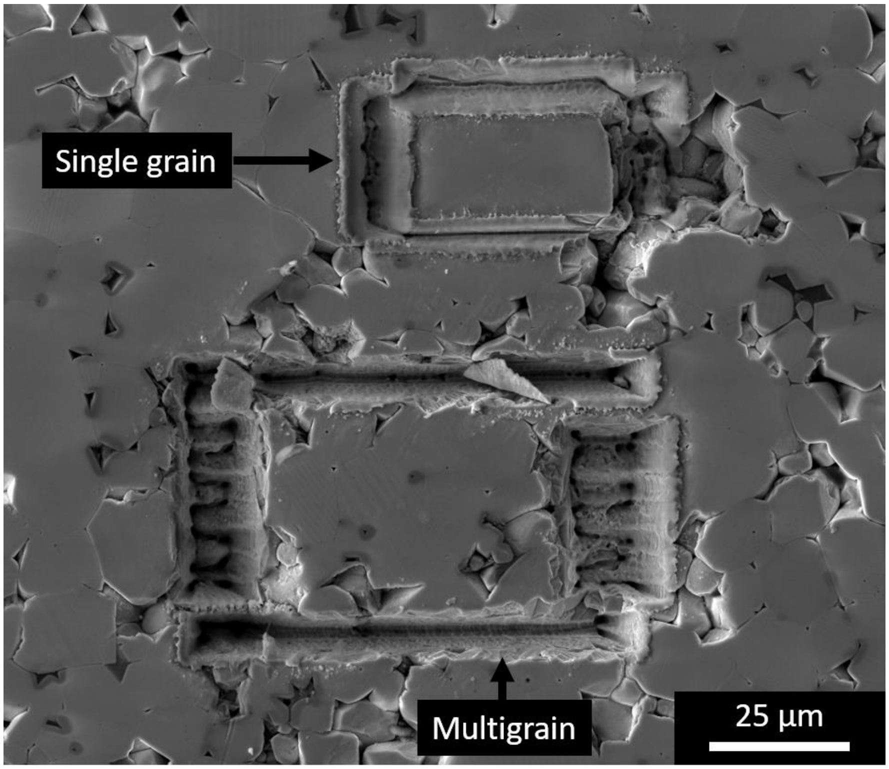

Figure 5-7: SE image of the sample surface after trenches were milled out. The upper trench encompasses a part of a single grain while the lower trench encompasses multiple grains.

Figure 5-7 is an SE image of the sample after the trenches were made, sample was polished and annealed. The upper trench surrounds a region of a single large grain, while the lower trench surrounds multiple grains. The trench width is non-uniform, presumably due to crack propagation through pores and attrition damage from the laser beam. The depth of the trenches was measured to be approximately 15 μm by using the optical microscope of the mill. The heights between the topmost and the lowermost points after they were brought into focus were noted. The difference in the height gives an approximate value of the trench depth.

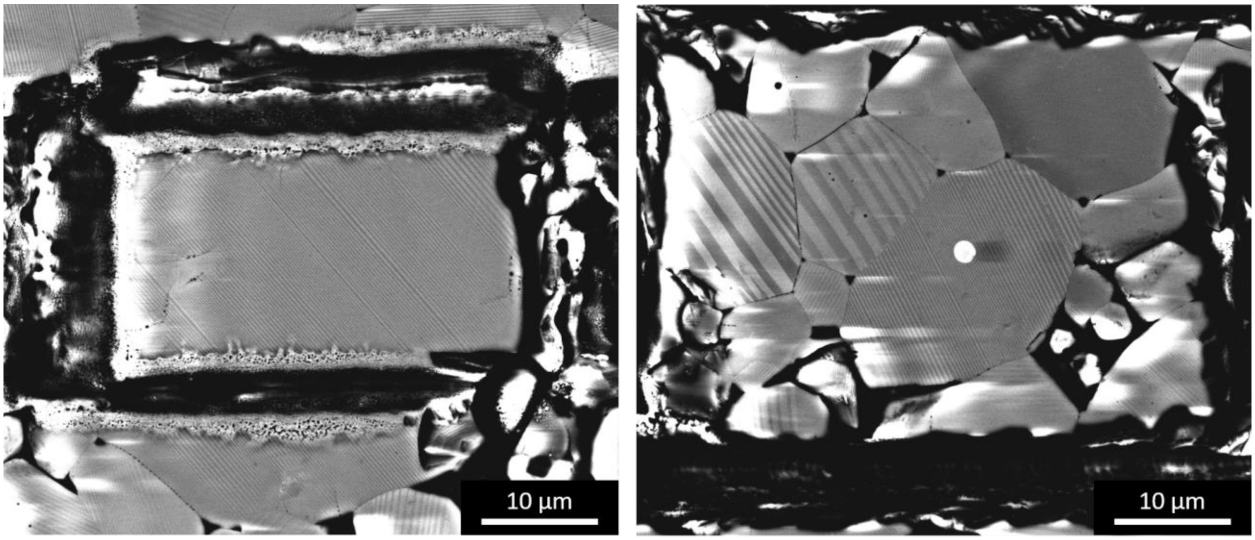

(a) Single grain

(b) Multigrain

Figure 5-8: BSE images showing ferroelastic domains in the (a) single grain and (b) multigrain regions within the perimeter of the trench.

Figure 5-8(a) is a BSE image of the single grain area labelled in Figure 5-7. The ferroelastic domains (alternating dark and bright contrast) can be seen going from bottom right to top left in the grain. The ferroelastic domains of the single crystal pillar are seen as alternating dark-bright oblique lines running north-west to south-east. The ferroelastic domains are very fine with widths of the order of ~100 nm. Figure 5-8(b) is a BSE image of the multigrain area from Figure 5-7. The ferroelastic domain structure can be seen clearly in some of the grains, while it is imperceptible in some due to the scale of the image. Ferroelastic domains were seen in all the grains within the trench.

The apparently porous substance on the top and bottom sides of the pillar is melted, possibly amorphous $BiVO_4$ from the laser-milling process, that is leftover debris after polishing. It is important to remove all debris from the region of interest when evaluating spatial selectivity. The $BiVO_4$ debris is made up of two morphologies. The first type consists of free or loosely-bound particles. These are removed by sonicating in water. The second type looks like solidified molten metal. It is most likely amorphous in nature, formed due to the extremely high heating and cooling rates associated with the laser milling process. It is largely present near the edges of the milled region. On imaging with an SEM in the BSE mode, ferroelastic domains are not observed on the debris, which is consistent with the theory that it may be amorphous. Thus, it is possible that if the second type of debris were to cover a grain, spatial selectivity of photoreactions would not be observed even if the original surface beneath it were spatially selective, leading to false negatives. Since this debris is fused to the sample and cannot be removed by sonication alone, I have tried to eliminate as much debris as possible from the surface by re-polishing and annealing my samples. In this case, the only debris is present on the edges of the pillars, which renders it inert for our purpose of determining spatial selectivity.

5.6.1.3 Piezoresponse of pillars

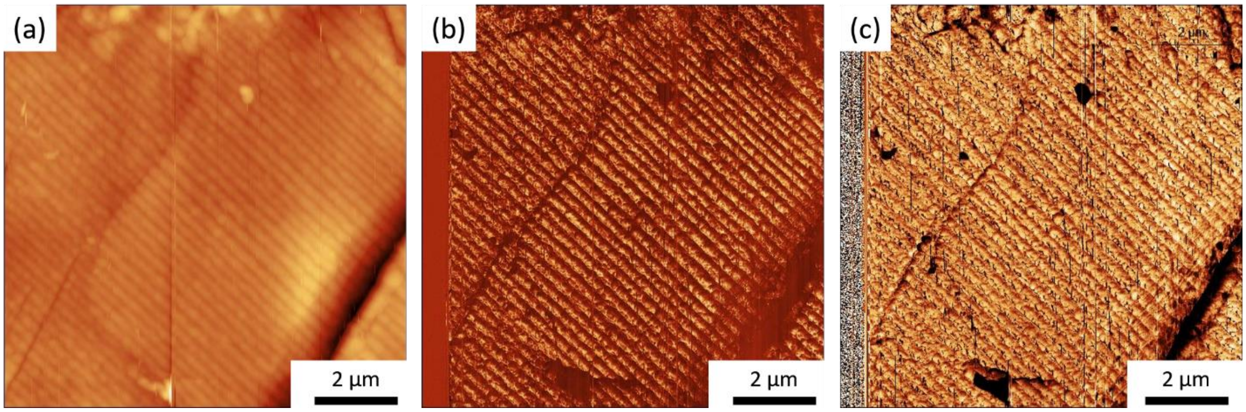

Figure 5-9: (a) AFM topography (b) PFM magnitude and (c) PFM phase of a 10x10 µm area taken from the single-grain pillar. Vertical scales: (a) 294 nm (b) 1.1 nA (c) 31 degrees

Figure 5-9 shows the piezoresponse of the trenched single-grain pillar. Figure 5-9(a) shows the AFM topography a part of the surface. Ferroelastic domains represented by alternating dark and bright stripes can be seen running from south-east to north-west. The alternating topography is due to surface relaxations of the ferroelastic domains. There is a scratch about 150 nm deep in the bottom right side of the image, running almost perpendicular to the ferroelastic domains. The bright spherical undulations in the top of the image presumably are the amorphous phase formed due to the laser-milling process. Figure 5-9(b) and (c) are the out-of-plane PFM magnitude and phase signals respectively. The PFM signals were obtained from left to right. The left sides of Figure 5-9(b) and (c) were formed during optimization of the excitation frequency, and are not representative of the actual response. Alternating Dark and bright stripes reflecting the ferroelastic domain structure in (a) are seen in (b) and (c) as well. The frequency-dependent response suggests that the ferroelastic domains are piezoresponsive, with alternating phase response indicative of alternating polarization.

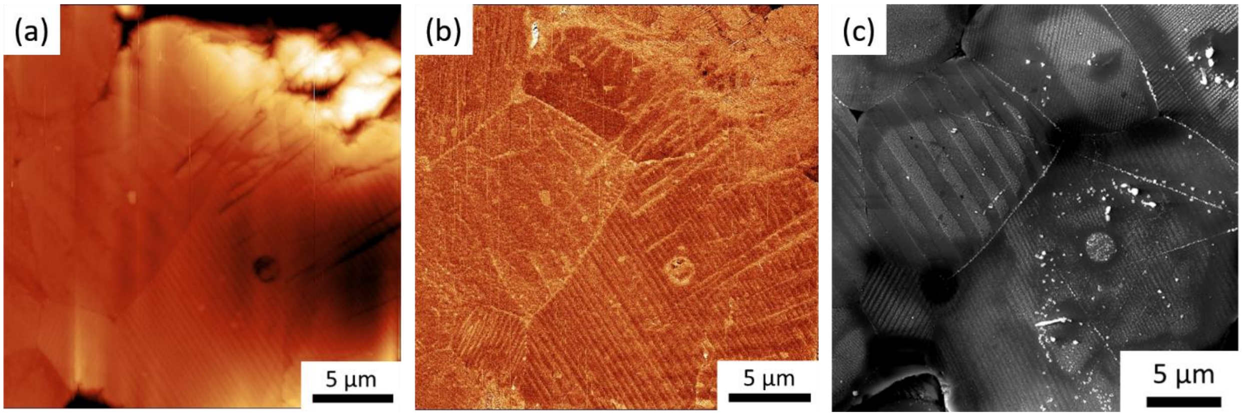

Figure 5-10: (a) AFM topography, (b) PFM phase, and (c) SE image after photodeposition of Ag of an area in the multi-grained pillar. Alternate ferroelastic domains are dark and bright in all three images. The white particles decorating the ferroelastic domains in (c) are silver.

Figure 5-10 shows the topography (a), piezoresponse (b), and the SEM image after photodeposition of Ag (c) of an area from the multi-grained region. Alternating dark and bright stripes can be seen in the topography as well as the PFM out-of-plane phase response. These are seen most clearly in the grain on the bottom right of the image. In the SEM image, dark and bright stripes are seen on multiple grains, suggesting that alternate ferroelastic domains promote photoreduction. Comparing the bottom right grain, the same ferroelastic domains are alternately dark and bright, consistent with the alternating PFM phase from Figure 5-10(b). Note that the photodeposition was done before imaging the AFM topography and piezoresponse. The top right of the multi-grain region was damaged in between these two steps.

5.6.1.4 Photodeposition on pillars

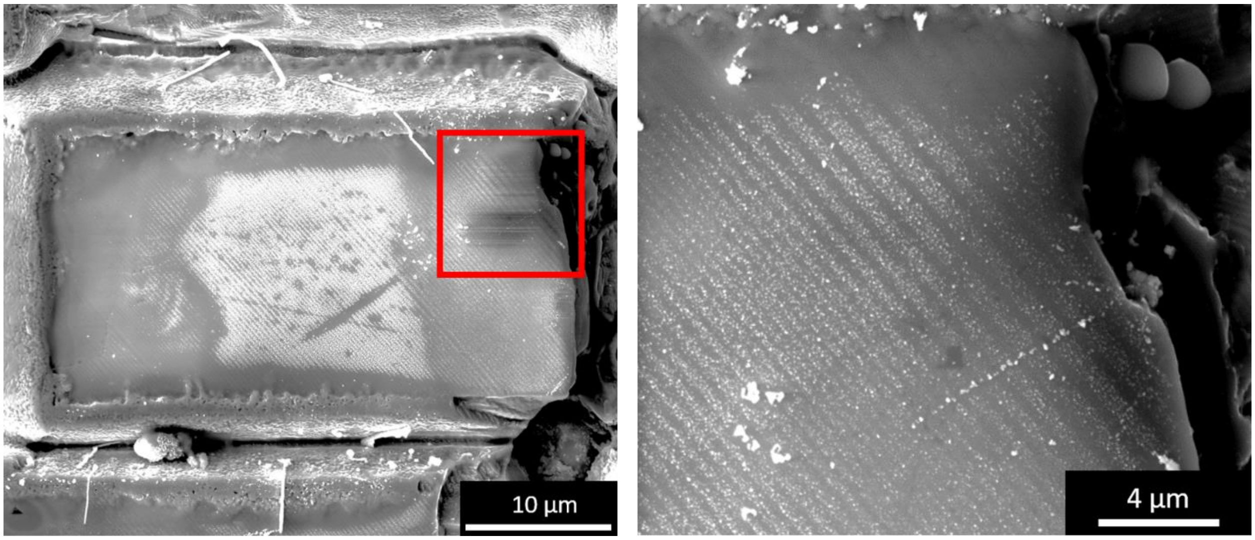

Figure 5-11: SE images after photoreduction of Ag^+, showing ferroelastic domain specific reactivity from (a) Single crystal region and (b) the region marked by the red box from (a)

The Figure 5-11(a) is an SE image of the single grain region after photochemical reduction of Ag^+ for 9.5 minutes at 150 W lamp power (with a visible light pass filter). The white particles in the images are silver particles. In Figure 5-11(a), the individual particles cannot be seen due to the magnification. However, a large white patch is easily discernable in the center of the region. The central region of the grain is highly reactive, while the other surrounding regions do not react as much. An area marked in the red box towards the edge of the trench in Figure 5-11(a) has been magnified and shown in Figure 5-11(b). The white spheres of silver are more concentrated on alternate ferroelastic domains. This implies that ferroelastic domain specific photoreduction is present all throughout the grain. From the images, the amorphous phase does not look to have a lot of white silver particles as compared to the ferroelastic domains.

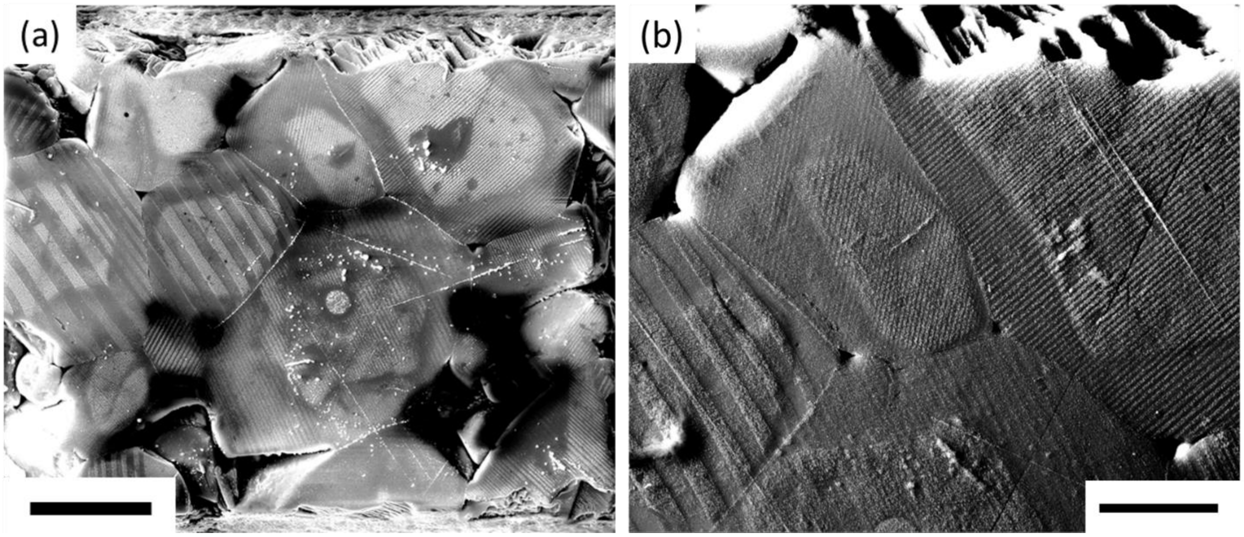

Figure 5-12: SE images of (a) the multi-grained pillar and (b) a zoomed-in version after photodeposition of Ag. White silver particles can be seen decorating alternating ferroelastic domains. Scale bars: (a) 10 µm (b) 5 µm

Figure 5-12(a) shows the SE image of the same area in Figure 5-8(b) after photodeposition of silver. The reactivity is very similar to that on the single crystal pillar in the earlier figure. There are patches of high reactivity in the center of the grains. However, spatial selectivity can be seen outside of these patches as well at higher magnifications, as seen in Figure 5-12(b).

From these figures, we can say that even after relaxing stresses from the neighboring grains, spatial selectivity of photodeposition reactions is present. Thus, it means that (a) The stresses from surrounding grains do not impact spatial selectivity or (b) The creation of trenches did not relax them to a large extent so as to de-polarize the ferroelastic domains. This maybe because of the fact that the trench depth is only 15 µm. This is possibly smaller than the grain in Figure 5-8(a) and some of the grains in Figure 5-8(b).

5.6.2 Photodeposition on Hydrothermally-grown crystals

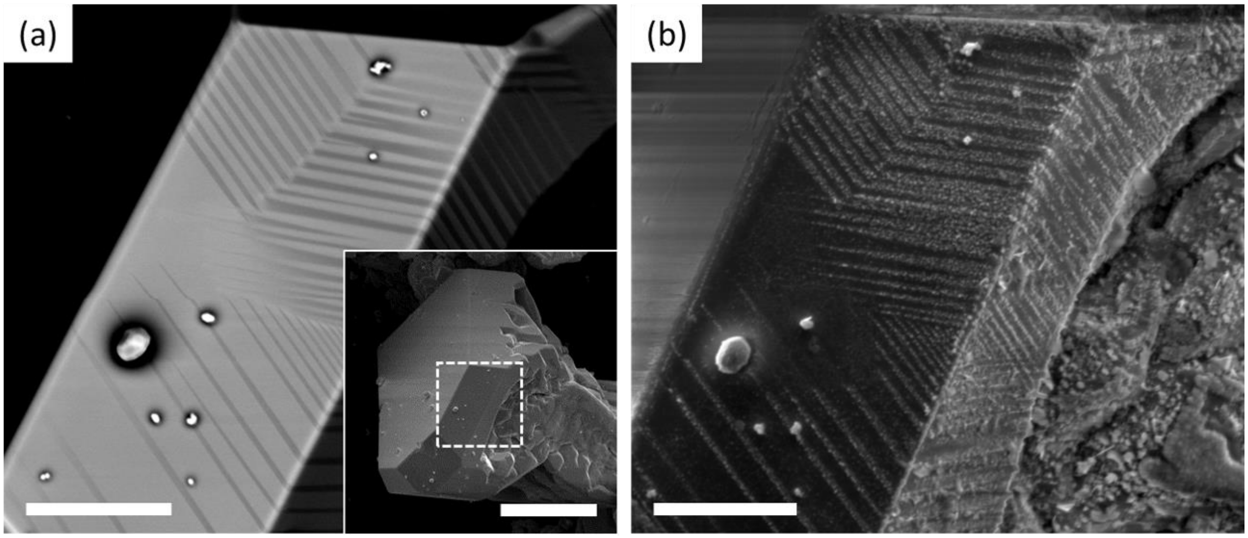

Figure 5-13: (a) BSE image of two facets of a hydrothermally-grown $BiVO_4$ crystal. The entire crystal is shown in the inset. The BSE image is of the area inside the dotted line. (b) SE image of the same two facets after photodeposition of Ag+. Scale bars: (a) – 5 µm; inset – 25 µm (b) 5 µm

Figure 5-13(a) is a BSE image of the ferroelastic domain structure on a facet of a hydrothermally grown crystal. The entire crystal is shown in the inset. A zoomed in version of the area in the dotted line in the inset is shown in Figure 5-13(a). The ferroelastic domains are seen as two sets of alternating dark-bright stripes. One set runs from north-west to south-east while the other set runs from left-right. Some bright particles can be seen on the facet in both figures. They are likely stray particles/small crystals of $BiVO_4$ stuck on the surface during sample preparation. Figure 5-13(b) is a SE image of the same area after photodeposition of silver. Spatial selectivity of the photodeposition is evident. In the set of ferroelastic domains that run left-right, the bright ferroelastic domains from Figure 14(a) are more reactive than the dark ferroelastic domains. This selectivity is clearly seen in the pinched-off ferroelastic domains in the central of the facet. In those ferroelastic domains that run obliquely, the dark ferroelastic domains from Figure 5-13(a) are more reactive than the bright ones. This selectivity is clearly seen in the ferroelastic domains towards the bottom of the facet, where the dark ferroelastic domains are spaced relatively further from each other.

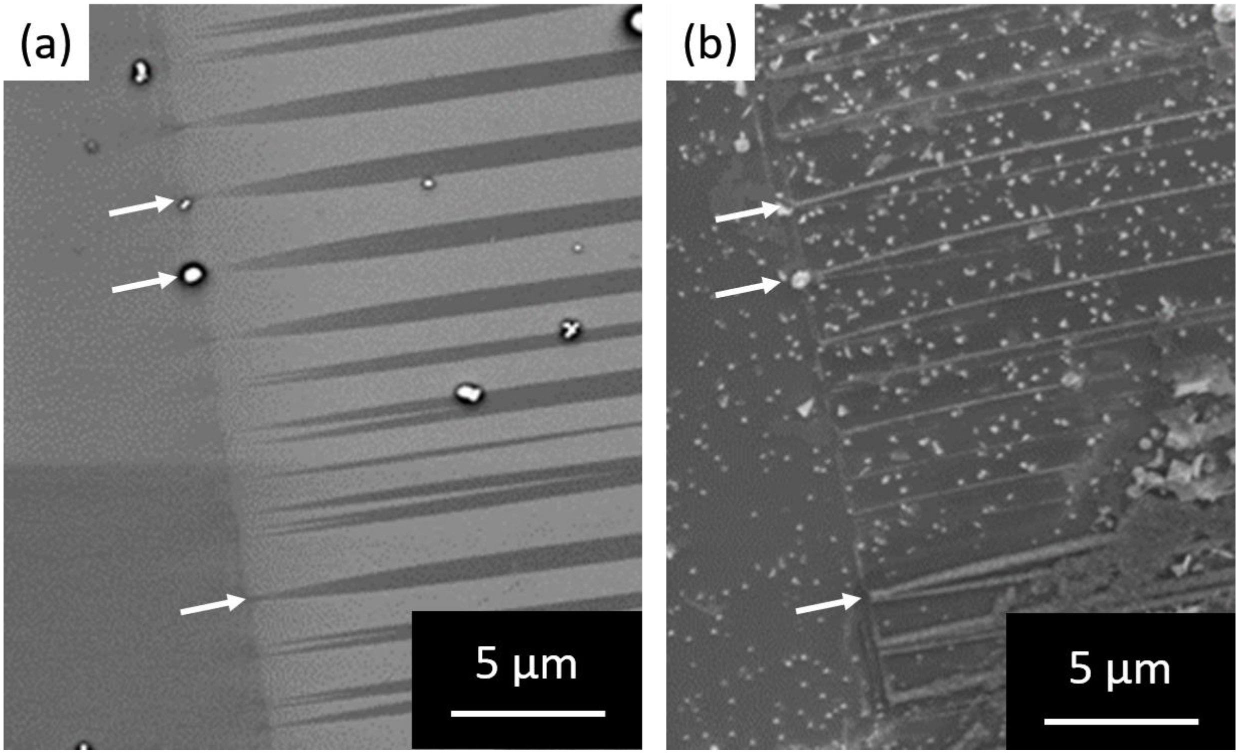

Figure 5-14: (a) BSE image and (b) SE image after photodeposition of Ag on an hydrothermally grown crystal. The white dots in (b) are silver particles. The white arrows point to the same ferroelastic domains in both images. White lines of small silver particles can be seen decorating the domain walls in (b).

In some crystals, the domain walls seem to be spatially selective instead of the ferroelastic domains. This is seen to simultaneously occur on the same crystal with ferroelastic domain-driven spatial selectivity on some facets. Figure 5-14(a) shows the BSE image of the ferroelastic domain structure on the crystal. The needle-like ferroelastic domains are seen running from right to left with alternating dark and bright contrast. Three of these are highlighted using white arrows. The domain walls for the same ferroelastic domains are seen to have a thin bright coating on them in Figure 5-14(b). Otherwise, white particles of photodeposited silver are seen to be dispersed evenly on all ferroelastic domains on the surface. Hence, it suggests that these domain walls preferentially promote the photoreduction of Ag on them as compared to the ferroelastic domains. Ferroelastic domain walls being spatially selective has not been seen in any of my polycrystalline pellet samples. However, Kim et. al. [31] have found polar domain walls in reduced single crystal WO_3, and this case is looks to be an $BiVO_4$ analog of it.

The important takeaway from this set of experiments remains that after removing any possible influence of surrounding grains, spatial selectivity is still observed. It implies stresses from surrounding grains are not necessary for spatial selectivity. These observations also support that bulk stresses create ferroelastic domain polarization in $BiVO_4$.

5.6.3 Experiments above the ferroelastic transition temperature

5.6.3.1 X-ray Diffraction

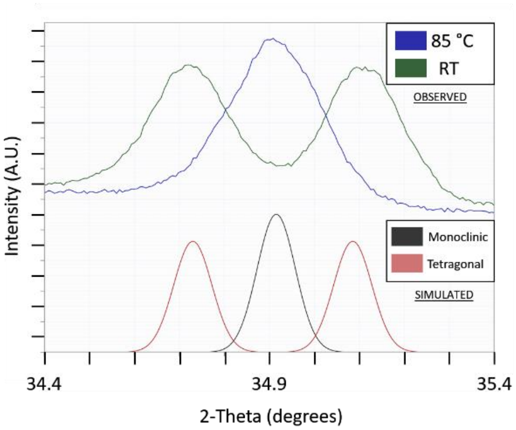

Figure 5-15: Top half - XRD patterns of the x=0.08 sample of $(Bi_{1-0.5x}Na_{0.5x})(V_{1-x}Mo_x)O_4$ at room temperature (in green) and at 85 °C on the hot plate (in blue). Bottom half – simulated XRD patterns of x=0.08 co-doped monoclinic (in black) and tetragonal (in pink) $(Bi_{1-0.5x}Na_{0.5x})(V_{1-x}Mo_x)O_4$. The lattice parameters were obtained from [29].

Figure 5-15 shows a part of the XRD diffraction pattern (2-Theta: 34.4° to 35.4°) of the co-doped sample at two different temperatures, along with the simulated patterns for monoclinic and tetragonal $BiVO_4$ co-doped at the same dopant concentration as the synthesized samples. The range of 2-Theta has been chosen to point out the phase change, as the splitting of the (200) peak at around 35° indicates a transition from tetragonal to monoclinic scheelite [29]. At room temperature (green), the structure is monoclinic scheelite, with two clearly distinct peaks at 34.7° (200) and 35.1° (020). When the same scan was done at 85 °C on the hot plate (blue), the two peaks were found to have merged into one. This is indicative of a phase transformation from monoclinic scheelite to tetragonal scheelite. The simulated patterns were obtained from Crystal diffract. The lattice parameters for our doping concentration were obtained from Zhou et. al. [29]. The angular difference between the (200) and (020) peaks (0.4°) in the observed pattern matches that of the simulated pattern, indicating that the actual doping concentrations of the synthesized samples are close to the theoretical value (x=0.08). Note that the patterns have been shifted laterally (RT by 1° and 85 °C by 1.2°). The large error is presumably due to the error caused by the in-house modifications to the XRD stage for heating. From these results, we can say that the phase in the bulk has transitioned from monoclinic scheelite to tetragonal scheelite at 85 °C for our concentration of co-doping.

5.6.3.2 Hot-stage SEM

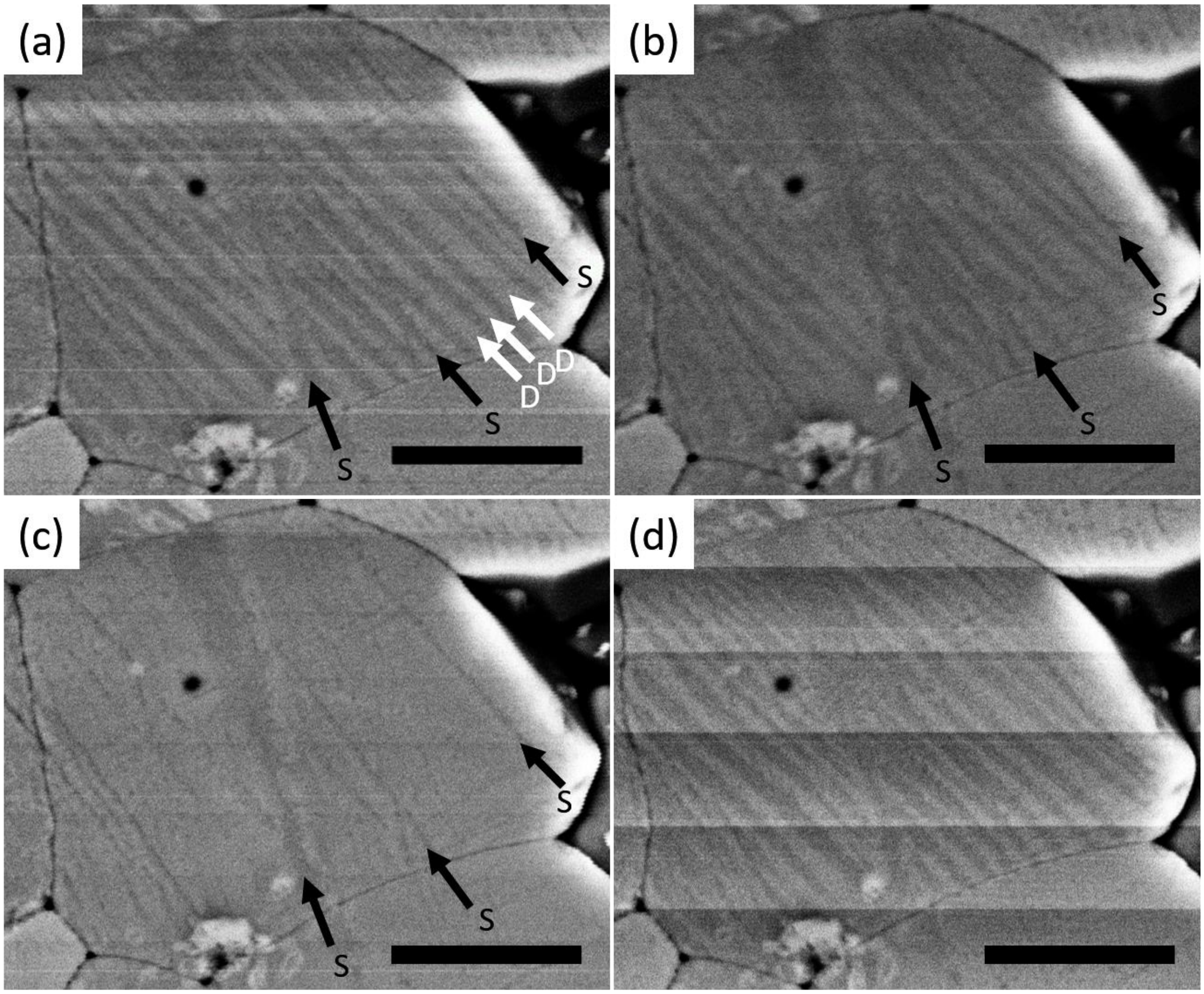

Figure 5-16: Hot-stage SEM images of a grain in x=0.08 sample of $(Bi_{1-0.5x}Na_{0.5x}V_{1-x}Mo_x)O_4$ at different temperatures. (a) – 40 °C (b) – 55 °C (c) – 70 °C (d) – after cooling back to 40 °C. S denotes a scratch and D denotes a ferroelastic domain in the images.

To confirm the phase change, hot-stage SEM was carried out. Figure 5-16 shows the gaseous secondary electron images recorded at different temperatures. The ferroelastic domains are seen as alternating dark-bright stripes running north-west to south-east. Some ferroelastic domains have been labelled as 'D' with white arrows in Figure 5-16(a). They are seen to progressively disappear from Figure 5-16(a) – 40 °C to 7(b) – 55 °C to 7(c) – 70 °C as the temperature of the sample is increased. To confirm that the image does not further deviate after

70 °C, we imaged the grain at 85 °C as well. The image at 85 °C was the same as that taken at 70 °C, for all practical purposes. The sample was covered by a metallic heat shield with a small orifice for imaging, which ensures that majority of the radiation from the heater as well as the sample is reflected back. Thus, the actual temperature of the sample should be close to the set temperature even in high vacuum. There are some scratches on the surface that are present in all images. Some of these have been labelled in Figure 5-16(a)-(c) as 'S' with black arrows to avoid confusion with ferroelastic domains. Figure 5-16(d) shows the ferroelastic domain structure after cooling back to 40 °C. It is very similar to the one seen in Figure 5-16(a). It indicates that there is some factor that enables replication of the ferroelastic domain structure after thermal cycling. The horizontal lines in all images are imaging defects due to sample charging. The ferroelastic to paraelastic phase transformation in $BiVO_4$ is second order [32] and it is possible that the spontaneous strain at 70 °C is too small to give contrast between ferroelastic domains in the SEM. Hence, there may be no contrast even when ferroelastic domains are present, if the temperature is very close to the FTT. In any case, the images are consistent with our results from XRD that the critical temperature of the phase transition (spontaneous strain = 0) is less than or equal to 85 °C.

5.6.3.3 Photodeposition after heating above the ferroelastic transition temperature

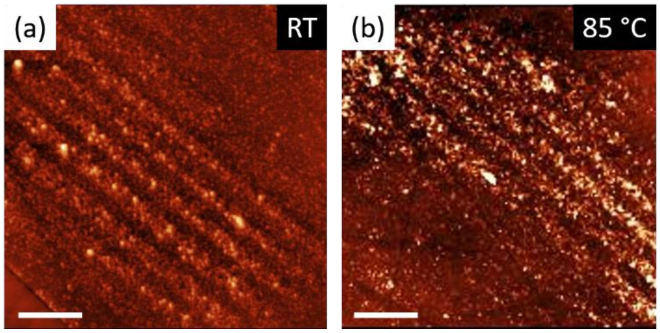

Figure 5-17: AFM topography after photodeposition of MnOx at (a) Room temperature and (b) at 85 °C. Vertical scales: (a) 32 nm (b) 14 nm. Scale bar – 1 µm

Figure 5-17(a) is a AFM topography image after the photodeposition of Mn^{2+} at room temperature. Alternating dark and bright stripes are seen in this figure. Since the topographically higher areas are brighter in a AFM topography image, brighter stripes indicate more photodeposition. Such a pattern of alternating high and low reactivity is an indicator of spatial selectivity, and have been reported in $BiVO_4$ and WO_3 previously for photodeposition of Ag, PbO_x, and MnO_x . Figure 5-17(b) shows the AFM topography after photodeposition of MnO_x at ~85 °C from a different area on the same grain. Both regions have ferroelastic domains going from south-east to north-west. Dark and bright stripes are seen similar to the image taken below the FTT. This implies that spatial selectivity of photodeposition reactions exists when there are no ferroelastic domains as well in $BiVO_4$.

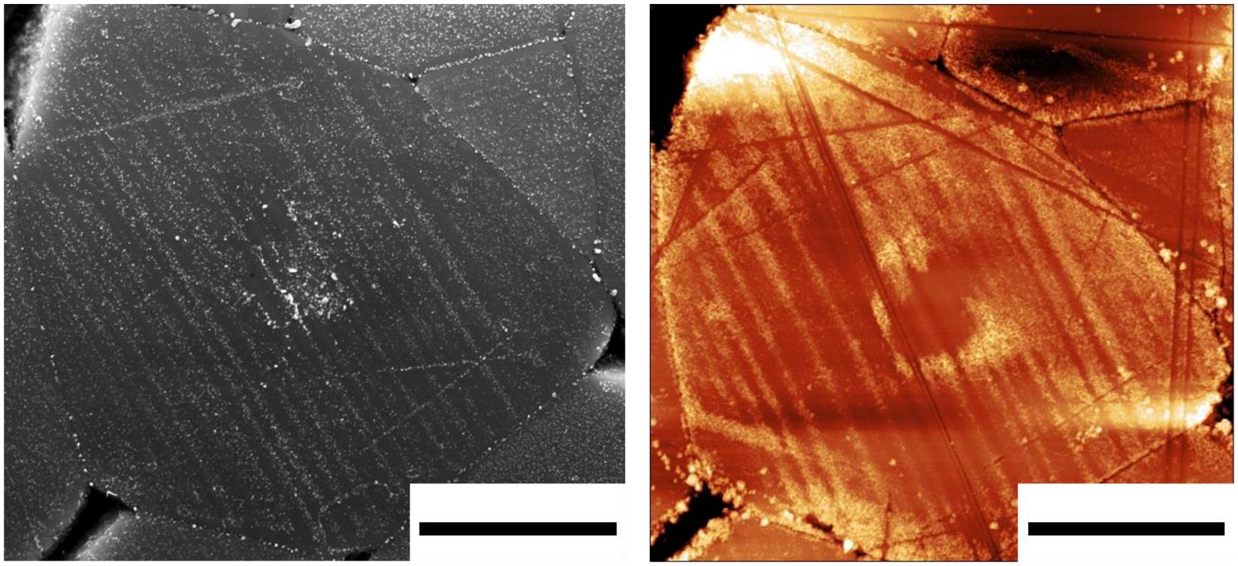

Photoreduction of Ag$^+$ (Room temperature)

Photo-oxidation of Mn^{2+} (85 °C)

Figure 5-18: (a) Photoreduction of Ag below FTT (b) Oxidation of Pb above FTT. Scale bar: 5 microns in both

Figure 5-18 shows another grain in the same sample showing spatial selectivity after heating above the FTT. Figure 5-18(a) shows a secondary electron image of a grain after photodeposition of Ag. The white dots are silver particles. Stripes of these white dots can be seen running along south-east to north-west. Similarly, in Fig. Figure 5-18(b), after photo-oxidation of Mn^{2+} above the FTT, stripes of MnO_x deposits can be seen along the same direction. This indicates that the reactivity above the FTT follows the same ferroelastic domain pattern that was present before heating above the FTT.

Thus, after removing the ferroelastic domains (effectively S and B), spatial selectivity is still present on the sample surface. Hence, there is some factor other than a domain-stress-strain coupling that definitely contributes to spatial selectivity. In fact, the reactivity seems to follow a similar pattern to the ferroelastic domain structure that existed at room temperature.

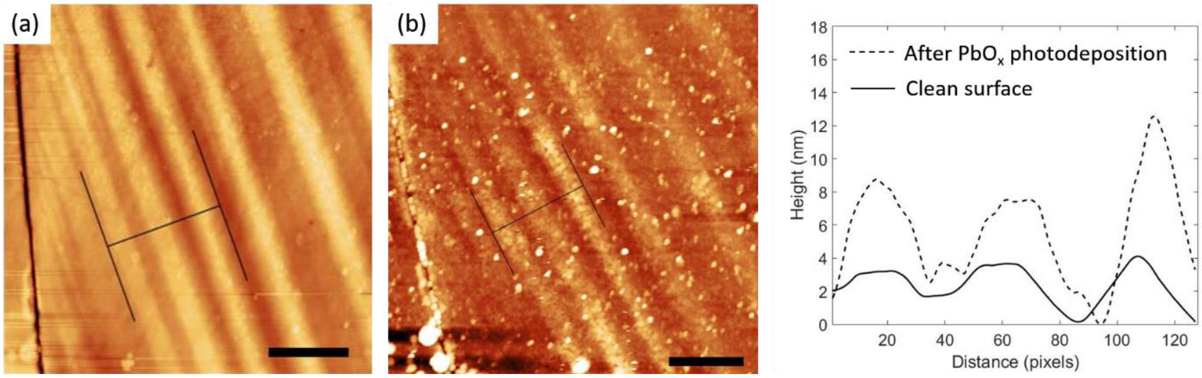

Figure 5-19: AFM topography of a grain (a) before and (b) after photodeposition of PbOx at 85 °C . The topography profiles of the same three ferroelastic domains in both are shown in (c). The profiles are averaged over 128 pixels.

Finally, we need to confirm that the stripes are higher in topography actually due to increased reactivity. There are two possibilities that can cause the stripes in Figure 5-19 to appear bright (higher in topography). Firstly, the photodeposition may be uniform on the grain after the ferroelastic domains have disappeared and on cooling, some ferroelastic domains may appear higher because of the natural surface relaxation on ferroelastic domain formation. Secondly, alternate ferroelastic domains may promote oxidation (as seen in previous reports) and hence, have more photodeposits on them as compared to the other set. This would cause the ferroelastic domains with higher reactivity to be higher in topography than the ones with a lower reactivity, in a particular photodeposition reaction. To test which of these two holds true in our case, we compared the differences in height between the peaks and valleys of the ferroelastic domains, before and after photodeposition of PbO_x. If the relative height between them doesn't change after reactivity, then it supports that the bright stripes are higher because of surface relaxation. If the relative height between them increases, It supports that some ferroelastic domains have more photodeposits on them, indicating higher reactivity. Figure 5-19(a) shows the AFM topography of the clean surface. The surface profile of three pairs of ferroelastic domains (averaged over 128 pixels) is taken from the black line labelled in the figure. This profile is shown with the solid black line in Figure 5-19(c). The height differences for the three pairs are approximately 1.5 nm, 3.5 nm, and 4 nm. Figure 20(b) shows the AFM topography after photodeposition of PbO_x. The surface profile (shown with the black line) is taken for the same three pairs as in Figure 5-19(a). It is shown with a dashed line in Figure 5-19(c). The height differences between peaks and valleys for the same three ferroelastic domains are approximately 7.2 nm, 7.5 nm, and 12.5 nm. These are significantly higher for every ferroelastic domain when compared to the differences in the clean surface. This supports the second possibility discussed earlier, that some ferroelastic domains are more reactive for photodeposition of PbO_x than others.

5.7 Discussion

In the first experiment, spatial selectivity is observed. It means that the creation of trenches did not cause a large enough relaxation to eliminate the strain gradients, or that the surrounding stresses do not play a role at all. It is still possible that the sample before trenching had a higher magnitude of ferroelastic domain polarization, and that creating the trenches reduced it, but not to the extent that spatial selectivity was not observed. Thus, we cannot comment on the role of the surrounding grains from this experiment alone.

In the second experiment where the effect of surrounding grains was completely eliminated, spatial selectivity was observed. This supports that the bulk stresses can create polar ferroelastic domains by themselves. It also implies that stresses from surrounding grains are not necessary for polarization of ferroelastic domains. It is possible that they modify the ferroelastic domain polarization, but it is clear that they are not necessary.

Interestingly, spatial selectivity was observed in the third experiment as well, in which the photodeposition was carried out in the absence of a ferroelastic domain structure. Hence, it implies that there is some factor other than the domain-stress-strain that causes spatial selectivity.

An important observation is that the pattern of photodeposits is similar to the ferroelastic domain structure at room temperature. This supports that an initial presence of a ferroelastic domain structure is required for spatial selectivity. This is consistent with the results of Munprom et. al. [13], where there was no spatial selectivity when the samples were co-doped at $x=0.175$ (as compared to $x=0.08$ for our samples). The monoclinic phase is stable at room temperature for $x<0.1$. [29] The higher doping concentration ensured that the FTT was driven below room temperature in their work. Thus, ferroelastic domains never formed during synthesis and photodeposition. In our case, ferroelastic domains existed at room temperature throughout the duration of the work and were taken away only during the high-temperature photodeposition reactions. We discuss the possible factors that could drive spatial selectivity after the ferroelastic domains were taken away during photodeposition, but existed otherwise.

A possible explanation to this can be given by considering segregation of point defects such as oxygen vacancies in ferroelastic domains. This is consistent with the fact that the ferroelastic domain structure that was formed after thermal cycling was the same, as seen in the hot-stage

SEM (Figure 5-16). It is likely that the ferroelastic domain structure that was formed in the first place led to a quasi-equilibrium state of point defect distribution. This distribution then maintained a stress state during thermal cycling that led to the nucleation and growth of the new but similar ferroelastic domain structure after cooling. Since the point defect distribution was initially formed by a particular ferroelastic domain structure, it is logical that the new structure should also follow the ferroelastic domain structure that existed before heating above the FTT. The existence of mobile oxygen vacancies that can Abdi et. al. [33] found that oxygen vacancies are the dominant intrinsic defects in monoclinic $BiVO_4$. Rossell et. al. [34] reported that a surface layer of around 5 nm has ~15% of oxygen vacancies. The ferroelastic domains in any given grain are in different stress conditions (as shown in Figure 3), and hence can lead to differential segregation of these vacancies by diffusion creep. Even though oxygen vacancy diffusion in Scheelite structures is traditionally difficult, $BiVO_4$ is an exception [35]. Thus, a set of ferroelastic domains in any grain can end up with a higher/lower concentration of surface oxygen vacancies than the other set. A similar differential segregation of mobile $CH_3NH_3^+$ ions on different sets of ferroelastic domains in a grain was observed by Liu et. al. [36] in $CH_3NH_3PbI_3$ films. Oxygen vacancies can have multiple effects on the photodeposition. They can increase majority carrier concentration by behaving as shallow donors [37]. Hence, this increased conductivity in ferroelastic domains that have a higher concentration of oxygen vacancies supports our observations that some ferroelastic domains are more reactive than others, even after the ferroelastic domain structure has been temporarily removed. This is because it is unlikely that the vacancies diffuse enough in the short time of the uniform strain state (caused due to absence of ferroelastic domains) during photodeposition (total 5 minutes) above the FTT.

Surface segregation of Na and Mo atoms (driven by differential strain in ferroelastic domains) is another possibility that can lead to increased reactivity in some ferroelastic domains. The Na (Mo) atoms on Bi (V) sites are very shallow acceptors (donors). [37] Surface Mo can lead to increased charge transfer efficiency (due to high electronegativity of Mo^{6+}), increasing the reaction rate. [38] Hence, any segregation of these in ferroelastic domains would lead to increase in local conductivity, increasing photodeposition.

Such a surface segregation of Na and Mo can also cause a difference in the FTT locally, as it is the co-doping concentration that affects it directly. [29] Hence, even if the bulk is seen to change its phase to tetragonal scheelite (as shown by the XRD and Hot-stage SEM) on heating above the bulk FTT, there is a possibility of alternating stripes of monoclinic and tetragonal scheelite existing on the surface, mimicking the ferroelastic domain pattern present at room temperature. This would lead to the formation of a surface polymorph junction. The slight difference in the band structure of these two phases [39] can lead to spatial separation of charge carriers, as described by Li et. al. [40]. Polymorph junctions have been shown to increase photocatalytic efficiency in TiO_2 [41] and Ga_2O_3 [42] as a result of charge separation. It is possible that two phases exist on the surface but are not visible in the hot-stage SEM. The penetration depth at 20 kV as calculated using Win X-Ray [43] is around 700 nm for $BiVO_4$. It is unlikely that a surface phase can create enough channeling contrast given these conditions.

5.8 Conclusions

Three sets of experiments were carried out in succession to test for stress states that could drive spatial selectivity through flexoelectricity on $BiVO_4$. Spatial selectivity of photodeposition reactions was seen on isolated regions of a polycrystalline sample, hydrothermally grown crystals and on a polycrystalline sample above the FTT. This implied that there is a factor other than domain-stress-strain coupling that results in spatial selectivity. From our results, it was not possible to conclude whether bulk stresses and stresses from surrounding grains contribute to creating spatial selectivity.

5.9 References

[1] Juan Zhao and Xudong Yang: *Build. Environ.*, 2003, vol. 38, pp. 645–54.

[2] Yash Boyjoo, Hongqi Sun, Jian Liu, Vishnu K. Pareek, and Shaobin Wang: *Chem. Eng. J.*, 2017, vol. 310, pp. 537–59.

[3] Agatino Di Paola, Elisa García-López, Giuseppe Marcì, and Leonardo Palmisano: *J. Hazard. Mater.*, 2011, vol. 211, pp. 3–29.

[4] A Fujishima and K Honda: *Nature*, 1972, vol. 238, pp. 37–38.

[5] Jeff Tsao, Nate Lewis, and George Crabtree: *US Dep. Energy*, 2006, pp. 1–24.

[6] *Key World Energy Statistics 2018*, 2018.

[7] Yiseul Park, Kenneth J. McDonald, and Kyoung-Shin Choi: *Chem. Soc. Rev.*, 2013, vol. 42, pp. 2321–37.

[8] Savio J A Moniz, Stephen A Shevlin, David James Martin, Zheng-Xiao Guo, and Junwang Tang: *Energy Environ. Sci.*, 2015, vol. 8, pp. 731–59.

[9] Conrado Martinez Suarez, Simelys Hernández, and Nunzio Russo: *Appl. Catal. A Gen.*, 2015, vol. 504, pp. 158–70.

[10] Bartek J. Trześniewski and Wilson A. Smith: *J. Mater. Chem. A*, 2016, vol. 4, pp. 2919–26.

[11] Carolin Zachäus, Fatwa F. Abdi, Laurence M. Peter, and Roel van de Krol: *Chem. Sci.*, 2017, vol. 8, pp. 3712–19.

[12] Ratiporn Munprom, Paul A. Salvador, and Gregory S. Rohrer: *Chem. Mater.*, 2014, vol. 26, pp. 2774–76.

[13] Ratiporn Munprom, Paul A. Salvador, and Gregory S. Rohrer: *J. Mater. Chem. A*, 2016, vol. 4, pp. 2951–59.

[14] Rengui Li, Fuxiang Zhang, Donge Wang, Jingxiu Yang, Mingrun Li, Jian Zhu, Xin Zhou, Hongxian Han, and Can Li: *Nat. Commun.*, 2013, vol. 4, pp. 1432–37.

[15] Linchao Mu, Yue Zhao, Ailong Li, Shengyang Wang, Zhiliang Wang, Jingxiu Yang, Yi Wang, Taifeng Liu, Ruotian Chen, Jian Zhu, Fengtao Fan, Rengui Li, and Can Li: *Energy Environ. Sci.*, 2016, vol. 9, pp. 2463–69.

[16] Ajay S. Pisat, Paul A. Salvador, and Gregory S. Rohrer: *Adv. Mater. Interfaces*, 2019.

[17] Yisi Zhu, Paul A Salvador, and Gregory S Rohrer: *Chem. Mater.*, 2016, vol. 28, pp. 5155–62.

[18] Yisi Zhu, Paul A. Salvador, and Gregory S. Rohrer: *Phys. Chem. Chem. Phys.*, 2017, vol. 19, pp. 7910–18.

[19] J L Giocondi and G S Rohrer: *J. Am. Ceram. Soc.*, 2003, vol. 86, pp. 1182–89.

[20] Jennifer L Giocondi and Gregory S Rohrer: *J. Phys. Chem. B*, 2001, vol. 105, pp. 8275–77.

[21] Jennifer L. Giocondi and Gregory S. Rohrer: *MRS Proc.*, 2000, vol. 654, pp. 1–10.

[22] J. L. Giocondi and G. S. Rohrer: *Chem. Mater.*, 2001, vol. 13, pp. 241–42.

[23] Ajay S. Pisat, Gregory S. Rohrer, and Paul A. Salvador: *J. Mater. Chem. A*, 2017, vol. 5, pp. 8261–66.

[24] Ajay S. Pisat, Gregory S. Rohrer, and Paul A. Salvador: *Semicond. Sci. Technol.*, 2017, vol. 32.

[25] J.D. Bierlein and A.W. Sleight: *Solid State Commun.*, 1975, vol. 16, pp. 69–70.

[26] J Sapriel: *Phys. Rev. B*, 1975, vol. 12, pp. 5128–40.

[27] Ae Ran Lim, Sung Ho Choh, and Min Su Jang: *J. Phys. Condens. Matter*, 1995, vol. 7, pp. 7309–23.

[28] James J. Glickstein, Paul A. Salvador, and Gregory S. Rohrer: *J. Mater. Chem. A*, 2016, vol. 4, pp. 16085–93.

[29] Di Zhou, Li-Xia Pang, Hong Wang, Jing Guo, Xi Yao, and Clive A. Randall: *J. Mater. Chem.*, 2011, vol. 21, pp. 18412–20.

[30] David NEČAS and Petr KLAPETEK: *Cent. Eur. J. Phys.*, 2012, vol. 10, pp. 181–88.

[31] Yunseok Kim, Marin Alexe, and Ekhard K H Salje: *Appl. Phys. Lett.*, 2010, vol. 96, pp. 1–4.

[32] Ae Ran Lim and Se-Young Jeong: n.d.

[33] Fatwa F. Abdi, Tom J. Savenije, Matthias M. May, Bernard Dam, and Roel van de Krol: *J.*

Phys. Chem. Lett., 2013, vol. 4, pp. 2752–57.

[34] Marta D Rossell, Piyush Agrawal, Andreas Borgschulte, Cécile Cécile, Hébert Hébert, Daniele Passerone, and Rolf Erni: *Chem. Mater*, 2015, vol. 27, p. 33.

[35] Xiaoyan Yang, Alberto J. Fernández-Carrión, Jiehua Wang, Florence Porcher, Franck Fayon, Mathieu Allix, and Xiaojun Kuang: *Nat. Commun.*, 2018, vol. 9, p. 4484.

[36] Yongtao Liu, Liam Collins, Roger Proksch, Songkil Kim, Brianna R Watson, Benjamin Doughty, Tessa R Calhoun, Mahshid Ahmadi, Anton V Ievlev, Stephen Jesse, Scott T Retterer, Alex Belianinov, Kai Xiao, Jingsong Huang, Bobby G Sumpter, Sergei V Kalinin, Bin Hu, and Olga S Ovchinnikova: *Nat. Mater.*, n.d.

[37] Wan-Jian Yin, Su-Huai Wei, Mowafak M. Al-Jassim, John Turner, and Yanfa Yan: *Phys. Rev. B*, 2011, vol. 83, p. 155102.

[38] Donghyung Kim, Zhuo Zhang, and Kijung Yong: *Nanoscale*, 2018, vol. 10, pp. 20256–65.

[39] Won Jun Jo, Hyun Joon Kang, Ki-Jeong Kong, Yun Seog Lee, Hunmin Park, Younghye Lee, Tonio Buonassisi, Karen K Gleason, and Jae Sung Lee: *Proc. Natl. Acad. Sci. U. S. A.*, 2015, vol. 112, pp. 13774–78.

[40] Li Li, Paul a Salvador, and Gregory S Rohrer: *Nanoscale*, 2014, vol. 6, pp. 24–42.

[41] Deanna C. Hurum, and Alexander G. Agrios, Kimberly A. Gray*, Tijana Rajh and, and Marion C. Thurnauer*: 2003.

[42] Yidong Hou, Ling Wu, Xinchen Wang, Zhengxin Ding, Zhaohui Li, and Xianzhi Fu: *J. Catal.*, 2007, vol. 250, pp. 12–18.

[43] Raynald Gauvin, Eric Lifshin, Hendrix Demers, Paula Horny, and Helen Campbell: 2006.

6 Summary and Future Work

6.1 List of results and Summary

6.1.1 Spatial selectivity from facets and chemical terminations in $SrTiO_3$

1) On annealing at 1250 °C for 8 hours, the surfaces of polycrystalline $SrTiO_3$ were composed of a combination of {100} and {110} facets.

2) The {100} facets appear to be uniformly photocathodic and serve as reduction sites. The {110} facets appear to be uniformly photoanodic and serve as oxidation sites.

3) On annealing again at 1100 °C for 4 hours in presence of 0.1 g $Sr_3Ti_2O_7$, the {110} facets were converted from completely photoanodic to part photoanodic – part photocathodic.

This study showed that tailoring spatial selectivity on polycrystalline photocatalysts is possible by taking advantage of the surface energy anisotropy of the material to create facets and using simple thermochemical treatments to change surface chemistry.

6.1.2 Spatial selectivity on ferroelastic domains of centrosymmetric polycrystalline WO_3

1) The ferroelastic domain structure at the surface of polished γ-WO_3 ceramics is hierarchical, having three levels of ferroelastic domains.

2) For all orientations, the coarser two tiers of ferroelastic domains (primary and secondary) are piezo-responsive (polar). The third tier was too fine to be analyzed for spatial selectivity and piezoresponse.

3) The photodeposited silver and lead oxide is correlated to the same two levels of ferroelastic domains that are piezoresponsive in PFM.

This study showed that the polarization of ferroelastic domains in centrosymmetric ferroelastics is not limited to $BiVO_4$. It is an encouraging result to push for the inclusion of ferroelastic photocatalysts in the materials space of spatially selective photocatalysts.

6.1.3 Investigating the effect of different stress states on polarization of ferroelastic domains in centrosymmetric $BiVO_4$

1) Spatial selectivity of photodeposition reactions was seen on isolated regions of a polycrystalline sample as well as hydrothermally grown crystals. This implied that the stresses from surrounding grains are not a necessary factor in creating ferroelastic domain specific spatial selectivity in $BiVO_4$.

2) Spatial selectivity was observed when photodeposition was carried out above the FTT. This implied that there is a factor other than domain-stress-strain coupling that results in spatial selectivity.

3) Because of the confirmed presence of this unknown factor that is not a domain-stress-strain coupling, no conclusion can be drawn as to whether bulk stresses contribute to the creation of ferroelastic domain specific spatial selectivity.

The main finding of this study was that there is at least one factor that is not a domain-stress-strain coupling that leads to spatial selectivity of photoreactions on the surface of centrosymmetric $BiVO_4$. Accumulation of point defects may be a possible reason for the existence of spatial selectivity above FTT.

6.1.4 Summary

The results show that spatial selectivity is present on two large classes of centrosymmetric oxide photocatalysts – Perovskites and Ferroelastics. The spatial selectivity on centrosymmetric Perovskite $SrTiO_3$ from two features creating charge separation (crystal facets and chemical terminations) simultaneously was studied. The possibility of tuning the photocathodic-photoanodic area on the same was shown. The results demonstrate a method to engineer other Perovskites with favorable band-gaps, to extract the best possible photocatalytic efficiency from them. For example, Hybrid inorganic-organic Perovskites show excellent properties conducive for solar applications: Ideal band gaps and long carrier diffusion lengths. Tuning the crystal facets as well as surface chemistry in such compounds has tremendous potential to further improve their usability in photocatalytic systems and solar cells (for efficient charge transport and collection).

While it was demonstrated that spatial selectivity could be engineered on centrosymmetric $SrTiO_3$, more work is needed to pinpoint the reason for spatial selectivity in centrosymmetric ferroelastics, which would make it possible to engineer the photocathodic-photoanodic area ratio as desired. That ferroelastic domain-driven spatial selectivity is not a feature unique to $BiVO_4$ was shown by demonstrating the same on centrosymmetric WO_3. This result supports that ferroelastic domain-driven spatial selectivity could be a general property of the class of ferroelastic materials. Thus, they could be potential candidate materials for photocatalytic systems. However, determining whether internal stresses from a change in crystal system or external stresses from surrounding grains proved to be inconclusive. Interestingly, a novel finding from this study was that there is a remnant effect that creates spatial selectivity even above the FTT, that reflects the ferroelastic domain structure present below the FTT. Also, the ferroelastic domain structure remained almost identical after thermal cycling above and below the FTT. This suggested that there is some imprinting factor causes the ferroelastic domains to re-appear with the same pattern. It is possible that point defects get accumulated due to the different stress states in the ferroelastic domains, but more work needs to be done to test this hypothesis.

6.2 Future work

6.2.1 Quantifying the change in reaction rate after tailoring the surface of a polycrystalline photocatalyst

While I have shown that it is possible to tailor the spatial selectivity on polycrystalline $SrTiO_3$, it is necessary to systematically investigate the effect of changing the photoanodic-photocathodic area ratio on overall reaction rate. It would be useful to study three reactions requiring different numbers of electrons and holes per mole of product. For example, hydrogen evolution requires 2 electrons for one mole of H_2 while oxygen evolution requires 4 holes per mole of O_2. Hence, my hypothesis would be that the highest reaction rate for such a reaction would be achieved for a photoanodic-photocathodic ratio greater than 0.5. Similarly, one reaction which requires more electrons than holes per mole of product as well as one where equal amounts of both are required should be studied. While it is difficult to quantify the exact ratio of photoanodic-photocathodic surface area in a polycrystal, by comparing the peak positions of the photoredox rates of three such reactions, we can test the following hypothesis: Assuming a graph of redox reaction rate (y-axis) vs. photocathodic-photoanodic area ratio (x-axis), the peak of a more electron intensive reaction will be achieved after carrying out a Sr-rich treatment of the polycrystalline surface that gives the peak of a lesser electron intensive reaction. Determining the shifts in reaction rates after effecting simple thermochemical treatments is of commercial importance.

6.2.2 Studying the diffusion of dopants/vacancies via strain gradients

Given that accumulation of point defects is a possible explanation to an anomalous spatial selectivity above the FTT, studying whether strain gradient induced diffusion of dopants or vacancies is possible is important. This is not just important for ferroelastic photocatalysts, but also in Perovskite solar cells where cell degradation due to phase separation is a big roadblock to commercialization [1,2]. There has been some work on modulating stress in these cells to improve stability [3], but the fundamental reason for segregation is still unknown.

Chapter 6: Summary and future work

I propose that simple experiments can be carried out on thin films to ascertain the effects of a strain gradient on chemical diffusion. Na, Mo doped $BiVO_4$ films can be synthesized and checked for surface composition via XPS. Then, out of say three films, one can be subjected to a tensile stress on the surface and another to a compressive stress by bending. The third film can be kept as is under the same atmospheric conditions. The surface composition of all three should be measured after a time interval. If possible, all three should be measured after a fixed time interval in the vacuum chamber to account for its effect in diffusion of Na/Mo.

If this experiment suggests that stress and strain gradients can cause diffusion of Na/Mo, then

It is worth studying the possible ferroelastic domain specific segregation of Na/Mo, due to different stress states and strain gradients present in adjacent ferroelastic domains. Such segregation can lead to spatial selectivity due to a phase heterojunction, as described in the discussion of chapter 5. One possible way to explore this is to carry out resonance tracking PFM and take the peak frequency map as a function of (x,y). Different elasticity due to different surface chemistry changes the resonant frequency locally [4], and it would be possible to comment on ferroelastic domain driven accumulation of point defects. Carrying out this experiment above the FTT would remove any crosstalk from topography or bulk stress effects in changing the local elasticity.

Further experiments to check local composition directly can be carried out using SIMS as shown by Liu et. al. [5]. If there is a change in elasticity but not change in surface chemistry, it suggests that vacancy accumulation could be a reason for the spatial selectivity above FTT.

6.3 References

[1] Aron Walsh and Samuel D. Stranks: *ACS Energy Lett.*, 2018, vol. 3, pp. 1983–90.

[2] Makhsud I. Saidaminov, Junghwan Kim, Ankit Jain, Rafael Quintero-Bermudez, Hairen Tan, Guankui Long, Furui Tan, Andrew Johnston, Yicheng Zhao, Oleksandr Voznyy, and Edward H. Sargent: *Nat. Energy*, 2018, vol. 3, pp. 648–54.

[3] Nicholas Rolston, Kevin A. Bush, Adam D. Printz, Aryeh Gold-Parker, Yichuan Ding, Michael F. Toney, Michael D. McGehee, and Reinhold H. Dauskardt: *Adv. Energy Mater.*, 2018, vol. 8, pp. 1–7.

[4] Boyuan Huang, Guoli Kong, Ehsan Nasr Esfahani, Shulin Chen, Qian Li, Junxi Yu, Ningan Xu, Ying Zhang, Shuhong Xie, Haidan Wen, Peng Gao, Jinjin Zhao, and Jiangyu Li: 2018, vol. 3, p. 30.

[5] Yongtao Liu, Liam Collins, Roger Proksch, Songkil Kim, Brianna R Watson, Benjamin Doughty, Tessa R Calhoun, Mahshid Ahmadi, Anton V Ievlev, Stephen Jesse, Scott T Retterer, Alex Belianinov, Kai Xiao, Jingsong Huang, Bobby G Sumpter, Sergei V Kalinin, Bin Hu, and Olga S Ovchinnikova: *Nat. Mater.*, n.d.

7 Appendix

A.1 Definitions for ferroelastics

Prototypic phase

The “parent” phase or the paraelastic phase in the ferroelastic transition under consideration

Ferroic phase

The “daughter” phase resulting from a symmetry lowering phase transition from the prototype

Non-ferroic phase transition

A phase transition where the point group symmetry does not change. For example, Cu_3Au – Fm3m to Pm3m [1]

Isomorphous phase transition

A phase transition where the space group symmetry does not change. E.g. Ce under high pressure [1]

Partial ferroelastics

Where the spontaneous strain tensor is the same in at least two orientation states. E.g. $BaTiO_3$ – 180 degree ferroelectric domains [2]

Full ferroelastics

Where the spontaneous strain tensor is different in all orientation states [2]

Chapter 7: Appendix

Co-elastic materials

The materials that display a spontaneous strain on phase transition but there is no breaking of symmetry. [3] These are not ferroelastic in nature.

Proper ferroelastics

Where a) The spontaneous strain is the order parameter. These are called true-proper ferroelastics or b) The spontaneous strain is coupled to the order parameter, which is an optical soft mode. These are called pseudo-proper ferroelastics. The transition in $BiVO_4$ is a pseudo-proper transition.

Improper ferroelastics

Where the order parameter symmetry is different from that of the spontaneous strain tensor [4]. For example, in $BaTiO_3$, the breaking of symmetry from cubic to tetragonal results in a spontaneous strain along the c-axis, but it does not account for the emergence of polarization. That can be only accounted for when this symmetry is intersected with that of a polar vector along the c-axis. Thus, the final symmetry is actually lower than that of the spontaneous strain. In this case, the material is termed as an improper ferroelastic. It is actually a proper ferroelectric transition.

A.2 Codes for determining facet orientation

Code C1

```
function C1_obtaining_surface_normals(path,range,step_size,e1,e2,e3)

    B = zeros(range);
    A = xlsread(path);
    matrixX = ones(range);
    matrixY = ones(range);
```

```
    matrixZ = ones(range);
    matrixX_corrected=ones(range);
    matrixY_corrected=ones(range);
    matrixZ_corrected=ones(range);

    n=1;
    for j =1:range
        for i=1:range
        matrixX(range-n+1,i) = A((n-1)*range+i,1);
        matrixY(range-n+1,i) = A((n-1)*range+i,2);
        matrixZ(range-n+1,i) = A((n-1)*range+i,3);
        end
        n=n+1;
    end


    %correction - to put (1,1) at the left bottom of matrix. This is
        %done by inverting the y values but keeping x values the same.
        for q=1:range

        matrixX_corrected(range+1-q,:)=matrixX(q,:);
        matrixY_corrected(range+1-q,:)=matrixY(q,:);
        matrixZ_corrected(range+1-q,:)=matrixZ(q,:);
        end

         xlswrite('gridX.xlsx',matrixX);
    xlswrite('gridY.xlsx',matrixY);
    xlswrite('gridZ.xlsx',matrixZ);
    xlswrite('gridX_corrected.xlsx',matrixX_corrected);
    xlswrite('gridY_corrected.xlsx',matrixY_corrected);
    xlswrite('gridZ_corrected.xlsx',matrixZ_corrected);

    %creating the 3D reconstruction---------------
[X,Y]=meshgrid(1*step_size:1*step_size:step_size*range,1*step_size:1*step_siz
e:step_size*range);
fig1=figure;
surf(X,Y,matrixZ,'EdgeColor','k')
colormap('gray')
brighten(0.3);
title('surface')
view([-6 46])
j=1;
%----------------------------------



z_values = xlsread('gridZ_corrected.xlsx');


[Nx,Ny,Nz] = surfnorm(X,Y,matrixZ);
%xlswrite('C:\Google                  Drive\Project\Images                  and
data\Matlab\3dsurf\surfacenormal.xlsx',[Nx,Ny,Nz]);
xlswrite('Znormal.xlsx',[Nz]);
xlswrite('Ynormal.xlsx',[Ny]);
xlswrite('Xnormal.xlsx',[Nx]);
surfnormmatrix=ones(range^2,3);
```

```
 %correction - to put (1,1) at the left bottom of matrix. This is
        %done by inverting the y values but keeping x values the same.
        for q=1:range

        Xnormal_corrected(range+1-q,:)=Nx(q,:);
        Ynormal_corrected(range+1-q,:)=Ny(q,:);
        Znormal_corrected(range+1-q,:)=Nz(q,:);

        end
xlswrite('Znormal_corrected.xlsx',Znormal_corrected);
xlswrite('Ynormal_corrected.xlsx',Ynormal_corrected);
xlswrite('Xnormal_corrected.xlsx',Xnormal_corrected);


%--------Interactive selection of normals from surfnorm---%
interactivenormals_surfnorm=zeros(50,7);
count2=1;
while count2<51
    dcm_obj=datacursormode(fig1);
datacursormode on;
k = waitforbuttonpress;

info_struct = getCursorInfo(dcm_obj);
x_coord = int8(info_struct.Position(1)/step_size);
y_coord = int8(info_struct.Position(2)/step_size);
interactivenormals_surfnorm(count2,1)=Xnormal_corrected(range+1-
y_coord,x_coord);
interactivenormals_surfnorm(count2,2)=Ynormal_corrected(range+1-
y_coord,x_coord);
interactivenormals_surfnorm(count2,3)=Znormal_corrected(range+1-
y_coord,x_coord);
A=C2_rotation_into_grain_frame_of_reference(e1+180,e2,e3,[interactivenormals_
surfnorm(count2,1)                         interactivenormals_surfnorm(count2,2)
interactivenormals_surfnorm(count2,3)]);
%e1+180 is to account for inconsistency between SEM and Euler angles from
%OXFORD
interactivenormals_surfnorm(count2,5)=A(1);
interactivenormals_surfnorm(count2,6)=A(2);
interactivenormals_surfnorm(count2,7)=A(3);
count2=count2+1
clear x_coord y_coord dcm_obj info_struct
end

xlswrite('interactive normals.xlsx',interactivenormals_surfnorm);
end
```

Code C2

```
function A=C2_rotation_into_grain_frame_of_reference (e1,e2,e3,vector)

%parameters - e1,e2,e3 - Euler angles of the grain obtained from EBSD
```

```
%(OXFORD System). Code has to be amended for other systems as the
%microscope frame of reference differs from system to system.

%vector - vector in the microscope frame of reference to be changed into
%grain frame of reference

%G -rotation matrix obtained by successive rotation in the order e1 - e2 -
%e3

%A - rotated vector normalized to magnitude = 1 i.e. A(1)^2 + A(2)^2 +
%A(3)^2 = 1

G                =               [cosd(e1)*cosd(e3)-sind(e1)*sind(e3)*cosd(e2)
sind(e1)*cosd(e3)+cosd(e1)*sind(e3)*cosd(e2) sind(e3)*sind(e2);
     -cosd(e1)*sind(e3)-sind(e1)*cosd(e3)*cosd(e2)                           -
sind(e1)*sind(e3)+cosd(e1)*cosd(e3)*cosd(e2) cosd(e3)*sind(e2);
     sind(e1)*sind(e2) -cosd(e1)*sind(e2) cosd(e2)];
A=(vector*transpose(G))*1/(norm(vector*transpose(G)));

end
```

Code C3

```
function C3_SST_projection(path,points)

%---Parameters-------%
%path - file path of input .xlsx file of a (points x 7) size matrix
%points - number of surface normals in the path file


% ----READING INPUT----
% Read input file - interactive normals.xlsx from surface normal code

Inputdata=xlsread(path);

% ----FITTING ALL POINTS IN CUBIC SST SPACE----
% Columns 5,6, and 7 are used since they are the components of surface
% normals after rotation by Euler angles of the grain (including 180 degree
% correction for discrepency between EBSD and microscope frame

    %Checking all possible combinations using cubic symmetry conditions for
    %each surface normal from input file
    for i=1:points

    X=Inputdata(i,5);
    Y=Inputdata(i,6);
    Z=Inputdata(i,7);

    %PointsToCheck lists all possible combinations of surface normal
    %components using symmetry conditions of the cubic system. There are 48
```

```
    %possibilities in total

    %The if condition checks for three things - 1) Whether the
    PointsToCheck=[ X Y Z ; -X -Y Z ; -X Y -Z ; X -Y -Z ; Z X Y ; Z -X -Y ; -Z
-X Y ; -Z X -Y ; Y Z X ; -Y Z -X ; Y -Z -X  ; -Y -Z X ; Y X -Z ; -Y -X -Z ; Y
-X Z ; -Y X Z ; X Z -Y ; -X Z Y ; -X -Z -Y ; X -Z Y ; Z Y -X ; Z -Y X ; -Z Y X
; -Z -Y -X ; -X -Y -Z ; X Y -Z ; X -Y Z ; -X Y Z ; -Z -X -Y ; -Z X Y ; Z X -Y
; Z -X Y ; -Y -Z -X ; Y -Z X ; -Y Z X ; Y Z -X ; -Y -X Z ; Y X Z ; -Y X -Z ; Y
-X -Z ; -X -Z Y ; X -Z -Y ; X Z Y ; -X Z -Y ; -Z -Y X ; -Z Y -X ; Z -Y -X ; Z
Y X];
    for j=1:48
        v1=atand(PointsToCheck(j,2)/PointsToCheck(j,1));
        A                                                                   =
(sqrt((PointsToCheck(j,1))^2+(PointsToCheck(j,2))^2))/(1+PointsToCheck(j,3));
        %checking whether the projection lies in the SST;
        if  (v1  >=  0)  &&  (v1  <=  45)  &&  (PointsToCheck(j,1)  >=  0)  &&
(PointsToCheck(j,2) >= 0) && (PointsToCheck(j,3) >= 0) && ((abs(A)*sind(v1)) <=
sqrt(1-2.*((abs(A)*cosd(v1))^2))) && ((abs(A)*cosd(v1)) <= 1/(1+sqrt(2)))

            break;
        else
        end
    end
    j
    if j==48
        v1
        A
        PointsToCheck(j,:)

    end

    %phi - angle of projection from x-axis
    %dist - radial distance from (0,0)
    %the projection coordinates are parametric (phi,dist)
    phi(i)=atand(PointsToCheck(j,2)/PointsToCheck(j,1));
    dist(i)=A;
    clear a x b X Y Z PointsToCheck j A;
    end



    %result.xlsx is the final file with parametric coordinates of projections
of
    %all normals
    %xlswrite('C:\Google  Drive\Project\Images  and  data\AFM  data\1d_1f_c2_afm
for    facet    orientation\Data    for    plotting    surface    normals    on
SST\result.xlsx',[cosd(phi(:)).*dist(:) sind(phi(:)).*dist(:)]);

    %scatter plot of the projections on the X-Y plane

scatter(cosd(phi(:)).*dist(:),sind(phi(:)).*dist(:),20,'MarkerFaceColor',(1/2
55)*[0 0 0],'MarkerEdgeColor',(1/255)*[0 0 0])
    title('oxidative');
    set(gca,'visible','off')
    hold on
```

```
   %Drawing the SST--------

    x1=0:0.01:1;
    y1=0:0.01:1;
    plot(x1,y1,'k')
    set(gca,'visible','off')
    hold on

   poleprojectionforplot = xlsread('-101_pole projection.xlsx');
   plot(poleprojectionforplot(:,1),poleprojectionforplot(:,2),'k')
    set(gca,'visible','off')

    hold on

    x2=0:0.01:1;
    y2=zeros(1,101);
    plot(x2(:),y2(1,:),'k')
    set(gca,'visible','off')
    hold on

end
```

-101_pole_projection.xlsx

These are the X-Y coordinates of the pole projection of the great circle of [-1 0 1] till X = 0.414, Y = 0. This file is used in Code C1. Copy these columns into an .xlsx file and keep it in the same folder as code C1 with the file name '-101_pole_projection.xlsx'.

0	1	0.014778	0.985	0.029126	0.97	0.043062	0.954998
0.000999	0.999	0.015748	0.984	0.030068	0.969	0.043977	0.953998
0.001996	0.998	0.016716	0.983	0.031008	0.967999	0.04489	0.952998
0.002991	0.997	0.017682	0.982	0.031946	0.966999	0.045802	0.951997
0.003984	0.996	0.018646	0.981	0.032882	0.965999	0.046711	0.950997
0.004975	0.995	0.019608	0.98	0.033816	0.964999	0.047619	0.949997
0.005964	0.994	0.020568	0.979	0.034749	0.963999	0.048525	0.948997
0.006951	0.993	0.021526	0.978	0.03568	0.962999	0.04943	0.947997
0.007937	0.992	0.022483	0.977	0.036609	0.961999	0.050332	0.946996
0.00892	0.991	0.023438	0.976	0.037536	0.960999	0.051233	0.945996
0.009901	0.99	0.02439	0.975	0.038462	0.959999	0.052133	0.944996
0.01088	0.989	0.025341	0.974	0.039385	0.958999	0.05303	0.943995
0.011858	0.988	0.02629	0.973	0.040307	0.957999	0.053926	0.942995
0.012833	0.987	0.027237	0.972	0.041227	0.956998	0.05482	0.941995
0.013807	0.986	0.028183	0.971	0.042146	0.955998	0.055713	0.940994

0.056604	0.939994	0.094203	0.895946	0.12892	0.851786	0.161074	0.807408
0.057493	0.938993	0.095023	0.894944	0.129678	0.850781	0.161777	0.806396
0.05838	0.937993	0.095841	0.893942	0.130435	0.849775	0.162479	0.805383
0.059266	0.936993	0.096658	0.89294	0.13119	0.848769	0.16318	0.804371
0.06015	0.935992	0.097473	0.891938	0.131944	0.847763	0.16388	0.803358
0.061033	0.934992	0.098287	0.890936	0.132697	0.846757	0.164578	0.802345
0.061914	0.933991	0.099099	0.889933	0.133449	0.84575	0.165275	0.801332
0.062793	0.932991	0.09991	0.888931	0.134199	0.844744	0.165972	0.800319
0.06367	0.93199	0.100719	0.887928	0.134948	0.843737	0.166667	0.799305
0.064546	0.930989	0.101527	0.886926	0.135696	0.842731	0.167361	0.798292
0.065421	0.929989	0.102334	0.885923	0.136442	0.841724	0.168053	0.797278
0.066293	0.928988	0.103139	0.884921	0.137187	0.840717	0.168745	0.796264
0.067164	0.927987	0.103943	0.883918	0.137931	0.83971	0.169435	0.795249
0.068034	0.926987	0.104745	0.882915	0.138674	0.838703	0.170124	0.794235
0.068901	0.925986	0.105546	0.881912	0.139415	0.837696	0.170813	0.79322
0.069767	0.924985	0.106345	0.880909	0.140155	0.836688	0.1715	0.792205
0.070632	0.923984	0.107143	0.879906	0.140893	0.835681	0.172185	0.79119
0.071495	0.922984	0.107939	0.878903	0.141631	0.834673	0.17287	0.790174
0.072356	0.921983	0.108734	0.8779	0.142367	0.833665	0.173554	0.789159
0.073216	0.920982	0.109528	0.876897	0.143102	0.832657	0.174236	0.788143
0.074074	0.919981	0.11032	0.875893	0.143836	0.831649	0.174917	0.787127
0.074931	0.91898	0.111111	0.87489	0.144568	0.830641	0.175598	0.786111
0.075786	0.917979	0.111901	0.873886	0.145299	0.829632	0.176277	0.785094
0.076639	0.916978	0.112689	0.872883	0.146029	0.828624	0.176955	0.784078
0.077491	0.915977	0.113475	0.871879	0.146758	0.827615	0.177632	0.783061
0.078341	0.914976	0.11426	0.870875	0.147485	0.826606	0.178307	0.782043
0.07919	0.913975	0.115044	0.869871	0.148211	0.825597	0.178982	0.781026
0.080037	0.912973	0.115827	0.868868	0.148936	0.824588	0.179655	0.780008
0.080882	0.911972	0.116608	0.867864	0.14966	0.823579	0.180328	0.77899
0.081726	0.910971	0.117387	0.866859	0.150382	0.822569	0.180999	0.777972
0.082569	0.90997	0.118166	0.865855	0.151104	0.82156	0.181669	0.776954
0.08341	0.908968	0.118943	0.864851	0.151824	0.82055	0.182339	0.775935
0.084249	0.907967	0.119718	0.863847	0.152542	0.81954	0.183007	0.774916
0.085087	0.906965	0.120493	0.862842	0.15326	0.81853	0.183673	0.773897
0.085923	0.905964	0.121265	0.861838	0.153976	0.81752	0.184339	0.772878
0.086758	0.904962	0.122037	0.860833	0.154691	0.816509	0.185004	0.771858
0.087591	0.903961	0.122807	0.859828	0.155405	0.815499	0.185668	0.770838
0.088423	0.902959	0.123576	0.858823	0.156118	0.814488	0.18633	0.769818
0.089253	0.901958	0.124343	0.857818	0.15683	0.813477	0.186992	0.768798
0.090082	0.900956	0.125109	0.856813	0.15754	0.812466	0.187652	0.767777
0.090909	0.899954	0.125874	0.855808	0.158249	0.811455	0.188312	0.766756
0.091735	0.898952	0.126638	0.854803	0.158957	0.810443	0.18897	0.765735
0.092559	0.89795	0.1274	0.853797	0.159664	0.809432	0.189627	0.764714
0.093382	0.896948	0.12816	0.852792	0.160369	0.80842	0.190283	0.763692

0.190939	0.76267	0.21875	0.71739	0.244713	0.671334	0.269006	0.624199
0.191593	0.761648	0.21936	0.716353	0.245283	0.670276	0.26954	0.623112
0.192246	0.760625	0.219969	0.715315	0.245852	0.669218	0.270073	0.622025
0.192897	0.759602	0.220577	0.714277	0.24642	0.668159	0.270605	0.620936
0.193548	0.758579	0.221184	0.713239	0.246988	0.667099	0.271137	0.619847
0.194198	0.757556	0.22179	0.7122	0.247555	0.666039	0.271668	0.618757
0.194847	0.756532	0.222395	0.711161	0.24812	0.664978	0.272198	0.617667
0.195495	0.755508	0.222999	0.710122	0.248685	0.663917	0.272727	0.616575
0.196141	0.754484	0.223602	0.709082	0.249249	0.662855	0.273256	0.615483
0.196787	0.753459	0.224205	0.708041	0.249812	0.661792	0.273784	0.61439
0.197432	0.752434	0.224806	0.707001	0.250375	0.660729	0.274311	0.613296
0.198075	0.751409	0.225407	0.705959	0.250936	0.659665	0.274837	0.612202
0.198718	0.750383	0.226006	0.704918	0.251497	0.658601	0.275362	0.611106
0.199359	0.749358	0.226605	0.703875	0.252057	0.657536	0.275887	0.61001
0.2	0.748331	0.227202	0.702833	0.252616	0.656471	0.276411	0.608913
0.200639	0.747305	0.227799	0.70179	0.253174	0.655404	0.276934	0.607815
0.201278	0.746278	0.228395	0.700746	0.253731	0.654338	0.277457	0.606716
0.201915	0.745251	0.22899	0.699703	0.254288	0.65327	0.277978	0.605617
0.202552	0.744224	0.229584	0.698658	0.254844	0.652202	0.278499	0.604516
0.203187	0.743196	0.230177	0.697613	0.255398	0.651134	0.279019	0.603415
0.203822	0.742168	0.230769	0.696568	0.255952	0.650064	0.279539	0.602312
0.204455	0.74114	0.23136	0.695522	0.256506	0.648994	0.280058	0.601209
0.205087	0.740111	0.231951	0.694476	0.257058	0.647924	0.280576	0.600105
0.205719	0.739082	0.23254	0.693429	0.25761	0.646853	0.281093	0.599
0.206349	0.738053	0.233129	0.692382	0.25816	0.645781	0.281609	0.597895
0.206979	0.737023	0.233716	0.691335	0.25871	0.644708	0.282125	0.596788
0.207607	0.735993	0.234303	0.690287	0.259259	0.643635	0.28264	0.59568
0.208234	0.734962	0.234889	0.689238	0.259808	0.642561	0.283154	0.594572
0.208861	0.733932	0.235474	0.688189	0.260355	0.641487	0.283668	0.593462
0.209486	0.732901	0.236058	0.687139	0.260902	0.640412	0.28418	0.592352
0.210111	0.731869	0.236641	0.686089	0.261448	0.639336	0.284692	0.591241
0.210734	0.730837	0.237223	0.685039	0.261993	0.638259	0.285204	0.590128
0.211356	0.729805	0.237805	0.683988	0.262537	0.637182	0.285714	0.589015
0.211978	0.728773	0.238385	0.682936	0.26308	0.636104	0.286224	0.587901
0.212598	0.72774	0.238965	0.681884	0.263623	0.635025	0.286733	0.586786
0.213218	0.726706	0.239544	0.680831	0.264165	0.633946	0.287242	0.58567
0.213836	0.725673	0.240122	0.679778	0.264706	0.632866	0.287749	0.584553
0.214454	0.724639	0.240699	0.678725	0.265246	0.631785	0.288256	0.583435
0.215071	0.723604	0.241275	0.67767	0.265786	0.630703	0.288762	0.582316
0.215686	0.72257	0.24185	0.676616	0.266324	0.629621	0.289268	0.581195
0.216301	0.721534	0.242424	0.675561	0.266862	0.628538	0.289773	0.580074
0.216915	0.720499	0.242998	0.674505	0.267399	0.627454	0.290277	0.578952
0.217527	0.719463	0.24357	0.673448	0.267936	0.62637	0.29078	0.577829
0.218139	0.718427	0.244142	0.672392	0.268471	0.625285	0.291283	0.576705

0.291785	0.57558	0.313187	0.524919	0.333333	0.471405	0.352332	0.413762
0.292286	0.574454	0.313658	0.523739	0.333777	0.470146	0.352751	0.41239
0.292786	0.573326	0.314129	0.522556	0.334221	0.468886	0.353169	0.411014
0.293286	0.572198	0.314599	0.521373	0.334664	0.467624	0.353588	0.409635
0.293785	0.571069	0.315068	0.520187	0.335106	0.466359	0.354005	0.408252
0.294284	0.569938	0.315537	0.519001	0.335548	0.465093	0.354422	0.406867
0.294781	0.568807	0.316005	0.517812	0.335989	0.463824	0.354839	0.405478
0.295278	0.567674	0.316473	0.516623	0.33643	0.462553	0.355255	0.404085
0.295775	0.56654	0.31694	0.515431	0.33687	0.461279	0.35567	0.402689
0.29627	0.565406	0.317406	0.514238	0.337309	0.460004	0.356085	0.40129
0.296765	0.56427	0.317872	0.513044	0.337748	0.458726	0.356499	0.399887
0.297259	0.563133	0.318337	0.511848	0.338187	0.457446	0.356913	0.39848
0.297753	0.561994	0.318801	0.51065	0.338624	0.456163	0.357326	0.39707
0.298246	0.560855	0.319265	0.509451	0.339061	0.454878	0.357739	0.395657
0.298738	0.559714	0.319728	0.50825	0.339498	0.453591	0.358151	0.394239
0.299229	0.558573	0.32019	0.507048	0.339934	0.452302	0.358563	0.392818
0.29972	0.55743	0.320652	0.505844	0.340369	0.45101	0.358974	0.391393
0.30021	0.556286	0.321113	0.504638	0.340804	0.449716	0.359385	0.389965
0.300699	0.555141	0.321574	0.503431	0.341238	0.448419	0.359795	0.388532
0.301188	0.553994	0.322034	0.502221	0.341672	0.447119	0.360205	0.387096
0.301676	0.552847	0.322493	0.501011	0.342105	0.445818	0.360614	0.385655
0.302163	0.551698	0.322952	0.499798	0.342538	0.444513	0.361022	0.384211
0.30265	0.550548	0.32341	0.498584	0.34297	0.443207	0.36143	0.382763
0.303136	0.549397	0.323867	0.497368	0.343401	0.441897	0.361838	0.38131
0.303621	0.548244	0.324324	0.49615	0.343832	0.440585	0.362245	0.379854
0.304106	0.547091	0.324781	0.494931	0.344262	0.439271	0.362651	0.378393
0.30459	0.545936	0.325236	0.49371	0.344692	0.437954	0.363057	0.376928
0.305073	0.544779	0.325691	0.492486	0.345121	0.436634	0.363463	0.375459
0.305556	0.543622	0.326146	0.491262	0.34555	0.435311	0.363868	0.373985
0.306037	0.542463	0.326599	0.490035	0.345978	0.433986	0.364272	0.372507
0.306519	0.541303	0.327052	0.488806	0.346405	0.432658	0.364676	0.371025
0.306999	0.540141	0.327505	0.487576	0.346832	0.431327	0.365079	0.369538
0.307479	0.538979	0.327957	0.486344	0.347258	0.429994	0.365482	0.368047
0.307958	0.537815	0.328408	0.48511	0.347684	0.428657	0.365885	0.366551
0.308437	0.536649	0.328859	0.483874	0.34811	0.427318	0.366286	0.36505
0.308915	0.535483	0.329309	0.482636	0.348534	0.425976	0.366688	0.363544
0.309392	0.534314	0.329759	0.481396	0.348958	0.424631	0.367089	0.362034
0.309869	0.533145	0.330208	0.480154	0.349382	0.423283	0.367489	0.360519
0.310345	0.531974	0.330656	0.47891	0.349805	0.421932	0.367889	0.358999
0.31082	0.530802	0.331104	0.477664	0.350227	0.420578	0.368288	0.357474
0.311295	0.529628	0.331551	0.476416	0.350649	0.419221	0.368687	0.355944
0.311769	0.528453	0.331997	0.475166	0.351071	0.417861	0.369085	0.354409
0.312242	0.527277	0.332443	0.473915	0.351492	0.416498	0.369483	0.352869
0.312715	0.526099	0.332889	0.472661	0.351912	0.415132	0.36988	0.351323

0.370277	0.349772
0.370673	0.348216
0.371069	0.346654
0.371464	0.345087
0.371859	0.343514
0.372254	0.341936
0.372647	0.340351
0.373041	0.338761
0.373434	0.337165
0.373826	0.335563
0.374218	0.333954
0.374609	0.33234
0.375	0.330719
0.37539	0.329092
0.37578	0.327458
0.37617	0.325817
0.376559	0.32417
0.376947	0.322516
0.377335	0.320856
0.377722	0.319188
0.378109	0.317513
0.378496	0.31583
0.378882	0.314141
0.379268	0.312444
0.379653	0.310739
0.380037	0.309026
0.380421	0.307306
0.380805	0.305578
0.381188	0.303841
0.381571	0.302096
0.381953	0.300343
0.382335	0.298581
0.382716	0.29681
0.383097	0.295031
0.383477	0.293242
0.383857	0.291444
0.384236	0.289637
0.384615	0.28782
0.384994	0.285993
0.385372	0.284156
0.385749	0.282309
0.386126	0.280452
0.386503	0.278584
0.386879	0.276706
0.387255	0.274816
0.38763	0.272915
0.388005	0.271003
0.388379	0.269078
0.388753	0.267142
0.389126	0.265194
0.389499	0.263233
0.389872	0.261259
0.390244	0.259272
0.390615	0.257271
0.390987	0.255257
0.391357	0.253229
0.391727	0.251186
0.392097	0.249129
0.392467	0.247056
0.392835	0.244968
0.393204	0.242864
0.393572	0.240744
0.393939	0.238606
0.394306	0.236452
0.394673	0.234279
0.395039	0.232089
0.395405	0.22988
0.39577	0.227651
0.396135	0.225403
0.3965	0.223134
0.396864	0.220843
0.397227	0.218532
0.39759	0.216197
0.397953	0.213839
0.398315	0.211458
0.398677	0.209051
0.399038	0.206619
0.399399	0.20416
0.39976	0.201674
0.40012	0.199158
0.40048	0.196613
0.400839	0.194038
0.401198	0.19143
0.401556	0.188788
0.401914	0.186111
0.402271	0.183398
0.402628	0.180647
0.402985	0.177856
0.403341	0.175024
0.403697	0.172147
0.404052	0.169224
0.404407	0.166253
0.404762	0.16323
0.405116	0.160153
0.40547	0.157019
0.405823	0.153824
0.406176	0.150565
0.406528	0.147236
0.40688	0.143834
0.407232	0.140352
0.407583	0.136785
0.407934	0.133127
0.408284	0.129368
0.408634	0.125501
0.408983	0.121514
0.409333	0.117396
0.409681	0.113132
0.410029	0.108705
0.410377	0.104095
0.410725	0.099275
0.411072	0.094214
0.411418	0.08887
0.411765	0.083189
0.412111	0.077096
0.412456	0.070486
0.412801	0.063194
0.413146	0.054952
0.41349	0.045241
0.413834	0.032783
0.414177	0.010181
0.414214	8.73E-09

The MATLAB files are with Prof. Gregory Rohrer for download.

A.3 Poling experiments

To check if ferroelastic domains in ferroelastics can be poled, an electric field was applied to small regions in the surfaces of these samples using contact AFM with a biased tip (+10 V).

Poling on WO_3

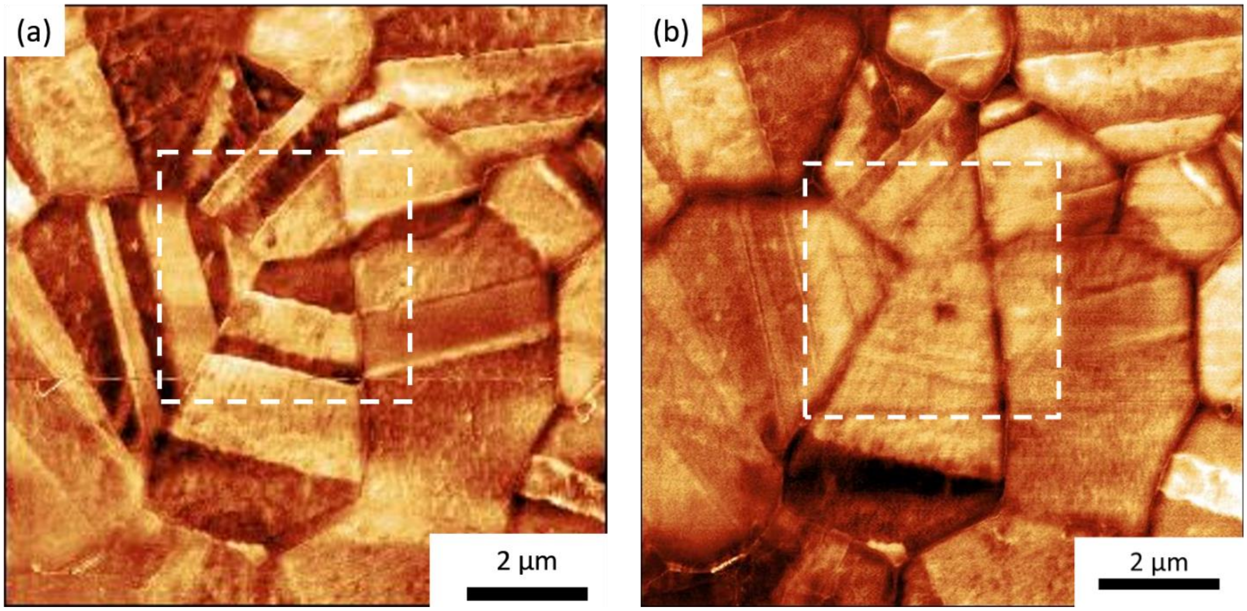

Figure 7-1: PFM phase of the WO_3 surface (a) before and (b) after poling by +10 V. The poled region is indicated by the white dashed line. Vertical scales (dark to bright): (a) 43° (b) 31°

Figure 1(a) shows the PFM phase signal of the WO_3 surface before poling. In every grain, alternate ferroelastic domains are seen to be dark and bright, consistent with earlier work. Only one tier of ferroelastic domains is seen in these large field of view images. Before application of the +10 V potential, the area enclosed in the dashed square has dark and bright regions. However, in

Figure 1(b), the region is quite uniformly bright. This is consistent with the theory that a stress/strain-driven stabilization of the ferroelectric ε-WO_3 phase is enabled by the ferroelastic domains of anti-ferroelectric γ-WO_3. On application of the field, alternate ferroelectric domains coupled to the underlying ferroelastic domains have their polarization vectors changed from pointing downwards to upwards, resulting in a uniform contrast in the poled region.

Another possibility is the accumulation of point charges during the poling phase. Such accumulation can lead to aggregation of adsorbates and create contrast in the PFM signal [5]. To confirm this possibility, we carried out similar poling experiments on $SrTiO_3$ (Not ferroelastic or ferroelectric at room temperature).

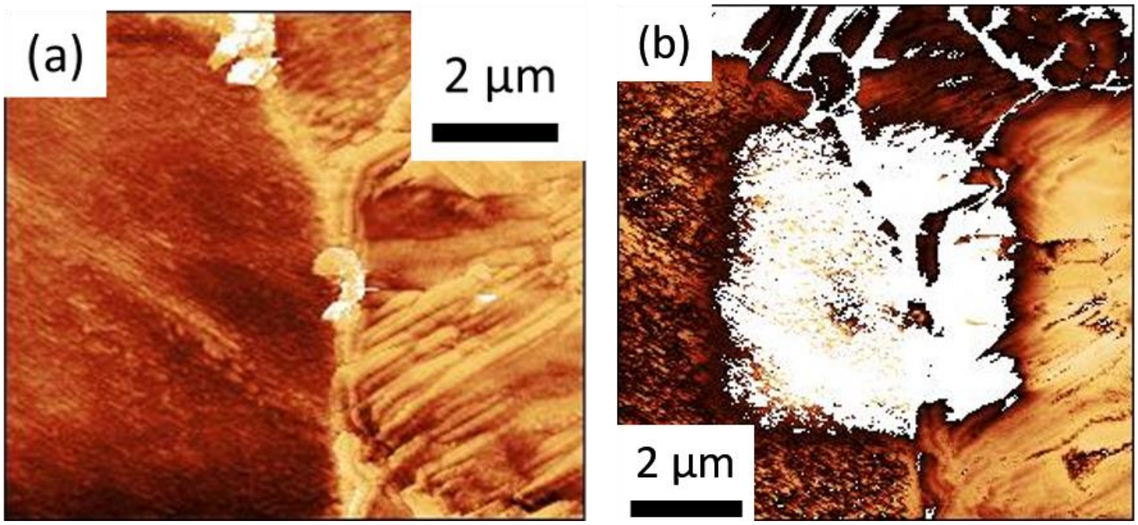

Figure 7-2: PFM phase of the $SrTiO_3$ surface (a) before and (b) after poling by +10 V. The poled region is indicated by the square in (b). Vertical scales (dark to bright): (a) 161° (b) 140°

Figure 2(a) shows the PFM phase of the $SrTiO_3$ surface before poling. Three grains are seen in the figure, with a triple junction near the center of the image. All three grains are faceted. There is some debris in the center of the image that is curved and bright. Figure 2(b) shows the same area after a square of 5x5 µm was poled by +10 V. The phase of the poled square is significantly and uniformly brighter. This implies that there need not be a ferroelectric phase present at the surface in order to obtain contrast in PFM after poling.

Poling on BiVO₄

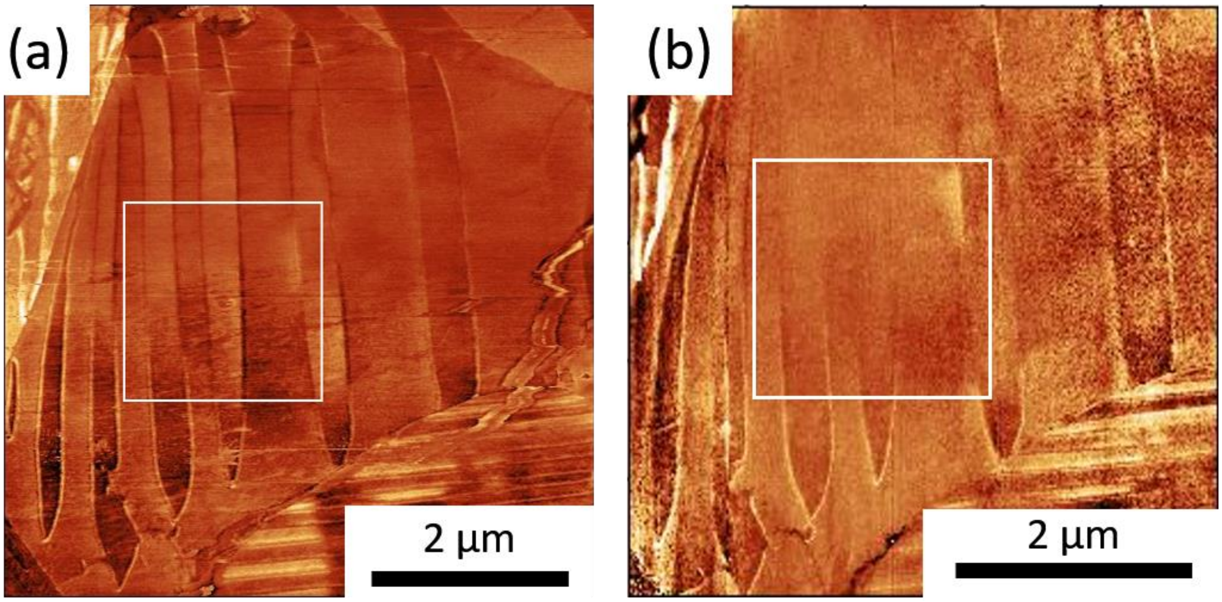

Figure 7-3: PFM phase of an undoped $BiVO_4$ surface (a) before and (b) after poling by +10 V. The poled region is indicated by the white square. Vertical scales (dark to bright): (a) 58° (b) 26°

Figure 3(a) shows the PFM phase on an undoped $BiVO_4$ surface before poling. The ferroelastic domains in the lower part of the central grain alternate dark and bright, with domain walls being the brightest amongst all three. The contrast flips in the middle of the grain. The ferroelastic domains that are brighter in the lower region are darker in the middle and vice versa, with domain walls being darkest. This is due to the anomalous patches of reactivity described in section XYZ. The region that was poled is shown in the white square in both figures. Figure 3(b) shows the PFM phase after poling. Unlike WO_3 and $SrTiO_3$, the phase signal has not changed. The dark ferroelastic domains in the lower part of the poled square were dark even before poling in figure 3(a). Similarly, the domain walls are also bright compared to the ferroelastic domains, as in Figure 3(a). Thus, even after poling with +10 V, we were unable to change the ferroelastic domain pattern in $BiVO_4$.

A.4 References

[1] V. K. Wadhawan: *Bull. Mater. Sci.*, 1984, vol. 6, pp. 733–53.

[2] Kêitsiro Aizu: *Phys. Rev. B*, 1970, vol. 2, pp. 754–72.

[3] E Salje: *Ferroelectrics*, 1990, vol. 104, pp. 111–20.

[4] Vinod K. Wadhawan: *Phase Transitions*, 1982, vol. 3, pp. 3–103.

[5] Sergei V Kalinin and Dawn A Bonnell: n.d.